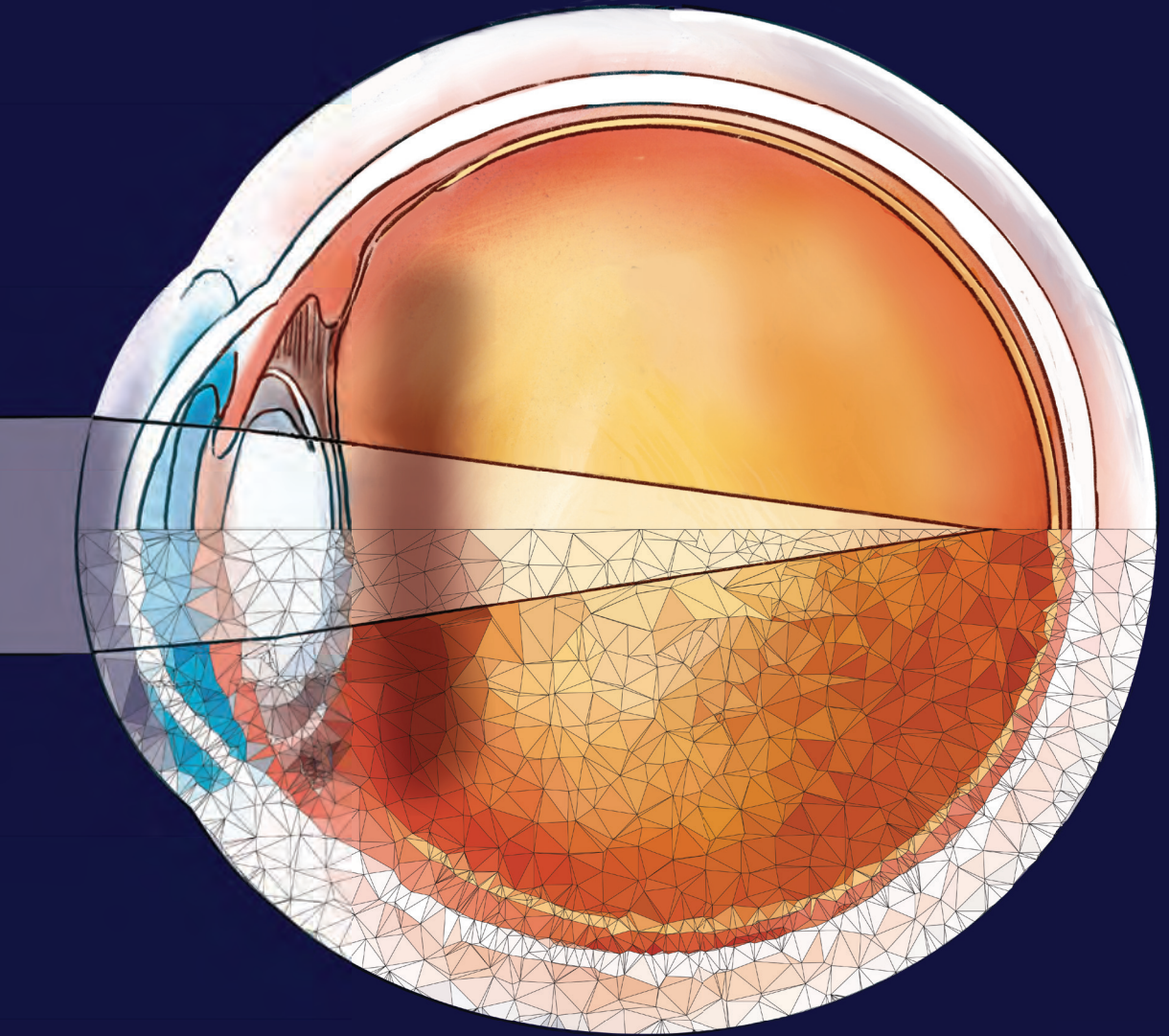


UNCOVERING THE ORIGIN OF NEGATIVE DYSPHOTOPSIA



Luc van Vught

Uncovering the origin of negative dysphotopsia

Luc van Vught

Uncovering the origin of negative dysphotopsia

Thesis, Leiden University, the Netherlands.

Cover design: Sieben Medical Art | siebenmedicalart.com

Layout: Luc van Vught & Anushiya Vanajan

Printing: Ridderprint | ridderprint.nl

ISBN: 978-94-6506-777-3

The research described in this thesis was financially supported by:

The European Society of Cataract and Refractive Surgery (ESCRS) as part of the Virtual Refractive Surgery for the Prevention Of Negative Dysphotopsia (vRESPOND) project, Stichting Leids Oogheekundig Ondersteuningsfonds (LOOF)

Financial support for the printing of this thesis was kindly provided by:

Stichting Leids Oogheekundig Ondersteuningsfonds (LOOF), Medical Workshop, ChipSoft

©Luc van Vught (lucvvught@gmail.com), 2024

No part of this thesis may be reproduced or transmitted in any form without prior written permission from the author.

Uncovering the origin of negative dysphotopsia

Proefschrift

ter verkrijging van
de graad van doctor aan de Universiteit Leiden,
op gezag van rector magnificus prof.dr.ir. H. Bijl,
volgens besluit van het college voor promoties
te verdedigen op dinsdag 18 februari 2025
klokke 16:00 uur

door

Luc van Vught
geboren te Berkel en Rodenrijs
in 1994

Promotoren

Dr. J.W.M. Beenakker
Prof. dr. G.P.M. Luyten

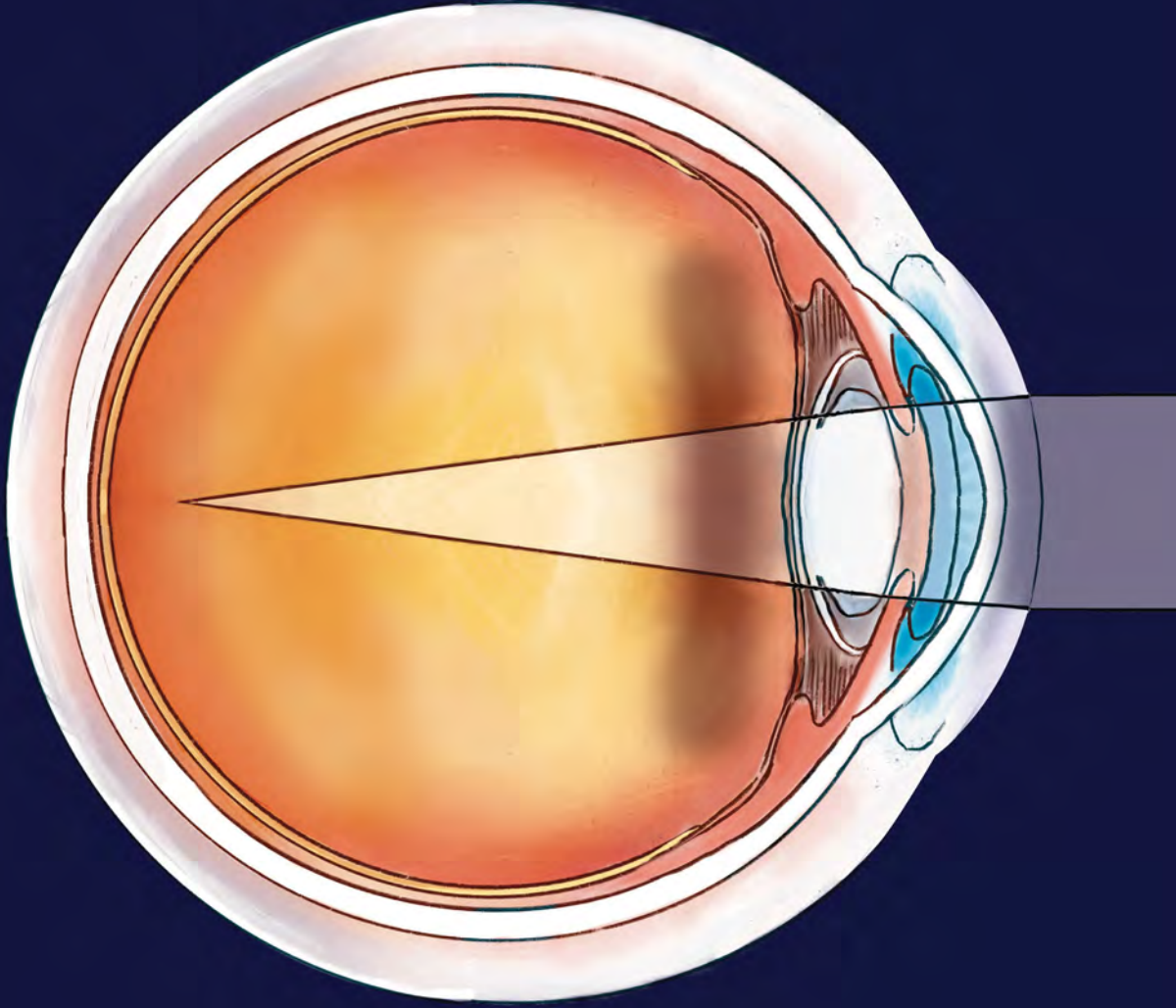
Promotiecommissie

Dr. Y.Y.Y. Cheng
Prof. dr. R.M.M.A. Nuijts (*Maastricht University Medical Centre*)
Prof. dr. ir. T. van Osch
Prof. dr. J.J. Rozema (*University of Antwerp*)

*For Lily
& Winston*

Contents

1. General introduction	9
2. Distinct differences in anterior chamber configuration and peripheral aberrations in negative dysphotopsia <i>Journal of Cataract & Refractive Surgery, 2020</i>	37
3. Evaluation of intraocular lens position and retinal shape in negative dysphotopsia using high-resolution magnetic resonance imaging <i>Journal of Cataract & Refractive Surgery, 2021</i>	61
4. ZOSPy: optical ray tracing in Python through OpticStudio <i>Journal of Open Source Software, 2024</i>	77
5. Accurate corneal modelling for personalized peripheral ray tracing	85
6. MRI-based 3D retinal shape determination <i>BMJ Open Ophthalmology, 2021</i>	121
7. Peripheral visual field shifts after intraocular lens implantation <i>Journal of Cataract & Refractive Surgery, 2023</i>	149
8. Effect of anatomical differences and intraocular lens design on negative dysphotopsia <i>Journal of Cataract & Refractive Surgery, 2022</i>	163
9. Summary and general discussion	185
Addendum	
Nederlandse samenvatting	209
List of publications	213
Curriculum Vitae	215
Acknowledgements	217



1

General introduction

A cataract is an opacification of the otherwise clear crystalline lens of the eye. It can be caused by a variety of reasons but is mostly due to aging.¹ If the cataract becomes severe enough to significantly impair vision, it can be treated with cataract surgery. In this surgery, the crystalline lens is replaced by an artificial intraocular lens (IOL). It is one of the most frequently performed surgeries in many countries,² and the surgery rate is still increasing.³

While cataract surgery is generally considered a safe and effective treatment,¹ patients might still suffer from subjective visual complaints after surgery.⁴ One of these complaints is negative dysphotopsia (ND).⁵ ND is often described as a bothersome shadow in the temporal peripheral visual field that is present directly after cataract surgery (Figure 1.1).^{6,7} Although ND resolves over time in most patients, it is still present in up to 3% of the patients one year after surgery.⁸

The exact origin of ND was still unknown when the research for this thesis was initiated, which hindered the design of preventative measures and treatments. This was mainly due to the lack of measurements that can quantify ND. Consequently, researchers have turned to ray tracing simulations,^{7,9,10} in which the path of light through a virtual model of the eye is calculated. While these simulations have offered some valuable insights, they were mainly performed using generic eye models and are yet to be confirmed using clinical data.

This thesis aims to obtain additional insight into the origin of ND by incorporating clinical data of patients with and without ND into ray tracing simulations to improve the agreement between the simulation and the actual function of the eye. The remainder of the introduction will provide relevant background knowledge, followed by a detailed description of the aims and outline of this thesis.



Figure 1.1: Example of negative dysphotopsia.

1.1 The eye

The eye enables humans to see the world around them. To do so, incident light has to be focused on the retina. In a normal eye, incident light passes several anatomical structures before it reaches the retina. These structures include the cornea, the anterior chamber, the iris and pupil, the posterior chamber, the crystalline lens, and the vitreous body (Figure 1.2). In short, the cornea and crystalline lens work together to focus the incident light, and the iris and pupil limit the amount of light that can reach the retina. The exact function of each structure as well as the axes to which they are referenced are further explained in Section 1.3: *Optics of the eye*.

Once light reaches the retina, photoreceptors within the retina transduce the light stimuli into electric impulses,¹¹ which are transmitted to the visual cortex in the occipital lobes of the brain where they are processed to generate an image of the world.¹²

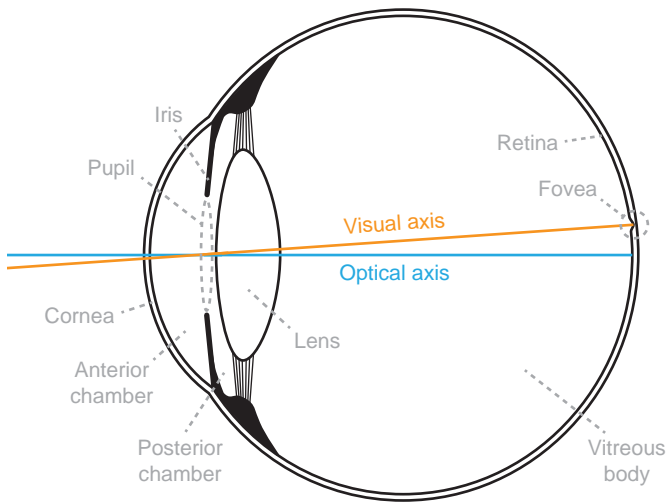


Figure 1.2: Schematic drawing of the human eye and its key optical components. Additionally, two commonly used ocular axes, the optical and visual axis, are shown.

1.2 Optic principles

Some basic knowledge of optic principles is required to understand the topics that are addressed within this thesis. Be aware that this section explains these topics in layman's terms by oversimplifying them.

Light

Much scientific research has been performed to determine the exact nature of light. In short, light can be described as either particles or electromagnetic waves, with the latter being of interest for the current section. Light can be considered to travel as a sinusoidal waveform with a certain wavelength, the distance required to complete one single sine wave. Several properties of light, such as its color, are determined by this wavelength (Figure 1.3).¹³

Refractive index and refraction

Rays of light travel straight within a homogeneous medium such as air. When a ray travels from one medium into another medium, it generally refracts, meaning that the ray changes direction (Figure 1.4). This directional change occurs at the optical interface, the boundary between the two media. The magnitude of this change is dependent on multiple factors, including the refractive index of each medium as well as the angle of incidence of the ray.¹⁴ The refractive index of a medium is the ratio between the speed of light in a vacuum and the speed of light within that specific medium.¹⁵ This index is furthermore dependent on the wavelength of the incident light. Consequently, a medium generally has different refractive indices for different wavelengths.¹⁶

The direction of a ray after refraction can be calculated using Snell's law:

$$n_1 \sin \theta_1 = n_2 \sin \theta_2 \quad (1.1)$$

where n_1 and n_2 are the refractive indices of respectively the first and second medium and θ_1 and θ_2 are respectively the angle of incidence and the angle of refraction measured with respect to the surface normal of the optical interface (Figure 1.4).

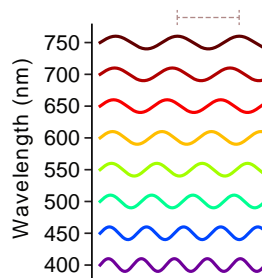


Figure 1.3: Waves of light within the visible spectrum as a function of wavelength. The wavelength of the topmost wave is indicated using a dotted line.

A special situation occurs when the incident ray is oriented such that it is perpendicular to the optical interface. In this instance, $\theta_1 = 0^\circ$ and thus $\sin \theta_1 = 0$, which requires θ_2 to be 0° as well. Therefore, the ray of light is not redirected but rather travels straight.¹⁴

Reflection

A ray of light can also be reflected, meaning that it does not enter the second medium but rather returns into the medium from which it originates (Figure 1.4). Reflection occurs in where n_1, n_2 and θ_1 are such that $\theta_2 > 90^\circ$.

Lenses

Lenses are objects that in their simplest form have two spherical optical surfaces centered around an optical axis. These surfaces work together to either converge or diverge a beam of light by inducing refraction. The degree to which the light is refracted is dependent on the optical power of the lens, expressed in Diopters (D).¹⁷ This power is mainly determined by the combined power of the two optical surfaces. For spherical surfaces, this power can be calculated as:

$$P = \frac{n_2 - n_1}{R} \quad (1.2)$$

where P is the optical power, n_1 and n_2 are the refractive indices of respectively the first and second medium and R is the radius of curvature of the surface.¹⁷

Image formation

Images are generally captured using an optical system that consists of one or more lenses, an aperture, and an image surface. The aperture controls the amount of light that enters the system and the image surface registers the light. Examples of the apertures include the aperture of a camera or the iris and pupil of the eye, and examples of the image surface include a CCD of a camera or the retina of the eye.

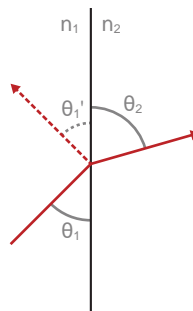


Figure 1.4: Basic optic principles. The refraction of a ray of light when traveling from a medium with refractive index n_1 to another with refractive index n_2 is indicated using a solid red ray. The angle of incidence θ_1 and the angle of refraction θ_2 with respect to the surface normal (dotted black line) are also indicated. The situation that occurs when the same ray is reflected is illustrated using the dashed line and the angle of reflection θ_1' .

The quality of the image captured by an optical system depends on how the rays reach the image surface. The best image quality is achieved when rays are focused on a single point on the image surface. This not only requires the use of a lens with the right amount of optical power, but also the absence of aberrations, which is generally not achieved.

Aberrations and wavefronts

In reality, rays are often not focused to one single point on the image surface but rather spread out over a larger region. This spread is induced by properties of the optical system called aberrations (Figure 1.5). Commonly used aberrations in ophthalmology include defocus, astigmatism, and spherical aberration. Defocus describes the case where the focus point is located in front of or behind the image plane and is normally corrected using a positive or negative lens (Figure 1.5A).¹⁸ Astigmatism describes the situation where rays in two perpendicular planes have different foci (Figure 1.5B),¹⁸ which can be corrected using cylindrical lenses, which have different refractive powers in their principal meridians. Spherical aberration occurs due to the difference in refraction between rays of light that strike a spherical surface on-axis and off-axis (Figure 1.5C).¹⁸ This difference arises from the sphericity of the surface and can theoretically be overcome by inducing the right amount of asphericity over the surface.

Generally, a combination of aberrations is present in an optical system. These aberrations are often assessed by evaluating the wavefront. The wavefront is the surface that a set of rays of light produce. A wavefront created by rays directly originating from a point source is spherical (Figure 1.6A), but this surface can be deformed due to aberrations in the optical

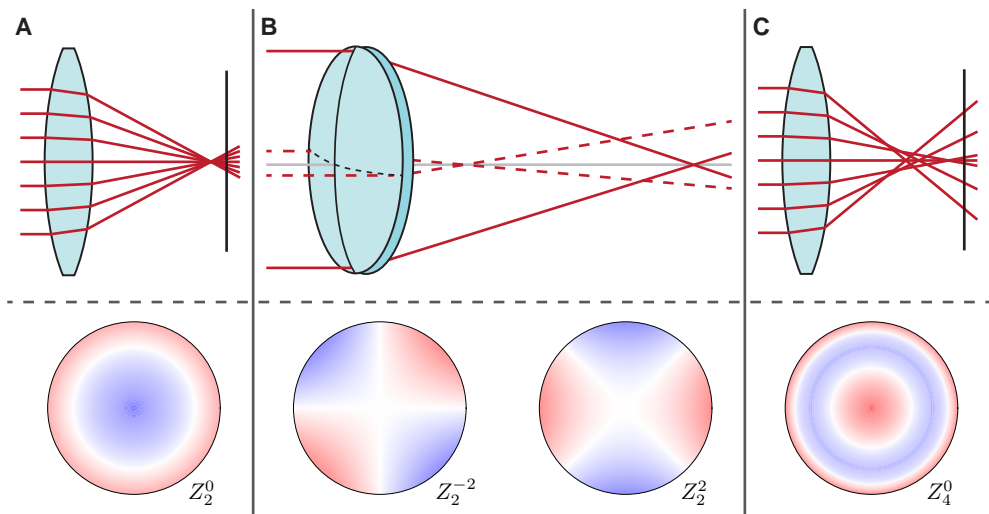


Figure 1.5: Different basic aberrations. Black vertical lines indicate image planes. A) An illustration of defocus (top) where the focal point lies in front of the image plane, and the corresponding Zernike polynomial Z_2^0 (bottom). B) An illustration of astigmatism (top) where rays in the horizontal and vertical meridional focus at different locations, and the corresponding Zernike polynomials Z_2^{-2} and Z_2^2 (bottom). C) An illustration of spherical aberration (top) where more peripheral rays are focused in front of the more central rays of light, and the corresponding Zernike polynomial Z_4^0 .

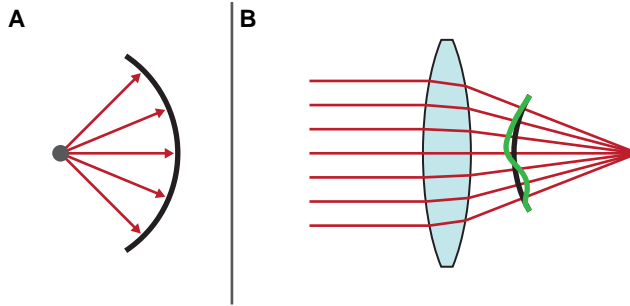


Figure 1.6: Formations of wavefronts. A) Rays originating from a point source form a perfect spherical wavefront (black). B) Rays traveling to an imperfect lens result in a deformed wavefront (green) that is slightly different from the ideal wavefront (black).

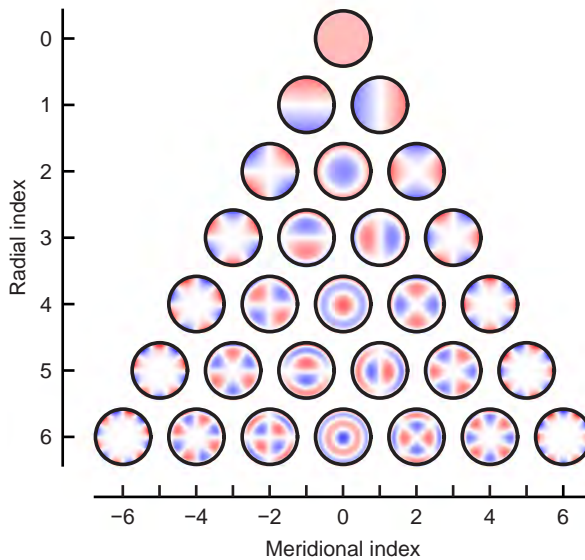


Figure 1.7: Zernike polynomials up to the 6th radial index showing an increase in complexity with higher indices.

system (Figure 1.6B).¹³ Inversely, the aberrations of an optical system can be determined from the wavefront.

Zernike polynomials

Zernike polynomials are a series of polynomials that can be used to describe the shape of a surface S :¹⁹

$$S(\rho, \theta) = \sum_{\substack{\text{all } n \\ \text{and } m}} c_n^m Z_n^m(\rho, \theta) \quad (1.3)$$

where ρ is the normalized radial parameter, θ is the meridional angle ranging from 0 to 2π , n is the radial index, m is the meridional index, c_n^m is the Zernike coefficient and Z_n^m is the Zernike polynomial. By increasing the radial and meridional indices, the used Zernike polynomials increase in complexity (Figure 1.7), which increases the complexity of the surfaces that they can approximate correctly. The agreement between the description of a surface using Zernike coefficients and the actual surface shape depends therefore both on the complexity of the surface and on the amount of Zernike terms that are used.

Zernike polynomials are used often in Ophthalmology, for instance to describe the shape of the corneal surface or to describe the shape of a wavefront.^{19,20} When used to describe a wavefront, certain Zernike polynomials correspond to certain aberrations. For example, Z_2^0 corresponds to defocus (Figure 1.5A), Z_2^{-2} and Z_2^2 to respectively oblique and horizontal astigmatism (Figure 1.5B), and Z_2^0 to spherical aberration (Figure 1.5C).^{19,21}

Following this correspondence, Zernike polynomials can also be converted into more clinical parameters such as ocular refraction. To achieve this, they have to be converted to Rectangular Fourier power vectors $[M, J_0, \text{ and } J_{45}]$,²² which can subsequently be converted into spherocylindrical refraction $[S, C \text{ x axis}]$.²³

Ray tracing simulations

Ray tracing simulations are simulations in which the path of rays of light through an optical system is calculated to obtain insight into the optical functioning of that system. Several pieces of software that are designed specifically for this purpose exist, including OpticStudio (Zemax LCC) and CODE V (Synopsys, Inc.).²⁴ Within this thesis, OpticStudio is used. In OpticStudio, ray tracing can be performed in sequential mode or non-sequential mode. In sequential mode, only rays that hit each defined surface of an optical model once in a sequential fashion are considered. This enables fast and powerful analyses such as wavefront calculations but does not provide insight into the full optical functioning of the system. In non-sequential mode, there is no restriction on analyzed rays of light. These rays are still considered when they for example miss one or more surfaces or hit a surface multiple times. This is computationally more intensive but provides more insight into the exact functioning of the system.

1.3 Optics of the eye

The eye can be characterized as an optical system. This requires accounting for several anatomical structures, including the cornea, the anterior chamber, the iris and pupil, the posterior chamber, the lens, the vitreous body, and the retina (Figure 1.8).

Optical structures of the eye

The cornea is the most anterior lens of the eye as well as the strongest refractive component of the eye. With an average refractive power of about 42 D, it accounts for approximately two-thirds of the refractive power of the eye.²⁵ The shape of the cornea is usually quantified using the radius of curvature of its anterior surface, determined at the apex. However, as the cornea is often curved differently in one direction than in another, this quantification is generally further specified using the radii of curvature in the two principal meridians. Furthermore, the corneal surface flattens away from the apex, making its shape aspherical rather than spherical. This asphericity is often given as Q-value Q or eccentricity e , related by $Q = -e^2$.²⁵ The shape of the posterior surface of the cornea is harder to determine, as its measurement is affected by the anterior surface. Initially, this was solved by adjusting the corneal refractive index such that it accounted for the posterior surface or by estimating the posterior shape from the anterior shape.²⁵⁻²⁷ Newer measurement techniques however allow the determination of the posterior corneal shape.²⁸

After being refracted by the cornea, light enters the anterior chamber of the eye. The anterior chamber is filled with aqueous fluid and extends up to the iris. The iris functions as the aperture of the eye. It controls how much light is able to reach the retina by altering the size of its central aperture, the pupil. Light passing through the pupil enters the posterior chamber, the space between the iris and the crystalline lens that is also filled with aqueous fluid.

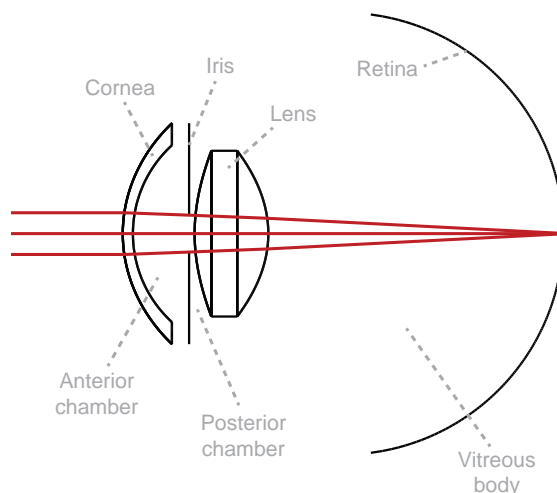


Figure 1.8: The eye as an optical system. All ocular structures of Figure 1.2 are indicated.

The crystalline lens is the second lens within the eye. It provides the ability to focus light from objects at various distances on the retina by changing its shape and therewith its refractive power. It accounts for approximately one-third, 20 D, of the total refractive power of the eye in the unaccommodated state, and its power changes upon accommodation. The properties of the lens change significantly with age. Its central thickness changes from about 3.5 mm at 20 years of age to 4.5 mm at 70 years of age.²⁹ Furthermore, the ability to accommodate reduces over time.³⁰

The last structure that light passes prior to reaching the retina is the vitreous body or vitreous humour, a semisolid mass that normally attaches to the retina. The retina is a curved surface that functions as the image surface of the eye. It is often considered to have a spherical shape,^{31,32} but in reality has a more ellipsoidal shape.^{33–35}

A schematic overview of the refractive indices of these ocular structures is given in Table 1.1.³¹

Axes of the eye

To combine the optical structures of the eye into an optical system, they have to be referenced to an axis. Several axes can be used when describing the structure of the eye. Two of the most common axes are the optical and the visual axis. The optical axis is the theoretical axis that goes through the center of each refractive surface within the eye (Figure 1.2).³⁶ In simple, symmetric, schematic representations of the eye, this axis can be considered correct as all refractive components are centered on one line. However, as these components are generally not perfectly centered on one single axis in real life, the best-fit line through the centers of each refractive component is generally taken as the optical axis. The visual axis is the line between a fixation point and the fovea, the part of the retina where the sharpest image can be formed (Figure 1.2).³⁶ This axis does not assume the centration of optical structures and should thus provide a better agreement between an optical system and the actual eye.

Table 1.1: Refractive indices of the ocular structures for a wavelength of 589.3 nm.³¹

	Refractive index
Cornea	1.376
Aqueous	1.3375
Lens	1.42
Vitreous	1.336

1.4 Measuring the ocular anatomy

From Section 1.3: *Optics of the eye*, it is clear that the optical function of the eye relies on the shape and position of various anatomical structures. These characteristics can be determined using various measurement techniques. This section provides some background on the measurement techniques relevant to this thesis.

Biometry

Biometry measures the positions of the interfaces between the various media of the eye, which can be used to calculate the thickness of various anatomical structures and/or the distance between them. Newer biometers rely on optical techniques such as partial coherence interferometry or low-coherence reflectometry for their measurements.³⁷ The output of these biometers includes (among others) the anterior chamber depth, the lens thickness, and the axial length, all measured along the visual axis. In addition, a keratometry measurement is also performed, which provides information on the basic shape of the cornea.³⁷ One of the main applications of these data is functioning as input for the intraocular lens (IOL) power calculation required for cataract surgery (see Section 1.7: *Cataract & cataract surgery*).^{37,38}

Topography and tomography

As the cornea is the strongest refractive component of the eye, an accurate measurement of its shape is often crucial. K-values are commonly used to represent the basic shape of the center of the cornea. While K-values suffice for the general assessments of the cornea or the calculation of IOL powers, a more elaborate measurement is often desired for diagnostic reasons or treatment planning. Topography measurements provide such insight by characterizing the geometry of a large part of the anterior corneal surface. Additionally, tomography measurements extend this insight by characterizing the geometry of the posterior corneal surface and the anterior chamber.³⁹

The data of topography and tomography measurements is often used in clinical settings, for example for the diagnosis and the follow-up of keratoconus.^{40,41} Furthermore, the raw measurement data has shown to be suitable for modelling the cornea accurately for simulations of central vision.^{20,42,43}

MRI

The use of Magnetic resonance imaging (MRI) within ophthalmology is increasing.^{44,45} As MRI, in contrast to most ophthalmic measurement devices, does not rely on optics, it has the ability to image the entire eye in 3D. However, acquiring an MRI scan takes considerable time and these scans are sensitive to motion during its acquisition. As a result, there is a trade-off between acquisition time and the resulting quality of the image.

Over time, these problems were addressed by using higher magnetic field strengths,^{46–48} implementing cued-blinking to reduce ocular motion,^{48,49} and improving the acquisition protocols.⁵⁰ Due to these improvements, MRI is now being used to improve the treatment of uveal melanoma,^{51,52} and MRI can be used to measure the retinal shape.^{35,47}

1.5 Evaluating the ocular function

There is a wide variety of methods available to evaluate the ocular function. To evaluate central vision, one can for example measure the refraction and visual acuity or perform a visual field test, all of which are commonly used in ophthalmic practice. Furthermore, aberrometry can be performed in more specific cases.

As this thesis addresses ND, which is located in the peripheral vision, methods to evaluate the peripheral vision are of interest. However, there are relatively few methods available to measure peripheral vision.⁵³ A common method to do so is visual field testing. Newer methods also include peripheral aberrometry and peripheral vision simulations, but thus far these are only used in research settings. This section provides a more elaborate description of the indications and limitations of methods used to evaluate both central and peripheral vision.

Refraction

In a relaxed state, the eye should ideally focus parallel rays of light to a single point on the retina. If that is the case, the eye is considered emmetropic and has sharp central vision. However, this focal point is often located in front of or behind the retina due to a refractive error.⁵⁴ The refractive error is usually a mismatch between the total refractive power of the eye and its axial length. The eye is considered myopic when the focal point is located in front of the retina, emmetropic when the focal point is on the retina, and hypermetropic when it is located behind the retina (Figure 1.9). Some eyes also have a certain amount of astigmatism. These eyes have two focal points as the eye has a different total refractive power in two perpendicular meridians.

As refractive errors will result in blurred vision, they are often corrected using spectacles. This requires a measurement of the exact refractive error, which can for example be determined using the combination of objective and subjective refraction measurements. The objective refraction measurement determines the central refraction of the eye without feedback from the patient. This central refraction can be further refined to the preference of the patient in the subjective refraction measurement.

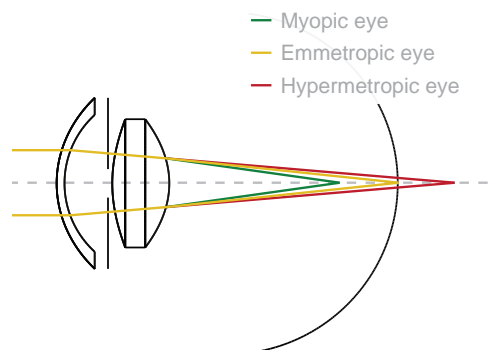


Figure 1.9: Refractive states of the eye. Three different refractive states are shown, myopic (green rays), emmetropic (yellow rays) and hypermetropic (red rays).

Visual acuity

The visual acuity of the eye is its ability to distinguish details of objects located at a certain distances. This ability can be reduced due to a variety of reasons, such as refractive errors and retinal pathologies.⁵⁵ It is often tested using reading charts such as the Snellen chart or the ETDRS chart.⁵⁶

Perimetry

The visual field of the eye can be measured using either static or kinetic perimetry. In static perimetry, light stimuli are positioned at predefined locations around a fixation target. One by one, the intensity of each stimulus is increased, and the patient has to report when the stimulus is seen.⁵⁷ There are multiple variants of static perimetry, such as the HFA 30-2 which measures up to 30 degrees in the visual field in steps of 2 degrees, and the HFA 60-4 which measures up to 60 degrees in the visual field in steps of 4 degrees.

In kinetic perimetry, a light stimulus with a fixed intensity moves from peripheral to central vision.⁵⁷ The maximal visual field angle that is tested is 90 degrees.⁵⁸ Similar to static perimetry, the patient has to report when the stimulus is visible.

Aberrometry

Objective refraction measurements provide insight into the refractive error of the eye. They assume that the eye refracts parallel rays of light to a single focal point, or two in the case of astigmatism. As the eye is not a perfect optical system, this is often not the case due to aberrations. These aberrations in central vision can be measured using aberrometry.⁵⁹

Aberrometers rely on wavefront sensing. They measure the ocular wavefront and subsequently expand that wavefront into Zernike polynomials (Figure 1.10). The data provided by aberrometry is used for various purposes. In a clinical setting, it is used as input for laser surgery to customize the ablation profile.⁵⁹ In a research setting, it can for example be used to optimize eye models for vision simulations.⁶⁰

Peripheral aberrometry

Following increased interest in peripheral vision, aberrometers that can measure peripheral ocular aberrations and therewith quantify peripheral vision have been developed.⁶¹ These devices can determine the ocular wavefront up to 40 degrees in the peripheral visual field (Figure 1.10).^{61,62} While these measurements are not yet performed in a clinical setting, they can be used to validate peripheral vision simulations in a research setting.^{63,64}

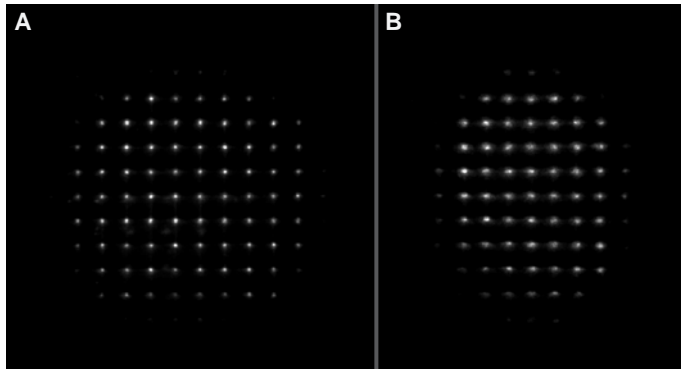


Figure 1.10: Aberrometry of an actual eye. A) Measurement for central vision. B) Measurement for peripheral vision, showing a more elliptical and more aberrated wavefront than the one acquired for central vision.

1.6 Peripheral vision simulations

Section 1.3: *Optics of the eye*, showed that it is possible to model the eye as an optical system, hereafter called an eye model. These eye models can then be analyzed using ray tracing simulations to gain additional insight into their optical functioning. In brief, their vision is simulated. The validity of these simulations, and thus their clinical relevance, depends on the agreement between the geometry of the eye model and the actual anatomy of the eye.⁶⁵

Initially, ray tracing simulations were performed using simpler eye models with a rotational-symmetric geometry.^{31,66} Multiple components of these eye models have subsequently been personalized to obtain more realistic, patient-specific results. Thus far, this personalization has mainly focused on central vision, for example by personalizing the cornea,^{20,42,43,67} the lens,⁶⁸⁻⁷⁰ and the axial positioning of refractive surfaces.^{42,71} These simulations are however not bound to central vision, but can also cover the peripheral vision.

Peripheral vision simulations

Peripheral vision simulations can provide unique insights into the field of ophthalmology. Currently, there are few methods to quantify the peripheral vision of the eye, and the available methods have their limitations. Perimetry measurements rely on the subjective response of the patient, and static perimetry can furthermore only measure up to visual field angles of 60 degrees. Peripheral aberrometry provides a fully objective measurement, but can only measure up to visual field angles of 40 degrees. Peripheral vision simulations do not have these limitations, they can theoretically simulate the entire visual field. However, three challenges have to be addressed to improve the validity and clinical relevance of these peripheral vision simulations.

The first challenge regards the peripheral geometry of the eye model. The peripheral geometry of the eye model should be optimized to increase the agreement with the actual peripheral anatomy of the eye. To that end, the peripheral characteristics of all anatomical structures listed in Section 1.3: *Optics of the eye* have to be addressed. With regards to the cornea, several methods are available to model it accurately for central vision simulations,^{20,42,43} but these methods are still to be evaluated for peripheral vision simulations. The iris is often modelled without a thickness and oriented perpendicular to the axis of the eye model,^{32,60,63,72} but in reality has a thickness and a tilt.^{73,74} Not accounting for these characteristics will likely have a negligible effect on central vision simulations, but can have a more severe impact on peripheral vision simulations. The peripheral shape of the lens cannot be measured in-vivo due to obscuration by the iris, but can potentially be extrapolated from OCT images of the central part of the lens. However, this thesis mostly addresses pseudophakic eyes, which have an artificially made IOL rather than a crystalline lens. The IOL manufacturers should know its peripheral shape. With regards to the retina, its shape is often assumed to be spherical,^{31,32,66} but this is not the case in real life.³⁴ Thus, this shape has to be adjusted for accurate peripheral vision simulations. Finally, all modelled individual anatomical structures have to be properly positioned with regards to a reference point or reference axis.

The second challenge regards the relationship between the simulation results and the vision experienced by the patient. Ray tracing simulations evaluate how light reaches the image

surface, which is represented by the retina in eye models. For clinical relevance, it is important the ray tracing results relate to the vision experienced by the patient. For certain peripheral vision simulations, especially non-sequential simulations, this requires accounting for which part of the retinal surface is used to see a certain part of the visual field. It is known that this relation is non-linear in the phakic eye.^{75,76} However, this thesis is centered around peripheral visual complaints of the pseudophakic eye, which has an artificial IOL rather than the intra-ocular lens. As the IOL refracts peripheral light differently,⁷⁷ it might induce a shift in the peripheral visual field which could affect peripheral visual complaints. Therefore, this relation has to be determined and corrected if necessary.

The third challenge regards how to validly perform a large number of peripheral vision simulations within a reasonable amount of time. Solving the other two challenges will require a large amount of simulations. Furthermore, after these challenges have been solved, a large number of simulations are also required to gain insight into peripheral visual complaints. Each simulation requires defining a large number of variables to define an eye model, and the simulation has to be completed before a new simulation can be started. This combination makes performing a large number of peripheral vision simulations both error-prone and time-consuming. Therefore, solutions are required to automate the entire process.

1.7 Cataract & cataract surgery

A cataract is an opacification of the otherwise clear crystalline lens of the eye. This clouding is often the result of aging but can have other causes such as congenital or traumatic.¹ Patients often experience visual complaints such as blurred vision due to this opacification. The severity of the opacification, and therefore the severity of the visual complaints, increases with age. When left untreated, cataract can result in blindness. Therefore, it is often treated by cataract surgery.

Epidemiology

In 2020, more than 94 million people were affected by cataracts worldwide,⁷⁸ making it one of the leading causes of visual impairment and blindness. The prevalence of cataracts increases with age and is highest in the elderly, with an estimated prevalence of 92.6% of people aged 80 years or more.¹ The amount of performed cataract surgeries as treatment is proportionally high, up to 11.000 per million people per year in developed countries.^{2,3} In the Netherlands, for example, more than 180.000 cataract surgeries are performed yearly.⁷⁹

Cataract surgery

During cataract surgery, the crystalline lens is removed from the eye while leaving the lens capsule in place. Generally, this is done by making a small aperture in the anterior capsule, the capsulorhexis, after which the lens is removed using phacoemulsification. Subsequently, an artificial intraocular lens (IOL) is implanted within the capsule, after which the eye is considered to be pseudophakic rather than phakic. The implanted IOLs are thinner than the crystalline lens (Figure 1.11), which facilitates their implantation through small incisions.

As IOLs are thinner, their anterior and posterior surfaces have a lower convexity compared to the surfaces of the crystalline lens. Therefore, they require a higher refractive index to achieve the same power as the crystalline lens. The width of IOLs is furthermore less than the width of the crystalline lens, requiring the addition of appendages called haptics that keep the IOL in place (Figure 1.11).⁸⁰ Additionally, newer IOLs often have a certain amount of asphericity to correct for the asphericity of the corneal surface.⁸¹

The risk of severe intraoperative or postoperative complications is generally considered to be low for cataract surgery.⁸² However, a significant number of patients experience unwanted optical phenomena, such as ND, after cataract surgery.⁸³

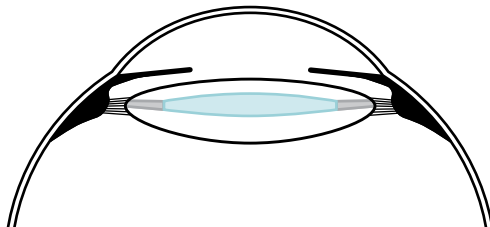


Figure 1.11: Overlay of a phakic and pseudophakic eye. The IOL is shown in light blue and its haptics in grey. The IOL is smaller and thinner than the crystalline lens.

1.8 Negative dysphotopsia

Negative dysphotopsia (ND) is commonly described as a shadow in the temporal peripheral visual field that is present after cataract surgery.^{5-7,84} The characteristics and severity of this shadow differ per patient, with some describing an arch where others describe a crescent (Figure 1.12).⁶

Epidemiology

Overall, the incidence of ND is reported to be up to 19% directly after surgery,^{8,83,85} where the incidence seems to be the highest when patients are actively asked about the presence of any shadow.⁸⁵ ND reduces over time in most patients, often to full resolution.^{6,8,83} However, ND is still present in 3% of all operated eyes one year after cataract surgery (Figure 1.13), with minimal chance of improvement thereafter.⁸ While the number of patients that experience persisting complaints of ND is small, the actual number of patients is large due to the high volume of cataract operations.^{2,3}

Origin

When the research for this thesis was initiated in 2016, there were many questions regarding the origin of ND. One of the biggest challenges for obtaining additional insight was the lack of methods to objectively quantify the shadow.⁶ Until then, only kinetic perimetry was able to quantify the shadow in some, but not all, patients.⁸⁶ Due to this lack of quantification methods, most insights were based on clinical examinations and theoretical ray tracing simulations. The clinical examinations indicated for example that ND can occur with many IOL designs as long as the IOL is implanted in the capsular bag, that ND is not induced by malpositioning of the IOL, and that ND is more severe with pupil constriction.⁸⁴ The theoretical ray tracing simulations extended these insights further by showing how the peripheral retinal illumination could be affected by for example the size of the pupil,^{7,9} the distance between the iris and the IOL,⁷ and the amount of overlap between the anterior capsulotomy and the IOL.⁹

Based on these insights, several hypotheses were formed. All hypotheses assumed that there is a local gap in the illumination of the peripheral retina,^{7,9,10,84} however each assumed a different causal mechanism. These hypotheses included: 1) The retinal illumination gap is



Figure 1.12: Different representations of the shadow experienced with ND. The temporal side of the visual field is considered to be on the left side. Note that the opacity of the shadow can differ between patients and is not by definition 0% as in these images. A) A dark arch in the temporal visual field. B) A dark crescent in the temporal visual field.

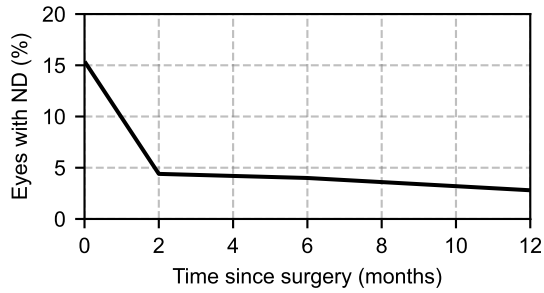


Figure 1.13: Incidence of ND over time, based on the data reported by Osher, RH. (JCRS, 2008).⁸

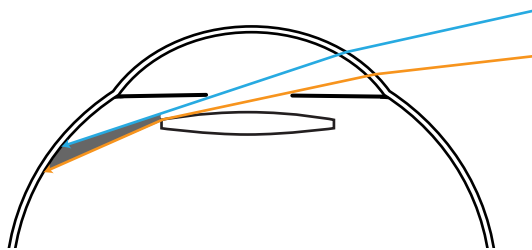


Figure 1.14: Schematic drawing of one of the hypotheses on the origin of ND. This hypothesis assumes that ND is caused by a gap in nasal retinal illumination (shaded area) that is the result of the difference between rays passing between the iris and the IOL (blue line) and rays that are refracted by the IOL (orange line).

caused by the discontinuity between light passing through the posterior IOL surface and light passing through the IOL edge in sharp-edged IOLs,⁷ *II*) The retinal illumination gap is the result of the discontinuity between light refracted by the IOL and light that passes through the gap between the iris and the IOL (Figure 1.14),¹⁰ and *III*) The retinal illumination gap is caused by an optical interaction between the anterior capsulotomy and the anterior surface of the IOL.⁸⁴

Treatment and prevention

Patients that suffer from bothersome persistent ND can suffer to such an extent that they can request a second operation. Based on the theories on the cause of ND, multiple treatments have been proposed and performed. These treatments include for example performing a laser anterior capsulotomy,⁸⁷ exchanging the IOL for a different IOL,^{88–91} the implantation of a secondary “piggyback” IOL,^{89,92,93} and a secondary reverse optic capture.⁸⁹ While these treatments show promising results, they do not cure ND in all patients. A treatment that gives a full resolution in all patients is yet to be found.

Next to treatments, the theories on the origin of ND have also been used to design preventative approaches. Thus far, these approaches include primary reverse optic capture and the implantation of the IOL with the haptics oriented in the horizontal meridian.^{50,94,95}

Required research

To improve the treatment and prevention of ND, the exact origin of ND has to be determined. Thus far, the theories on this origin are based on ray tracing simulations with theoretical eye models that do not incorporate the actual anatomy of patients. As a result, these hypothesized mechanisms might not occur in the actual eye. Furthermore, it is unclear if these mechanisms would only occur in pseudophakic eyes with ND or also in pseudophakic eyes without ND. Therefore, the simulations should be repeated using eye models that incorporate the actual anatomy of patients with and without ND to gain more insight. To address these limitations, we initiated the vRESPOND study (CCMO registry number: NL58358.058.16) in cooperation with the European Society for Cataract and Refractive Surgeons (ESCRS). That study forms the basis for this thesis.

1.9 Aim and outlines of this thesis

The overall aim of this thesis is to provide more insight into the origin of ND by performing peripheral vision simulations with eye models that incorporate the anatomy of patients with ND and of pseudophakic controls without ND. To that end, several underlying questions had to be answered:

- I. Are there anatomical differences between the eyes of pseudophakic patients with and without ND that affect peripheral vision?
- II. How to incorporate the anatomy of patients with and without ND into the eye models that are used for peripheral vision simulations?
- III. How do the results of peripheral vision simulations relate to the peripheral vision experienced by the patient?

Each of these questions is (partially or fully) answered in different chapters of this thesis.

Question I is addressed in **Chapters 2 and 3**. These chapters mainly evaluate the ocular anatomy of a group of patients with ND and a group of pseudophakic controls. In **Chapter 2** the anatomy of the anterior segment of the eye as well as the peripheral wavefront aberrations are measured in groups and compared between them. In addition, theoretical ray tracing simulations to gain insight into the effect of the ocular anatomy on peripheral vision are performed. In **Chapter 3**, the IOL position and retinal shape are derived from MR-images of both groups and compared between them.

Question II is addressed in **Chapters 4, 5, and 6**. In **Chapter 4**, a software package is introduced that can be used to automate ray tracing simulations, which enables performing ray tracing simulations with a large number of eye models. In **Chapter 5**, 7 different methods to model the cornea are evaluated to determine the optimal way to model the cornea for peripheral vision simulations. In **Chapter 6**, the optimal way to determine the 3D retinal shape from MR-images is determined.

Question III is addressed in **Chapter 7**. In this chapter, ray tracing simulations are used to determine how the illuminated retina translates back into the visual field using both phakic and pseudophakic eye models. Subsequently, these results are used to determine whether the pseudophakic visual field is shifted with regard to the phakic visual field.

Chapter 8 combines all obtained insights. In this chapter, two eye models are created, one eye model that incorporates the anatomy of patients with ND and one eye model that incorporates the anatomy of pseudophakic controls. Each model is furthermore combined with four different IOL designs. Subsequently, the retinal illumination is determined in all eye models and compared between them to determine the effect of anatomy and IOL design on ND.

Chapter 9 contains the discussion of this thesis. This chapter is divided into two sections. The first section discusses the implications of this thesis for ND and the second section discusses other applications of this thesis.

1.10 References

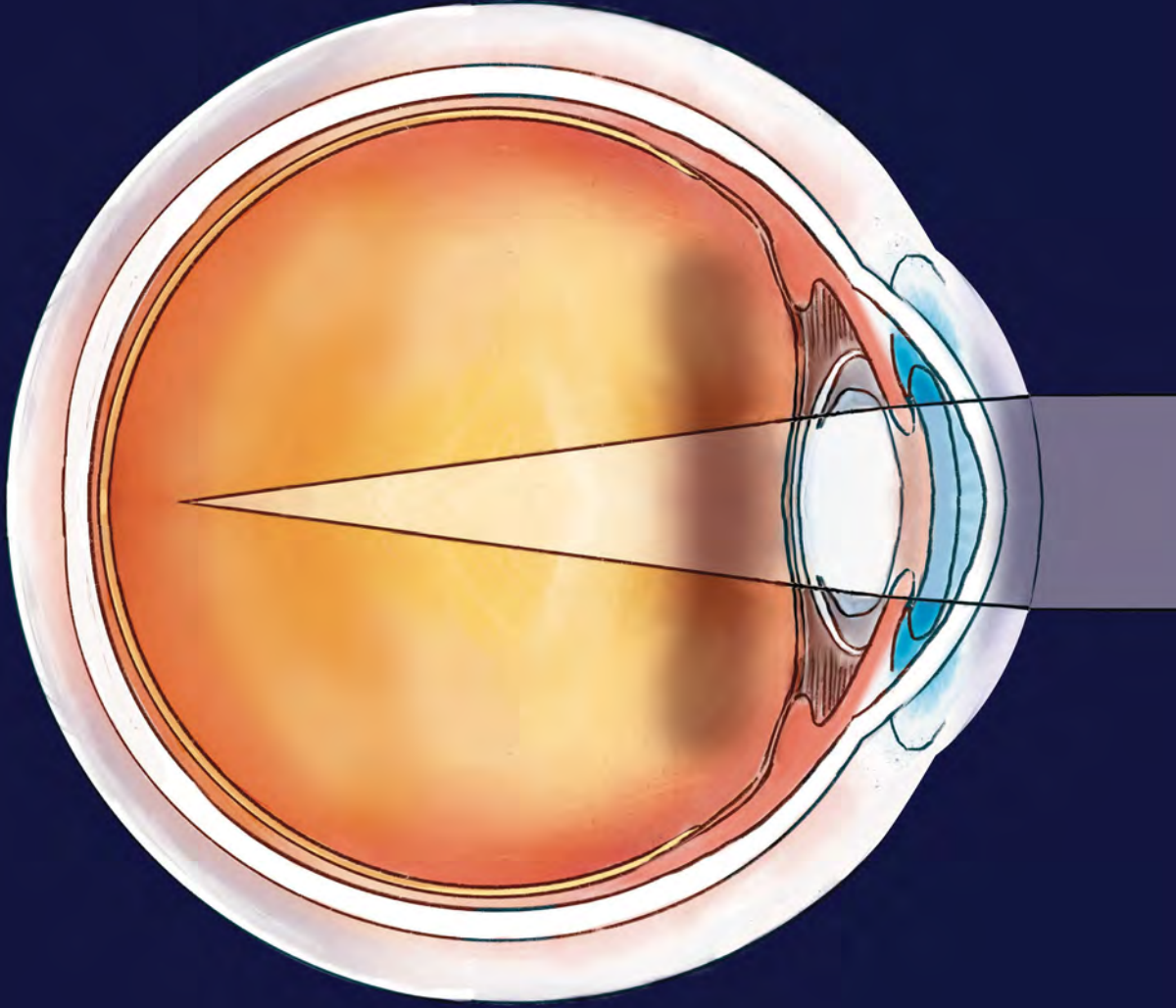
1. Liu YC, Wilkins M, Kim T, Malyugin B, Mehta JS. Cataracts. *Lancet*. 2017;390(10094):600–612. doi: 10.1016/s0140-6736(17)30544-5.
2. Wang W, Yan W, Fotis K, Prasad NM, Lansingh VC, Taylor HR, Finger RP, Facciolo D, He M. Cataract Surgical Rate and Socioeconomics: A Global Study. *Invest Ophthalmol Vis Sci*. 2016;57(14):5872–5881. doi: 10.1167/iovs.16-19894.
3. Erie JC. Rising cataract surgery rates: demand and supply. *Ophthalmology*. 2014;121(1):2–4. doi: 10.1016/j.optha.2013.10.002.
4. Hood CT, Sugar A. Subjective complaints after cataract surgery: common causes and management strategies. *Curr Opin Ophthalmol*. 2015;26(1):45–9. doi: 10.1097/icu.0000000000000112.
5. Davison JA. Positive and negative dysphotopsia in patients with acrylic intraocular lenses. *J Cataract Refract Surg*. 2000;26(9):1346–55. doi: 10.1016/s0886-3350(00)00611-8.
6. Henderson BA, Geneva I. Negative dysphotopsia: A perfect storm. *J Cataract Refract Surg*. 2015;41(10):2291–312. doi: 10.1016/j.jcrs.2015.09.002.
7. Holladay JT, Zhao H, Reisin CR. Negative dysphotopsia: the enigmatic penumbra. *J Cataract Refract Surg*. 2012;38(7):1251–65. doi: 10.1016/j.jcrs.2012.01.032.
8. Osher RH. Negative dysphotopsia: long-term study and possible explanation for transient symptoms. *J Cataract Refract Surg*. 2008;34(10):1699–707. doi: 10.1016/j.jcrs.2008.06.026.
9. Hong X, Liu Y, Karakelle M, Masket S, Fram NR. Ray-tracing optical modeling of negative dysphotopsia. *J Biomed Opt*. 2011;16(12):125001. doi: 10.1117/1.3656745.
10. Simpson MJ. Double image in far peripheral vision of pseudophakic eye as source of negative dysphotopsia. *J Opt Soc Am A Opt Image Sci Vis*. 2014;31(12):2642–9. doi: 10.1364/josaa.31.002642.
11. Atchison DA, Smith G. The human eye: an overview. In: DA Atchison, G Smith, eds. *Optics of the Human Eye*. Butterworth-Heinemann; 2000:3–10. doi: 10.1016/b978-0-7506-3775-6.50005-5.
12. Thomas FF, Edward C. The Optic Nerve and Visual Pathways. In: FF Thomas, C Edward, eds. *Anatomy of the Eye and Orbit: The Clinical Essentials*. Wolters Kluwer Health; 2017:322–346.
13. Dereniak EL, Dereniak TD. Light propagation. In: *Geometrical and Trigonometric Optics*. Cambridge University Press; 2008:1–29.
14. Guenther BD. Reflection and Refraction. In: *Modern optics simplified*. Oxford University Press; 2020:53–91. doi: 10.1093/oso/9780198842859.001.0001.
15. Guenther BD. Electromagnetic Theory. In: *Modern Optics Simplified*. Oxford University Press; 2019:20–52. doi: 10.1093/oso/9780198842859.003.0002.
16. Guenther BD. Aberrations. In: *Modern Optics Simplified*. Oxford University Press; 2019:215–248. doi: 10.1093/oso/9780198842859.003.0007.
17. Geary JM. Paraxial world. In: JM Geary, ed. *Introduction to Lens Design: With Practical ZEMAX Examples*. Willmann-Bell; 2002:33–42.
18. Kingslake R, Barry Johnson R. Aberration Theory. In: R Kingslake, RB Johnson, eds. *Lens Design Fundamentals*. Academic Press; 2010:101–135. doi: 10.1016/b978-0-12-374301-5.00008-5.
19. American National Standards Institute. *ANSI Z80.28-2010: Methods for Reporting Optical Aberrations of Eyes*. Standard. 2010.
20. Canovas C, Artal P. Customized eye models for determining optimized intraocular lenses power. *Biomed Opt Express*. 2011;2(6):1649–62. doi: 10.1364/boe.2.001649.
21. Noll RJ. Zernike Polynomials and Atmospheric-Turbulence. *Journal of the Optical Society of America*. 1976;66(3):207–211. doi: doi10.1364/josa.66.000207.
22. Robert Iskander D, Davis BA, Collins MJ, Franklin R. Objective refraction from monochromatic wavefront aberrations via Zernike power polynomials. *Ophthalmic Physiol Opt*. 2007;27(3):245–55. doi: 10.1111/j.1475-1313.2007.00473.x.
23. Thibos LN, Wheeler W, Horner D. Power vectors: an application of Fourier analysis to the description and statistical analysis of refractive error. *Optom Vis Sci*. 1997;74(6):367–75. doi: 10.1097/00006324-199706000-00019.

24. Geary JM. ZEMAX. In: JM Geary, ed. *Introduction to Lens Design: With Practical ZEMAX Examples*. Willmann-Bell; 2002:11–20.
25. Atchison DA, Smith G. Refracting components: cornea and lens. In: DA Atchison, G Smith, eds. *Optics of the Human Eye*. Butterworth-Heinemann; 2000:11–20. doi: 10.1016/b978-0-7506-3775-6.50006-7.
26. Olsen T. On the calculation of power from curvature of the cornea. *Br J Ophthalmol*. 1986;70(2):152–4. doi: 10.1136/bjo.70.2.152.
27. Patel S, Marshall J, Fitzke FW. Shape and radius of posterior corneal surface. *Refract Corneal Surg*. 1993;9(3):173–81. doi: 10.3928/1081-597x-19930501-05.
28. Mohammadi SF, Khorrami-Nejad M, Hamidirad M. Posterior corneal astigmatism: a review article. *Clin Optom (Auckl)*. 2019;11:85–96. doi: 10.2147/opto.s210721.
29. Atchison DA, Markwell EL, Kasthurirangan S, Pope JM, Smith G, Swann PG. Age-related changes in optical and biometric characteristics of emmetropic eyes. *J Vis*. 2008;8(4):29 1–20. doi: 10.1167/8.4.29.
30. Anderson HA, Hentz G, Glasser A, Stuebing KK, Manny RE. Minus-lens-stimulated accommodative amplitude decreases sigmoidally with age: a study of objectively measured accommodative amplitudes from age 3. *Invest Ophthalmol Vis Sci*. 2008;49(7):2919–26. doi: 10.1167/iovs.07-1492.
31. Escudero-Sanz I, Navarro R. Off-axis aberrations of a wide-angle schematic eye model. *J Opt Soc Am A Opt Image Sci Vis*. 1999;16(8):1881–91. doi: 10.1364/josaa.16.001881.
32. Holladay JT, Simpson MJ. Negative dysphotopsia: Causes and rationale for prevention and treatment. *J Cataract Refract Surg*. 2017;43(2):263–275. doi: 10.1016/j.jcrs.2016.11.049.
33. Atchison DA, Jones CE, Schmid KL, Pritchard N, Pope JM, Strugnell WE, Riley RA. Eye shape in emmetropia and myopia. *Invest Ophthalmol Vis Sci*. 2004;45(10):3380–6. doi: 10.1167/iovs.04-0292.
34. Atchison DA, Pritchard N, Schmid KL, Scott DH, Jones CE, Pope JM. Shape of the retinal surface in emmetropia and myopia. *Invest Ophthalmol Vis Sci*. 2005;46(8):2698–707. doi: 10.1167/iovs.04-1506.
35. Pope JM, Verkicharla PK, Sepelband F, Suheimat M, Schmid KL, Atchison DA. Three-dimensional MRI study of the relationship between eye dimensions, retinal shape and myopia. *Biomed Opt Express*. 2017;8(5):2386–2395. doi: 10.1364/boe.8.002386.
36. Arba Mosquera S, Verma S, McAlinden C. Centration axis in refractive surgery. *Eye Vis (Lond)*. 2015;2:4. doi: 10.1186/s40662-015-0014-6.
37. Song AL, Rizzuti A. Optical Biometry. In: *StatPearls*. StatPearls Publishing LLC.; 2023.
38. Haigis W. Challenges and approaches in modern biometry and IOL calculation. *Saudi J Ophthalmol*. 2012;26(1):7–12. doi: 10.1016/j.sjopt.2011.11.007.
39. Kanclerz P, Khoramnia R, Wang X. Current Developments in Corneal Topography and Tomography. *Diagnostics (Basel)*. 2021;11(8). doi: 10.3390/diagnostics11081466.
40. Deshmukh R, Ong ZZ, Rampat R, Alio Del Barrio JL, Barua A, Ang M, Mehta JS, Said DG, Dua HS, Ambrosio R. J, Ting DSJ. Management of keratoconus: an updated review. *Front Med (Lausanne)*. 2023;10:1212314. doi: 10.3389/fmed.2023.1212314.
41. Gomes JA, Tan D, Rapuano CJ, Belin MW, Ambrosio R. J, Guell JL, Malecaze F, Nishida K, Sangwan VS, Group of Panelists for the Global Delphi Panel of K, Ectatic D. Global consensus on keratoconus and ectatic diseases. *Cornea*. 2015;34(4):359–69. doi: 10.1097/ico.0000000000000408.
42. Rosales P, Marcos S. Customized computer models of eyes with intraocular lenses. *Opt Express*. 2007;15(5):2204–18. doi: 10.1364/oe.15.002204.
43. Canovas C, Azena S, Alcon E, Villegas EA, Marin JM, Artal P. Effect of corneal aberrations on intraocular lens power calculations. *J Cataract Refract Surg*. 2012;38(8):1325–32. doi: 10.1016/j.jcrs.2012.03.033.
44. Jaarsma-Coes MG, Klaassen L, Marinkovic M, Luyten GPM, Vu THK, Ferreira TA, Beenakker JWM. Magnetic Resonance Imaging in the Clinical Care for Uveal Melanoma Patients-A Systematic Review from an Ophthalmic Perspective. *Cancers (Basel)*. 2023;15(11). doi: 10.3390/cancers15112995.
45. Niendorf T, Beenakker JWM, Langner S, Erb-Eigner K, Bach Cuadra M, Beller E, Millward JM, Niendorf TM, Stachs O. Ophthalmic Magnetic Resonance Imaging: Where Are We (Heading To)? *Curr Eye Res*. 2021;46(9):1251–1270. doi: 10.1080/02713683.2021.1874021.

46. Richdale K, Wassenaar P, Teal Bluestein K, Abduljalil A, Christoforidis JA, Lanz T, Knopp MV, Schmalbrock P. 7 Tesla MR imaging of the human eye in vivo. *J Magn Reson Imaging*. 2009;30(5):924–32. doi: 10.1002/jmri.21959.
47. Beenakker JWM, Shamonin DP, Webb AG, Luyten GP, Stael BC. Automated retinal topographic maps measured with magnetic resonance imaging. *Invest Ophthalmol Vis Sci*. 2015;56(2):1033–9. doi: 10.1167/iov.14-15161.
48. Beenakker JWM, Rijn GA van, Luyten GP, Webb AG. High-resolution MRI of uveal melanoma using a microcoil phased array at 7 T. *NMR Biomed*. 2013;26(12):1864–9. doi: 10.1002/nbm.3041.
49. Berkowitz BA, McDonald C, Ito Y, Tofts PS, Latif Z, Gross J. Measuring the human retinal oxygenation response to a hyperoxic challenge using MRI: eliminating blinking artifacts and demonstrating proof of concept. *Magn Reson Med*. 2001;46(2):412–6. doi: 10.1002/mrm.1206.
50. Ferreira TA, Grech Fonk L, Jaarsma-Coes MG, Haren GGR van, Marinkovic M, Beenakker JWM. MRI of Uveal Melanoma. *Cancers (Basel)*. 2019;11(3). doi: 10.3390/cancers11030377.
51. Beenakker JWM, Ferreira TA, Soemarwoto KP, Genders SW, Teeuwisse WM, Webb AG, Luyten GP. Clinical evaluation of ultra-high-field MRI for three-dimensional visualisation of tumour size in uveal melanoma patients, with direct relevance to treatment planning. *MAGMA*. 2016;29(3):571–7. doi: 10.1007/s10334-016-0529-4.
52. Jaarsma-Coes MG, Ferreira TA, Marinkovic M, Vu THK, Vught L van, Haren GR van, Rodrigues MF, Klaver YLB, Verbist BM, Luyten GPM, Rasch CRN, Beenakker JWM. Comparison of Magnetic Resonance Imaging-Based and Conventional Measurements for Proton Beam Therapy of Uveal Melanoma. *Ophthalmol Retina*. 2023;7(2):178–188. doi: 10.1016/j.oret.2022.06.019.
53. Simpson MJ. Mini-review: Far peripheral vision. *Vision Res*. 2017;140:96–105. doi: 10.1016/j.visres.2017.08.001.
54. Atchison DA, Smith G. Refractive anomalies. In: DA Atchison, G Smith, eds. *Optics of the Human Eye*. Butterworth-Heinemann; 2000:57–66. doi: 10.1016/b978-0-7506-3775-6.50008-0.
55. Daiber HF, Gnugnoli DM. *Visual Acuity*. StatPearls Publishing, Treasure Island (FL); 2022.
56. Bailey IL, Lovie-Kitchin JE. Visual acuity testing. From the laboratory to the clinic. *Vision Res*. 2013;90:2–9. doi: 10.1016/j.visres.2013.05.004.
57. Groth SL. New Strategies for Automated Perimetry: Historical Perspective and Future Innovations. *J Curr Glaucoma Pract*. 2021;15(3):103–105. doi: 10.5005/jp-journals-10078-1321.
58. Ma X, Tang L, Chen X, Zeng L. Periphery kinetic perimetry: clinically feasible to complement central static perimetry. *BMC Ophthalmol*. 2021;21(1):343. doi: 10.1186/s12886-021-02056-5.
59. Maeda N. Clinical applications of wavefront aberrometry - a review. *Clin Exp Ophthalmol*. 2009;37(1):118–29. doi: 10.1111/j.1442-9071.2009.02005.x.
60. Navarro R, Gonzalez L, Hernandez-Matamoros JL. On the prediction of optical aberrations by personalized eye models. *Optom Vis Sci*. 2006;83(6):371–81. doi: 10.1097/01.opx.0000221399.50864.c7.
61. Jaeken B, Lundstrom L, Artal P. Fast scanning peripheral wave-front sensor for the human eye. *Opt Express*. 2011;19(8):7903–13. doi: 10.1364/oe.19.007903.
62. Shen J, Thibos LN. Measuring ocular aberrations and image quality in peripheral vision with a clinical wave-front aberrometer. *Clin Exp Optom*. 2009;92(3):212–22. doi: 10.1111/j.1444-0938.2009.00376.x.
63. Polans J, Jaeken B, McNabb RP, Artal P, Izatt JA. Wide-field optical model of the human eye with asymmetrically tilted and decentered lens that reproduces measured ocular aberrations. *Optica*. 2015;2(2):124–134. doi: 10.1364/optica.2.000124.
64. Wei X, Thibos L. Modeling the eye's optical system by ocular wavefront tomography. *Opt Express*. 2008;16(25):20490–502. doi: 10.1364/oe.16.020490.
65. Li T, Reddy A, Stein JD, Nallasamy N. Ray tracing intraocular lens calculation performance improved by AI-powered postoperative lens position prediction. *Br J Ophthalmol*. 2023;107(4):483–487. doi: 10.1136/bjophthalmol-2021-320283.
66. Liou HL, Brennan NA. Anatomically accurate, finite model eye for optical modeling. *J Opt Soc Am A Opt Image Sci Vis*. 1997;14(8):1684–95. doi: 10.1364/josaa.14.001684.
67. Lotmar W. Theoretical Eye Model with Aspherics*. *Journal of the Optical Society of America*. 1971;61(11):1522–1529. doi: 10.1364/josa.61.001522.

68. Chen YC, Jiang CJ, Yang TH, Sun CC. Development of a human eye model incorporated with intraocular scattering for visual performance assessment. *J Biomed Opt.* 2012;17(7):075009. doi: 10.1117/1.jbo.17.7.075009.
69. Navarro R, Palos F, Gonzalez L. Adaptive model of the gradient index of the human lens. I. Formulation and model of aging ex vivo lenses. *J Opt Soc Am A Opt Image Sci Vis.* 2007;24(8):2175–85. doi: 10.1364/josaa.24.002175.
70. Navarro R, Palos F, Gonzalez LM. Adaptive model of the gradient index of the human lens. II. Optics of the accommodating aging lens. *J Opt Soc Am A Opt Image Sci Vis.* 2007;24(9):2911–20. doi: 10.1364/josaa.24.002911.
71. Olsen T, Hoffmann P. C constant: new concept for ray tracing-assisted intraocular lens power calculation. *J Cataract Refract Surg.* 2014;40(5):764–73. doi: 10.1016/j.jcrs.2013.10.037.
72. Rozema JJ, Rodriguez P, Navarro R, Tassignon MJ. SyntEyes: A Higher-Order Statistical Eye Model for Healthy Eyes. *Invest Ophthalmol Vis Sci.* 2016;57(2):683–91. doi: 10.1167/iovs.15-18067.
73. Invernizzi A, Cigada M, Savoldi L, Cavuto S, Fontana L, Cimino L. In vivo analysis of the iris thickness by spectral domain optical coherence tomography. *Br J Ophthalmol.* 2014;98(9):1245–9. doi: 10.1136/bjophthalmol-2013-304481.
74. Wang X, Dong J, Wang X, Wu Q. IOL tilt and decentration estimation from 3 dimensional reconstruction of OCT image. *PLoS One.* 2013;8(3):e59109. doi: 10.1371/journal.pone.0059109.
75. Drasdo N, Fowler CW. Non-linear projection of the retinal image in a wide-angle schematic eye. *Br J Ophthalmol.* 1974;58(8):709–14. doi: 10.1136/bjo.58.8.709.
76. Suheimat M, Zhu HF, Lambert A, Atchison DA. Relationship between retinal distance and object field angles for finite schematic eyes. *Ophthalmic Physiol Opt.* 2016;36(4):404–10. doi: 10.1111/opo.12284.
77. Jaeken B, Mirabet S, Marin JM, Artal P. Comparison of the optical image quality in the periphery of phakic and pseudophakic eyes. *Invest Ophthalmol Vis Sci.* 2013;54(5):3594–9. doi: 10.1167/iovs.13-11956.
78. Steinmetz JD et al. Causes of blindness and vision impairment in 2020 and trends over 30 years, and prevalence of avoidable blindness in relation to VISION 2020: the Right to Sight: an analysis for the Global Burden of Disease Study. *The Lancet Global Health.* 2021;9(2):e144–e160. doi: 10.1016/s2214-109x(20)30489-7.
79. Lundstrom M, Goh PP, Henry Y, Salowi MA, Barry P, Manning S, Rosen P, Stenevi U. The changing pattern of cataract surgery indications: a 5-year study of 2 cataract surgery databases. *Ophthalmology.* 2015;122(1):31–8. doi: 10.1016/j.ophtha.2014.07.047.
80. Findl O. Intraocular Lens Materials and Design. In: DM Colvard, ed. *Achieving Excellence in Cataract Surgery: A Step-by-step Approach*; 2009:95–104.
81. Chu YR. Aspheric Intraocular Lenses. In: DM Colvard, ed. *Achieving Excellence in Cataract Surgery: A Step-by-step Approach*; 2009:105–114.
82. Clark A, Morlet N, Ng JQ, Preen DB, Semmens JB. Whole population trends in complications of cataract surgery over 22 years in Western Australia. *Ophthalmology.* 2011;118(6):1055–61. doi: 10.1016/j.ophtha.2010.11.001.
83. Masket S, Fram NR. Pseudophakic Dysphotopsia: Review of Incidence, Cause, and Treatment of Positive and Negative Dysphotopsia. *Ophthalmology.* 2021;128(11):e195–e205. doi: 10.1016/j.ophtha.2020.08.009.
84. Masket S, Fram NR. Pseudophakic negative dysphotopsia: Surgical management and new theory of etiology. *J Cataract Refract Surg.* 2011;37(7):1199–207. doi: 10.1016/j.jcrs.2011.02.022.
85. Makhotkina NY, Nijkamp MD, Berendschot TTJM, Borne B van den, Nuijts RMMA. Effect of active evaluation on the detection of negative dysphotopsia after sequential cataract surgery: discrepancy between incidences of unsolicited and solicited complaints. *Acta Ophthalmologica.* 2018;96(1):81–87. doi: 10.1111/aos.13508.
86. Makhotkina NY, Berendschot TT, Nuijts RM. Objective evaluation of negative dysphotopsia with Goldmann kinetic perimetry. *J Cataract Refract Surg.* 2016;42(11):1626–1633. doi: 10.1016/j.jcrs.2016.09.016.
87. Cooke DL, Kasko S, Platt LO. Resolution of negative dysphotopsia after laser anterior capsulotomy. *J Cataract Refract Surg.* 2013;39(7):1107–9. doi: 10.1016/j.jcrs.2013.05.002.
88. Cooke DL. Negative dysphotopsia after temporal corneal incisions. *J Cataract Refract Surg.* 2010;36(4):671–2. doi: 10.1016/j.jcrs.2010.01.004.
89. Masket S, Fram NR, Cho A, Park I, Pham D. Surgical management of negative dysphotopsia. *J Cataract Refract Surg.* 2018;44(1):6–16. doi: 10.1016/j.jcrs.2017.10.038.

90. Vamosi P, Csakany B, Nemeth J. Intraocular lens exchange in patients with negative dysphotopsia symptoms. *J Cataract Refract Surg.* 2010;36(3):418–24. doi: 10.1016/j.jcrs.2009.10.035.
91. Weinstein A. Surgical experience with pseudophakic negative dysphotopsia. *J Cataract Refract Surg.* 2012;38(3):561, author reply 561. doi: 10.1016/j.jcrs.2011.12.021.
92. Makhotkina NY, Berendschot TT, Beckers HJ, Nuijts RM. Treatment of negative dysphotopsia with supplementary implantation of a sulcus-fixated intraocular lens. *Graefes Arch Clin Exp Ophthalmol.* 2015;253(6):973–7. doi: 10.1007/s00417-015-3029-8.
93. Makhotkina NY, Dugrain V, Purchase D, Berendschot T, Nuijts R. Effect of supplementary implantation of a sulcus-fixated intraocular lens in patients with negative dysphotopsia. *J Cataract Refract Surg.* 2018;44(2):209–218. doi: 10.1016/j.jcrs.2017.11.013.
94. Henderson BA, Yi DH, Constantine JB, Geneva I. New preventative approach for negative dysphotopsia. *J Cataract Refract Surg.* 2016;42(10):1449–1455. doi: 10.1016/j.jcrs.2016.08.020.
95. Pamulapati SV, Saeed JM, Pompey N, Gomez KD, Vakharia MR. Randomized Controlled Trial of Intraocular Lens Orientation for Dysphotopsia. *Am J Ophthalmol.* 2022;243:28–33. doi: 10.1016/j.ajo.2022.06.018.



2

Distinct differences in anterior chamber configuration and peripheral aberrations in negative dysphotopsia

This chapter is published as:

L. van Vught, G.P.M. Luyten, J.W.M. Beenakker
**Distinct differences in anterior chamber configuration
and peripheral aberrations in negative dysphotopsia**
Journal of Cataract & Refractive Surgery, 2020
DOI: 10.1097/j.jcrs.0000000000000206

Abstract

Purpose: Provide insight in the anatomical characteristics associated with negative dysphotopsia using quantitative clinical data.

Setting: Department of Ophthalmology, Leiden University Medical Center, Leiden, the Netherlands.

Design: Case-control study.

Methods: Anterior chamber tomography and peripheral aberrometry were measured in twenty-seven pseudophakic patients with negative dysphotopsia (ND) and thirty pseudophakic controls. Based on these measurements, the total corneal power, anterior chamber depth, pupil location and diameter, iris tilt and peripheral ocular wavefront up to 30 degrees eccentricity were compared between both groups. Additionally, ray-tracing simulations using pseudophakic eye models were performed to establish a connection between these clinical measurements and current hypotheses on the aetiology of ND.

Results: Patients with ND have a smaller ($p=0.03/p<0.01$) and more decentered ($p<0.01$) pupil than pseudophakic controls. Additionally, an increased temporal tilted iris ($p<0.01$) and an asymmetric peripheral aberration profile were observed in patients with ND, of which the latter was also apparent in a number of ray tracing models. The combination of these in vivo results and ray tracing simulations indicates that patients with ND have a temporal rotated eye, which confirms the hypothesised relation between ND and an increased angle kappa.

Conclusions: Patients with negative dysphotopsia have a smaller pupil and an increased angle kappa, which make them more susceptible to experience a shadow in the temporal visual field.

2.1 Introduction

Cataract, the clouding of the crystalline lens inside of the eye, is one of the principal causes of visual impairment¹ and it is generally treated by replacing that lens with an artificial intraocular lens (IOL). Although cataract surgery has a very low rate of intra- and postoperative complications, recent studies have revealed that up to 19% of the patients experience an unwanted visual complaint known as negative dysphotopsia (ND) directly after cataract surgery,^{2,3} that persists for more than a year in 3.2%.³ As the cataract surgery rate is very high, estimated as 4000 per million people in 2020,⁴ this would result in roughly 6 million people being affected by ND each year, of which at least 1 million will have persistent complaints.

ND is commonly described as a shadow in or missing part of the peripheral temporal visual field.^{5–8} It has been reported with a wide variety of IOL types,⁷ and is generally more pronounced under photopic conditions.⁸ Although the reported incidence of ND, when actively surveyed, is quite high, the severity of the complaints often reduces over time, in many cases resolving fully. However, for the 3.2% of the patients that are still experiencing ND one year postoperatively, the chance of spontaneous reduction or resolution of the complaints is minimal.³

While clinical evaluations revealed no evident abnormalities in patients with ND, for example no abnormalities in IOL position,⁸ optical ray tracing simulations revealed various methods to induce a shadow in the peripheral visual field.^{6,9,10} One of the main hypothesized mechanisms is the occurrence of an unilluminated area on the peripheral nasal retina that is experienced as a shadow in the temporal visual field.^{9,11} Such an unilluminated retina could for instance be the result of a discontinuity in illumination between light that is refracted by the optic and light that misses the optic and passes through the gap between the iris and IOL (the iris-IOL gap).^{9,11}

Multiple factors that potentially affect this discontinuity in retinal illumination have also been investigated using these same simulations. For instance, an evaluation of the pupil size showed that the shadow is more profound with small pupils,⁹ which was also reported in clinical evaluations.⁸ In addition, a relationship was found between the discontinuity in retinal illumination and a positive angle kappa,⁹ the angle between the pupillary axis and the visual axis.¹² At a larger angle, more light rays would be able to pass between the IOL and iris, increasing the experienced discontinuity in retinal illumination. Furthermore, the optic diameter, edge design, aspheric surface design, material, and alignment of the IOL have been proposed to affect the occurrence and severity of ND, although their effect is likely to be minor.⁹ Other studies identified various optical effects caused by the capsular bag that could lead to ND. These optical effects include the lack of blockage of peripheral light rays by a non-translucent capsular bag,⁶ a reduction in peripheral transmitted light due to the capsular bag,⁹ and visible arcs and bands caused by the capsulorrhexis-IOL interaction.¹⁰

Although multiple of these mechanisms could lead to ND, no definite conclusion on its origin has been made. Nevertheless, these proposed mechanisms have formed the basis for various preventive approaches, such as performing a primary reverse optic capture or implanting the IOL with a horizontal orientation of the haptics,^{13,14} as well as many different treatments for ND.^{6,7,9,11,14–22} Some of these treatments showed to be successful in small groups of patients, but none gave full resolution in all patients. This lack of a definite strategy to

resolve ND is mainly due to the lack of clinical data that could discriminate between the different proposed origins of ND, as this would give a clear indication of more successful treatment strategies.

In this study, we therefore aim to provide quantitative clinical data of pseudophakic eyes with and without ND to gain a better understanding of the anatomical characteristics that are associated with ND. Firstly, the anterior segment configuration, evaluated by anterior segment tomography and biometry, are analysed, as small geometrical differences could result in significant differences in peripheral vision and therefore have a relation to ND. Secondly, the ocular wavefront aberrations are evaluated along the horizontal meridian to quantify potential objective refractive differences in the peripheral vision. Finally, the relation between differences in anterior segment configuration and peripheral ocular aberrations are studied via ray tracing simulations, to relate the effects of the various proposed origins of ND to the clinical data.

2.2 Methods

Pseudophakic patients with and without clinically reported ND were studied at the Leiden University Medical Center. Patients were excluded if they had any additional ocular surgery, such as LASIK, that would severely modify the optical properties of the eye. The study was performed to conform with the tenets of the Declaration of Helsinki and approved by the local Medical Ethics Committee (CCMO-registry number: NL58358.058.16).

In total, fifty-seven pseudophakic eyes of twenty-seven patients with ND and thirty pseudophakic controls were prospectively included between November 2016 and May 2019. The pseudophakic controls were included from three centers and the patients with ND were referred from seventeen different centers after an otherwise uneventful cataract surgery. For all referred patients with ND, the diagnosis of ND was confirmed prior to inclusion. The criteria for this diagnosis consisted of a patient-reported shadow or dark region in the temporal peripheral visual field that occurred after an otherwise uncomplicated cataract surgery, no evident cause of this visual complaint and no clear anomalies in IOL positioning upon slit lamp examination. Although the pseudophakic controls had not reported any complaints during the regular follow-up after cataract surgery, four controls reported the presence of a temporal shadow when they were they were actively screened for ND at the beginning of the study.² These four subjects, and one other control with a raised suspicion of staphyloma after inclusion, were excluded from further analysis.

Study procedures were performed after the patients provided written informed consent. The study procedures included anterior segment tomography, ocular biometry and peripheral aberrometry for one eye (Figure 2.1). The baseline equality of both resulting groups of subjects was assessed by comparing the sex and age of the patients, and the laterality, keratometry, axial length and implanted IOL type of the studied eye.

Anterior segment tomography and biometry

The combined optical effect of the central 8.0 mm of the anterior and posterior corneal surface was evaluated with the Pentacam anterior segment tomographer (software version 1.20r41, Oculus, Optikgeräte GmbH, Wetzlar, Germany) in terms of total corneal wavefront, expressed in Zernike coefficients²³ using the Pentacam's built-in software. To limit the number of tested metrics, only the Zernike coefficients with a strong effect on the variation along the horizontal meridian, being Z_1^1 , Z_2^0 , Z_2^2 and Z_3^1 , were selected for analysis.

The internal anterior chamber depth (ACD), horizontal decentration of the pupil center with respect to the corneal vertex and the pupil diameter were obtained from tomography. As it has been reported that the automated ACD measurement might fail in pseudophakic eyes,²⁴ the ACDs were measured manually for each eye on three different Scheimpflug images and averaged. The horizontal decentration of the pupil center with respect to the visual axis was also measured with the Lenstar LS900 biometer (Haag-Streit AG, Köniz, Switzerland), together with the pupil diameter, keratometry and axial length. Based on the rationale that a larger angle kappa results in a temporal rotation of the eye, the tilt of the iris was calculated by fitting a 3D plane through the central 6.0 mm of the iris surface as measured by the Pentacam using a custom-written program in Python 3.6.

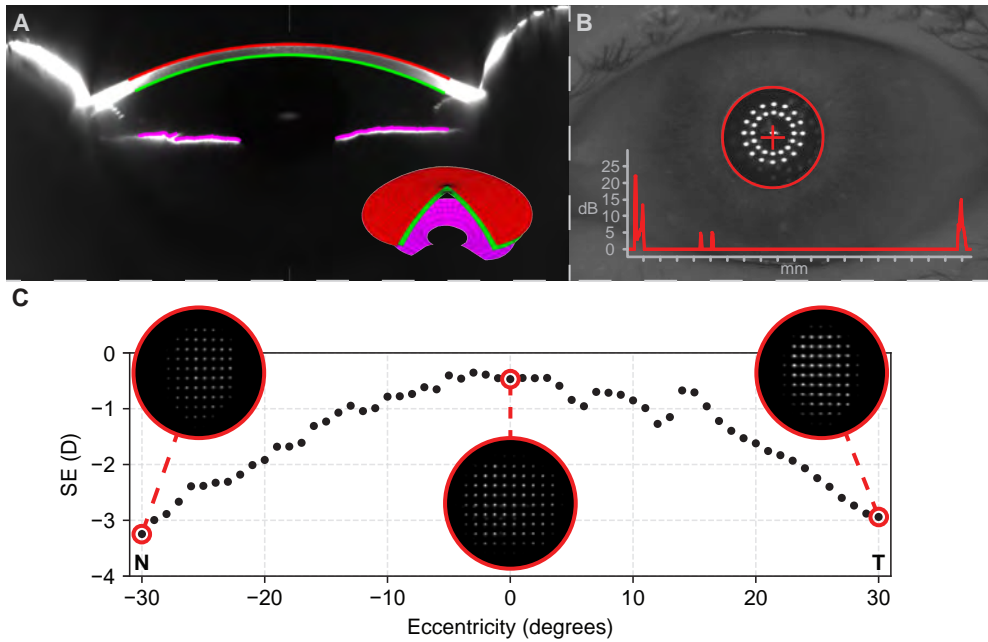


Figure 2.1: Overview of the performed clinical measurements. A) Anterior segment tomography showing the measured anterior (red) and posterior (green) corneal surface, from which the corneal wavefront was calculated. Additionally, the measured iris (pink) from which the iris tilt was calculated is shown. The insert shows the 3D model of the anterior segment, as obtained from the Pentacam. B) Biometry analysis showing the location of the pupil center with respect to the visual axis, and the biometry result as insert. C) The peripheral ocular aberrations, expressed as spherical equivalent of refraction (SE) in Diopters (D), along the horizontal meridian up. The inserts show the Hartmann-Slack images from which the refraction is calculated. At around 15 degrees eccentricity in the temporal visual field (T), a distortion is visible that is not apparent on the nasal (N) side. This distortion caused by reflection from the optic nerve head.

Peripheral ocular aberrations

Peripheral ocular aberrations along the horizontal meridian were measured using the VPR peripheral aberrometer (vOPTICA, Murcia, Spain) as described by Jaeken et al.²⁵ Earlier studies with this technique showed that emmetropic eyes are relatively myopic at peripheral eccentricities,²⁶ and that pseudophakic eyes have stronger peripheral aberrations than phakic eyes.²⁷

The aberrometer quantifies the ocular aberrations up to 30 degrees eccentricity with a 1 degree step size using Hartmann-Shack wavefront sensor integrated in a rotating arm. The patient is instructed to look at a fixation target while the arm rotates and the Hartmann-Shack images are acquired. Four measurements are performed per eccentricity, expressed in Zernike terms over the central 3.0 mm and averaged. Each individual measurement takes about 2 seconds to complete. When the observer noted erroneous or missing results for certain eccentricities during the measurement, e.g. due to blinking, an additional measurement was performed. With the instructions, evaluations and optional additional measurements, a full peripheral aberrometry measurement took on average 5 minutes per subject.

The aberration profiles were converted to spherical equivalent of refraction (SE, also known as power vector M),²⁸ astigmatism (also known as power vector J),²⁸ and spherical aberration. From the aberration profiles, the SE, astigmatism and spherical aberration as measured for central vision and for peripheral vision at 30 degrees nasal and temporal visual field eccentricity were selected for statistical analysis. At 30 degrees eccentricity, the refraction relative to the central refraction was used for SE and astigmatism to correct for an intended offset in central refraction.²⁷

Ray tracing simulations

Ray tracing simulations were performed to assess the relation between the peripheral ocular aberrations and various anterior segment configurations with a potential relation to ND. A geometrical eye-model was created in Zemax OpticStudio 18.9 (Zemax, LCC, Kirkland, Washington, USA) and aberrations at 543 nm were calculated up to 30 degrees eccentricity with a 1 degree step size. Actual pupil size was adjusted to obtain a 3.0 mm apparent pupil size, in order to match the peripheral ocular aberration measurements. The calculated aberrations were subsequently converted into SE.^{28,29} All simulations and analyses were automated using Python 3.6 and the PyZDDE library.³⁰

The eye-model was based on the Escudero-Sanz wide-angle schematic eye model.³¹ For accurate use in the evaluation of ND, two adjustments were made to this model. Firstly, the iris was moved 0.5 mm forward and given a thickness of 0.5 mm. Secondly, the crystalline lens was replaced by a simple IOL instead of the crystalline lens, placed 0.5 mm behind the posterior iris. The IOL had a refractive index of 1.47 and a thickness of 1.0 mm. The anterior radius of curvature, anterior conic constant and posterior radius of curvature were chosen such to match the central ocular aberrations of the phakic Escudero-Sanz eye model. This resulted in an IOL with an anterior radius of curvature of 19.5 mm, an anterior conic constant of -13.7 mm, a posterior radius of curvature of -11.2 mm and an in-situ paraxial power of 18.5 D.⁹

The variations in anterior segment configurations that were analysed included IOL positioning, horizontal iris and IOL tilt and an increase in angle kappa. Two modifications in IOL positioning were evaluated, being a 0.4 mm increase in axial distance between the iris

2 and IOL, which would increase the iris-IOL gap, and a 1.0 mm temporal decentration of the IOL, which would increase the iris-IOL gap nasally. Since a temporal tilt or either the iris or both the iris and IOL would allow for easier passage of light through the nasal iris-IOL gap, both were evaluated. To this end, a temporal tilt of 5.0 degrees temporally was induced in either the iris or both the iris and IOL. Finally, as a larger angle kappa would result in an outward rotation of the eye with respect to the visual axis, and therefore also in easier passage of light through the nasal iris-IOL gap, an angle kappa of 5.0 degrees was induced and evaluated. This angle kappa was created by adding 5.0 degrees to the incident angle. Since the IOL design is one of the potential factors of influence, these simulations were also performed using the pseudophakic eye-models of Holliday and Simpson, both with the acrylic and the silicone IOL.⁹

Statistical analyses

All statistical analyses were performed with the presence of ND as dependent or grouping variable. Firstly, the baseline characteristics were compared between both groups. Secondly, the relation between ND and the total corneal wavefront, expressed in Zernike coefficients, was assessed using a logistic regression analysis. Thirdly, all evaluated anterior segment configurations were compared using independent-samples t-tests. Finally, the central and peripheral ocular aberrations were compared using Mann-Whitney U tests. The statistical analyses were performed using SPSS Statistics 23 (IBM Corp., Armonk, New York, USA), except for the ocular aberrations, which were analysed in Python 3.6 using the SciPy library version 1.1.0.³² An alpha of 0.05 was set as critical value for significance for every test. No multiple testing correction was applied as many of the tested parameters are geometrically correlated with each other.

2.3 Results

In the baseline comparison, the group of patients with ND showed a higher percentage of females than the pseudophakic controls ($p < 0.01$), with percentages of 88.9% and 48.0% respectively. Furthermore, the pseudophakic controls had on average slightly longer eyes ($p = 0.02$). All other baseline parameters were comparable between both groups (Table 2.1). Some patients and controls were excluded from one of the performed analyses, due to missing or erroneous data (Figure 2.2).

A wider variety of IOL types was seen in patients with ND than in pseudophakic controls. In the patients with ND, a total of ten different types were implanted. The majority of this group (51.9%) had a TECNIS ZCB00 implanted. In the group of pseudophakic controls, two IOL types were implanted, the TECNIS ZCB00 (76.0%) and the Quadrimax (24.0%). All IOLs were implanted within the capsular bag. For one patients with ND, the capsulorrhexis did not completely cover the IOL in the temporal inferior quadrant.

Table 2.1: Demographics of both groups. The group of patients with ND had a higher percentage of females and slightly shorter eyes than the pseudophakic controls. Ocular refraction data are shown in Table 2.2 and Figure 2.5. Baseline equality for sex and laterality was assessed using chi-square tests, astigmatism using a Mann-Whitney U test and all other samples using independent-samples t-tests.

	Patients with ND	Pseudophakic controls	p-value
N Subjects	27	25	
Sex (%Female)	88.9	48.0	<0.01
Laterality (%Right)	40.7	48.0	0.78
Age (Years)			
Mean \pm SD	65.9 \pm 8.1	69.0 \pm 8.2	0.18
Km, corneal (D)			
Mean \pm SD	44.1 \pm 1.4	44.1 \pm 1.3	0.90
Astigmatism, corneal (D)			
Mean \pm SD	-1.0 \pm 0.8	-0.8 \pm 0.5	0.49
Axial length (mm)			
Mean \pm SD	23.3 \pm 1.1	24.2 \pm 1.5	0.02
Implanted IOL			
Type (n)	ZCB00 (14) SN60WF (3) Quadrimax (2) iSert 251 (2) Other* (6)	ZCB00 (19) Quadrimax (6)	

* The other IOLs include: CT LUCIA (1), Fine Vision (1), MI60 (1), MX60 (1), MPlus (1) and SA60AT (1).

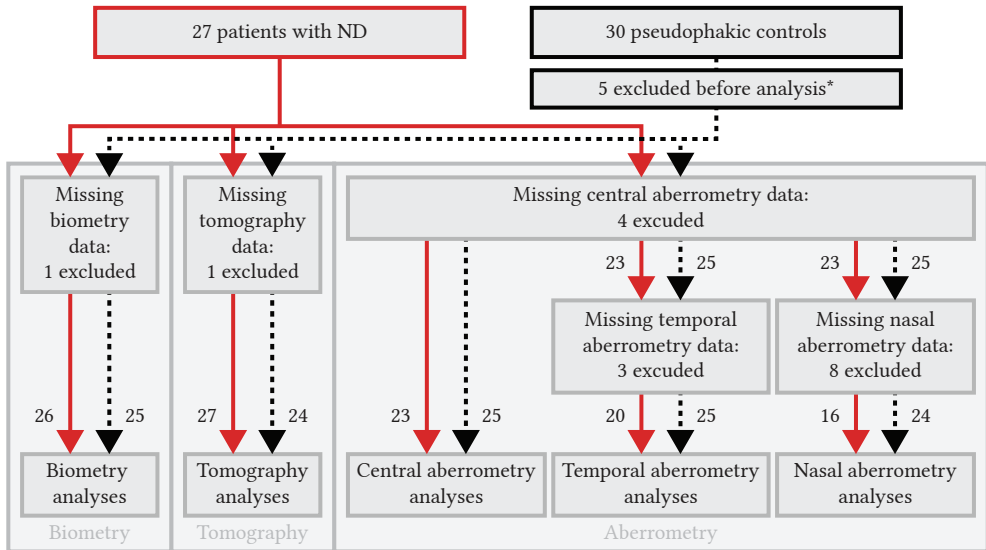


Figure 2.2: A flowchart depicting the amount of patients included in various analyses. Patients with ND are represented by the red continuous lines and pseudophakic controls by the black dashed lines. Next to each line, the number of patients is stated. *Five pseudophakic controls were excluded from all analyses, four due to a reported presence of ND during the study measurements and one due to a raised suspicion of staphyloma after inclusion.

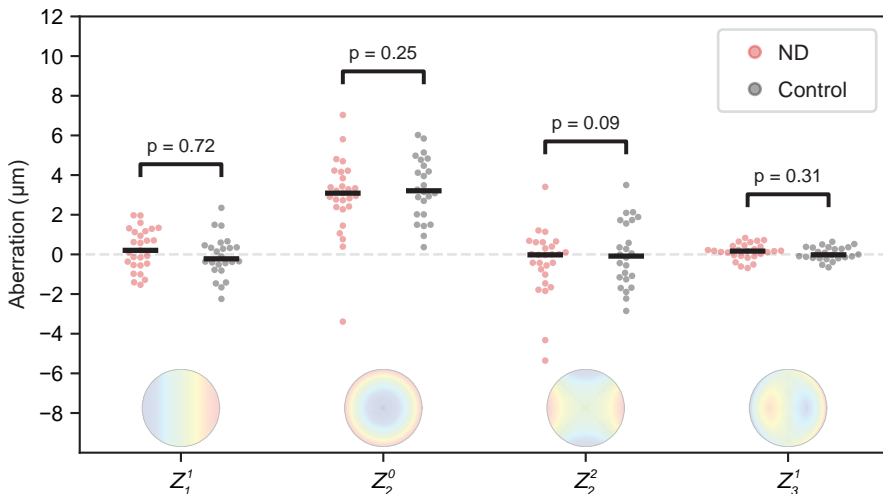


Figure 2.3: Distribution of the total corneal wavefront, expressed in the Zernike coefficients with a major influence on deviations along the horizontal meridian. No clear differences are observed between ND (red) and pseudophakic controls (grey). The horizontal lines depict the medians per group.

Corneal wavefront

The total corneal wavefront along the horizontal meridian was similar for patients with ND and pseudophakic controls, with equal distributions for all four evaluated Zernike coefficients in both groups (Figure 2.3). Additionally, the logistic regression analysis showed no significant relationship between the coefficients and the presence of ND, with all p-values being 0.09 or higher (Figure 2.3).

Anterior chamber depth

The ACDs of patients with ND and pseudophakic controls showed to be similar with average ACDs of 4.17 mm (Standard deviation (SD): 0.38) and 4.30 mm (SD: 0.26) respectively (p=0.184, Figure 2.4A).

Iris tilt

The average horizontal tilt of the iris was significantly larger for patients with ND than for pseudophakic controls (p<0.01; Figure 2.4B), with average tilts of 6.3 degrees (SD: 1.4), and 4.6 degrees (SD: 5). The larger positive tilt indicates a more temporally tilted iris in patients with ND.

Pupil decentration

The pupil center of patients with ND was located significantly more temporally than in pseudophakic controls on both the anterior segment tomography and ocular biometry. On anterior segment tomography, the average horizontal distance from the corneal vertex was 0.17 mm (standard deviation (SD): 0.14) and 0.01 mm (SD: 0.16) for patients with ND and pseudophakic controls respectively (p<0.01, Figure 2.4C). Similar results were obtained from biometry, with an average decentrations of respectively 0.19 mm (SD: 0.21) and 0.03 mm (SD: 0.16) from the visual axis (p<0.01; Figure 2.4C).

Pupil diameter

Patients with ND showed to have a significant smaller pupil than the pseudophakic controls on both the anterior segment tomography and ocular biometry. On tomography, the average pupil diameters were 2.4 mm (SD: 0.4) and 2.7 mm (SD: 0.4) for patients with ND and pseudophakic controls respectively (p<0.01; Figure 2.4D). These diameters were 3.7 mm (SD: 0.6) and 4.1 mm (SD: 0.7) on biometry (p=0.03; Figure 2.4D).

Peripheral ocular aberrations

In general, peripheral aberrometry showed the earlier described trend of a decreasing SE of up to -2 Dioptres at 30 degrees eccentricity,²⁷ while the astigmatism increases up to 3 Dioptres (Figure 2.5A, B; Table 2.2). Centrally, there was no difference between both groups in SE, astigmatism and spherical aberrations.

Peripherally, however, a difference between patients with and without ND is visible, as a clear asymmetry between relative SE at nasal and temporal eccentricities in patients with ND, which was not visible in pseudophakic controls (Figure 2.5A).

At temporal visual field eccentricities, where ND is manifested, median relative SEs of -1.5

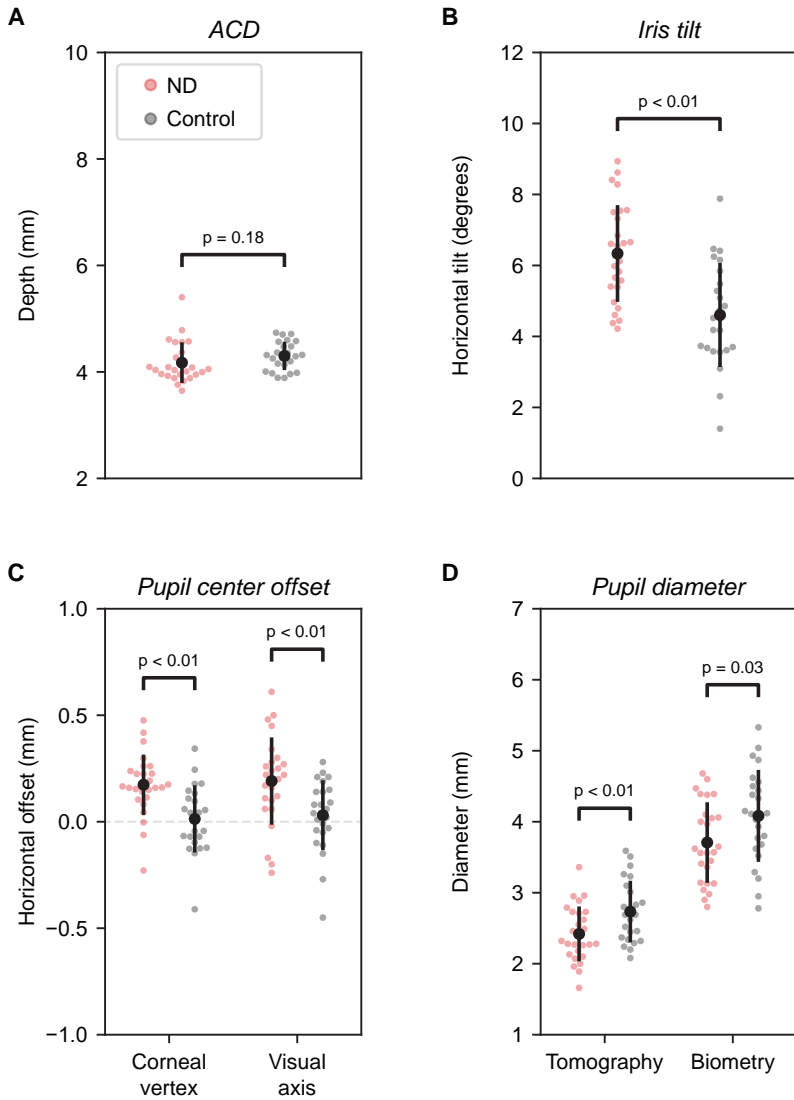


Figure 2.4: Anterior chamber configurations for patients with ND (red) and controls (grey), showing that patients with ND on average have a temporally shifted and smaller pupil and a more tilted iris. Black dots display the means, the vertical lines the standard deviation. A) The anterior chamber depth (ACD). B) The horizontal iris tilt. A positive tilt indicates a temporal tilt. C) Horizontal decentration of the pupil center with respect to the corneal vertex and the visual axis. A positive decentration indicates a temporal shift of the pupil. D) The pupil diameter as measured by tomography and biometry.

Diopter (D) and -1.4 D were measured for patients with ND and pseudophakic controls respectively ($p = 0.9$; Table 2.2). However, for nasal eccentricities, a statistically significant difference in relative SE was found, with -3.6 D for patients with ND and -1.8 D for pseudophakic controls ($p = 0.04$; Table 2.2). The astigmatism as a function of horizontal visual field showed a comparable, although not statistically different, course between both groups (Figure 2.5B; Table 2.2). The spherical aberration was relatively constant as a function of horizontal visual field and did not show a difference between patients with or without ND (Figure 2.5C; Table 2.2).

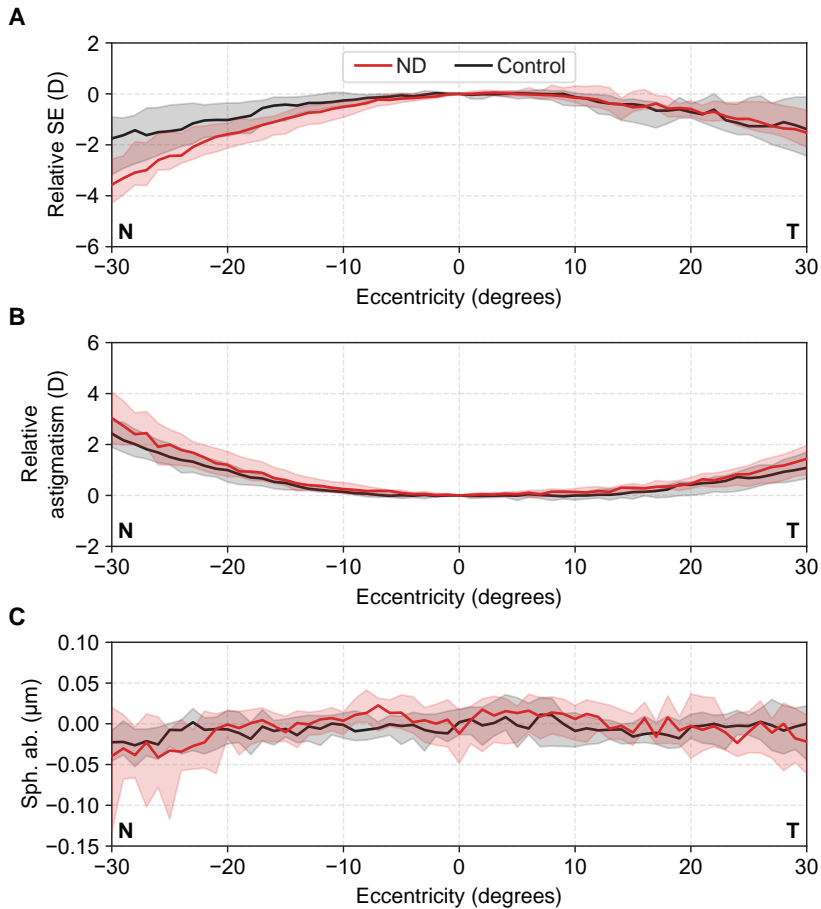


Figure 2.5: A) Relative spherical equivalent of refraction (SE) in Diopters (D), B) Relative astigmatism (D) and C) spherical aberration (μm) as function of visual field eccentricity. Negative eccentricities are acquired at the nasal visual field (N). Patients with ND (red) show a stronger decrease in SE at nasal eccentricities than controls (black). The median value at each eccentricity is indicated by the solid line and the inter-quartile range is depicted by the shaded area.

Table 2.2: Peripheral aberrometry shows a significant difference in nasal relative spherical equivalent of refraction (SE). Nasal and temporal aberrations are measured at 30 degrees visual field eccentricity. Q1 and Q3 are the 25th and 75th percentile. The peripheral SE en astigmatism are relative to the central measured values.

	Patients with ND			Pseudophakic controls			p-value
	Median	Q1	Q3	Median	Q1	Q3	
<i>Central aberrations</i>							
SE (D)	-0.73	-1.02	-0.44	-0.85	-2.50	-0.41	0.64
Astigmatism (D)	0.38	0.26	0.57	0.44	0.24	0.71	0.41
Sph. Ab. (μm)	0.001	-0.048	0.019	0.002	-0.016	0.021	0.40
<i>Nasal aberrations</i>							
Rel. SE (D)	-3.56	-4.29	-2.56	-1.75	-3.17	-0.91	0.04
Rel. Astigmatism (D)	3.04	2.04	4.05	2.43	1.89	2.91	0.11
Sph. Ab. (μm)	-0.040	-0.132	0.020	-0.023	-0.046	-0.008	0.59
<i>Temporal aberrations</i>							
Rel. SE (D)	-1.52	-2.09	-0.64	-1.38	-2.44	-0.12	0.90
Rel. Astigmatism (D)	1.44	0.83	1.96	1.08	0.66	1.70	0.43
Sph. Ab. (μm)	-0.022	-0.061	0.011	0.000	-0.044	0.022	0.95

Ray tracing simulation

The ray tracing simulations using the pseudophakic Escudero-Sanz eye model without additional modifications showed a symmetric decrease of the SE of refraction in the peripheral visual field, similar to the in-vivo aberrometry of the pseudophakic controls (Figure 2.6A, G). Increasing the axial distance between the iris and IOL by 0.4 mm resulted in an overall increase in SE of approximately 1 Dioptre (Figure 2.6B, G). A temporally decentered IOL resulted in an asymmetric change in SE, where a more negative SE was seen at nasal eccentricities than at temporal eccentricities (Figure 2.6C, G).

Tilting solely the iris had almost no effect on the resulting aberration profile (Figure 2.6D, G). A combined temporal tilt of the iris and the IOL, however, resulted in an asymmetric change similar to the change induced by a temporal decentration of the IOL, with a more negative SE at nasal eccentricities (Figure 2.6E, G).

Inducing a positive degree angle kappa, which is equivalent to a temporal rotation of the eye, also resulted in an asymmetric peripheral aberration profile. Similar to the simulation with a temporal decentration of the IOL, a stronger decrease in SE was observed at nasal eccentricities (Figure 2.6F, G). The amount of asymmetry (0.7 D) was however smaller compared to a decentration of the IOL (1.6 D) or a combined tilt the iris and the IOL (1.2 D, Figure 2.6G). The simulations using the two eye-models described by Holladay and Simpson provided similar results,⁹ although with differences in magnitude of both the peripheral aberrations and their asymmetric development to higher eccentricities due to the differences in the eye geometry and IOL properties (Supplementary Figure 2.1).

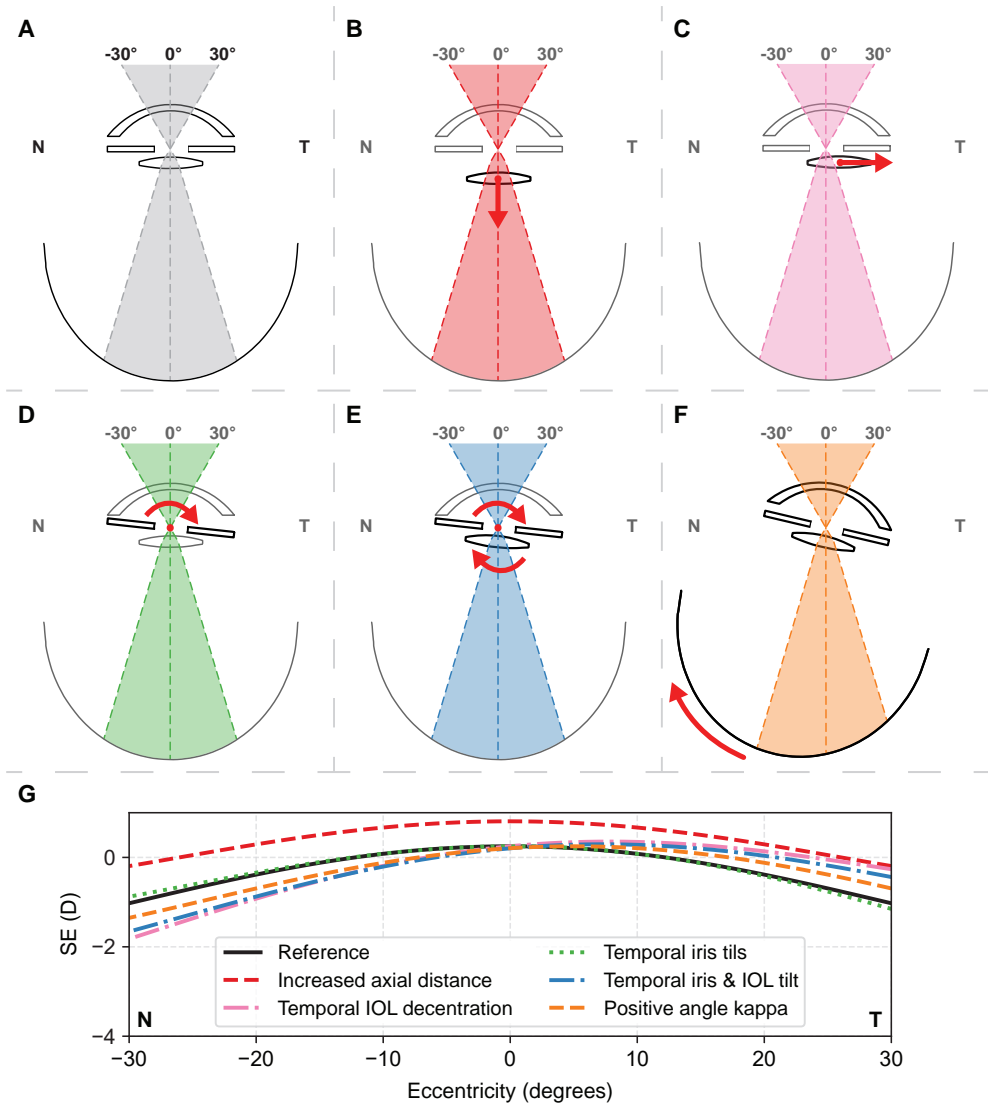


Figure 2.6: Ray tracing analyses on the effect of several of the proposed origins of ND on the peripheral ocular aberrations. A-F) Schematic representation of the tested conditions. A) reference model. B) an increased axial distance between the iris and IOL. C) temporal decentration of the IOL. D) temporal tilt of the iris. E) combined temporal tilt of the iris and IOL. F) positive angle kappa. G) The simulations for decentered IOL, a tilted iris and IOL and an increased angle kappa show a similar asymmetry in the peripheral spherical equivalent of refraction (SE) as observed in patients with ND.

2.4 Discussion

Since the initial description of negative dysphotopsia in 2000,⁵ various aetiological theories have been proposed.^{6,8-10} These theories have however not yet been confirmed nor disproved due to a lack of clinical data on the anterior chamber configuration in ND. In this study, we present an elaborated combination of quantitative geometrical and optical measurements in pseudophakic eyes with and without ND in order to provide clinical insights in anatomical differences that are associated with ND.

The group of patients with ND was comparable to the group of pseudophakic controls, except for a higher percentage of females, a shorter axial length and a larger variation in IOL types (Table 2.1). Both the higher percentage of females and the shorter axial length have been reported earlier for patients with ND,^{2,14} and might be related to each other.³³ Additionally, a wide variety of IOL types was implanted in the studied group of patients with ND, confirming the earlier reports that ND is not just occurring with certain IOL types.¹⁶ As the pseudophakic controls were included from a limited number of clinics, a smaller variety of IOLs were implanted in this cohort. Although this is a limit of the study design, we do not expect this to influence the results, as the outcome measurements, such as pupil diameter, are relatively invariant of IOL design and the IOL types of the control group are also present in the ND group.

As the cornea is the strongest refractive element of the eye, any distinct difference in corneal shape could result in severe visual complaints, both centrally and peripherally. The main components of the total corneal wavefront along the horizontal meridian were comparable between patients with and without ND (Figure 2.3), rendering it unlikely that ND originates from an abnormal corneal shape. Although the location of the corneal incision of the cataract surgery could affect the peripheral aberrations, a direct causal relation with ND is unlikely as no significant differences were observed in the total corneal wavefront.

Although anterior segment imaging showed no abnormalities in either the cornea or the ACD of patients with ND, it revealed three significant differences in the iris configuration. Firstly, a smaller pupil diameter was found in patients with ND, which is in line with the theoretically demonstrated relationship between pupil size and ND.^{6,10} Secondly the pupil centers of patients with ND were more temporally located with respect to both the corneal vertex and the visual axis. This pupil decentration is probably related to the third difference, a significantly stronger tilted iris towards the temporal side with respect to the visual axis in patients with ND. This stronger tilt indicates that, with respect to the visual axis, either the iris is tilted more temporally within the eye or the eye is rotated more temporally. Such a temporal rotation of the eye could be caused by a larger positive angle kappa,^{9,12,34} which is one of the possible causes of ND.⁹ Although a correlation between angle kappa and axial length has been reported,³⁵ it cannot be the cause of the 1.5 degrees increase in angle kappa, as the 0.9 mm increase in axial length would correlate to less than a 0.5 degrees increase in angle kappa.³⁶

Clear differences were also found in the peripheral ocular aberrations. Overall, patients with ND show an asymmetric decrease in SE towards the nasal visual field, which results in a significant lower relative SE at 30 degrees. These peripheral aberration measurements would ideally have been performed at higher eccentricities as ND is generally not apparent at 30 degrees. Unfortunately, there are currently no techniques available to assess the

2

optical wavefronts at higher eccentricities, as the quality of the Hartmann-Shack images deteriorates at the far peripheral field. Although the peripheral aberrations are partly affected by the slightly different axial lengths and implanted IOL types between both study groups, these differences are not likely to be causative of the observed asymmetry in the peripheral myopization. The relatively low eccentricities at which the aberrations were assessed in this study explain why no direct effect of ND, such as a loss of signal, was observed in the temporal visual field. These measured differences in mid-peripheral eccentricities between both groups do, however, aid in the understanding of ND, as they provide a link to the ray tracing simulations in which the effect of a difference in ocular geometry is evaluated.

Ray tracing simulations showed that several of the tested potential factors of influence on the origin of ND result in an asymmetric change in SE towards higher eccentricities, similarly to patients with ND. In particular, these asymmetries could be induced by a temporal decentration of the IOL, a combined temporal tilt of the iris and the IOL, and a temporal rotation of the eye with respect to the visual axis resulting from a positive angle kappa (Figure 2.6C, E, F). As the clinical slit lamp evaluations revealed no evident abnormalities, a strong temporal decentration of the IOL is unlikely.⁸ This confirms earlier ray tracing studies that suggest a minor role of IOL decentration in the aetiology of ND.⁹ Furthermore, since a tilt of solely the iris only had a very minor effect on the peripheral refraction (Figure 2.6D), the observed asymmetric peripheral refraction in ND is likely caused by either a combined tilt of the iris and IOL or from a rotation of the eye with respect to the visual axis. Both of these effects would result in the observed increased iris tilt in the subjects with ND, but only a rotation of the complete eye would result in the increased decentration of the pupil center.

Earlier ray tracing stimulations have shown a clear relationship between a larger positive angle kappa, and discontinuity in retinal illumination.⁹ It has furthermore been suggested that such an temporal rotation of the eye with respect to the visual axis would additionally result in a more anterior position of the function nasal retina (Figure 2.6F), thereby increasing the perception of ND.^{6,7} Although the combined analysis of the data of this study provides a strong support for an increased angle kappa as one of the main contributing factors to ND, other factors can play an additional role in the origin of ND. The potential role of neural adaptation,^{37,38} for example, requires a different set of examinations to gain insight in its potential contribution to the spontaneous resolution of the complaints in some patients. The results of this study can, however, explain the reported preventative effect of implanting IOLs with the haptics oriented horizontally,¹³ as this orientation could put the haptics in the path of rays of light passing through the gap between the iris and IOL. Ray tracing simulations using fully personalized eye models could aid to identify these factors.^{11,19} For a clinically relevant assessment using these analyses, however, the orientation of the iris and the location of the IOL with respect to the iris need to be personalized as well.

These, fully personalized, simulations could also aid in the design of an effective treatment for ND which takes the increased angle kappa into account. They might furthermore provide insight in the suboptimal results of treatments such as laser capsulotomy,^{17,18} implanting a piggyback IOL^{11,19} or exchanging the IOL.²⁰ Any of these treatments can change the configuration of the anterior eye chamber, and thereby potentially reduce the chance of light rays passing through the iris-IOL gap.

Overall, this study identified several anatomical differences between patients with and with-

out ND that provide a basis for further research. There are however some study limitations that should be considered while interpreting these results. Ideally, the study would have been a prospective cohort study in which the patients were included before cataract surgery. This would also result in a more uniform distribution of IOL types and allow for the inclusion of peroperative data, such as the location of the corneal incision, in the analysis. However, given the low incidence of persistent ND of about 3%,³ this is not feasible. Furthermore, the group differences in axial length and sex could have introduced a bias in the measurements, but this could also be a predisposition to ND as other studies also observed a similar difference.^{2,14} Additionally, other studies reported a higher incidence of ND in the left eye,^{3,5,14} which was not present in our study population. Finally, the eye models for the ray tracing analyses were not fully personalized to completely match the eyes of individual ND patients, which would allow for a more in-depth analysis of the optical interplay between the anatomy of the eye and the IOL.

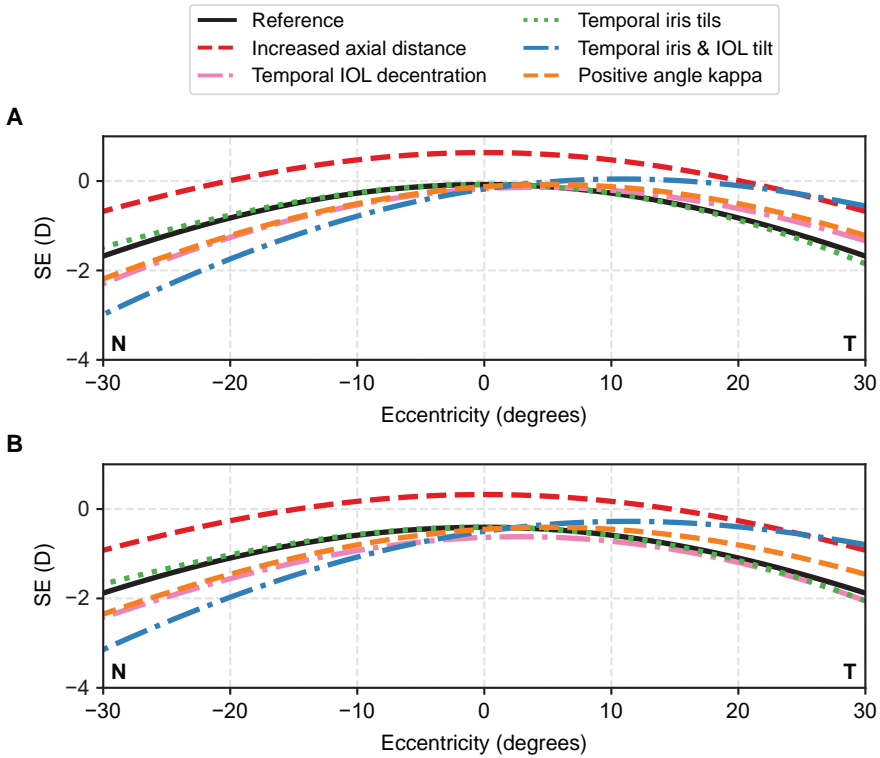
This study provides, despite these limitations, valuable insight in the aetiology of ND based on clinically measured data, which yields a base for further research on the origin, management and prevention of ND. The measurement and simulation results show that the iris and IOL plane are rotated temporally with respect to the visual axis, which corresponds to the role of an increased angle kappa in earlier ray-tracing studies on the aetiology of ND. While these anatomical differences cannot be modified easily, IOL designs can be optimized mitigate the effect of differences, which could benefit the treatment of ND or might even prevent it from occurring. Furthermore, the presented anatomical differences might be able to pre-operatively select patients which have a high risk of ND after cataract surgery, but larger, prospective studies are needed to develop and validate this. In conclusion, this study presents the first clinical insight in anatomical differences between patients with and without ND that both substantiate one of the leading theories behind the aetiology of ND and provides a basis for further research.

2.5 References

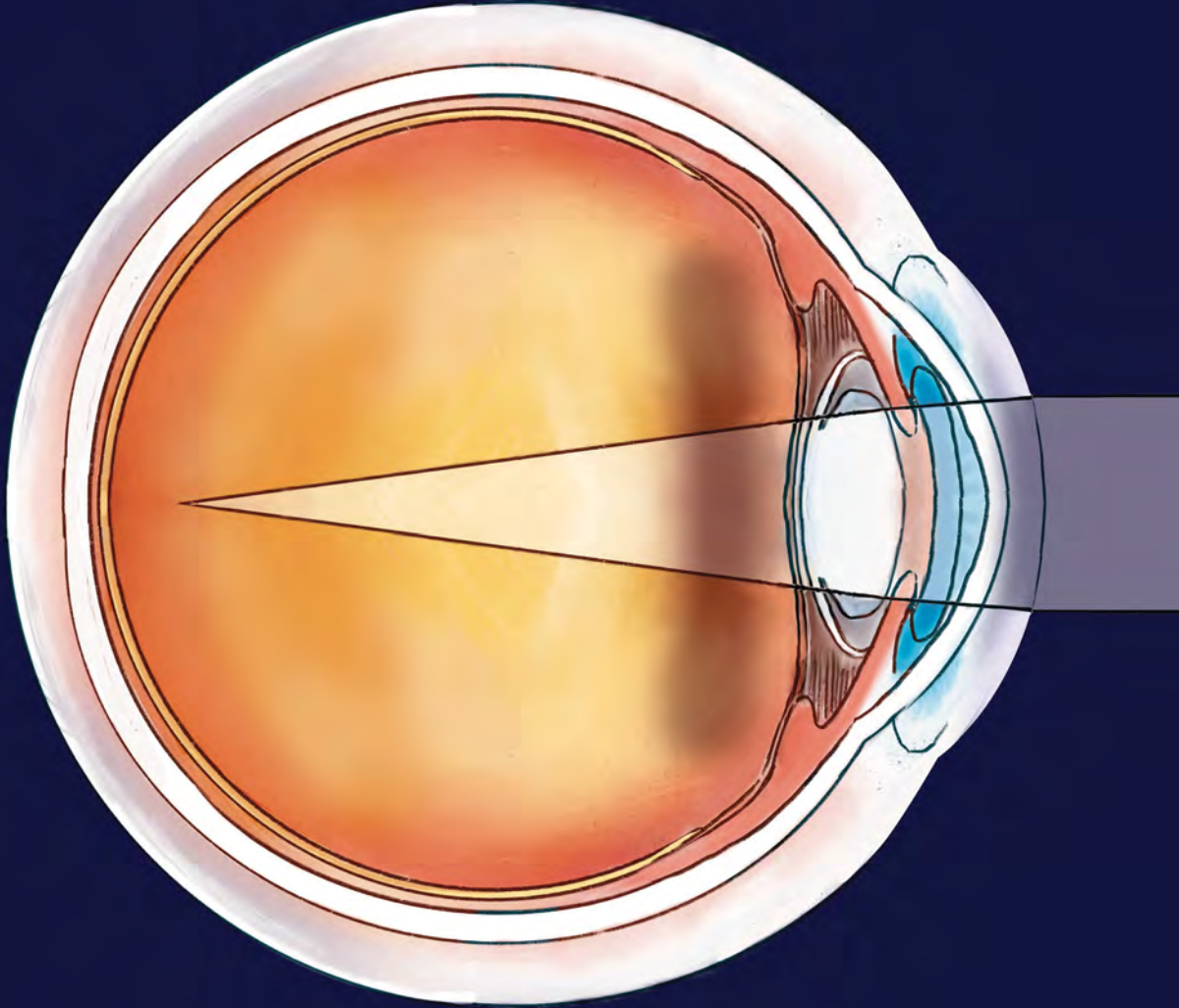
1. Pascolini D, Mariotti SP. Global estimates of visual impairment: 2010. *Br J Ophthalmol*. 2012;96(5):614–8. doi: 10.1136/bjophthalmol-2011-300539.
2. Makhotkina NY, Nijkamp MD, Berendschot T, Borne B van den, Nuijts R. Effect of active evaluation on the detection of negative dysphotopsia after sequential cataract surgery: discrepancy between incidences of unsolicited and solicited complaints. *Acta Ophthalmol*. 2018;96(1):81–87. doi: 10.1111/aos.13508.
3. Osher RH. Negative dysphotopsia: long-term study and possible explanation for transient symptoms. *J Cataract Refract Surg*. 2008;34(10):1699–707. doi: 10.1016/j.jcrs.2008.06.026.
4. World Health Organization. Programme for the Prevention of Blindness and Deafness. *Global initiative for the elimination of avoidable blindness*. Report. 2000.
5. Davison JA. Positive and negative dysphotopsia in patients with acrylic intraocular lenses. *J Cataract Refract Surg*. 2000;26(9):1346–55.
6. Holladay JT, Zhao H, Reisin CR. Negative dysphotopsia: the enigmatic penumbra. *J Cataract Refract Surg*. 2012;38(7):1251–65. doi: 10.1016/j.jcrs.2012.01.032.
7. Henderson BA, Geneva I. Negative dysphotopsia: A perfect storm. *J Cataract Refract Surg*. 2015;41(10):2291–312. doi: 10.1016/j.jcrs.2015.09.002.
8. Masket S, Fram NR. Pseudophakic negative dysphotopsia: Surgical management and new theory of etiology. *J Cataract Refract Surg*. 2011;37(7):1199–207. doi: 10.1016/j.jcrs.2011.02.022.
9. Holladay JT, Simpson MJ. Negative dysphotopsia: Causes and rationale for prevention and treatment. *J Cataract Refract Surg*. 2017;43(2):263–275. doi: 10.1016/j.jcrs.2016.11.049.
10. Hong X, Liu Y, Karakelle M, Masket S, Fram NR. Ray-tracing optical modeling of negative dysphotopsia. *J Biomed Opt*. 2011;16(12):125001. doi: 10.1117/1.3656745.
11. Erie JC, Simpson MJ, Bandhauer MH. Effect of a sulcus-fixated piggyback intraocular lens on negative dysphotopsia: Ray-tracing analysis. *J Cataract Refract Surg*. 2019;45(4):443–450. doi: 10.1016/j.jcrs.2018.10.041.
12. Basmak H, Sahin A, Yildirim N, Papakostas TD, Kanellopoulos AJ. Measurement of angle kappa with synophore and Orbscan II in a normal population. *J Refract Surg*. 2007;23(5):456–60.
13. Henderson BA, Yi DH, Constantine JB, Geneva I. New preventative approach for negative dysphotopsia. *J Cataract Refract Surg*. 2016;42(10):1449–1455. doi: 10.1016/j.jcrs.2016.08.020.
14. Masket S, Fram NR, Cho A, Park I, Pham D. Surgical management of negative dysphotopsia. *J Cataract Refract Surg*. 2018;44(1):6–16. doi: 10.1016/j.jcrs.2017.10.038.
15. Simpson MJ. Mini-review: Far peripheral vision. *Vision Res*. 2017;140:96–105. doi: 10.1016/j.visres.2017.08.001.
16. Geneva I, Henderson BA. The Complexities of Negative Dysphotopsia. *Asia Pac J Ophthalmol (Phila)*. 2017;6(4):364–371. doi: 10.22608/apo.2017111.
17. Cooke DL, Kasko S, Platt LO. Resolution of negative dysphotopsia after laser anterior capsulotomy. *J Cataract Refract Surg*. 2013;39(7):1107–9. doi: 10.1016/j.jcrs.2013.05.002.
18. Folden DV. Neodymium:YAG laser anterior capsulectomy: surgical option in the management of negative dysphotopsia. *J Cataract Refract Surg*. 2013;39(7):1110–5. doi: 10.1016/j.jcrs.2013.04.015.
19. Makhotkina NY, Dugrain V, Purchase D, Berendschot T, Nuijts R. Effect of supplementary implantation of a sulcus-fixated intraocular lens in patients with negative dysphotopsia. *J Cataract Refract Surg*. 2018;44(2):209–218. doi: 10.1016/j.jcrs.2017.11.013.
20. Weinstein A. Surgical experience with pseudophakic negative dysphotopsia. *J Cataract Refract Surg*. 2012;38(3):561, author reply 561. doi: 10.1016/j.jcrs.2011.12.021.
21. Burke TR, Benjamin L. Sulcus-fixated intraocular lens implantation for the management of negative dysphotopsia. *J Cataract Refract Surg*. 2014;40(9):1469–72. doi: 10.1016/j.jcrs.2013.11.037.
22. Vamosi P, Csakany B, Nemeth J. Intraocular lens exchange in patients with negative dysphotopsia symptoms. *J Cataract Refract Surg*. 2010;36(3):418–24. doi: 10.1016/j.jcrs.2009.10.035.
23. American National Standards Institute. *ANSI Z80.28-2010: Methods for Reporting Optical Aberrations of Eyes*. Standard. 2010.

24. Savini G, Olsen T, Carbonara C, Pazzaglia S, Barboni P, Carbonelli M, Hoffer KJ. Anterior chamber depth measurement in pseudophakic eyes: a comparison of Pentacam and ultrasound. *J Refract Surg*. 2010;26(5):341–7. doi: 10.3928/1081597x-20090617-02.
25. Jaeken B, Lundström L, Artal P. Fast scanning peripheral wave-front sensor for the human eye. *Optics Express*. 2011;19(8):7903–7913. doi: 10.1364/oe.19.007903.
26. Jaeken B, Artal P. Optical quality of emmetropic and myopic eyes in the periphery measured with high-angular resolution. *Invest Ophthalmol Vis Sci*. 2012;53(7):3405–13. doi: 10.1167/iops.11-8993.
27. Jaeken B, Mirabet S, Marin JM, Artal P. Comparison of the optical image quality in the periphery of phakic and pseudophakic eyes. *Invest Ophthalmol Vis Sci*. 2013;54(5):3594–9. doi: 10.1167/iops.13-11956.
28. Thibos LN, Wheeler W, Horner D. Power vectors: an application of Fourier analysis to the description and statistical analysis of refractive error. *Optom Vis Sci*. 1997;74(6):367–75.
29. Iskander DR, Davis BA, Collins MJ, Franklin R. Objective refraction from monochromatic wavefront aberrations via Zernike power polynomials. *Ophthalmic Physiol Opt*. 2007;27(3):245–55. doi: 10.1111/j.1475-1313.2007.00473.x.
30. Sinharoy I, xy124, Holloway C, Nummela V, ng110, Stuermer, magro11. *indranilsinharoy/PyZDDE: Release version v2.0.3*. Software. 2016.
31. Escudero-Sanz I, Navarro R. Off-axis aberrations of a wide-angle schematic eye model. *J Opt Soc Am A Opt Image Sci Vis*. 1999;16(8):1881–91.
32. Jones E, Oliphant T, Peterson P. *SciPy: Open source scientific tools for Python*. Software. 2001. doi: citeulike-article-id:13344001.
33. Jongenelen S, Rozema JJ, Tassignon MJ, Evicr.net, Project Gullstrand Study G. Distribution of the Crystalline Lens Power In Vivo as a Function of Age. *Invest Ophthalmol Vis Sci*. 2015;56(12):7029–35. doi: 10.1167/iops.15-18047.
34. Atchison DA. Chapter 3: The Pupil. In: G Smith, ed. *Optics of the human eye*. Butterworth-Heinemann; 2000:35–36.
35. Arba Mosquera S, Verma S, McAlinden C. Centration axis in refractive surgery. *Eye Vis (Lond)*. 2015;2:4. doi: 10.1186/s40662-015-0014-6.
36. Choi SR, Kim US. The correlation between angle kappa and ocular biometry in Koreans. *Korean journal of ophthalmology : KJO*. 2013;27(6):421–424. doi: 10.3341/kjo.2013.27.6.421.
37. Masket S, Rupnik Z, Fram NR. Neuroadaptive changes in negative dysphotopsia during contralateral eye occlusion. *J Cataract Refract Surg*. 2019;45(2):242–243. doi: 10.1016/j.jcrs.2018.12.010.
38. Wenzel M, Langenbucher A, Eppig T. [Causes, Diagnosis and Therapy of Negative Dysphotopsia]. *Klin Monbl Augenheilkd*. 2019;236(6):767–776. doi: 10.1055/s-0043-112855.

2.6 Supplementary material



Supplementary Figure 2.1: Ray tracing results for the analysis shown in Figure 2.6 but with eye-models as defined by Holladay and Simpson.⁹ A) Eye-model with an acrylic IOL. B) Eye-model with a silicone IOL. The results show similar asymmetries as the results shown in Figure 2.6, however with a different magnitude of asymmetry due to the difference in eye-model and IOL design. These results indicate that the observed changes in peripheral refraction are not dependent on IOL design.



3

Evaluation of intraocular lens position and retinal shape in negative dysphotopsia using high-resolution magnetic resonance imaging

This chapter is published as:

L. van Vught, C.E. Dekker, B.C. Stoel, G.P.M. Luyten, J.W.M. Beenakker
**Evaluation of intraocular lens position and retinal shape in negative
dysphotopsia using high-resolution magnetic resonance imaging**
Journal of Cataract & Refractive Surgery, 2021
DOI: 10.1097/j.jcrs.0000000000000576

Abstract

Purpose: Assessment of potential relationships of intraocular lens (IOL) position and retinal shape in negative dysphotopsia.

Setting: Department of Ophthalmology, Leiden University Medical Center, Leiden, the Netherlands.

Design: Case-control study.

Methods: High-resolution ocular MRI scans were performed in thirty-seven patients with negative dysphotopsia (ND) and twenty-six pseudophakic controls and used to determine the displacement and tilt of the in-the-bag IOL with respect to the pupil and iris. Additionally, anterior segment tomography was used to assess the iris-IOL distance. Furthermore, the retinal shape was quantified from the MRI-scans by fitting an ellipse to the segmented inner boundary of the retina. Both the IOL position and retinal shape were compared between groups to assess their potential role in the etiology of ND.

Results: The average displacement and tilt of the IOL were below 0.1 mm and 0.5 degrees, respectively, in both groups and all directions. The corresponding average iris-IOL distance was 1.1 mm in both groups. Neither of these values differed significantly between groups (all p-values > 0.6). The retinal shape showed large variations but was not significantly different between the groups in both the left-right (p=0.10) and the anterior-posterior (p=0.56) direction.

Conclusions: In this study, we showed that the in-the-bag IOL position and retinal shape are not significantly different between patients with ND and the general pseudophakic population. Given the large variation in retinal shape between subjects, however, it could still be an important factor in a multifactorial origin of ND.

3.1 Introduction

Negative dysphotopsia (ND) is a visual complaint that can occur after an otherwise uneventful cataract surgery and is generally described as a shadow or dark region in the far peripheral visual field that is mainly experienced under photopic conditions.^{1,2} The incidence of ND is reported to be up to 19% directly after cataract surgery when actively asked.^{3,4} Although it generally improves or fully disappears over time,⁴ 3.2% of patients are still experiencing complaints one year after surgery,⁴ making additional treatment often necessary. The treatments proposed for ND are mostly surgical, and are generally aimed at affecting the path of light within the eye.^{1,2,5-13} None of the proposed treatments have shown to fully resolve ND in all cases and additional understanding of the exact origin of ND is required to fully resolve this condition. Many potential factors of influence have been proposed, including pupil size, angle kappa, size of the capsular overlap, diffusiveness of the capsular bag, position of the IOL with respect to the iris, design of the IOL and extent of the functional nasal retina.^{2,5,9,10,14-17}

For most of these factors, clinical validation based on evaluations of larger patient groups has not yet been reported. Recently, we combined multiple optical evaluations to establish clinical support for a smaller pupil size, a more temporally displaced pupil center, a stronger temporally tilted iris, and a difference in peripheral refraction in patients with ND compared to pseudophakic patients without complaints.¹⁸ These optical measurements can, however, not assess all the factors that are potentially involved in ND, as visual inspection of part of the eye is prevented by the iris. For example, the IOL position cannot be accurately determined behind the natural, non-widened, pupil. Furthermore, optical techniques are not able to evaluate the peripheral retinal shape, which could be a contributing factor to ND, since it is experienced in the far peripheral field.

Magnetic Resonance Imaging (MRI) is, unlike conventional ophthalmic imaging modalities, in principle able to provide insight in a number of these factors, as it is able to image the complete eye. MRI can therefore visualize the location of the IOL and the shape of the retina. Unfortunately, as high-resolution ocular MR-images are generally affected by eye motion, the resolution of ocular MRI was too limited for detailed anatomical mapping of the retina and IOL.^{19,20} Recent advances in MRI, such as ultra-high field MRI, have however enabled the acquisition of high resolution ocular MR-images without increasing the acquisition time.^{21,22} Furthermore, dedicated eye-protocols have made the MR acquisition less prone to eye-motion related artefacts that would otherwise prevent clinical interpretation.^{22,23} As a result of these advances, the complete eye can now be imaged with MRI with high accuracy.²⁴⁻²⁶ In this study we used these high resolution MRI-techniques to quantify both the in-the-bag position of the IOL and the retinal shape in the pseudophakic population in order to assess their potential relation with ND.

3.2 Methods

Thirty-seven patients with ND and twenty-six pseudophakic controls with in-the-bag implanted IOLs were prospectively studied at the Leiden University Medical Center as part of the ESCRS vRESPOND study (CCMO-registry number: NL58358.058.16). The study was performed in conformance with the tenets of the Declaration of Helsinki and approved by the local Medical Ethics Committee. The criteria for the diagnosis of ND consisted of a patient-reported shadow or dark region in the temporal peripheral visual field that occurred after an otherwise uncomplicated cataract surgery and the absence of any other evident cause of this visual complaint. Thirty-three of the thirty-seven patients with ND (89%) actively reported ND-like complaints to their ophthalmologist after cataract surgery, while four patients with ND (11%) reported a temporal shadow upon active screening in the context of a scientific study. In total twenty-eight of the thirty-seven patients with ND (76%) were referred from other hospitals or clinics. Twenty-six pseudophakic controls were included from three different sites after reporting no temporal shadow upon active screening at inclusion. One control was excluded during the study as the MR-images revealed staphyloma. As a result, the final analyses were performed on thirty-seven patients with ND and twenty-five pseudophakic controls.

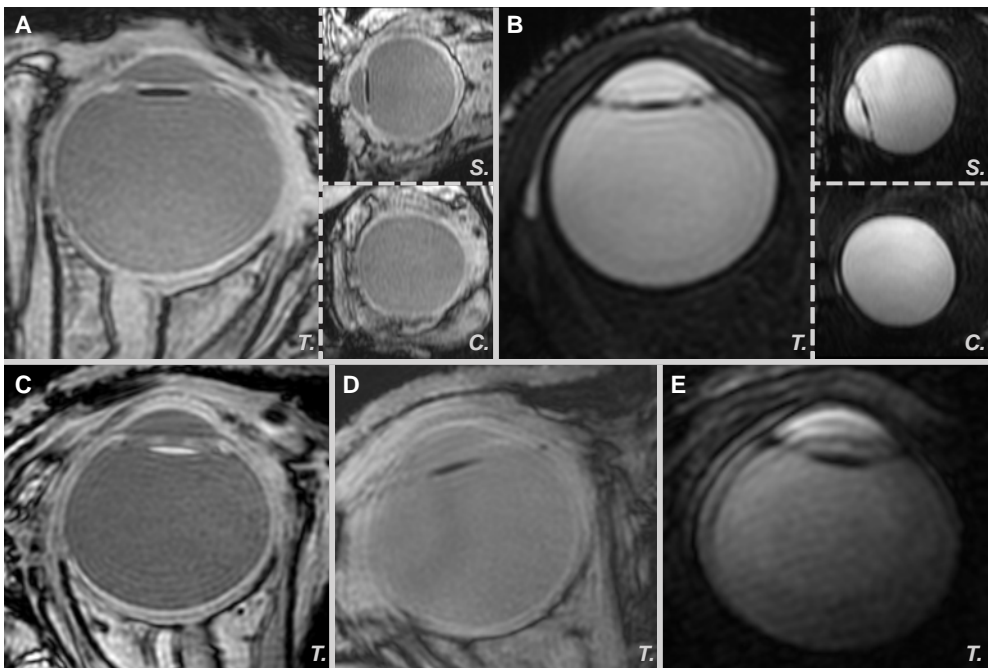


Figure 3.1: Examples of high-resolution 3D MRI scans. A) A 3DT1 scan with normal quality in transversal (T.) view, showing a hypointense IOL. The sagittal (S.) and coronal (C.) reconstructions are also shown B) A 3DT2 scan with normal quality. C) 3DT1 scan with normal quality and a hyperintense, hydrophilic, IOL. D) A 3DT1 scan with mild motion artefacts that required manual correction of the segmentation. E) A 3DT2 scan with movement artefacts that required the use of a scan with a slightly lower resolution that did not have cued-blinking motion control.

For each subject, one eye was imaged on a 7 Tesla Philips Achieva MRI (Phillips, Best, the Netherlands) using a dedicated eye coil.²⁷ Two types of three-dimensional MR-images were acquired, a T1 weighted scan (3DT1) with a resolution of $0.45 \times 0.45 \times 0.90 \text{ mm}^3$ (Figure 3.1A) and a T2 weighted scan (3DT2) with a resolution of $0.6 \times 0.6 \times 0.6 \text{ mm}^3$ (Figure 3.1B). A cued-blinking protocol was used to minimize ocular motion in both scans.^{22,23} For subjects who had difficulty to adhere to the cued blinking instructions, a faster scan with a slightly lower resolution of $0.75 \times 0.75 \times 0.75 \text{ mm}^3$ that required no blinking was added. Additionally, the eye was evaluated with the Lenstar LS900 biometer (Haag-Streit AG, Köniz, Switzerland) and the Pentacam anterior segment tomographer (Oculus Optikgeräte GmbH, Wetzlar, Germany).

The 3DT1 MRI-scan was acquired with a gradient echo readout with an echo time of 2.5 ms, a repetition time of 4.9 ms and a flip angle of 10 degrees. For the 3DT2-scan, the acquisition was performed using a turbo spin echo readout with an echo time of 254 ms, a repetition time of 2500 ms and a refocusing angle of 35 degrees. The geometrical relationship between the iris and the IOL was assessed on the T1-weighted images, as they had the highest resolution, while the retinal shape was evaluated on the T2-weighted images due to their increased contrast to noise ratio between the vitreous and retina.

To assess the alignment and tilt of the IOL with respect to the pupil and iris on the MR-images, dedicated software was in-house developed in MeVisLab (version 3.0.2, MeVis Medical Solutions AG, Bremen, Germany). Within this software, two 3D multiplanar reconstructions (MPRs) were created from the 3DT1-scans to accurately define the IOL and iris plane for each subject (Figure 3.2A). On these MPRs, the pupil and IOL were annotated manually by a best-fit circle (Figure 3.2B, C), after which their relative alignment and tilt in 3D were assessed in the horizontal and vertical direction. This procedure was fully repeated for the horizontal alignment in 15 randomly selected healthy controls to assess the reproducibility of the analysis. Additionally, to assess the distance between the anterior surface of the iris and the IOL, a 2D plane was automatically fitted to the iris on the topography measurement as described previously,¹⁸ and the difference between the axial location of this plane and the anterior chamber depth (ACD) was calculated. As the Pentacam's ACD measurements are reported to be incorrect in some pseudophakic patients,²⁸ the ACDs were measured manually on three different Scheimpflug images and subsequently averaged.

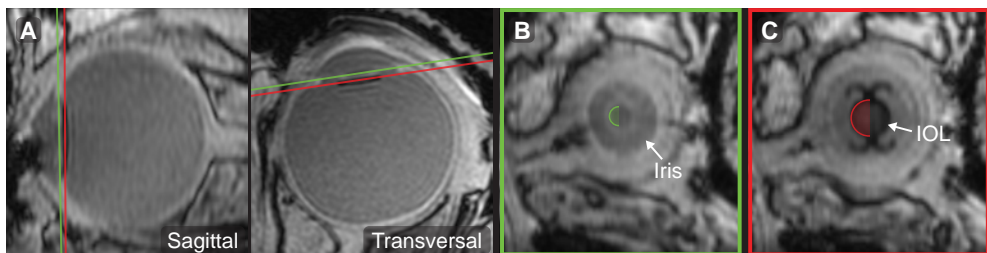


Figure 3.2: Example of the determination of the geometrical relation between the iris and the IOL using the 3DT1 MR-images. A) The multiplanar reconstruction planes defined through the iris (green line) and through the IOL (red line) on a sagittal and transversal view. B) The reconstructed image of the iris with a manual annotation of the pupil by a best-fit circle (green semi-circle). C) The reconstructed view of the IOL with a manual annotation of the IOL optic by a best-fit circle (red semi-circle).

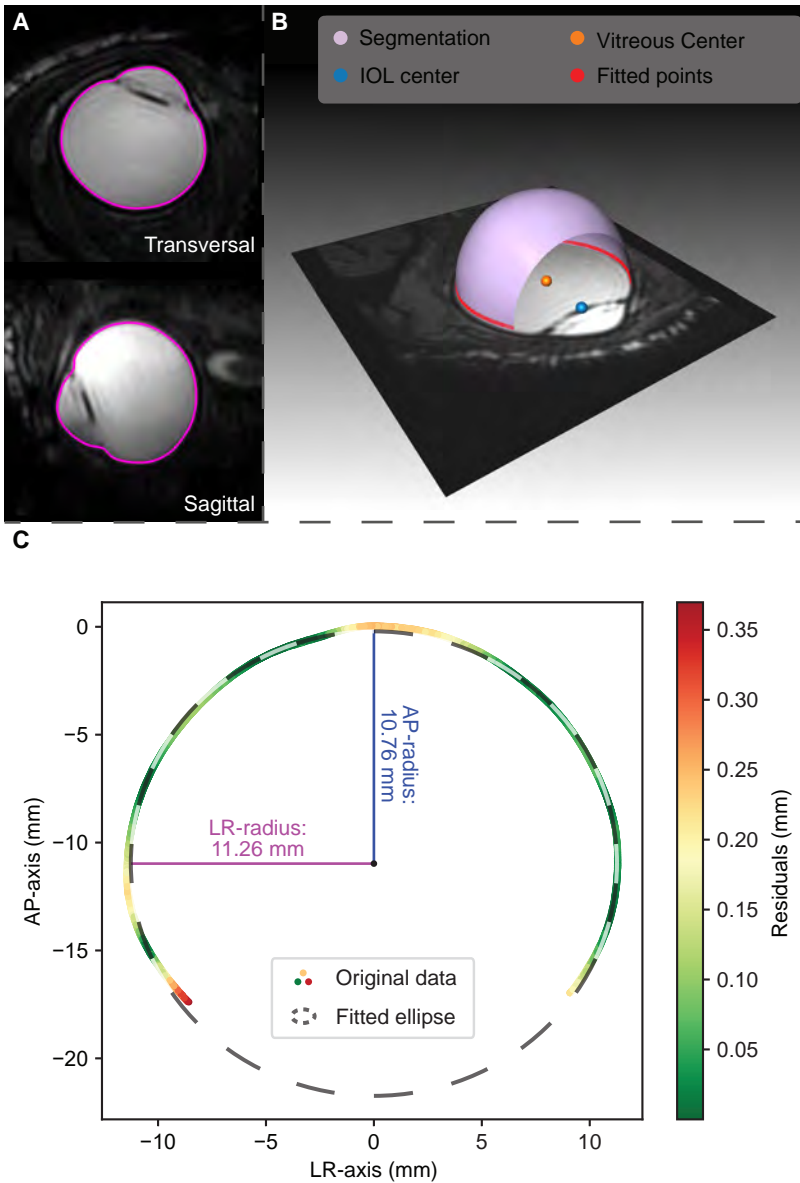


Figure 3.3: Example of the determination of the retinal shape using the 3DT2 scan. A) The segmented boundary of the vitreous body (purple). B) The segmented vitreous body (light purple), the IOL center (blue), the vitreous center (orange) and the horizontal slice selected for ellipse fitting (red). C) The ellipse fitted to the retinal surface for one subject (dashed black line), as well as the original data that was fitted. The color of the data depicts the fitting residuals at each data point.

The retinal shape was evaluated by automatically segmenting the inner boundary of the retina-sclera complex on the 3DT2-scan using 3D subdivision fitting in MevisLab,²⁴ providing a 3D shape of the vitreous body that includes posterior vitreous detachments if present (Figure 3.3A). The central axis of the eye was then defined as the line through the center of the vitreous body and the center of the manually annotated IOL (Figure 3.3B). An ellipse was subsequently fitted through a horizontal cross-section of the retina (Figure 3.3B, C) by minimizing the orthogonal distance between the segmented retina and the ellipse, using the SciPy library in Python (version 3.6, Python Software Foundation, Beaverton, Oregon, USA).²⁹ The degrees of freedom of the ellipse in the fitting process were limited to its left-right (LR) radius, its anterior-posterior (AP) radius and the AP position of its center (Figure 3.3C).

In the statistical analysis, the axial length, the geometrical relationship between the iris and IOL were compared between groups using Levene's tests for the variation and unpaired t-tests for the averages. Furthermore, the relation between axial length and retinal shape was assessed by calculating the Pearson correlation coefficient between the axial length and the radii of the fitted ellipse. Finally, the retinal shape, represented by the width and height of the fitted ellipse, was compared using an ANCOVA test with the axial length as covariant. All statistics were performed in SPSS 25 (IBM Corp., Armonk, New York, USA) with an alpha below 0.05 as threshold for statistical significance.

3.3 Results

The demographic characteristics showed similar lateralities of the measured eyes ($p=1.00$) and keratometry values ($p=0.67$) for both groups. The group of patients with ND however contained a significantly higher percentage of females ($p<0.01$) as well as younger subjects ($p=0.04$) than the group of pseudophakic controls (Table 3.1). The average internal ACD was 4.2 ± 0.4 mm [mean \pm standard deviation (SD)] for the patients with ND and 4.3 ± 0.2 mm for the pseudophakic controls. These ACDs showed no significant difference in variation (Levene's $p=0.14$) or in mean value between both groups ($p=0.32$). The corresponding axial lengths were on average 23.3 ± 1.0 mm for the patients with ND and 24.0 ± 1.5 mm for the pseudophakic controls, with an unequal variation (Levene's $p=0.04$) and significant difference ($p=0.04$) between both groups (Table 3.1).

All patients completed the full MRI-protocol (Figure 3.1A, B), however, the faster scan with a slightly lower resolution that required no blinking was added for two subjects as they had difficulty to adhere to the cued blinking instructions. The IOL could be clearly discriminated from the surrounding structures on both T1- and T2-weighted images. On T1, the hydrophobic IOLs appeared hypointense (Figure 3.1A) whereas the hydrophilic IOL types were hyperintense (Figure 3.1C). On T2-weighted images, all IOLs appeared hypointense compared to the vitreous (Figure 3.1B). The 3DT1 was of insufficient quality to determine the iris and/or IOL location in 3 pseudophakic controls (Figure 3.1D), and the automated quantification of the retinal shape based on the 3DT2 required manual correction in 4 patients with ND and 2 pseudophakic controls due to movement artefacts (Figure 3.1E). All other ocular measurements were completed successfully. On the tomography images of two patients with ND and one control, however, the IOL could not be visualized, preventing the determination of the iris-IOL distance.

Table 3.1: Demographic characteristics of patients with ND and pseudophakic controls. The groups were similar in all parameters except for a higher percentage of female subjects in the group of patients with ND and slightly longer eyes in the group of pseudophakic controls.

	Patients with ND	Pseudophakic controls	p-value
N Subjects	37	25	
Sex (%Female)	86.5	48.0	<0.01
Laterality (%Right)	43.2	44.0	1.00
Age (Years)			
Mean \pm SD	66.1 \pm 8.1	70.4 \pm 8.1	0.04
Km, corneal (D)			
Mean \pm SD	44.0 \pm 1.5	44.1 \pm 1.3	0.67
Anterior Chamber Depth (internal)[†] (mm)			
Mean \pm SD	4.2 \pm 0.4	4.3 \pm 0.2	0.32
Axial length (mm)			
Mean \pm SD	23.3 \pm 1.0	24.0 \pm 1.5	0.04

[†] The anterior chamber depth was measured manually on three different Scheimpflug images and averaged. This measurement was not possible for 2 patients with ND and 1 pseudophakic control.

The average distance between the iris and the IOL, as determined with anterior chamber tomography, was 1.1 ± 0.2 mm in both patients with ND and pseudophakic controls and did not differ significantly between both groups ($p=0.75$; Figure 3.4A). The displacement of the IOL center with respect to the pupil center, as determined on the 3DT1 MRI scan, was on average 0.0 ± 0.2 mm in the horizontal plane and 0.0 ± 0.3 mm in the vertical plane for the patients with ND. For the pseudophakic controls, this displacement was 0.1 ± 0.3 mm horizontally and 0.0 ± 0.3 mm vertically. No significant differences in IOL alignment were apparent in either horizontal ($p = 0.36$) or vertical ($p=0.71$) direction (Figure 3.4B, Table 3.2). The reproducibility analysis of the horizontal IOL alignment showed a small non-significant bias of 0.01 mm with a standard deviation of 0.23 mm between both analyses.

The average tilt of the IOL with respect to the iris, as obtained from the T1 weighted images, was 0.0 ± 0.5 degrees horizontally and 0.3 ± 1.3 degrees vertically for the patients with ND. For the pseudophakic controls, this tilt was 0.0 ± 0.3 degrees horizontally and 0.5 ± 0.9 degrees vertically. Neither in the horizontal ($p=0.70$) nor vertical ($p=0.54$) direction, did these findings differ significantly between both groups.

The determined retinal shapes, quantified by the radii of the fitted ellipses, showed significant correlation with the axial length, with all p -values being <0.01 (Figure 3.5). For the patients with ND, the average radius was 10.4 ± 0.6 mm in the AP direction and 11.7 ± 0.5 mm in the LR direction. For the controls, these average radii were 10.7 ± 0.8 mm and 11.8 ± 0.6 mm, respectively (Figure 3.5, Table 3.3). When the axial length was taken as a covariate, no significant differences were found between the LR-radii ($p=0.10$) or the AP-radii ($p=0.56$) of both groups.

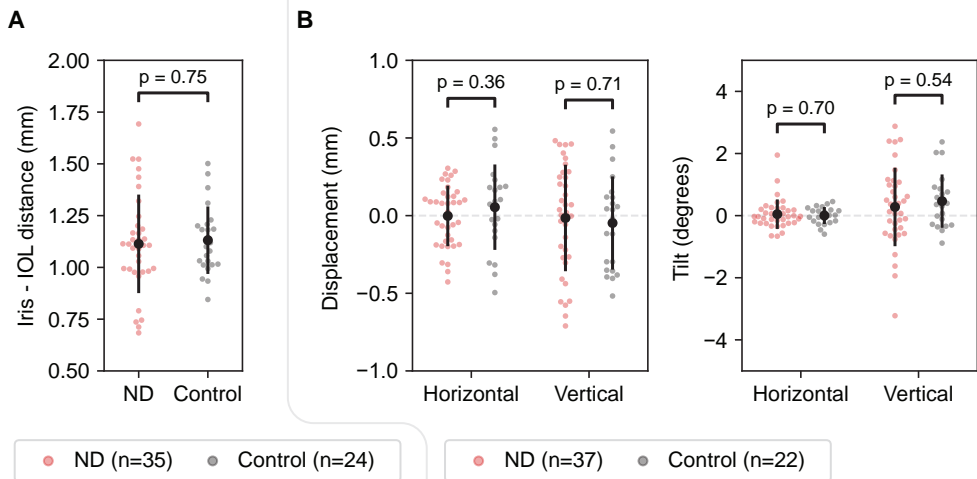


Figure 3.4: Evaluation of the geometric relation between the iris and IOL. A) Distance between the iris and the IOL as measured with anterior segment tomography for patients with ND (red) and pseudophakic controls (gray) together with the groupwise means (black dots) and standard deviations (vertical black lines). B) Displacement of the IOL center with respect to the pupil center and tilt of the IOL with respect to the iris as measured with ocular MRI. Positive values indicate a displacement or tilt towards the temporal or superior side.

Table 3.2: Evaluation of the geometric relation between the iris and IOL using the 3DT1 MR-images. Displacement of the IOL is reported with respect to the pupil center and the IOL tilt relative to the iris plane. Positive values indicate a displacement or tilt towards the temporal or superior side. No significant differences were found between the groups.

	Patients with ND	Pseudophakic controls	p-value
Included subjects (<i>n</i>)	37	22	
IOL displacement, horizontal (<i>mm</i>)			
Mean ± SD	0.0 ± 0.2	0.1 ± 0.3	0.36
IOL displacement, vertical (<i>mm</i>)			
Mean ± SD	0.0 ± 0.3	0.0 ± 0.3	0.71
IOL tilt, horizontal (<i>degrees</i>)			
Mean ± SD	0.0 ± 0.5	0.0 ± 0.3	0.70
IOL tilt, vertical (<i>degrees</i>)			
Mean ± SD	0.3 ± 1.3	0.5 ± 0.9	0.54

Table 3.3: Evaluation of the retinal shape. The radii of the ellipse fitted to the retinal surface. AP = Anterior-posterior; LR = left-right. No significant differences were found between both groups.

	Patients with ND	Pseudophakic controls	p-value
Included subjects (<i>n</i>)	37	25	
Fitted ellipse, AP Radius (<i>mm</i>)			
Mean ± SD	10.4 ± 0.6	10.7 ± 0.8	0.10
Fitted ellipse, LR Radius (<i>mm</i>)			
Mean ± SD	11.7 ± 0.5	11.8 ± 0.6	0.56

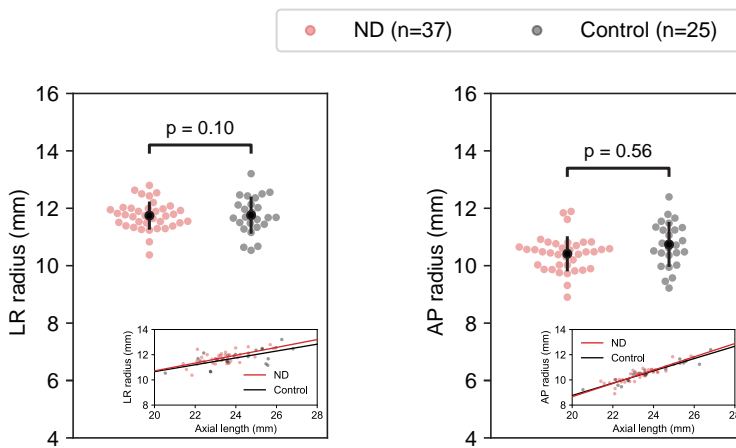


Figure 3.5: Evaluation of the retinal shape. The shape is quantified by radii in the left-right (LR) and anterior-posterior (AP) direction for patients with ND (red) and pseudophakic controls (gray) together with the groupwise means (black dots) and standard deviations (vertical black lines). Additionally, the insets show the correlations between these radii and the axial length. All correlations are significant ($p < 0.01$), with Pearson r values of ≥ 0.65 for the LR-radius and of ≥ 0.88 for the AP-radius. When the axial length was taken as a covariate, no significant differences were found between the LR-radii ($p = 0.10$) or the AP-radii ($p = 0.56$) of both groups.

3.4 Discussion

The exact mechanism behind ND has been unknown since its original description in 2000,¹ and even though various studies on the origin of this complaint have been performed, many potential factors of influence are still to be evaluated in clinical studies. In this study, we compared the in-the-bag position of the IOL as well as the retinal shape between a group of patients with ND and a group of pseudophakic controls. Using these groups, we were not able to identify significant differences between patients with and without ND in either the in-the-bag position of the IOL or in the retinal shape.

Both groups showed similar demographic characteristics, except for a significantly higher percentage of females ($p < 0.01$), a significantly younger age ($p = 0.04$) and a small, but significantly shorter axial length ($p = 0.04$) in the patients with ND. Both the younger age and shorter axial lengths of patients with ND were also reported in the study of Makhotkina et al.³ In a different study, they also reported a higher percentage of females than males within their evaluated treatment group.⁸ Furthermore, a relation might exist between the percentage of females and the shorter axial length, but the nature of such a relation cannot be inferred from the current data.³⁰

The axial position of the IOL was similar in both groups, with an approximately equal distance between the iris and the IOL (Figure 3.4A). Additionally, only small variations were seen in both the horizontal and vertical displacement of the IOL with respect to the pupil center in both groups, with all displacements being below 0.8 mm (Figure 3.4B, Table 3.2). Furthermore, the tilt of the IOL with respect to the iris showed minor within-groups variations for horizontal tilts, with all tilts below 2.0 degrees, and a slightly larger variation in the vertical direction, with all tilts below 4.0 degrees (Figure 3.4B, Table 3.2). Overall, the variation of these measurements was also comparable between both groups (Figure 3.4A, B, Table 3.2), not resulting in significant differences with p -values of 0.6 and higher. The larger variation in vertical direction might be the result of haptic design and haptic orientation, but more knowledge on the exact IOL design is required for a more in-depth analysis of this difference. In an earlier study, largely based on the same group of subjects, it was found that the iris of patients with ND showed a significantly larger tilt towards the temporal side of the head compared to the iris of pseudophakic controls.¹⁸ As the current result showed that the IOL is aligned with the iris, it strengthens the idea that the complete eye of patients with ND is rotated more towards the temporal side of the head instead of solely the iris, which is in line with the thought that patients with ND might have a larger angle between the optical and visual axis.^{14,18}

The retinal shape, quantified by the radii of a fitted ellipse in AP and LR direction, showed comparable radii in both patients with ND and pseudophakic controls that were on average larger in the LR-direction in both groups (Figure 3.5, Table 3.3). These radii correlated significantly with the axial length, which correspond to the earlier described correlations of similar measurements with refraction and of axial length with refraction.^{30,31} Additionally, the difference between the AP and LR-radii correspond to a positive asphericity of the retinal surface,³² which is in agreement with the study of Atchison et al.²⁶ The lack of difference between both groups indicates that it is unlikely that ND is primarily caused by a difference in retinal shape. It is furthermore noteworthy that the width of the eye was similar in both groups, as this width, together with the location of the ora serrata, will affect the peripheral visual field eccentricities from which light is perceived on the functional retina, as well as

how it is perceived. However, the location of the ora serrata cannot be obtained from the MR-images, so this cannot yet be fully assessed.

Although this study did not reveal differences in IOL position or retinal shape between patients with and without ND, this absence of differences could potentially be the result of study limitations such as the limited resolution of the MRI or the number of evaluated subjects. However, the reproducibility of the MRI measurement shows that given the size of our cohort, the mean horizontal IOL displacement of patients with ND was less than 0.1 mm ($p=0.05$), making it unlikely to be the primary cause of ND. Additionally, an earlier study showed a high, subpixel, reproducibility of 0.1 mm in the retinal shape description using a similar high-resolution MRI protocol.²⁴ The observed high, >2 mm, inter-subject variation in radii of the eye in both groups are therefore not the result of a measurement uncertainty, but caused by the natural variation in eye shape. Given the similar variation in retinal shape within both groups, this shape is therefore unlikely to be directly linked to ND. The inter-subject variation of the retinal shape will however be of interest for future studies using ray-tracing simulations to assess peripheral vision and related complaints such as ND. For these assessments, a more accurate retinal description will allow for a more accurate determination of whether a peripheral shadow would be sufficiently in focus to be perceived by the subject or not. However, future studies should fully personalize eye-models to enable patient-specific ray tracing analyses for these assessments.

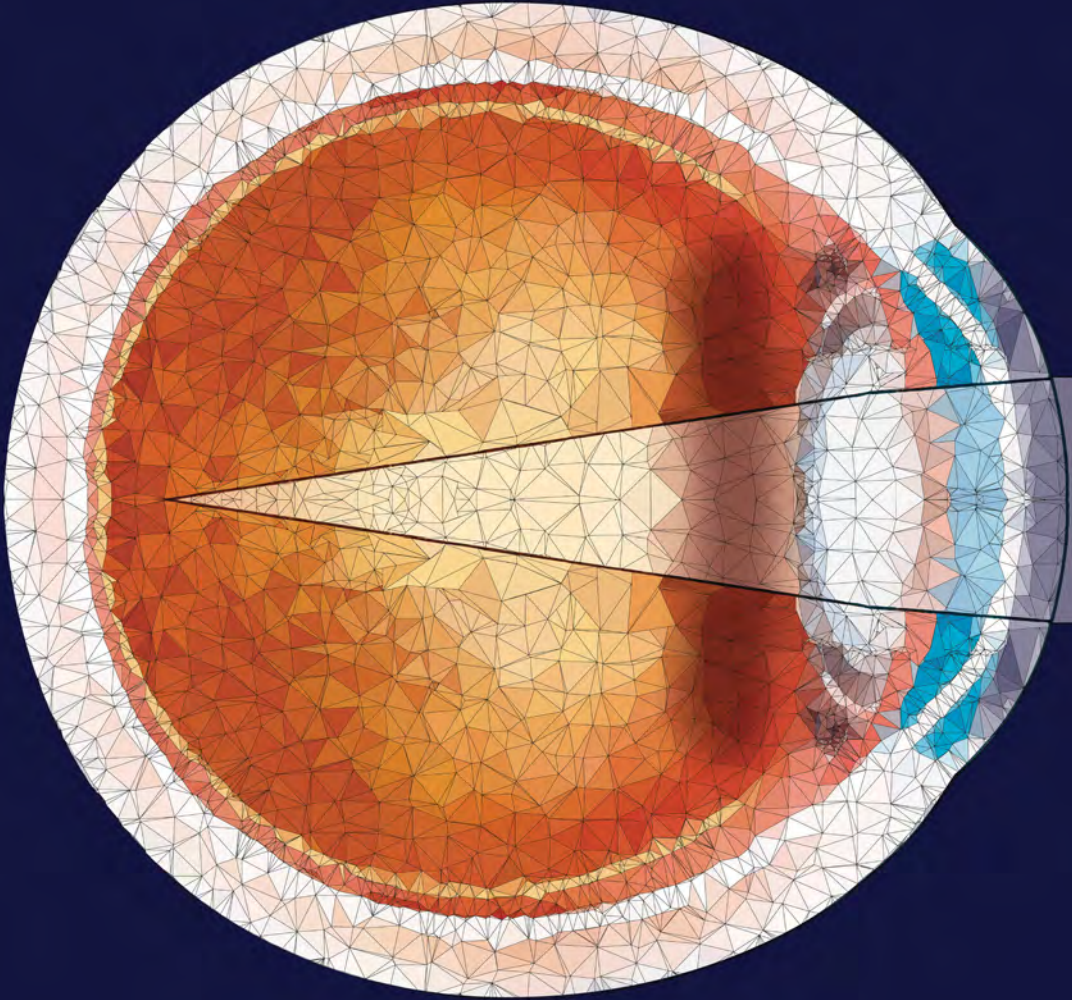
These patient-specific ray tracing analyses could furthermore aid in linking these factors with the earlier described differences in the anterior chamber configuration of patients with ND, such as an increased angle kappa.¹⁸ Additionally, these analyses can potentially provide insight in the exact mechanism of certain reported treatments, including for example placement of a secondary sulcus IOL,⁸⁻¹⁰ reverse optic capture,^{9,10} and various types of IOL-exchange,⁹⁻¹³ and link them to the ocular anatomy. Furthermore, they could include the proposed optical effects caused by the lens capsule,^{14,16} although this should not exclude clinical measurements confirming their presence in the ND population. As MRI, CT and ultrasound are generally not sensitive to these optical changes of the tissue, an optical imaging modality, capable of assessing the edge of the IOL, is probably required.

In this study, we used high resolution MR-images to show that the alignment of the in-the-bag IOL and its tilt with respect to the iris, as well as the retinal shape of patients with ND is not significantly different from the general pseudophakic population. Given the wide distribution of retinal shapes, however, the retinal shape could still be an important factor in a multifactorial origin of ND and should therefore not be ignored.

3.5 References

1. Davison JA. Positive and negative dysphotopsia in patients with acrylic intraocular lenses. *J Cataract Refract Surg.* 2000;26(9):1346–55. doi: 10.1016/s0886-3350(00)00611-8.
2. Geneva I, Henderson BA. The Complexities of Negative Dysphotopsia. *Asia Pac J Ophthalmol (Phila).* 2017;6(4):364–371. doi: 10.22608/apo.20171111.
3. Makhotkina NY, Nijkamp MD, Berendschot T, Borne B van den, Nuijts R. Effect of active evaluation on the detection of negative dysphotopsia after sequential cataract surgery: discrepancy between incidences of unsolicited and solicited complaints. *Acta Ophthalmol.* 2018;96(1):81–87. doi: 10.1111/aos.13508.
4. Osher RH. Negative dysphotopsia: long-term study and possible explanation for transient symptoms. *J Cataract Refract Surg.* 2008;34(10):1699–707. doi: 10.1016/j.jcrs.2008.06.026.
5. Henderson BA, Geneva I. Negative dysphotopsia: A perfect storm. *J Cataract Refract Surg.* 2015;41(10):2291–312. doi: 10.1016/j.jcrs.2015.09.002.
6. Cooke DL, Kasko S, Platt LO. Resolution of negative dysphotopsia after laser anterior capsulotomy. *J Cataract Refract Surg.* 2013;39(7):1107–9. doi: 10.1016/j.jcrs.2013.05.002.
7. Folden DV. Neodymium:YAG laser anterior capsulectomy: surgical option in the management of negative dysphotopsia. *J Cataract Refract Surg.* 2013;39(7):1110–5. doi: 10.1016/j.jcrs.2013.04.015.
8. Makhotkina NY, Berendschot TT, Beckers HJ, Nuijts RM. Treatment of negative dysphotopsia with supplementary implantation of a sulcus-fixated intraocular lens. *Graefes Arch Clin Exp Ophthalmol.* 2015;253(6):973–7. doi: 10.1007/s00417-015-3029-8.
9. Masket S, Fram NR, Cho A, Park I, Pham D. Surgical management of negative dysphotopsia. *J Cataract Refract Surg.* 2018;44(1):6–16. doi: 10.1016/j.jcrs.2017.10.038.
10. Masket S, Fram NR. Pseudophakic negative dysphotopsia: Surgical management and new theory of etiology. *J Cataract Refract Surg.* 2011;37(7):1199–207. doi: 10.1016/j.jcrs.2011.02.022.
11. Vamosi P, Csakany B, Nemeth J. Intraocular lens exchange in patients with negative dysphotopsia symptoms. *J Cataract Refract Surg.* 2010;36(3):418–24. doi: 10.1016/j.jcrs.2009.10.035.
12. Taubenslag KJ, Groos EB, Parker MG, Ewald MD, Pilkinton RD. Successful treatment of negative dysphotopsia with in-the-bag intraocular lens exchange using a wide ovoid IOL. *J Cataract Refract Surg.* 2016;42(2):336–7. doi: 10.1016/j.jcrs.2016.01.012.
13. Burke TR, Benjamin L. Sulcus-fixated intraocular lens implantation for the management of negative dysphotopsia. *J Cataract Refract Surg.* 2014;40(9):1469–72. doi: 10.1016/j.jcrs.2013.11.037.
14. Holladay JT, Simpson MJ. Negative dysphotopsia: Causes and rationale for prevention and treatment. *J Cataract Refract Surg.* 2017;43(2):263–275. doi: 10.1016/j.jcrs.2016.11.049.
15. Holladay JT, Zhao H, Reisin CR. Negative dysphotopsia: the enigmatic penumbra. *J Cataract Refract Surg.* 2012;38(7):1251–65. doi: 10.1016/j.jcrs.2012.01.032.
16. Hong X, Liu Y, Karakelle M, Masket S, Fram NR. Ray-tracing optical modeling of negative dysphotopsia. *J Biomed Opt.* 2011;16(12):125001. doi: 10.1117/1.3656745.
17. Simpson MJ. Mini-review: Far peripheral vision. *Vision Res.* 2017;140:96–105. doi: 10.1016/j.visres.2017.08.001.
18. Vught L van, Luyten GPM, Beenakker JWM. Distinct differences in anterior chamber configuration and peripheral aberrations in negative dysphotopsia. *J Cataract Refract Surg.* 2020. doi: 10.1097/j.jcrs.000000000000206.
19. Lemke AJ, Alai-Omid M, Hengst SA, Kazi I, Felix R. Eye imaging with a 3.0-T MRI using a surface coil—a study on volunteers and initial patients with uveal melanoma. *Eur Radiol.* 2006;16(5):1084–9. doi: 10.1007/s00330-005-0087-z.
20. Graaf P de, Goricke S, Rodjan F, Galluzzi P, Maeder P, Castelijns JA, Brisse HJ, European Retinoblastoma Imaging C. Guidelines for imaging retinoblastoma: imaging principles and MRI standardization. *Pediatr Radiol.* 2012;42(1):2–14. doi: 10.1007/s00247-011-2201-5.
21. Richdale K, Wassenaar P, Teal Bluestein K, Abduljalil A, Christoforidis JA, Lanz T, Knopp MV, Schmalbrock P. 7 Tesla MR imaging of the human eye in vivo. *J Magn Reson Imaging.* 2009;30(5):924–32. doi: 10.1002/jmri.21959.

22. Beenakker JWM, Rijn GA van, Luyten GP, Webb AG. High-resolution MRI of uveal melanoma using a microcoil phased array at 7 T. *NMR Biomed.* 2013;26(12):1864–9. doi: 10.1002/nbm.3041.
23. Berkowitz BA, McDonald C, Ito Y, Tofts PS, Latif Z, Gross J. Measuring the human retinal oxygenation response to a hyperoxic challenge using MRI: eliminating blinking artifacts and demonstrating proof of concept. *Magn Reson Med.* 2001;46(2):412–6. doi: 10.1002/mrm.1206.
24. Beenakker JWM, Shamonin DP, Webb AG, Luyten GP, Stoel BC. Automated retinal topographic maps measured with magnetic resonance imaging. *Invest Ophthalmol Vis Sci.* 2015;56(2):1033–9. doi: 10.1167/iovs.14-15161.
25. Atchison DA, Jones CE, Schmid KL, Pritchard N, Pope JM, Strugnell WE, Riley RA. Eye shape in emmetropia and myopia. *Invest Ophthalmol Vis Sci.* 2004;45(10):3380–6. doi: 10.1167/iovs.04-0292.
26. Atchison DA, Pritchard N, Schmid KL, Scott DH, Jones CE, Pope JM. Shape of the retinal surface in emmetropia and myopia. *Invest Ophthalmol Vis Sci.* 2005;46(8):2698–707. doi: 10.1167/iovs.04-1506.
27. Beenakker JWM, Ferreira TA, Soemarwoto KP, Genders SW, Teeuwisse WM, Webb AG, Luyten GP. Clinical evaluation of ultra-high-field MRI for three-dimensional visualisation of tumour size in uveal melanoma patients, with direct relevance to treatment planning. *MAGMA.* 2016;29(3):571–7. doi: 10.1007/s10334-016-0529-4.
28. Savini G, Olsen T, Carbonara C, Pazzaglia S, Barboni P, Carbonelli M, Hoffer KJ. Anterior chamber depth measurement in pseudophakic eyes: a comparison of Pentacam and ultrasound. *J Refract Surg.* 2010;26(5):341–7. doi: 10.3928/1081597x-20090617-02.
29. Jones E, Oliphant T, Peterson P. SciPy: Open source scientific tools for Python 2001. doi: citeulike-article-id:13344001.
30. Zocher MT, Rozema JJ, Oertel N, Dawczynski J, Wiedemann P, Rauscher FG, Evicr.net. Biometry and visual function of a healthy cohort in Leipzig, Germany. *BMC Ophthalmol.* 2016;16:79. doi: 10.1186/s12886-016-0232-2.
31. Pope JM, Verkicharla PK, Sepehrband F, Suheimat M, Schmid KL, Atchison DA. Three-dimensional MRI study of the relationship between eye dimensions, retinal shape and myopia. *Biomed Opt Express.* 2017;8(5):2386–2395. doi: 10.1364/boe.8.002386.
32. Atchison DA, Smith G. Chapter 2 - Refracting components: cornea and lens. In: DA Atchison, G Smith, eds. *Optics of the Human Eye.* Butterworth-Heinemann; 2000:11–20. doi: <https://doi.org/10.1016/b978-0-7506-3775-6.50006-7>.



4

ZOSPy: optical ray tracing in Python through OpticStudio

This chapter is published as:

L. van Vught, C. Haasjes, J.W.M. Beenakker
ZOSPy: optical ray tracing in Python through OpticStudio
Journal of Open Source Software, 2024
DOI: 10.21105/joss.05756

Summary

Zemax OpticStudio (Ansys, Inc) is a commonly used software package for designing optical setups and performing ray tracing simulations. It offers an Application Programming Interface (API) but interacting with this API is complex. Consequently, current ray tracing simulations generally require substantial manual user interaction, which in turn hampers the sharing of methods between scientists. We have therefore developed ZOSPy, a Python package that provides an accessible interface as well as unit tests. As a result, ZOSPy enables scientists to focus more on optical modelling instead of coding and contributes to open science as optical setups and analyses can easily be shared amongst users.

4.1 Statement of need

Ray tracing simulations are widely used to design, optimize and analyze optical systems. Its applications are diverse, ranging from designing spectrometers¹ or telescopes,² to understanding the optics of the human eye.³⁻⁵ Moreover, in ophthalmology, ray tracing is used to optimize the outcomes of cataract surgery^{6,7} and evaluate the accuracy of ocular radiotherapy.⁸ These optical simulations are often performed in OpticStudio, which offers a powerful set of tools to design, optimize and evaluate optical systems.

Although OpticStudio offers an API, the ZOS-API, using this API in Python is complex and time-consuming. It involves, for example, establishing a connection with the API through the .NET framework, casting between .NET and Python datatypes, identifying which constants need to be set in specific cases, and working around non-uniform methods of parsing the output.⁹ This leads to studies which, in practice, largely rely on user interaction. Although OpticStudio can perform Monte Carlo analyses, where a large number of random perturbations of the system are generated and analysed in an automated way, this type of automation is not suitable when large sets of specific, non-random, combinations of parameters need to be analysed. In vision science, for example, ray tracing is used to design artificial lenses for the eye,^{10,11} but their evaluation in a large set of patients is hindered as the anatomical parameters of each subject's eye need to be entered manually. As a result, clinical studies typically describe vision-related complaints in cohorts of hundreds of eyes,¹² but the ray tracing studies aiming to link these outcomes to the subject's ocular optics are limited to a small number of eyes.^{3,13}

With ZOSPy, we provide an easy-to-use and accessible interface to the OpticStudio API, enabling the user to focus on optical modelling instead of complex coding. As a result, those who are not familiar with the intricacies of the ZOS-API interface will be able to read and comprehend scripts that use ZOSPy. Thereby, ZOSPy provides greater accessibility to conducting analyses in OpticStudio through Python, than directly using the ZOS-API.

4.2 Functionality

ZOSPy is, in its most basic form, a Python wrapper around the OpticStudio API. It facilitates the .NET connection required to connect to OpticStudio through its API, as well as all subsequent casting of variables between .NET and Python. Additionally, it provides object-oriented methods to define surfaces and their optical properties. Furthermore, it offers single-line, easy to understand, methods to perform analyses that return the analysis results in a uniform way. As a result, ZOSPy enables a straight-forward interaction with OpticStudio and improves code readability, which facilitates method sharing between scientists.

4 ZOSPy also offers autocompletion. Interacting with OpticStudio through its API requires the use of many constants, for example to define the shape of an optical surface or initiate an analysis. These constants do not autocomplete in IDEs such as PyCharm or VS Code as the API is built on the .NET framework. As a result, the user has to know the exact name of each constant, for example *ZOSAPI.Analysis.Settings.Mtf.MtfTypes.Modulation*. ZOSPy, however, includes stubs for all constants and functions, enabling full autocompletion.

Finally, ZOSPy offers a set of unit tests to assure that the software provides correct results. These tests provide means to compare results across ZOSPy and Python versions, as well as across versions of OpticStudio. The current version of ZOSPy provides basic tests for the most common optical surfaces and analyses.

4.3 Use cases

Multiple examples, from modelling the effect of a coated prism on the polarization of light to assessing the optical characteristics of the human eye have been contributed to ZOSPy. These examples provide new users with an easy start with ZOSPy. Part of a simple example of using ZOSPy to create and evaluate a thick lens is shown in example code 4.1, and the corresponding results are shown in Figure 4.1.

Furthermore, ZOSPy has been used in different ophthalmic studies. In one of these studies, ZOSPy was used to evaluate the relation of ocular anatomy to peripheral visual complaints.⁴ In another study, ZOSPy showed that the extent of an intra-ocular tumor can be overestimated during surgery due to its shadow (Figure 4.2).⁸

Example code 4.1: Part of a simple example of using ZOSPy to create and evaluate a thick lens

```
# ...

# Make a 10 mm thick lens with a radius of curvature of 30 mm and
# material type BK10
front_surface = oss.LDE.GetSurfaceAt(2)
front_surface.Radius = 30
front_surface.Thickness = 10
front_surface.SemiDiameter = 15
front_surface.Material = "BK10"

back_surface = oss.LDE.InsertNewSurfaceAt(3)
back_surface.Radius = -30
back_surface.Thickness = 29
back_surface.SemiDiameter = 15

# ...

# Render the model
draw3d = zp.analyses.systemviewers.viewer_3d(oss)

# Calculate the Point Spread function (PSF) of the system and
# subsequently determine the Modulation Transfer Function (MTF)
# as a function of the location of the imaging plane.
huygens_psf = zp.analyses.psf.huygens_psf(
    oss, pupil_sampling="512x512", image_sampling="512x512",
    normalize=True)

mtf = zp.analyses.mtf.fft_through_focus_mtf(
    oss, sampling="512x512", deltafocus=2.5, frequency=3,
    numberofsteps=51)

# ...
```

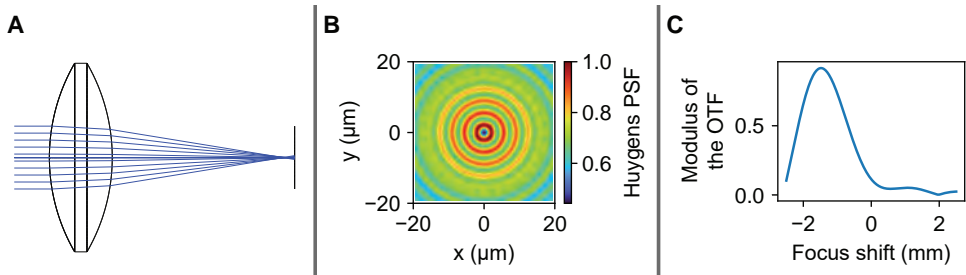


Figure 4.1: Results of the example code 4.1. A) The created optical system results in a slightly out of focus image. B) The Huygens Point Spread Function (PSF) shows the aberrations of the system. C) The Modulation Transfer Function (MTF) as a function of image plane location shows a maximum at -1.3mm, indicating that the system will be in focus when the imaging plane is shifted by 1.3mm towards the lens.

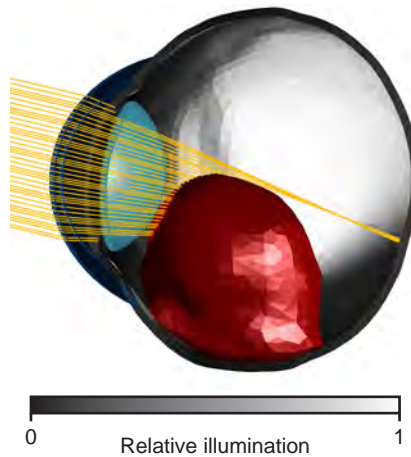
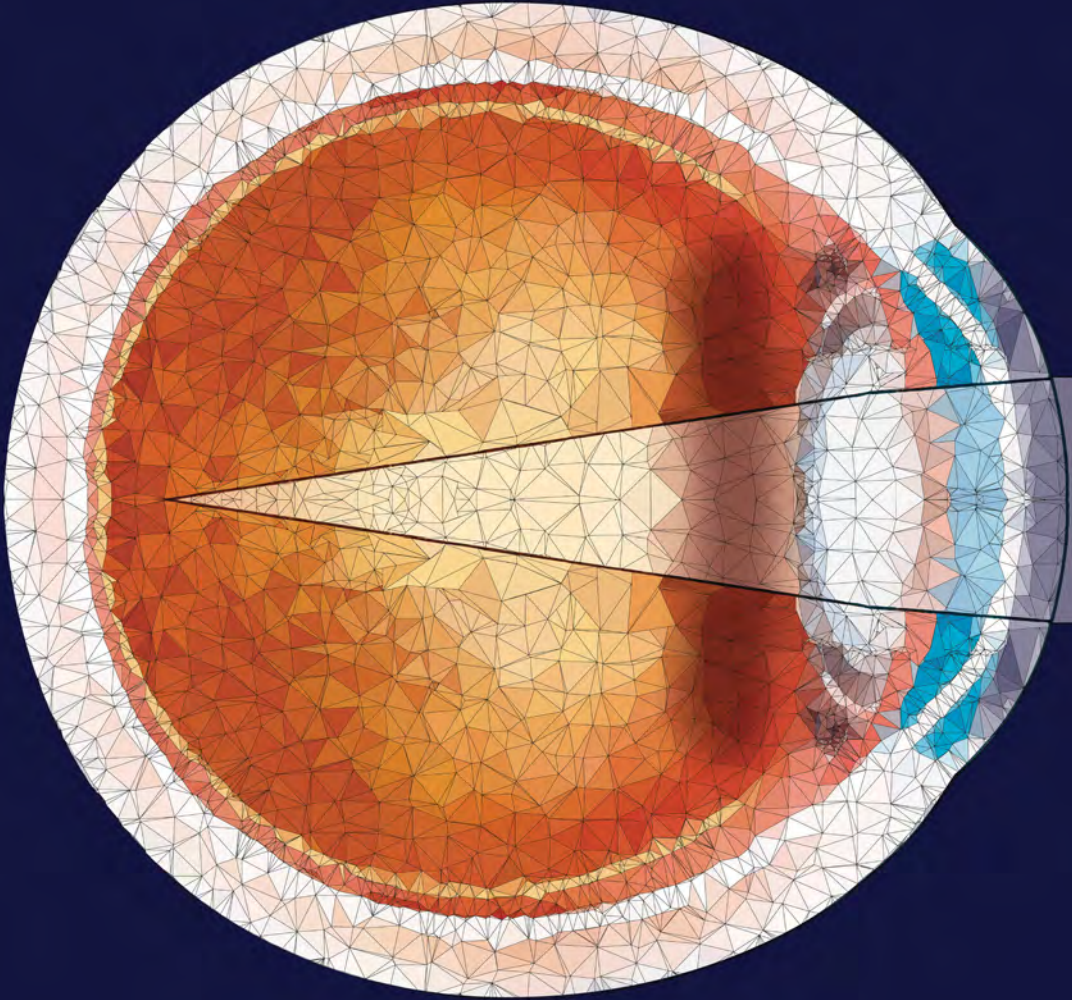


Figure 4.2: Simulation mimicking the clip surgery for radiotherapy of an intraocular tumor.⁸ The ocular geometry including the dimension of the tumor were loaded into OpticStudio using ZOSPy and the *CAD Part: STL* object type, after which the retinal illumination was simulated. The results were rendered using the non-sequential Shaded Model analysis (*zospy.analyses.systemviewers.nsc_shaded_model*).

4.4 References

1. Naeem M, Imran T, Hussain M, Bhatti AS. Design Simulation and Data Analysis of an Optical Spectrometer. *Optics*. 2022;3(3):304–312. doi: 10.3390/opt3030028.
2. Zhang Y, Jiang H, Shectman S, Yang D, Cai Z, Shi Y, Huang S, Lu L, Zheng Y, Kang S, et al. Conceptual design of the optical system of the 6.5 m wide field multiplexed survey telescope with excellent image quality. *PhotonIX*. 2023;4(1):1–25. doi: 10.1186/s43074-023-00094-4.
3. Simpson MJ. Intraocular lens far peripheral vision: image detail and negative dysphotopsia. *Journal of Cataract & Refractive Surgery*. 2020;46(3):451–458. doi: 10.1097/j.jcrs.000000000000103.
4. van Vught L, Que I, Luyten GP, Beenakker JW. Effect of anatomical differences and intraocular lens design on Negative Dysphotopsia. *Journal of Cataract & Refractive Surgery*. 2022;10–1097. doi: 10.1097/j.jcrs.0000000000001054.
5. Hong X, Liu Y, Karakelle M, Masket S, Fram NR. Ray-tracing optical modeling of negative dysphotopsia. *Journal of biomedical optics*. 2011;16(12):125001–125001. doi: 10.1117/1.3656745.
6. Canovas C, Artal P. Customized eye models for determining optimized intraocular lenses power. *Biomedical optics express*. 2011;2(6):1649–1662. doi: 10.1364/boe.2.001649.
7. Artal P, Ginis H, Charitaras D, Villegas EA, Tabernero J, Prieto PM. Inverted meniscus intraocular lens as a better optical surrogate of the crystalline lens. *Biomedical Optics Express*. 2023;14(5):2129–2137. doi: 10.1364/boe.490089.
8. Jaarsma-Coes MG, Ferreira TA, Marinkovic M, Vu TK, Vught L van, Haren GR van, Rodrigues MF, Klaver YL, Verbist BM, Luyten GP, et al. Comparison of Magnetic Resonance Imaging–Based and Conventional Measurements for Proton Beam Therapy of Uveal Melanoma. *Ophthalmology Retina*. 2023;7(2):178–188. doi: 10.1016/j.oret.2022.06.019.
9. Zemax LLC. *Getting Started with ZOS-API*. 2021. <https://www.zemax.com/blogs/free-tutorials/getting-started-with-zos-api>.
10. Ellis MF. Sharp-edged intraocular lens design as a cause of permanent glare. *Journal of Cataract & Refractive Surgery*. 2001;27(7):1061–1064. doi: 10.1016/s0886-3350(00)00856-7.
11. Holladay JT, Lang A, Portney V. Analysis of edge glare phenomena in intraocular lens edge designs. *Journal of Cataract & Refractive Surgery*. 1999;25(6):748–752. doi: 10.1016/s0886-3350(99)00038-3.
12. Alfonso JF, Fernández-Vega L, Baamonde MB, Montés-Micó R. Prospective visual evaluation of apodized diffractive intraocular lenses. *Journal of Cataract & Refractive Surgery*. 2007;33(7):1235–1243. doi: 10.1016/j.jcrs.2007.03.034.
13. van Vught L, Luyten GP, Beenakker JW. Distinct differences in anterior chamber configuration and peripheral aberrations in negative dysphotopsia. *Journal of Cataract and Refractive Surgery*. 2020;46(7):1007. doi: 10.1097/j.jcrs.0000000000000206.



5

Accurate corneal modelling for personalized peripheral ray tracing

Abstract

Under
embargo

5.1 Introduction

Under
embargo

Under
embargo

5.2 Methods

Under
embargo

Under
embargo

Under
embargo

Under
embargo

Under
embargo

5.3 Results

Under
embargo

Under
embargo

Under
embargo

Under
embargo

Under
embargo

Under
embargo

Under
embargo

5.4 Discussion

Under
embargo

Under
embargo

5.5 References

Under
embargo

Under
embargo

5.6 Supplementary data

Under
embargo

Under
embargo

Under
embargo

Under
embargo

Under
embargo

Under
embargo

Under
embargo

Under
embargo

Under
embargo

Under
embargo

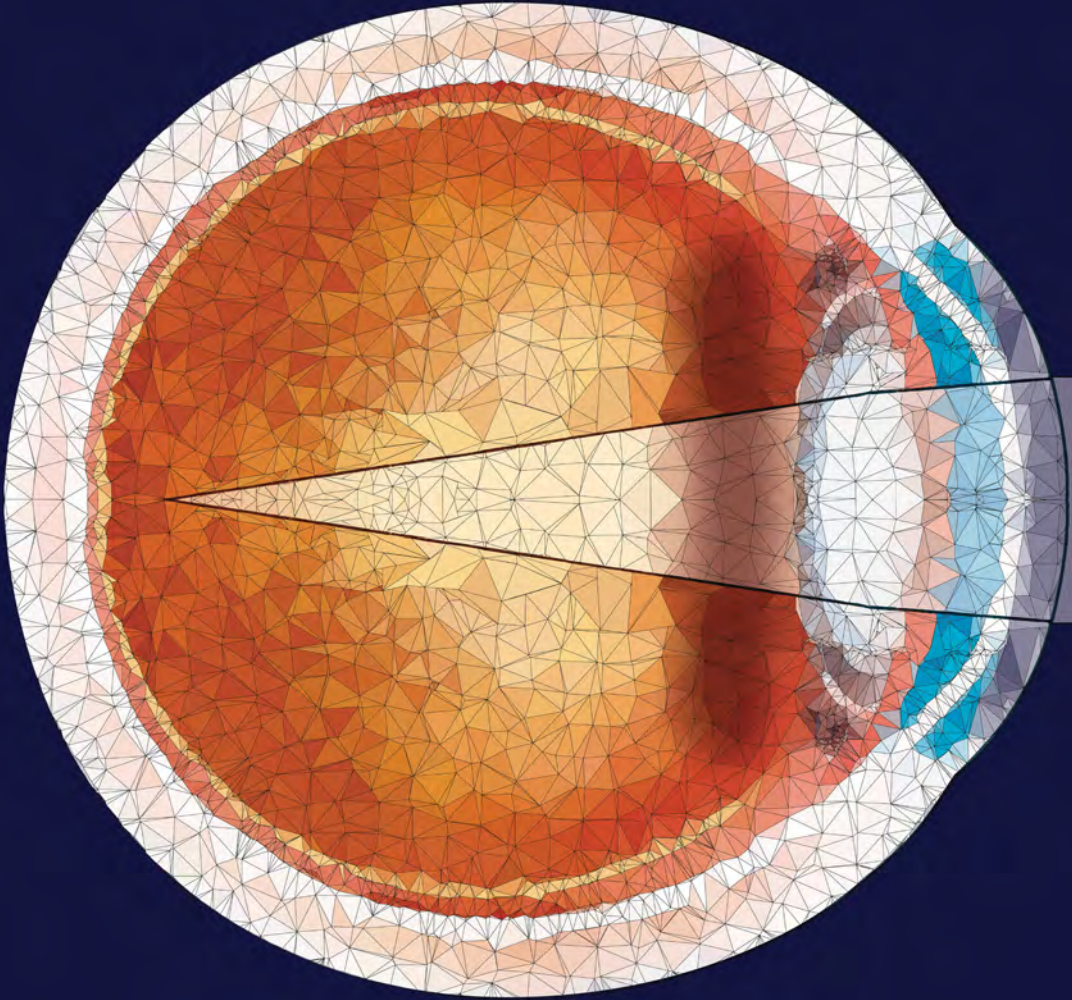
Under
embargo

Under
embargo

Under
embargo

Under
embargo

Under
embargo



6

MRI-based 3D retinal shape determination

This chapter is published as:

L. van Vught, D.P. Shamonin, G.P.M. Luyten, B.C. Stoel, J.W.M. Beenakker
MRI-based 3D retinal shape determination
BMJ Open Ophthalmology, 2021
DOI: 10.1136/bmjophth-2021-000855

Abstract

Objective: To establish a good method to determine the retinal shape from MRI using 3D ellipsoids as well as evaluate its reproducibility.

Methods: The left eyes of thirty-one volunteers were imaged using high-resolution ocular magnetic resonance imaging (MRI). The 3D MR-images were segmented and ellipsoids were fitted to the resulting contours. The dependency of the resulting ellipsoid parameters on the evaluated fraction of the retinal contour was assessed by fitting ellipsoids to 41 different fractions. Furthermore, the reproducibility of the complete procedure was evaluated in four subjects. Finally, a comparison with conventional 2D methods was made.

Results: The mean distance between the fitted ellipsoids and the segmented retinal contour was 0.03 ± 0.01 mm (mean \pm standard deviation) for the central retina and 0.13 ± 0.03 mm for the peripheral retina. For the central retina, the resulting ellipsoid radii were 12.9 ± 0.9 , 13.7 ± 1.5 and 12.2 ± 1.2 mm along the horizontal, vertical and central axes. For the peripheral retina, these radii decreased to 11.9 ± 0.6 , 11.6 ± 0.4 and 10.4 ± 0.7 mm, which was accompanied by a mean 1.8 mm posterior shift of the ellipsoid center. The reproducibility of the ellipsoid fitting was 0.3 ± 1.2 mm for the central retina and 0.0 ± 0.1 mm for the peripheral retina. When 2D methods were used to fit the peripheral retina, the fitted radii differed a mean 0.1 ± 0.1 mm from the 3D method.

Conclusion: An accurate and reproducible determination of the 3D retinal shape based on MR-imaging is provided together with 2D alternatives, enabling wider use of this method in the field of ophthalmology.

6.1 Introduction

Measurements of the geometrical shape of the eye have obtained an important position within the field of ophthalmology. Biometry and corneal topography measurements, for example, have shown to be important for the diagnosis, treatment and follow-up of patients with refractive conditions.^{1,2} Additionally, such measurements have been used to create and analyze personalized models of the eye in research settings.³⁻⁶ Thus far, these geometrical assessments have mainly focused on the anterior segment of the eye, and the three-dimensional shape of the retina is often disregarded. This three-dimensional shape, however, is suggested to be of clinical relevance for peripheral vision and ocular radiotherapy planning.⁷⁻⁹

Several assessments of the retinal shape have already been performed using off-axis laser interferometry.¹⁰⁻¹³ These evaluations were, however, limited to measuring the visual field up to 35 degrees in the horizontal and vertical meridian, covering the central 70 degrees of the visual field and thus only the more central retina.^{11,12} The use of magnetic resonance imaging (MRI) as an alternative to off-axis interferometry has also been proposed, since it is not limited by the optical opacity of tissues and can therefore evaluate the complete eye in 3D.^{7,14,15} These 3D MR-images enable direct modelling of the retina as an ellipsoid, but were initially hindered by their limited resolution. Improvements in MRI-techniques have enabled acquisition of three-dimensional images of the eye with a higher, sub-millimeter, resolution,¹⁶⁻¹⁸ enabling the determination of topographic maps of the complete retinal contour,¹⁷ and increasing the accuracy of the determined ellipsoid descriptions.

However, multiple methodological choices, such as the location of the ellipsoid center and the definition of an optical or central axis, potentially affect the resulting ellipsoidal model. Unfortunately, the exact effect of these choices on the ellipsoid parameters is not known, hampering comparisons between different studies. Additionally, even though an earlier study showed good agreement between MRI and biometry based axial length determinations,¹⁷ the reproducibility and accuracy of an MR-based retinal shape determination has not been determined. These insights are required to further implement retinal shape determination techniques in ophthalmic research and clinical care. Therefore, we assessed the accuracy, comparability and reproducibility of MRI-based 3D retinal shape determination to provide a basis for further incorporation of this method in ophthalmic research and therewith move towards clinical implementations.

6.2 Methods

The left eyes of thirty-one volunteers without prior ocular surgery were examined at the Leiden University Medical Center. The study was performed in accordance with the Declaration of Helsinki and was approved by the local medical ethical committee (CCMO-registry number: NL45166.058.13). Patients were not involved in the design of this study. Written informed consent was obtained from all subjects prior to enrolment in the study. Subjects were required to have no contraindications for MRI-scanning.

Measurements

Ocular MR-imaging was performed with a Philips Achieva 7 Tesla whole-body magnet (Philips, Best, The Netherlands) using a custom-made receive eye coil and a volume transmit coil (Nova Medical Inc., Wilmington, MA, USA).^{17,19} T1-weighted MR-images were acquired using a 3D inversion recovery turbo gradient echo technique (Figure 6.1A). The scan had a spatial acquisition resolution of $0.5 \times 0.5 \times 1.0 \text{ mm}^3$, a field of view of $46 \times 46 \times 38 \text{ mm}^3$, a total scan time of slightly less than 3 minutes, an inversion time of 1280 ms and a shot interval of 3 s. The repetition time, echo time and flip angle were 2.5 ms, 4.55 ms and 16 degrees respectively. A cued-blinking protocol was used to minimize eye-motion artefacts.^{19,20} In addition to the MRI measurement, the axial length of the eye from cornea to inner limiting membrane was measured using laser interferometry (Lenstar LS 900, Haag-Streit AG, Koeniz, Switzerland; mean of two scans).

Segmentation

The retinal contour, defined as the boundary between the hypointense vitreous and the hyperintense retina-sclera complex, was automatically segmented on the T1-weighted MR-images using in-house-developed software based on the MevisLab image-processing platform (Version 2.5.1, Fraunhofer MeVis, Bremen, Germany), as previously described.^{19,21} In short, the outer borders of the lens and vitreous body were automatically detected using a subdivision fitting algorithm.^{21,22} This algorithm utilizes intensity-based cost functions to delineate the lens and vitreous body with subvoxel precision and returns 3D meshes of the lens and retina (Figure 6.1B). The algorithm requires an initial guess as a starting point, which was automatically derived from the MR-images using a combination of intensity-based labelling and region growing, noise reduction, anisotropic diffusion filtering, multi-thresholding and morphological operations, as described by Beenakker et al.¹⁷ Prior to the subdivision fitting, all initial guesses were inspected and manually corrected if necessary.

Eye orientation

Due to the positioning within the MRI-scanner, the subjects' gazing direction does not correspond to any axis of the acquired MR-image. Moreover, the fovea and the associated visual axis are not visible on MR-images.¹⁷ As a result, the MR-derived retinal shape data cannot be compared between subjects or with other ophthalmic measurements without defining a common axis. Therefore, a central axis was defined as the line between the center of the segmented lens and the center of the segmented vitreous body.¹⁷ This central axis was subsequently aligned with the anterior-posterior axis by rotating the eye around the center of the lens.

In vivo, such eye rotations are accompanied by cyclotorsion, a rotation around the visual axis of which both the magnitude and direction are related to the change in ocular gazing direction.^{23–25} Similarly, the alignment of the MR-data with a common axis will also induce a rotation around the central axis,²⁴ and the magnitude of this induced rotation will likely be affected by chosen alignment method. To evaluate the relevance of this potential variation in induced rotation, three different alignment methods were applied and compared. In the first method, two consecutive rotations were performed in a head-fixed coordinate system. In the second method, two consecutive rotations were performed in an eye-fixed coordinate system, where the second rotation axis is affected by the first rotation. In the third method, only one rotation was performed around the axis defined by Euler's theorem. A visual and mathematical description of these methods can be found in the supplementary methods.

After these rotations, the principal axes of the MR-data correspond to the horizontal, vertical and central axes. All three methods will thus result in the same gaze-direction, but potentially with different amounts of cyclotorsion. The differences between the retinal shapes resulting from three rotation methods were evaluated by comparing the resulting cyclotorsion and calculating the mean distance between the three retinal shapes using k-dimensional trees.²⁶

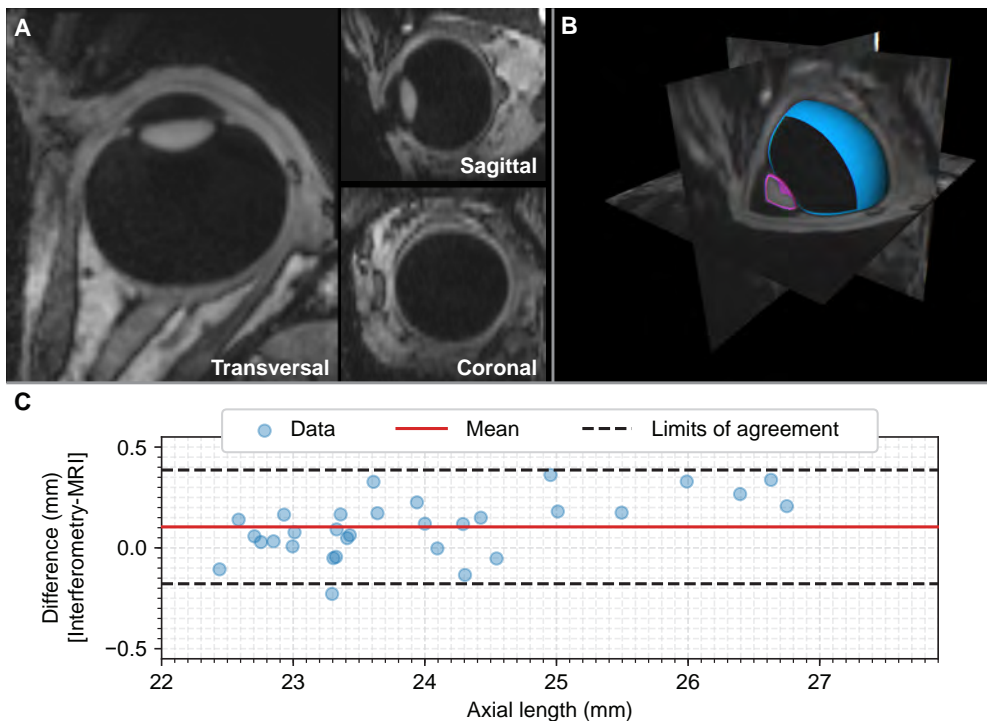


Figure 6.1: MRI acquisition and automated segmentation results. A) A transversal, sagittal and coronal reformat of the same 3D acquisition. B) The result of the segmentation of this MR-image. C) The agreement between MRI and laser interferometry in distance between the lens center and inner limiting membrane of the retina. The mean difference between the measurements was 0.10 mm, with Bland-Altman limits of agreement of -0.18 and 0.39 mm.

Agreement between MRI and laser interferometry

To evaluate the accuracy of the boundary definition of the automatic segmentation of the retinal contour, a comparison with the axial length measured using laser interferometry was performed. As the presence of air in front the eye and under the eyelids can locally affect MR-imaging and therewith potentially the shape of the cornea on the resulting images, the cornea was not segmented. Therefore, an adjusted axial length, defined as the distance from the center of the lens to the inner limiting membrane of the retina, was used to compare laser interferometry and MRI.¹⁷

Retinal shape determination

Retinal shapes were quantified by fitting a 3D ellipsoid to the segmented retinal contour points after correcting for gazing differences. The 3D ellipsoid was defined as:

$$\frac{h^2}{R_h} + \frac{v^2}{R_v} + \frac{c^2}{R_c} = 1 \quad (6.1)$$

where h , v and c are the coordinates of the contour points in the horizontal, vertical and central axis, and R_h , R_v and R_c are the radii of the ellipsoid along its principal axes. These contour points were expressed relative to the center coordinates of the ellipsoid, (C_h , C_v , C_c), and the principal axes of the ellipsoid could be angulated around this center by angles α , β and γ . The ellipsoid radii, center coordinates and angulations provided nine degrees of freedom to the fitting algorithm.

The fitting algorithm consisted of three phases, being the generation of an initial guess, the determination of the center coordinates and the determination of the radii and angulation. To ensure that the fitting algorithm was not biased or dependent on the coordinate transformations, a geometric fit rather than an algebraic fit was performed.²⁷ A detailed description of the complete fitting algorithm can be found in the supplementary methods. The correspondence between each fitted ellipsoid and the retinal contour points was defined as the mean of the absolute shortest 3D-distances between the retinal contour points and the ellipsoid.

Reproducibility

To assess the reproducibility of the 3D retinal shape determination, four subjects were examined twice in two subsequent MRI sessions. The reproducibility was evaluated per subject by comparing the parameters of the 3D fitted ellipsoids.

Comparison between 3D and 2D fitting methods

To evaluate the agreement between 3D and 2D retinal shape fitting, 2D ellipse fits were performed on transversal and sagittal slices of the retinal contour and combined into a 3D ellipsoid. Three different methods to define the 2D ellipse center were evaluated. In the first method, the ellipse center was one of the fitting parameters, similar to the 3D ellipsoid fitting method. In the second method, the ellipse center was fixed to the vitreous body center. In the third method, the ellipse center was fixed at half the laser interferometry measured axial length from the posterior pole and centered on the visual axis. A complete overview of the 2D fitting procedures can be found in the supplementary methods. The 2D-derived

ellipsoids were compared to the 3D fitted ellipsoid in terms of ellipsoidal parameters and in terms of the mean of the absolute shortest 3D distances to the MRI-based retinal contour.

Considered retinal contour fraction

The dependency of the fitted retinal shape parameters on the evaluated fraction of the retinal contour was assessed by subdividing the contour using on the angle with the vitreous body center, and subsequently fitting 41 different fractions of the contour, ranging from the central 60 degrees to a maximum of 300 degrees in steps of 6 degrees (Figure 6.2). Based on this analysis, the stability of the retinal shape parameters as function of retinal fraction as well as the optimal fractions to describe the central or peripheral retina were determined.

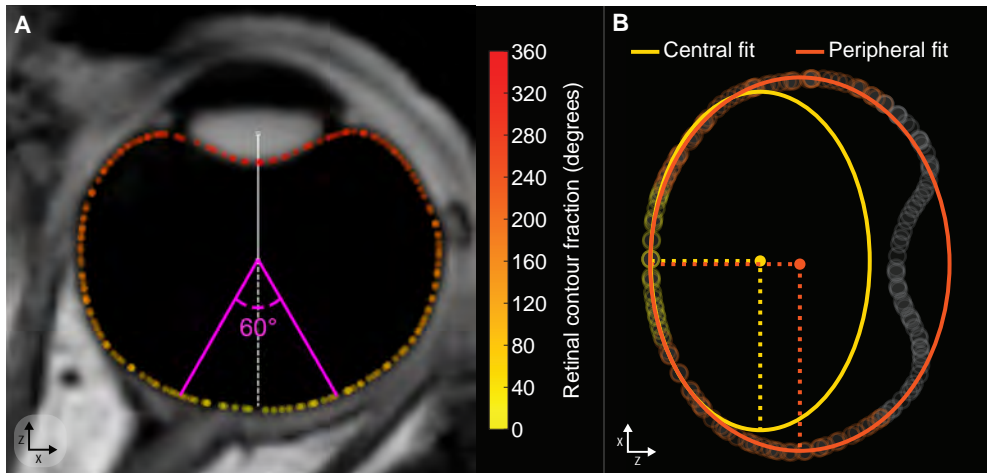


Figure 6.2: Quantification of the retinal shape for multiple fractions of the retinal contour. A) The reported angles for specific retinal contour fractions are calculated with respect to the vitreous body center. B) Example of a 2D fit for the central and peripheral retina.

6.3 Results

The 31 included subjects had a mean age of 31.1 ± 16.2 years (mean \pm standard deviation) and a mean spherical equivalent of -1.9 ± 2.1 Diopter. 21 subjects (68%) were female. The laser interferometry measurements showed a mean internal anterior chamber depth of 3.1 ± 0.3 mm and a mean axial length of 24.0 ± 1.2 mm. The MRI scans were successfully acquired for all subjects, and segmentation succeeded automatically for most subjects. Due to locally lower image contrast caused by movement artefacts, the initial guess of the retinal contour had to be manually adjusted prior to the automatic segmentation for two subjects, and the initial guess of the lens contour for one subject.

Eye orientation

The three evaluated methods to correct for gazing differences between subjects required a mean rotation of 17.3 ± 8.6 degrees. These three evaluated methods resulted in very similar contours, with a mean distance between contours of 0.03 ± 0.03 mm (5th percentile: 0.00 mm, 95th percentile: 0.07 mm). Additionally, the amount of cyclotorsion induced by the gazing correction was similar with a mean difference of 1.6 ± 1.9 degrees. As these contour differences are within one tenth of the acquisition voxel size, and therefore below the accuracy of the MR-data, all subsequent assessments were performed with the Euler method, which was spatially located in between the other two methods.

Agreement between MRI and laser interferometry

The distance between the center of lens and the retina differed significantly between MRI and laser interferometry (paired-samples t-test: $p < 0.01$). The distance measured with MRI was generally shorter than the distance measured with laser interferometry, with a mean difference of 0.10 mm and Bland-Altman limits of agreement of -0.18 and 0.39 mm (Figure 6.1C).

3D fitting

The 3D fitting succeeded automatically for all eyes and all fractions of the retinal contour. Overall, an increase in evaluated fraction resulted in a larger mean distance between the 3D ellipsoid and the retinal contour (Figure 6.3). For the central retina, the fitted ellipsoid parameters showed a high variation between different evaluated fractions. However, when more than the central 120 degrees of the retinal contour was evaluated, the parameters remained relatively stable, with the most stable description being achieved between 220 and 280 degrees (Figure 6.3). For fractions larger than 280 degrees, the ciliary body was often included in the fit and the mean distance between the fitted ellipsoid and the measured retinal contour was relatively large (Figure 6.3).

The ellipsoid radii and center coordinates differed between evaluated retinal fractions, while the rotations remained relatively constant. (Supplementary Figure 6.2). For α and β , 96% of all fitted rotations were below 15 degrees, with a mean of -0.2 ± 5.4 degrees. Additionally, 54% of all fitted ellipsoids had less than 0.5 mm difference between the horizontal and vertical radius. For these symmetric ellipsoids, virtually all possible angles were observed for γ . For asymmetric ellipsoids, however, 69% of all observed γ 's showed a mean exorotation of 7.1 ± 21.3 degrees. More details about these rotations can be found in the supplementary data.

Overall, two different sets of ellipsoids describing the retinal shape were distinguishable for each subject. The first set describing the central retina, ranging from 60 to 120 degrees of the retinal contour, and the second set describing the complete retina including the peripheral parts, ranging from 220 to 280 degrees of the retinal contour. For numerical comparisons, the results for 60 degrees were used as representation of the central retina and the results for 240 degrees as representation of the peripheral retina. The primary difference between these central and peripheral results was a mean shift of the ellipsoid center of 1.8 mm posteriorly when the peripheral retina was included. This shift directly affected the other ellipsoid parameters, especially the radii.

For the central retina, the mean distance between the 3D fitted ellipsoid and the considered retinal contour was 0.03 ± 0.01 mm. The corresponding mean ellipsoid radii were 12.9 ± 0.9 mm for R_h , 13.7 ± 1.5 mm for R_v , and 12.2 ± 1.2 mm for R_c . The ellipsoid center was generally located within 0.7 mm of the central axis in the horizontal and vertical direction, with a mean axial position of 6.2 ± 1.3 mm posterior of the center of the lens. (Figure 6.3 and 6.4; Supplementary Table 6.1).

For the peripheral retina, the mean absolute distance with the retinal contour increased to 0.13 ± 0.03 mm. The mean axial center of the ellipsoid, C_c , was located 8.0 ± 0.5 mm posterior of the center of the lens. Additionally, a decrease of the ellipsoid radii to 11.9 ± 0.6 mm for R_h , 11.6 ± 0.4 mm for R_v , and 10.4 ± 0.7 mm for R_c was observed. (Figure 6.3 and 6.4,

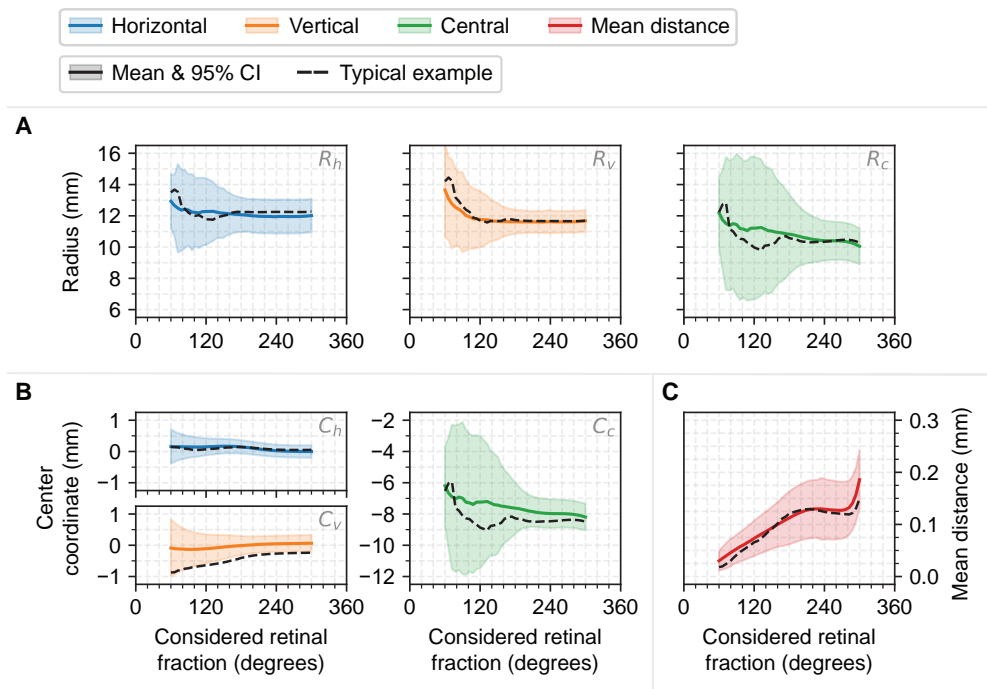


Figure 6.3: 3D ellipsoid fitting results as function of the considered retinal contour fraction A) The radii of the 3D ellipsoids. B) The center coordinates of the 3D ellipsoids. C) The mean distance between the resulting ellipsoid and the evaluated retinal contour.

Supplementary Table 6.1). The absolute mean difference between R_h and R_v was 0.5 ± 0.4 , and the decrease in R_c was directly correlated with the change in C_c ($r^2: 0.98$, $p < 0.01$). In 13 subjects (42%) the difference between R_h and R_v was larger than 0.5 mm. On the individual level, the radii of the fitted ellipsoids decreased in size in the majority (91%) of the subjects between the central and peripheral retina, with only two subjects (6%) showing an increase in all three radii and one subject (3%) showing an increase of only R_h (Figure 6.4).

Reproducibility

The reproducibility analysis showed a mean difference of 0.12 ± 0.13 mm between the determined retinal contours. The reproducibility of the subsequently fitted ellipsoids was dependent on the evaluated fraction of the retinal contour, with a higher reproducibility for larger evaluated fractions. For smaller fractions, up to the central 180 degrees, the mean difference between the ellipsoid radii was 0.3 ± 1.2 mm, with a maximal difference of 5.9 mm (Supplementary Figure 6.3). For larger fractions, this mean difference was 0.0 ± 0.1 mm, with a maximal difference of 0.5 mm (Supplementary Figure 6.3).

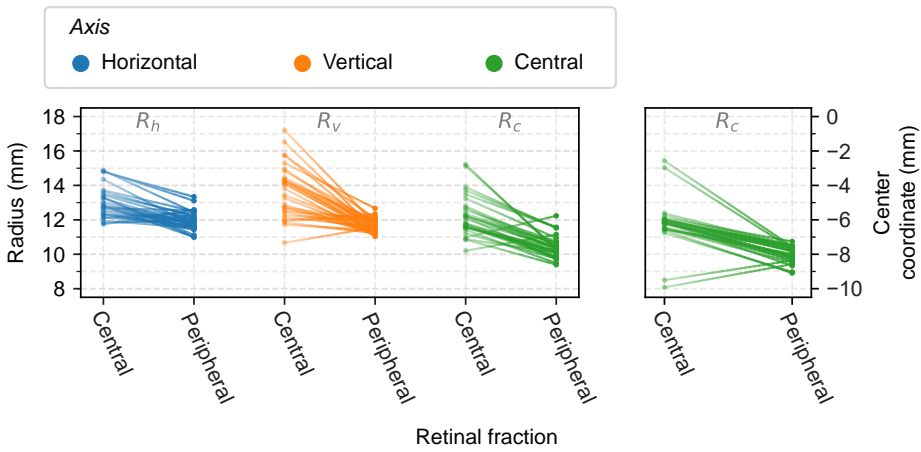


Figure 6.4: Differences in 3D ellipsoid parameters between the central and peripheral retina. Left: The ellipsoid radii along the horizontal (blue), vertical (orange) and central (green) axis showing a decrease in all three radii for an increase in evaluated retinal contour for the majority of the subjects. Right: Location of the ellipsoid center along the central axis, where a lower center-coordinate corresponds to a more posterior location in the eye. The center-coordinates shift posteriorly for an increase in evaluated retinal contour for the majority of the subjects.

Comparison between 3D and 2D fitting methods

Irrespective of the used 2D fitting method, the 3D fitting method resulted in smaller mean distances between the fit and the retinal contour (Figure 6.5). The mean difference in centrally determined ellipsoid radii between 3D and 2D fitting methods was 2.9 ± 0.9 mm when using the free center 2D fit, 1.7 ± 1.0 mm when using the vitreous body fixed 2D fit and 0.2 ± 0.9 mm when using the axial length fixed 2D fit (Supplementary Figure 6.4), where a positive difference indicates that the measured radius is larger in 3D than 2D. These differences in ellipsoid radii changed to respectively 0.1 ± 0.1 mm, 0.2 ± 0.3 mm and 0.5 ± 1.0 mm for when the peripheral retina was included (Figure 6.5C).

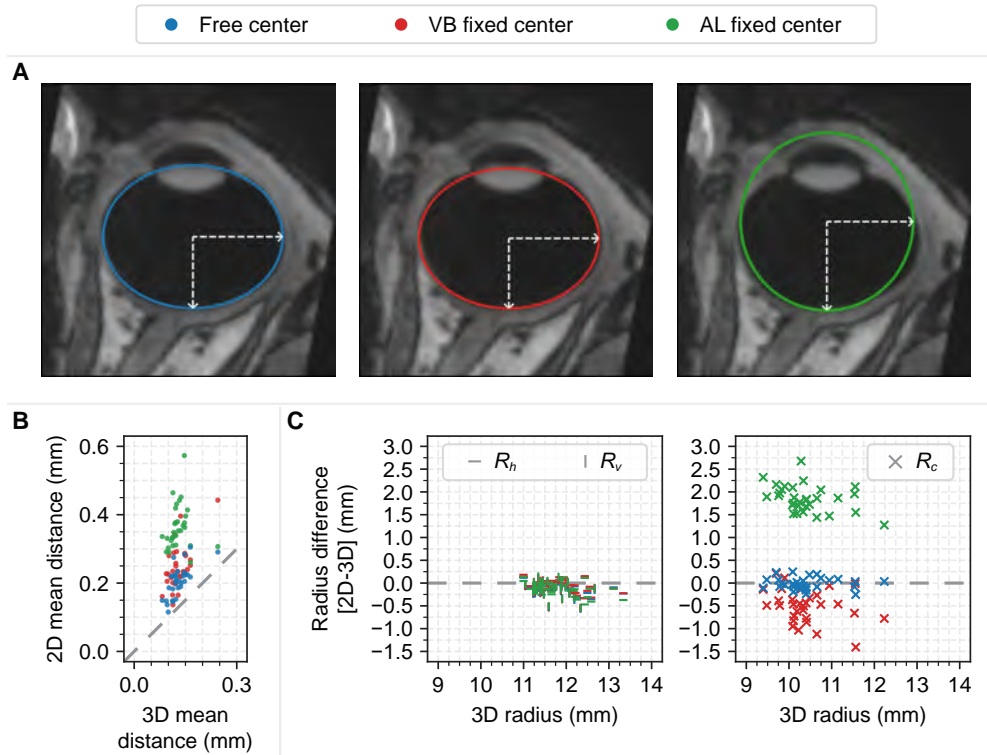


Figure 6.5: Comparison between 2D-derived and 3D ellipsoids fitted to the peripheral retina. Three different two 2D fitting methods are shown, one with a free center (blue), one with a vitreous body fixed center (red) and one with an axial length fixed center (green). A) Examples of the 2D fitted ellipses for a representative subject. B) Mean distance to the original 3D contour of the ellipsoid model based on the 3D and 2D fits. The 3D fits consistently provided a more accurate description. C) differences between the 3D and 2D determined ellipsoid radii of the ellipsoids as function of the 3D radii.

6.4 Discussion

In this study, we successfully combined high-resolution MRI scans with an automated segmentation and 3D ellipsoid fitting to describe the shape of 31 eyes. Additionally, the dependency of the resulting parametrization on the included retinal contour and its reproducibility were evaluated. Finally, a 3D ellipsoid description based on 2D imaging data was compared with the 3D results.

The used MRI acquisition methods resulted in high-resolution 3D MR-images of the eye that provided a base for accurate segmentation of the eye. With mean differences of only 0.1 mm, the segmented contours showed to be in line with laser interferometry results for the central retina. Although different methods can be used to correct these contours for differences in gazing direction during MR-imaging by aligning them to the same axis, these methods resulted in almost identical data with negligible mean differences of 0.03 mm. Furthermore, the reproducibility of the 3D segmented retinal contours was high, with a mean difference of 0.12 mm. Although these results were obtained using a high-resolution 7 Tesla MRI and a custom-made eye coil, it has recently been shown that images with a similar resolution and quality can be obtained using clinical 3 Tesla MRI-scanners and commercially available eye-coils,^{18,28} enabling clinical application of these methods.

The obtained MRI-derived retinal contours could be accurately described by ellipsoids, with mean differences of 0.03 mm for the central and 0.13 mm for the peripheral retina. Optically, these differences correspond to refractive differences of approximately 0.1 and 0.3 Diopter, which is sufficient to study for example the effect of peripheral vision on the progression of myopia in children.⁹ However, the parameters for the central retina, such as the horizontal radius, showed a high within-subject variability for small changes in evaluated retinal fraction, even though the resulting ellipsoids accurately describe the measured contour. For these evaluations, a 1.6 mm decrease in the central radius R_c can for example be compensated by 1.5 mm posterior shift of the ellipsoid center (Figure 6.3). The resulting ellipsoids, however, differ less than 0.1 mm over the central 60 degrees, explaining the lower reproducibility and strong variation of the individual ellipsoid parameters for different included retinal fractions (Supplementary Figure 6.3). A similar variation was observed when the central retina would be described in terms of vertex radius of curvature and asphericity (Supplementary Figure 6.5).^{7,12,16} When the shape of the central retina is however obtained using 3D fitting with the center of the ellipsoid fixed to the central axis at half the axial length, stable and reproducible ellipsoidal parameters are obtained without a significant increase in fitting residuals (Supplementary Figures 6.6 and 6.7). This indicates that such a reduction in degrees of freedom is required for meaningful comparison of the central retinal shape between subjects.

For the peripheral retina, a reproducible and stable ellipsoid description was found between 220 and 280 degrees of the retinal contour. At these fractions, the horizontal and vertical ellipsoid center coordinates as well as the corresponding rotations remain close to zero. As a result, these parameters could be fixed in future studies, resulting in a faster fitting procedure. In 42% of the subjects, the horizontal and vertical radii differed more than 0.5 mm. This asymmetry could be relevant for ocular proton therapy planning, which currently uses a geometric eye model in which the eye is assumed to be rotational symmetrical.²⁹ For such applications, an ellipsoid based on two orthogonal 2D images would already be an improvement, but will still result in larger differences with the measured 3D contours than

a full 3D fit. The resulting differences in ellipsoid radii are however small, generally ≤ 0.2 mm, when the ellipse center is fixed to the half the axial length when describing the central retina, or when this ellipse center is included in the fitting or fixed to the center of the vitreous body when describing the peripheral retina.

The results obtained within this study are in accordance with earlier MRI-based retinal shape studies. For the central retina, the data of the emmetropic population of Pope et al. show mean horizontal and central ellipsoid radii of approximately 12 and 11 mm, which are comparable to the results of this study. Additionally, their data shows a similar large variation between subjects, for example 6 mm for the horizontal radius.^{7,16} For the peripheral retina, Lim et al. present results for 240 degrees of the retinal contour and Pope et al. evaluated a slightly larger part, 270 degrees of the retinal contour.^{15,16} Both studies report similar horizontal and vertical radii, 11 to 12 mm and 10 to 11 mm, respectively. The radii reported by Lim et al. are slightly smaller than the values reported by Pope et al. and the values reported within this study. This could be explained by the difference in the MRI resolution, as a lower resolution can result in an apparent inward shift of the retina due to partial volume effects,³⁰ resulting in smaller radii.

While the presented results are in line with earlier MR-based retinal shape research, they differ from earlier studies using laser interferometry. The mean vertex radii of curvature for the central retina determined using laser interferometry by Verkicharla et al. was about 2.0 mm larger than the currently presented vertex radius of curvature (Supplementary Figure 6.5).¹² Even though this difference could be the result of the unstable central fit, it might also result from the difference in used imaging methods or the limited amount of data points, < 20 , available with laser interferometry. Due to its much larger amount of data points and the availability of 3D assessments, MRI might be more reliable than laser interferometry to quantify the retinal shape. Additionally, MRI is not influenced by refraction and is not limited to assessments of the central 80 degrees of the retina or less, making it a more favourable method to measure the retinal shape.

Other methods to image the eye, such as Computed Tomography (CT) and B-scan ultrasonography, are also not affected by refraction and could therefore be considered as an alternative to MRI, especially since they are generally faster to acquire. However, CT-scans expose a subject to radiation and have a lower resolution than MRI, and B-scan ultrasonography is generally limited to a 2D field of view and has a high inter-observer variability for geometrical measurements.³¹⁻³³ As a result, both are less suitable than MRI to assess the 3D retinal shape.

It should be noted that the current results are based upon a relatively small group of volunteers, and the presented parametric description of the retinal shape might therefore not hold for the entire population. However, the same methodology could directly be used to determine these metrics for a specific group of subjects. An additional concern could be that the presented method might be unable to describe pathological retinal shapes, for example upon the presence of a staphyloma or intraocular mass. Although different authors have shown that the segmentation of the MR-Images can be adopted to include such ocular pathologies,^{34,35} these pathologies might result in a retinal shape that is not accurately described by an ellipsoid.³⁶ Depending on the application, an approximate ellipsoidal description might still be sufficient in such instances, but using alternatives such as the complete 3D retinal contour should be considered.

In conclusion, this study provides a method to reproducibly determine and quantify the 3D retinal shape from MR-imaging data. Two models are proposed, one which describes the complete posterior segment of the eye and an additional one for only the more central retina. Due to the high precision and reproducibility of this method, the resulting 3D shapes can be used as input in other research, such as optical ray-tracing simulations or the analysis of myopia progression. Furthermore, they can be utilized to improve the accuracy of the retinal shapes used in eye model-based treatment planning, which can for instance improve the proton therapy planning for eye tumours. With that, this study provides a complete base for widespread implementation of the 3D retinal shape as a parameter in the evaluation of the eye.

6.5 References

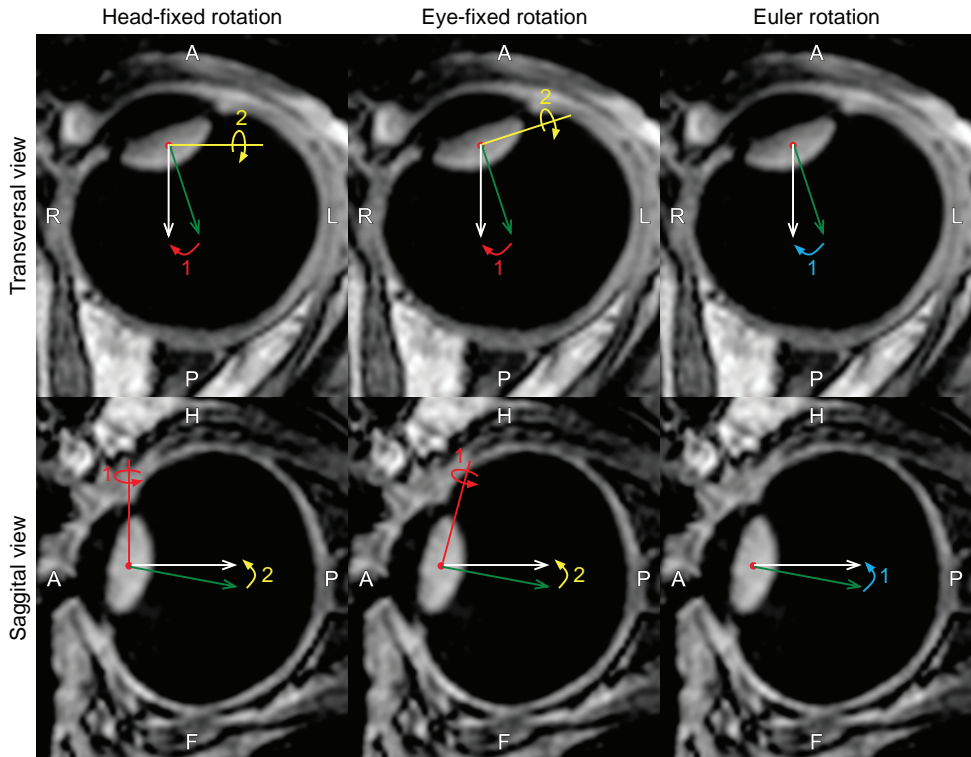
1. Olsen T. Calculation of intraocular lens power: a review. *Acta Ophthalmol Scand.* 2007;85(5):472–85. doi: 10.1111/j.1600-0420.2007.00879.x.
2. Gokul A, Vellara HR, Patel DV. Advanced anterior segment imaging in keratoconus: a review. *Clin Exp Ophthalmol.* 2018;46(2):122–132. doi: 10.1111/ceo.13108.
3. Taberero J, Piers P, Benito A, Redondo M, Artal P. Predicting the optical performance of eyes implanted with IOLs to correct spherical aberration. *Invest Ophthalmol Vis Sci.* 2006;47(10):4651–8. doi: 10.1167/iovs.06-0444.
4. Canovas C, Artal P. Customized eye models for determining optimized intraocular lenses power. *Biomed Opt Express.* 2011;2(6):1649–62. doi: 10.1364/boe.2.001649.
5. Makhotkina NY, Dugrain V, Purchase D, Berendschot T, Nuijts R. Effect of supplementary implantation of a sulcus-fixated intraocular lens in patients with negative dysphotopsia. *J Cataract Refract Surg.* 2018;44(2):209–218. doi: 10.1016/j.jcrs.2017.11.013.
6. Vught L van, Luyten GPM, Beenakker JWM. Distinct differences in anterior chamber configuration and peripheral aberrations in negative dysphotopsia. *J Cataract Refract Surg.* 2020;46(7):1007–1015. doi: 10.1097/j.jcrs.0000000000000206.
7. Atchison DA, Pritchard N, Schmid KL, Scott DH, Jones CE, Pope JM. Shape of the retinal surface in emmetropia and myopia. *Invest Ophthalmol Vis Sci.* 2005;46(8):2698–707. doi: 10.1167/iovs.04-1506.
8. Fleury E, Trnkova P, Erdal E, Hassan M, Stoel B, Jaarma-Coes M, Luyten G, Herault J, Webb A, Beenakker JWM, Pignol JP, Hoogeman M. Three-dimensional MRI-based treatment planning approach for non-invasive ocular proton therapy. *Med Phys.* 2021;48(3):1315–1326. doi: 10.1002/mp.14665.
9. Smith MJ, Walline JJ. Controlling myopia progression in children and adolescents. *Adolesc Health Med Ther.* 2015;6:133–40. doi: 10.2147/ahmt.s55834.
10. Atchison DA, Charman WN. Can partial coherence interferometry be used to determine retinal shape? *Optom Vis Sci.* 2011;88(5):E601–7. doi: 10.1097/oxp.0b013e318212ae56.
11. Verkicharla PK, Suheimat M, Pope JM, Sepehrband F, Mathur A, Schmid KL, Atchison DA. Validation of a partial coherence interferometry method for estimating retinal shape. *Biomed Opt Express.* 2015;6(9):3235–47. doi: 10.1364/boe.6.003235.
12. Verkicharla PK, Suheimat M, Schmid KL, Atchison DA. Peripheral refraction, peripheral eye length, and retinal shape in myopia. *Optom Vis Sci.* 2016;93(9):1072–8. doi: 10.1097/oxp.0000000000000905.
13. Verkicharla PK, Mathur A, Mallen EA, Pope JM, Atchison DA. Eye shape and retinal shape, and their relation to peripheral refraction. *Ophthalmic Physiol Opt.* 2012;32(3):184–99. doi: 10.1111/j.1475-1313.2012.00906.x.
14. Kuo AN, Verkicharla PK, McNabb RP, Cheung CY, Hilal S, Farsiou S, Chen C, Wong TY, Ikram MK, Cheng CY, Young TL, Saw SM, Izatt JA. Posterior eye shape measurement with retinal OCT compared to MRI. *Invest Ophthalmol Vis Sci.* 2016;57(9):OCT196–203. doi: 10.1167/iovs.15-18886.
15. Lim LS, Matsumura S, Htoon HM, Tian J, Lim SB, Sensaki S, Chen C, Hilal S, Wong TY, Cheng CY, Kuo A, Saw SM. MRI of posterior eye shape and its associations with myopia and ethnicity. *Br J Ophthalmol.* 2019. doi: 10.1136/bjophthalmol-2019-315020.
16. Pope JM, Verkicharla PK, Sepehrband F, Suheimat M, Schmid KL, Atchison DA. Three-dimensional MRI study of the relationship between eye dimensions, retinal shape and myopia. *Biomed Opt Express.* 2017;8(5):2386–2395. doi: 10.1364/boe.8.002386.
17. Beenakker JWM, Shamonin DP, Webb AG, Luyten GP, Stoel BC. Automated retinal topographic maps measured with magnetic resonance imaging. *Invest Ophthalmol Vis Sci.* 2015;56(2):1033–9. doi: 10.1167/iovs.14-15161.
18. Ferreira TA, Grech Fonk L, Jaarsma-Coes MG, Haren GGR van, Marinkovic M, Beenakker JWM. MRI of uveal melanoma. *Cancers (Basel).* 2019;11(3). doi: 10.3390/cancers11030377.
19. Beenakker JWM, Rijn GA van, Luyten GP, Webb AG. High-resolution MRI of uveal melanoma using a microcoil phased array at 7 T. *NMR Biomed.* 2013;26(12):1864–9. doi: 10.1002/nbm.3041.
20. Berkowitz BA, McDonald C, Ito Y, Tofts PS, Latif Z, Gross J. Measuring the human retinal oxygenation response to a hyperoxic challenge using MRI: eliminating blinking artifacts and demonstrating proof of concept. *Magn Reson Med.* 2001;46(2):412–6. doi: 10.1002/mrm.1206.

21. Kitslaar PH, Klooster R van't, Staring M, Lelieveldt BPF, Geest RJ van der. "Segmentation of branching vascular structures using adaptive subdivision surface fitting". In: ed. by S Ourselin, MA Styner. Vol. 9413. Proceedings of SPIE. 94133Z–94133Z. doi: 10.1117/12.2082222.
22. Loop C. "Smooth subdivision surfaces based on triangles". MA thesis. The University of Utah, 1987.
23. Porrill J, Ivins JP, Frisby JP. The variation of torsion with vergence and elevation. *Vision Res.* 1999;39(23):3934–50. doi: 10.1016/s0042-6989(99)00102-9.
24. Quaia C, Optican L. Three-dimensional rotations of the eye. In: P Kaufman, A Alm, F Adler, eds. *Adler's Physiology of the Eye: Clinical Application*. 10th ed. Mosby; 2003.
25. Tweed D, Vilis T. Geometric relations of eye position and velocity vectors during saccades. *Vision Res.* 1990;30(1):111–27. doi: 10.1016/0042-6989(90)90131-4.
26. Maneewongvatana S, Mount DM. "Analysis of approximate nearest neighbor searching with clustered point sets". In: *Data Structures, Near Neighbor Searches, and Methodology*.
27. Ahn SJ, Rauh W, Oberdorfer B. "Least squares fitting of circle and ellipse". In: *Mustererkennung 1998*. Ed. by P Levi, M Schanz, RJ Ahlers, F May. Springer Berlin Heidelberg. Pp. 333–340.
28. Niendorf T, Beenakker JWM, Langner S, Erb-Eigner K, Bach Cuadra M, Beller E, Millward JM, Niendorf TM, Stachs O. Ophthalmic Magnetic Resonance Imaging: where are we (heading to)? *Curr Eye Res.* 2021;1–20. doi: 10.1080/02713683.2021.1874021.
29. Varian Medical Systems. *Planning reference guide for Eclipse Ocular Proton Planning*. 2007.
30. Soret M, Bacharach SL, Buvat I. Partial-volume effect in PET tumor imaging. *J Nucl Med.* 2007;48(6):932–45. doi: 10.2967/jnumed.106.035774.
31. Bhatt AB, Scheffler AC, Feuer WJ, Yoo SH, Murray TG. Comparison of predictions made by the intraocular lens master and ultrasound biometry. *Arch Ophthalmol.* 2008;126(7):929–33. doi: 10.1001/archophth.126.7.929.
32. Haritoglou C, Neubauer AS, Herzum H, Freeman WR, Mueller AJ. Interobserver and intraobserver variability of measurements of uveal melanomas using standardised echography. *Br J Ophthalmol.* 2002;86(12):1390–4. doi: 10.1136/bjo.86.12.1390.
33. Char DH, Kroll S, Stone RD, Harrie R, Kerman B. Ultrasonographic measurement of uveal melanoma thickness: interobserver variability. *British Journal of Ophthalmology.* 1990;74(3):183. doi: 10.1136/bjo.74.3.183.
34. Hassan MK, Fleury E, Shamonin D, Fonk LG, Marinkovic M, Jaarsma-Coes MG, Luyten GPM, Webb A, Beenakker JW, Stoel B. An automatic framework to create patient-specific eye models from 3D MR-images for treatment selection in patients with uveal melanoma. *Advances in Radiation Oncology.* 2021:100697. doi: https://doi.org/10.1016/j.adro.2021.100697.
35. Strijbis VIJ, Bloeme CM de, Jansen RW, Kebiri H, Nguyen HG, Jong MC de, Moll AC, Bach-Cuadra M, Graaf P de, Steenwijk MD. Multi-view convolutional neural networks for automated ocular structure and tumor segmentation in retinoblastoma. *Scientific Reports.* 2021;11(1):14590. doi: 10.1038/s41598-021-93905-2.
36. Ohno-Matsui K. Proposed classification of posterior staphylomas based on analyses of eye shape by three-dimensional Magnetic Resonance Imaging and wide-field fundus imaging. *Ophthalmology.* 2014;121(9):1798–1809. doi: https://doi.org/10.1016/j.ophtha.2014.03.035.
37. Kraft D. A software package for sequential quadratic programming. *Forschungsbericht- Deutsche Forschungs- und Versuchsanstalt für Luft- und Raumfahrt.* 1988.
38. Nocedal J, Wright SJ. Quasi-Newton Methods. In: *Numerical Optimization*. Springer New York; 2006:135–163. doi: 10.1007/978-0-387-40065-5_6.

6.6 Supplementary methods

6.6.1 Mathematical description of the eye rotations

As the gazing direction during the MRI-examination will differ between subjects, there will be small rotational differences between the segmented eyes of these subjects. To allow for comparisons between subjects, all segmentations were aligned towards the same coordinate system. To this end, the segmentations were rotated around the center of the lens to orient the central axis of the eye parallel to the z-axis. Three different rotation-methods, a head-fixed rotation method, an eye-fixed rotation method and an Euler rotation method were evaluated (Supplementary Figure 6.1). The mathematical description of these rotation-methods is given below.



Supplementary Figure 6.1: Overview of the three methods used to align the MR-segmentations to the same orientation in transversal and sagittal view. Left: the first (red) and second (yellow) rotation performed using a head-fixed rotation method. Middle: the first (red) and second (yellow) rotation performed using an eye-fixed rotation method. Right: the only (blue) rotation performed using an Euler rotation method.

Head-fixed rotation

The head-fixed rotation method is applied by performing two subsequent rotations, an initial rotation around the feed-head (FH) axis and a second rotation around the left-right (LR) axis. In our implementation, these axes are defined as the coordinate system of the MRI scanner.

Let \hat{g}_{init} be the unit vector pointing from the center of the lens to the center of the vitreous body and \hat{g}_{final} the unit vector in the desired direction. The angle for the rotation around the FH-axis, θ_{FH} , is defined by:

$$\theta_{FH} = \arccos(\hat{g}_{proj} \cdot \hat{g}_{final}) \quad (s6.1)$$

with \hat{g}_{proj} the normalized projection of \hat{g}_{init} onto the AP-LR-plane. The intermediate gaze direction, \hat{g}_{inter} is defined by:

$$\hat{g}_{inter} = R_{FH}(\theta_{FH}) \hat{g}_{init} \quad (s6.2)$$

with R_{FH} the rotation matrix for a rotation around the FH-axis.

The angle for the subsequent rotation around LR-axis, θ_{LR} , is calculated similarly:

$$\theta_{LR} = \arccos(\hat{g}_{inter,proj} \cdot \hat{g}_{final}) \quad (s6.3)$$

with $\hat{g}_{inter,proj}$ the normalized projection of \hat{g}_{inter} onto the AP-FH-plane.

With R_{LR} , the rotation matrix for a rotation around the LR-axis, the full transformation can be defined by:

$$R_{head} = R_{FH}(\theta_{FH}) R_{LR}(\theta_{LR}) \quad (s6.4)$$

Eye-fixed rotation

The second method to align data is similar to the head-fixed method, but the axes of rotation are defined with respect to the eye instead of the head. As a result, the axis of rotation for the second rotation depends on the first rotation. To this end an eye-fixed coordinate system is constructed in which the rotations are calculated in this coordinate system, using a transformation-matrix to express all the vectors in the eye-fixed coordinate system.

Let \hat{g}_{init} be the unit vector pointing from the center of the lens to the center of the vitreous body, \hat{g}_{final} the unit vector in the desired direction and \hat{u}_{FH} the unit vector in FH-direction, all in the original, head-fixed, coordinate system. The basis-set for the eye-fixed coordinate system, $\hat{h}_1, \hat{h}_2, \hat{h}_3$ is defined as:

$$\hat{h}_1 = \hat{g}_{init} \quad (s6.5)$$

$$h_{tmp} = \hat{u}_{FH} - (\hat{u}_{FH} \cdot \hat{g}_{init}) \hat{g}_{init} \quad (s6.6)$$

$$\hat{h}_2 = \frac{h_{tmp}}{\|h_{tmp}\|} \quad (s6.7)$$

$$\hat{h}_3 = \hat{h}_1 \times \hat{h}_2 \quad (s6.8)$$

and with

$$T = \begin{bmatrix} \hat{h}_1^T \\ \hat{h}_2^T \\ \hat{h}_3^T \end{bmatrix}^{-1} \quad (s6.9)$$

as the coordinate transformation matrix from the MRI basis-set to the eye basis-set.

Subsequently, the desired gazing direction is expressed in the eye coordinate system, $\hat{g}'_{final} = T\hat{g}_{final}$, and the rotation matrix R'_{eye} within this system is calculated in the same manner as with head-fixed coordinate system, using \hat{h}_2 and \hat{h}_3 as the two axes of rotation and \hat{g}'_{final} as target. The final rotation matrix in the MRI coordinate system, R_{eye} , can be obtained by:

$$R_{eye} = T^{-1}R'_{eye}T \quad (s6.10)$$

Euler rotation

Euler's method uses a single rotation to align the segmented eye-data. Let \hat{g}_{init} be the unit vector pointing from the center of the lens to the center of the vitreous body and \hat{g}_{final} the unit vector in the desired direction. Euler's rotation theorem defines the needed rotation around the vector \hat{r}_e of angle θ_e as:

$$\hat{r}_e = \frac{(\hat{g}_{init} \times \hat{g}_{final})}{\|\hat{g}_{init} \times \hat{g}_{final}\|} = \begin{bmatrix} r_x \\ r_y \\ r_z \end{bmatrix} \quad (s6.11)$$

$$\theta_e = \arccos(\hat{g}_{init} \cdot \hat{g}_{final}) \quad (s6.12)$$

which can be expressed as the matrix R_{Euler} :

$$\hat{g}_{final} = R_{Euler}\hat{g}_{init} \quad (s6.13)$$

$$R_{Euler} = \begin{bmatrix} 1 + (1 - \cos \theta_e)(r_x^2 - 1) & -r_z \sin \theta_e + (1 - \cos \theta_e)r_x r_y & r_y \sin \theta_e + (1 - \cos \theta_e)r_x r_z \\ r_z \sin \theta_e + (1 - \cos \theta_e)r_x r_y & 1 + (1 - \cos \theta_e)(r_y^2 - 1) & -r_x \sin \theta_e + (1 - \cos \theta_e)r_y r_z \\ -r_y \sin \theta_e + (1 - \cos \theta_e)r_x r_z & r_x \sin \theta_e + (1 - \cos \theta_e)r_y r_z & 1 + (1 - \cos \theta_e)(r_z^2 - 1) \end{bmatrix} \quad (\text{s6.14})$$

6.6.2 3D fitting algorithm

The fitted 3D ellipsoid was defined as:

$$\frac{x'^2}{R_{x'}} + \frac{y'^2}{R_{y'}} + \frac{z'^2}{R_{z'}} = 1 \quad (\text{s6.15})$$

were x' , y' and z' are the three principal axes, referred to as the horizontal, vertical and central axis within the main manuscript, and $R_{x'}$, $R_{y'}$ and $R_{z'}$ are the radii of the ellipsoid along these. These radii, together with the center coordinates of the ellipsoid, $C_{x',y',z'}$, and the angulations of its principal axes, α , β and γ provide nine degrees of freedom to the fitting algorithm.

The fitting algorithm consists of three phases, being the generation of an initial guess, the determination of the center coordinates $C_{x',y',z'}$, and the determination of the radii $R_{x'}$, $R_{y'}$ and $R_{z'}$ and angulations α , β and γ . In each phase, the optimal parameters were determined by minimizing the error between the ellipsoid and the contour points using SLSQP-minimization.³⁷ To this end, the fitting algorithm follows the same protocol, sometimes with minor deviations, as listed below:

1. The selected retinal contour points are translated by $-[C_{x'}, C_{y'}, C_{z'}]$, making the center of the ellipsoid the origin of the coordinate system.
2. The retinal contour points are rotated around the center of the ellipsoid by angles α , β and γ .
3. As the ellipsoid is symmetrical in the principal axes coordinate system, all contour points are mapped to the first quadrant, $x' \rightarrow |x'|$, $y' \rightarrow |y'|$, and $z' \rightarrow |z'|$.
4. The shortest distance between each contour point and the ellipsoid defined by Equation s6.15 is calculated. As there is no algebraic expression to calculate the distance between a point and a 3D ellipsoid, an iterative minimization is performed using the quasi-Newton BFGS method.³⁸ This algorithm finds the location on the ellipsoid, defined by the angles θ and ϕ , that has the shortest distance, d , to the contour point:

$$d^2 = (R_{x'} \cos \theta \sin \phi - x')^2 + (R_{y'} \sin \theta \cos \phi - y')^2 + (R_{z'} \cos \phi - z')^2 \quad (\text{s6.16})$$

The sum of all squared distances is returned to the fitting algorithm as a measure of the goodness of the fit.

In the first fitting phase, an initial estimate of the center of the ellipsoid and its radii is made, which is used as an initial guess for the following steps. As such an initial guess does not need the highest accuracy, step 4 of the fitting protocol was adjusted such that θ and ϕ are not iteratively determined, but defined by $\theta = \tan^{-1}(y'/x')$ and $\phi = \cos^{-1}(z'/\sqrt{x'^2 + y'^2 + z'^2})$. This approximation has a bias towards a more spherical ellipsoid and is therefore not suitable for the final assessment of the retinal shape, but is multiple orders of magnitude faster than the unbiased iterative distance determination and therefore suitable for providing an initial guess.

In the second fitting phase, the center of the ellipsoid is determined. This center is determined separately from the other parameters as the angulations of the ellipsoid are closely

related to its radii and center coordinates, especially if only a relatively small portion of the retina is used as an input. In this intermediate phase, the fitting is performed with the angulations fixed to 0 degrees. This phase is further accelerated by using an adapted ellipsoid description with a single parameter for the horizontal and vertical ellipsoid radii:

$$\frac{x'^2 + y'^2}{R_{x'y'}} + \frac{z'^2}{R_{z'}} \quad (\text{s6.17})$$

In the final fitting phase, the radii and angulations are determined while the center is fixed to the coordinates calculated in the second fitting phase. The duration of the fitting process depends on the size of the evaluated retinal fraction, with a duration of half a minute or less for the central retina and three to four minutes for the more peripheral retina.

6.6.3 2D fitting algorithm

For the 2D-fits, Equation s6.15 was adjusted to define an ellipse instead of ellipsoid:

$$\frac{x'^2}{R_{x'}} + \frac{z'^2}{R_{z'}} = 1 \quad (\text{s6.18})$$

were $R_{x'}$ and $R_{z'}$ are the radii of the ellipse along the principal axes x' and z' of the used slice. As such, principal axis x' is oriented in the left-right direction for the transversal slices and in the feet-head direction for sagittal slices. Furthermore, the described fitting protocol was adjusted in all four steps to ignore the 2nd dimension. To that end, parameters $C(y')$, β and y' of steps 1, 2 and 3 were disregarded, and Equation s6.16 was redefined as:

$$d^2 = (R_{x'} \cos \theta - x')^2 + (R_{z'} \sin \theta - z')^2 \quad (\text{s6.19})$$

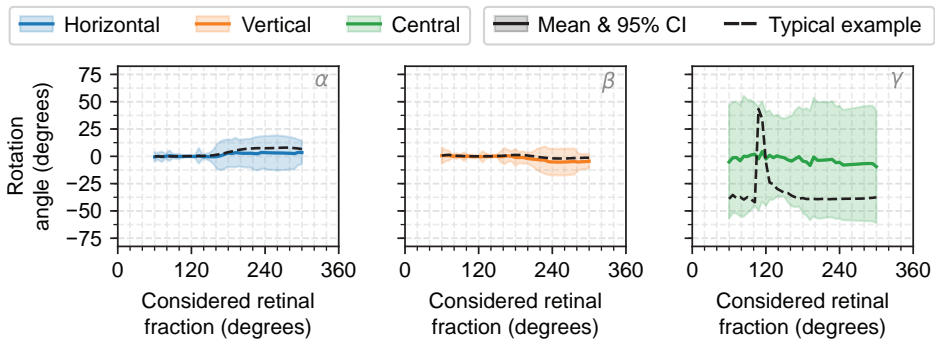
6.7 Supplementary data

Supplementary Table 6.1: 3D ellipsoid fitting results for the central and peripheral retina. All data is presented as mean \pm standard deviation.

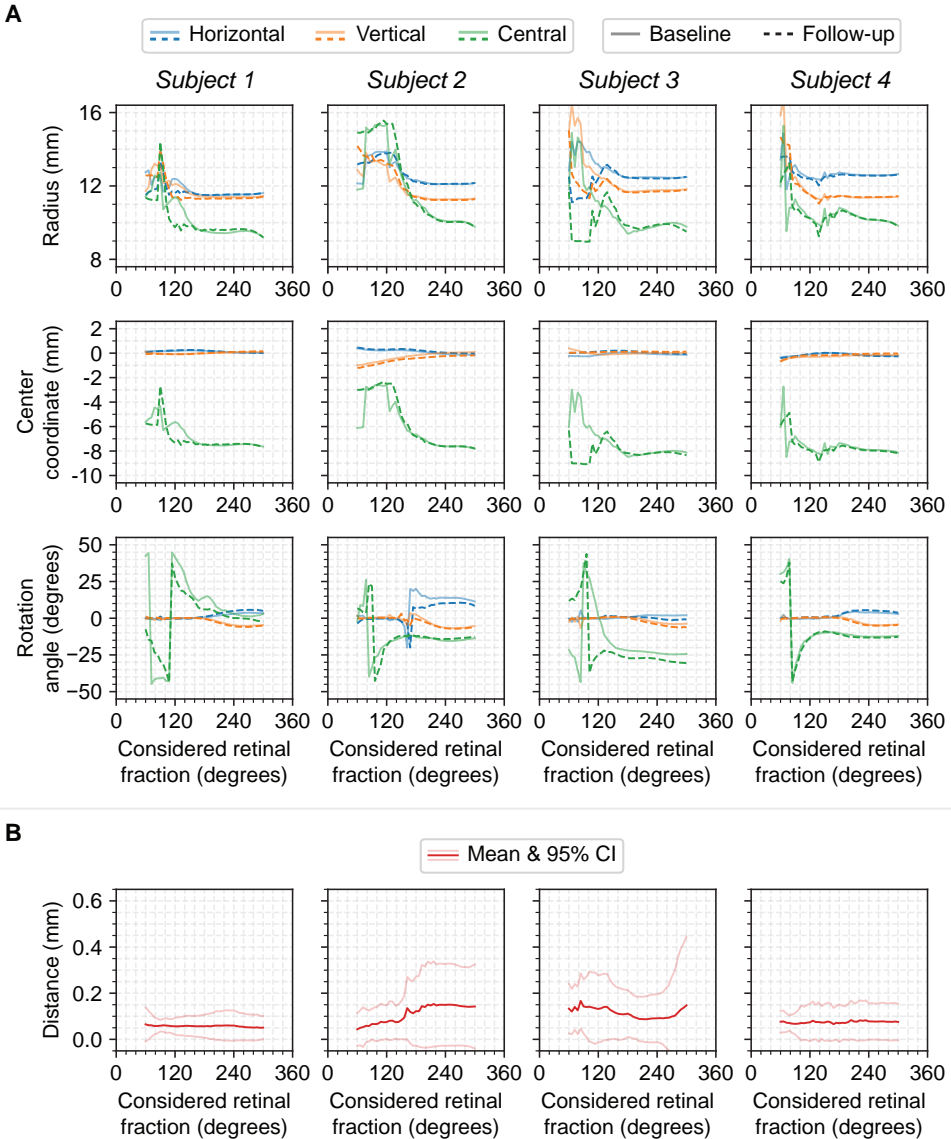
	Central retina	Peripheral retina
Distance		
Ellipsoid - retina (<i>mm</i>)	0.03 \pm 0.01	0.13 \pm 0.03
Radii		
R_h (<i>mm</i>)	12.9 \pm 0.9	11.9 \pm 0.6
R_v (<i>mm</i>)	13.7 \pm 1.5	11.6 \pm 0.4
R_c (<i>mm</i>)	12.2 \pm 1.2	10.4 \pm 0.7
Center coordinates[†]		
C_h (<i>mm</i>)	0.2 \pm 0.3	0.0 \pm 0.1
C_v (<i>mm</i>)	-0.1 \pm 0.5	0.0 \pm 0.1
C_c (<i>mm</i>)	-6.2 \pm 1.3	-8.0 \pm 0.5
Rotations[‡]		
α (<i>degrees</i>)	-0.5 \pm 2.0	3.4 \pm 7.7
β (<i>degrees</i>)	0.6 \pm 3.9	-5.2 \pm 6.2
γ (<i>degrees</i>)	-5.2 \pm 26.5	-5.5 \pm 26.3

[†] The center coordinates are given with respect to the crystalline lens center. A positive coordinate indicates a temporal, superior or anterior position.

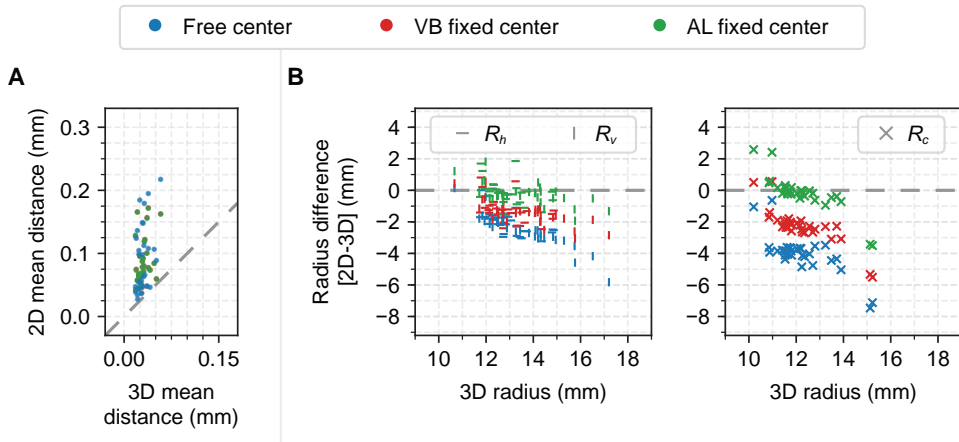
[‡] Rotations are defined as rotations around the ellipsoid center. A positive rotation indicates a downward, outward or endorotation of the ellipsoid.



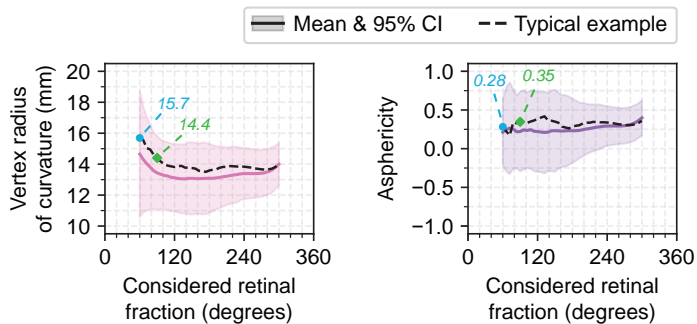
Supplementary Figure 6.2: 3D ellipsoid rotations around the principal axes. The results are displayed as function of the considered retinal contour fraction. For the rotations around the horizontal and vertical axis, the average and 95% CI remain close to 0 for every considered retinal fraction. The large variation for a rotation around the central axis is likely attributed to eyes with similar horizontal and vertical radii, making the fitted ellipsoid invariant to rotations around the central axis (Figure 6.4).



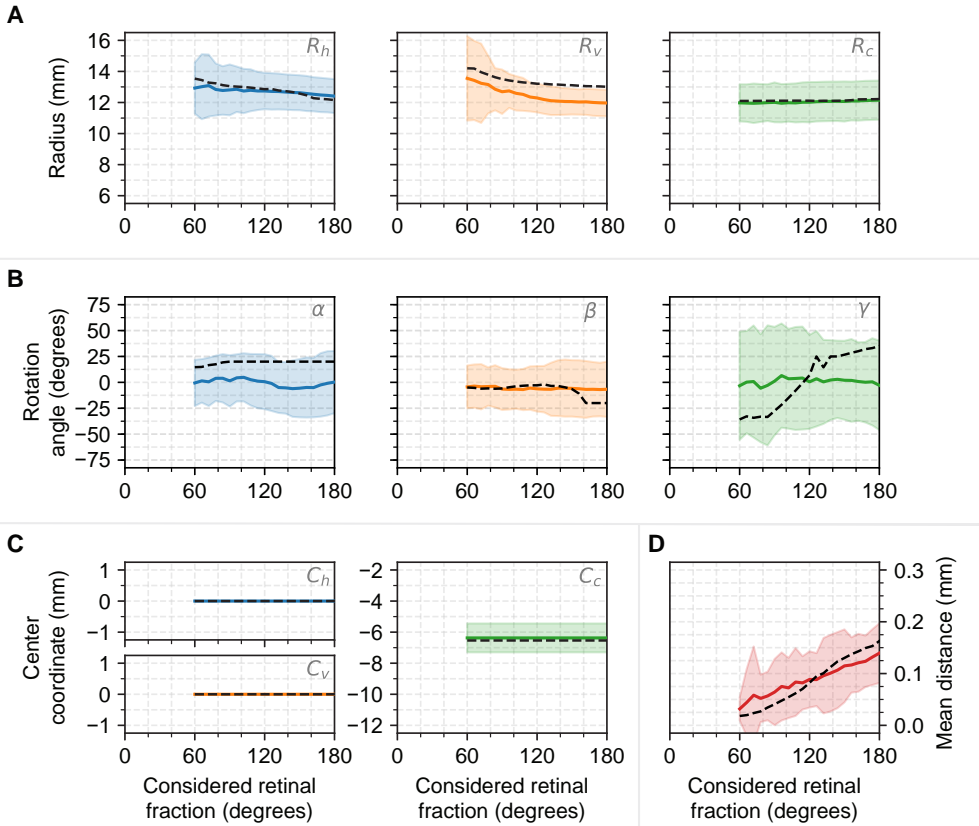
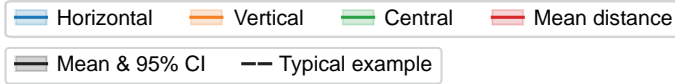
Supplementary Figure 6.3: Reproducibility analysis for the 3D ellipsoid fitting. A) Reproducibility of the ellipsoid parameters. Data of the baseline scan is depicted using continuous lines and data for the follow-up scans using dashed lines, both as a function of considered retinal contour fraction. Each column represents the analysis of one subject. Larger differences can be seen for smaller retinal fractions. B) Mean distance between both ellipses within the considered retinal fraction. The average distance remains relatively similar between smaller and larger retinal fractions, indicating that the changes in ellipsoid parameters between baseline and follow-up compensate each other and result in a similar ellipsoid shape within the evaluated fraction.



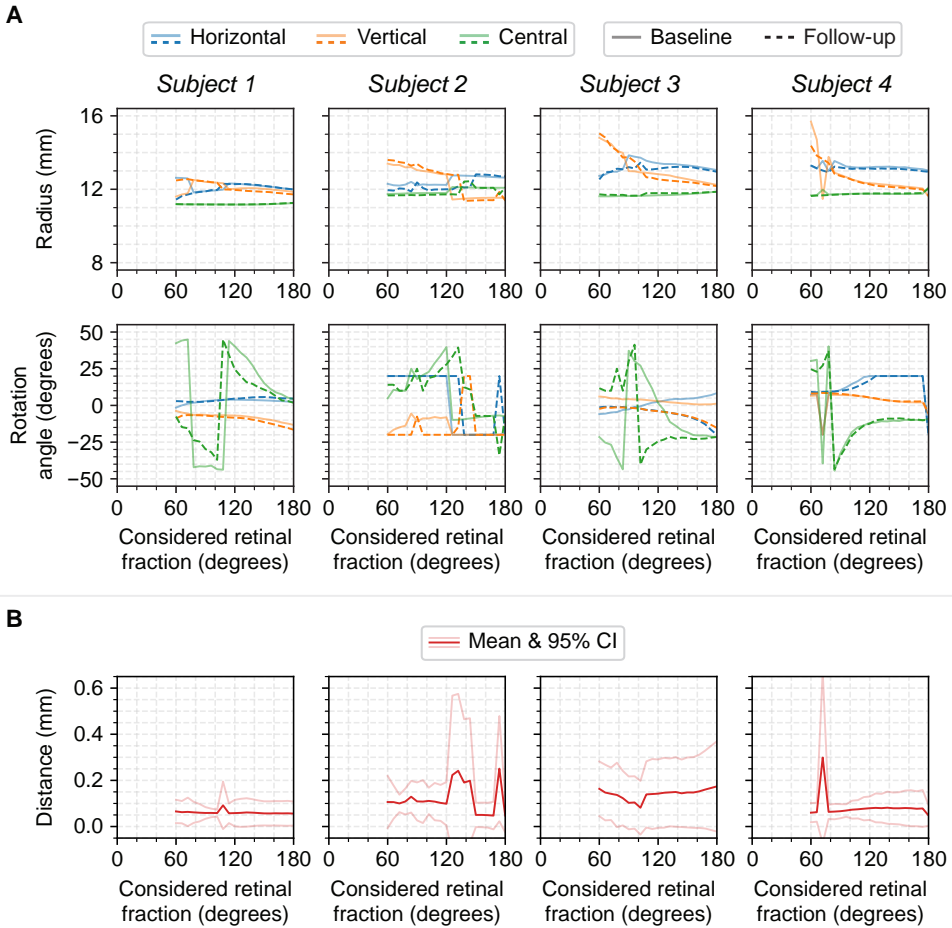
Supplementary Figure 6.4: Comparison between 2D-derived and 3D ellipsoids fitted to the central retina. Three different two 2D fitting methods are shown, one with a free center (blue), one with a vitreous body fixed center (red) and one with an axial length fixed center (green). A) Mean distance to the original 3D contour of the ellipsoid model based on the 3D and 2D fits. The 3D fits consistently provided a more accurate description. B) differences between the 3D and 2D determined ellipsoid radii of the ellipsoids as function of the 3D radii.



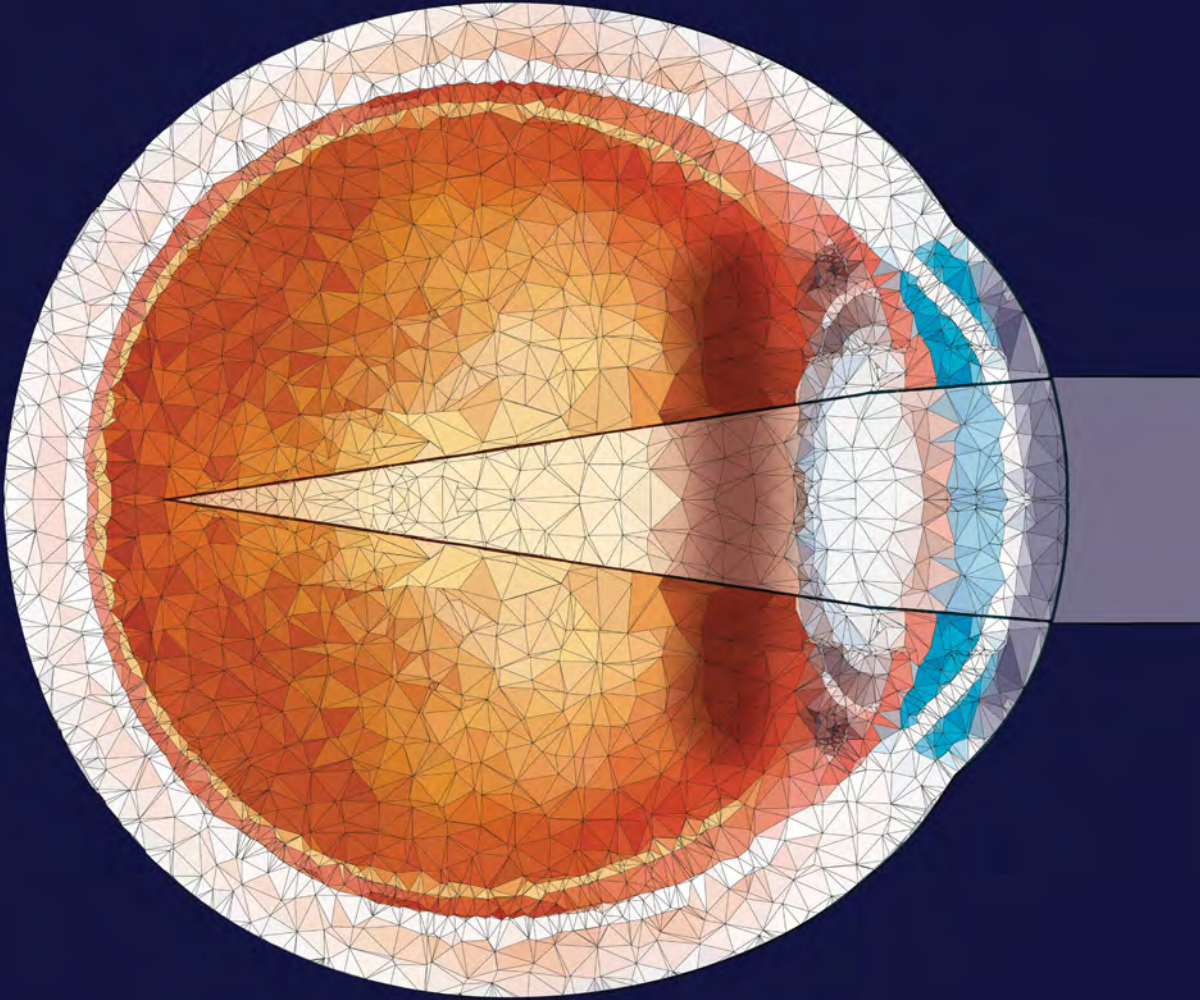
Supplementary Figure 6.5: 3D ellipsoid fitting results presented as vertex radius of curvature and asphericity as function of the retinal contour fraction. All results are given as function of the considered retinal contour fraction. The presented data are the average of the data calculated in the horizontal and vertical direction. For the typical subject, the magnitude of both parameters as determined over 60 (blue) and 90 (green) degrees of the retinal contour is annotated. The 1.3 mm decrease in vertex radius of curvature is accompanied by a 0.07 increase in asphericity, indicating that the smaller radius is compensated by a more oblate shape and highlighting the interdependence between both parameters.



Supplementary Figure 6.6: 3D ellipsoid fitting results for the central retina with the ellipsoid center fixed to half the axial length as function of the considered retinal contour fraction. A) The radii of the 3D ellipsoids. B) The rotations of the 3D ellipsoids. C) The center coordinates of the 3D ellipsoids, which are invariant as they are fixed. D) The mean distance between the resulting ellipsoid and the evaluated retinal contour.



Supplementary Figure 6.7: Reproducibility analysis for the 3D ellipsoid fitting of the central retina with the ellipsoid center fixed to half the axial length during the fitting. A) Reproducibility of the ellipsoid parameters. Data of the baseline scan is depicted using continuous lines and data for the follow-up scans using dashed lines, both as a function of considered retinal contour fraction. Each column represents the analysis of one subject. B) Mean distance between both ellipses within the considered retinal fraction. The average distance remains relatively similar between smaller and larger retinal fractions, indicating that the ellipsoids determined using the baseline and the follow-up scans are similar.



7

Peripheral visual field shifts after intraocular lens implantation

This chapter is published as:

L. van Vught, G.P.M. Luyten, J.W.M. Beenakker
Peripheral visual field shifts after intraocular lens implantation
Journal of Cataract & Refractive Surgery, 2023
DOI: 10.1097/j.jcrs.0000000000001299

Abstract

Purpose: To assess whether intraocular lens (IOL) implantation induces shifts in the peripheral visual field.

Setting: Department of Ophthalmology, Leiden University Medical Center, Leiden, the Netherlands.

Design: Ray tracing study.

Methods: Non-sequential ray tracing simulations were performed with phakic and pseudophakic versions of the same eye model to assess potential shifts in the visual field after IOL implantation. Two different IOL designs were evaluated and for each design 5 different axial positions and 7 different intrinsic powers were tested. The relation between the physical position of the light source and the location where the retina was illuminated was determined for each eye model. Subsequently, these relations were used to calculate whether the visual field shifts in pseudophakic eyes.

Results: The pseudophakic visual field shift was below 1 degree for central vision in all evaluated models. For peripheral vision, the light rays in the pseudophakic eyes were refracted to a more central retinal location compared to phakic eyes, resulting in a central shift of the peripheral visual field. The magnitude of the shift depended on the IOL design and its axial position, but could be as high as 5.4 degrees towards central vision.

Conclusion: IOL implantation tends to have little effect on the central visual field but can induce an over 5 degrees shift in the peripheral visual field. Such a shift can affect the perception of peripheral visual complaints.

7.1 Introduction

Ray tracing, a simulation method to study the path of light through the eye, is increasingly used to evaluate factors that affect the quality of vision. In pseudophakia, for example, it provides a method to assess how light rays are refracted or reflected by an intraocular lens (IOL), which revealed the origin of glare symptoms in positive dysphotopsia.¹ Another application of ray tracing is the evaluation of the peripheral vision, as clinical techniques to quantitatively assess this part of vision are limited. In negative dysphotopsia (ND), for example, ray tracing was used to develop the hypothesis that the bothering shadow that patients experience in the temporal visual could be caused by light rays passing between the IOL and iris.^{2,3} Later studies confirmed this hypothesis,⁴⁻⁶ and ray tracing subsequently contributed to the development of various treatments of this condition.^{7,8}

As with any simulation technique, special care needs to be taken that to assure that the outcomes of the calculations resemble the real-life quantity one is interested in. Therefore, different methods have been proposed to relate ray tracing outcomes to clinical metrics, such as wavefront aberrations,⁹ modulation transfer functions (MTF),¹⁰ and retinal illumination intensities.² Furthermore, different geometrical eye models have been developed to reproduce the optical characteristics of the general population,^{9,11} while others have incorporated distinct anatomical features of eyes with specific conditions, such as ND.^{6,7} In ray tracing simulations related to peripheral vision, however, one also needs to consider which segment of the retinal surface is used to see a specific part of the visual field. For this purpose, Simpson et al. determined the relation between the position of a light source, relative to the optical axis of their eye model, and the part of the retina which was illuminated.⁵ However, as in vivo the optical elements of the eye are not aligned along one axis,¹² van Vught et al. extended this approach by using the visual axis as a reference, thereby aiming to provide a more direct link to clinical measurements.⁶ Although these approaches aid the correlation of ray training analyses with measurements that use a fixation target as reference, such as peripheral aberrometry^{9,13,14} and perimetry,^{15,16} it does not necessarily reflect the spatial perception of a subject.

To closer match this spatial perception in ray tracing simulations, it is important to consider how the visual field is projected on the retina. For a phakic eye, it is known that the relation between the position of an object in visual field and the retinal image of that object is approximately linear for central visual field and non-linear for the peripheral visual field.^{17,18} Since an IOL refracts light rays differently than the approximately four times thicker crystalline lens,¹⁹ this relation might change when the crystalline lens is exchanged for an IOL. In turn, this change can potentially induce a shift in the peripheral visual field, which could affect how peripheral visual phenomena, such as negative dysphotopsia, are experienced by patients. Therefore, this study aims to evaluate whether IOL implantation induces shifts in the peripheral visual field.

7.2 Methods

The effect of IOL implantation on the peripheral visual field was assessed using ray tracing simulations with phakic and pseudophakic versions of the Escudero-Sanz eye model.¹¹ All simulations were performed in OpticStudio (version 20.3.2, Zemax LCC) through the ZOSPy package (version 0.6.1).^{6,20} A wavelength of 543 nm and corresponding refractive indices were used.¹¹

Two different IOL designs were used for the pseudophakic eye model. These IOL designs included a simple biconvex IOL and a biconvex IOL with a conical flange on the anterior surface that approximately matches the geometry of the ZCB00 IOL (Johnson & Johnson Vision), hereafter named respectively the biconvex IOL and the clinical IOL. Both IOLs had a refractive index of 1.47 and a power of 20 Diopter (D).^{6,21} The IOLs were positioned 4.51 mm posteriorly from the corneal endothelium (internal ACD) to create a distance of 1.46 mm between the anterior iris surface and anterior IOL, as reported in literature.²² The position of the iris was not adjusted between the phakic and pseudophakic eye models. The radius of curvature and conic constant of the posterior surface of both IOLs were chosen such that the defocus of the total eye with a 3.0 mm pupil diameter was equal to the phakic model.

Two additional sets of pseudophakic eye models were created to evaluate the potential impact of a different IOL location or power. In the first set, the ACD was adjusted by ± 0.31 mm (± 1 SD) and ± 0.62 mm (± 2 SD) while maintaining the same IOL geometry.²² In the second set, additional defocus of ± 1 D, ± 2 D and ± 3 D was induced in the eye model by altering the IOL power through modifications of the posterior IOL surface.

For each eye model, the relation between the position of a source object in the visual field and the corresponding retinal location was assessed using non-sequential ray tracing and a 6.0 mm pupil diameter. The position of the object in the visual field, hereafter called the visual field angle, was defined as the angle between the object, the center of the pupil and the optical axis through that center, omitting the influence of refraction induced by the cornea (Figure 7.1). The objects were positioned from central vision (visual field angle of 0 degrees) to peripheral vision (maximum visual field angle of 100 degrees) with steps of 1 degree. Each object emitted one ray of light aimed at the pupil center. For each ray the location where it illuminated the retina was determined, which was expressed as the angle with respect to the center of the retina (Figure 7.1).⁶

The relation between visual field angle and illuminated retinal location in the phakic eye model was used as a reference to determine exchanging the crystalline lens for an IOL would induce a shift in the visual field. To that end, the illuminated retinal locations of the pseudophakic eye were mapped onto the illuminated retinal locations of the phakic eye. Using that mapping, the illuminated retinal locations of the pseudophakic eye models were projected back into the phakic visual field. Subsequently, the difference between that projection and the actual source objects was calculated, providing the visual field shift (Figure 7.1B). Within this manuscript, a negative visual field shift indicates a shift towards central vision in pseudophakic eyes.

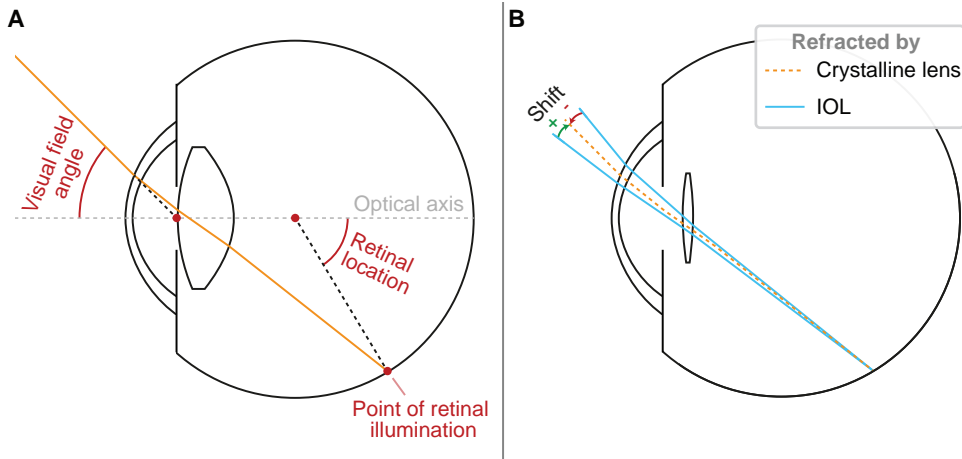


Figure 7.1: Definition of the visual field angle, retinal location and visual field shift. A) Definition the visual field angle, the angle between input ray, the optical axis, and the corresponding retinal location. B) For the pseudophakic subjects, the visual field shift is defined as the shift in the visual field that is required to illuminate the same retinal location in the phakic eye. This example shows both a positive and a negative shift. A positive shift indicates that the pseudophakic visual field is shifted towards peripheral vision and negative shift that it is shifted towards central vision. Note that the shift is exaggerated for illustration purposes.

7.3 Results

The relation between visual field angle and illuminated retinal location was similar in the phakic and pseudophakic eye models for the central visual field, with absolute differences below 1.0 degree for visual field angles up to 28 degrees (Figure 7.2). Over this range, the relationship between the visual field angle and the retinal location was nearly linear (all $R^2 \approx 1.00$), in which a 1.0-degree increase in visual field angle corresponded to a change in retinal location of 1.4 degrees.

Further into the peripheral visual field, larger differences in retinal location were apparent between the phakic and pseudophakic eye models. However, the results in the far periphery of certain eye models were affected by two distinct effects, light being refracted by the edge of the IOL and light missing the IOL. These effects only occurred in pseudophakic eye models in which the IOL was positioned further away from the iris than in the average eye, thereby creating a larger physical gap between the iris and the IOL. In the eye model with the biconvex IOL positioned with an internal ACD of 5.12 mm (+2 SD) for example, light rays originating from visual field angles between 74 and 79 degrees pass through the biconvex IOL edge or even completely miss the IOL (Figure 7.3). This resulted in abrupt changes in illuminated retinal location from 92 to 81 degrees and subsequently to 102 degrees.

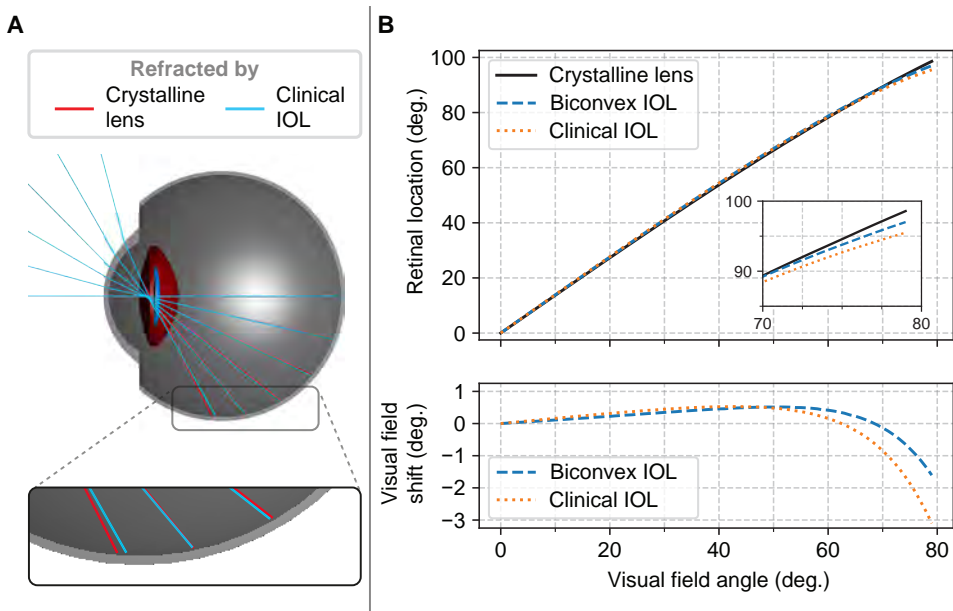


Figure 7.2: Visual field shift in pseudophakic eyes. A) Overlay of non-sequential ray tracing in phakic and pseudophakic eye models, showing that rays originating from large visual field angles are refracted relatively more towards the center of the retina by the clinical IOL (cyan rays) than by the crystalline lens (red rays). B) Simulation results for the phakic eye and the pseudophakic eyes with the IOL positioned such that it reflected to average position in the population. Top: The retinal location of illumination as function of visual field angle for the crystalline lens, the biconvex IOL and the clinical IOL. Bottom: the resulting visual field shift for both IOLs. A negative shift indicates a shift towards central vision.

For light rays passing through the posterior IOL surface, light originating from far peripheral visual field angles was refracted to a relatively more central retinal location by the IOL than by the crystalline lens in almost all pseudophakic eye models. The maximal shift in retinal location between the phakic and pseudophakic eye models was -5.5 degrees, which related to a -5.1 degrees shift of the visual field towards central vision. Some variation in the maximal visual field shift was present between the pseudophakic eye models (Figure 7.4). For the pseudophakic models with the IOL positioned such that it reflected the average position in the population, the maximum shift was -3 degrees with the clinical IOL and -1.5 degrees with the biconvex IOL (Figure 7.2B). Changing the axial location of the IOL affected the magnitude of the visual field shift for both IOL designs, although to a different extent. Overall, a more anteriorly located IOL resulted in a more peripheral visual field shift, with a maximum observed shift of +4.7 degrees toward peripheral at a visual field angle of 79 degrees (Figure 7.4A). Changing the axial location of the biconvex IOL towards posterior had little additional effect on the visual field shift, with an additional shift of less than 0.2 degrees. This change in axial location had a larger effect with the clinical IOL, with a maximal observed visual field shift of -5.4 degrees at a visual field angle of 76 degrees (Figure 7.4A). Changing the IOL power had a relatively small additional effect on the shift of both the central and peripheral visual field (Figure 7.4B). Overall, changing the IOL power to induce a defocus of up to ± 3 D shifted the visual field over a range of approximately 1.0 degrees with the biconvex IOL design and approximately 2.7 degrees with the clinical IOL design.

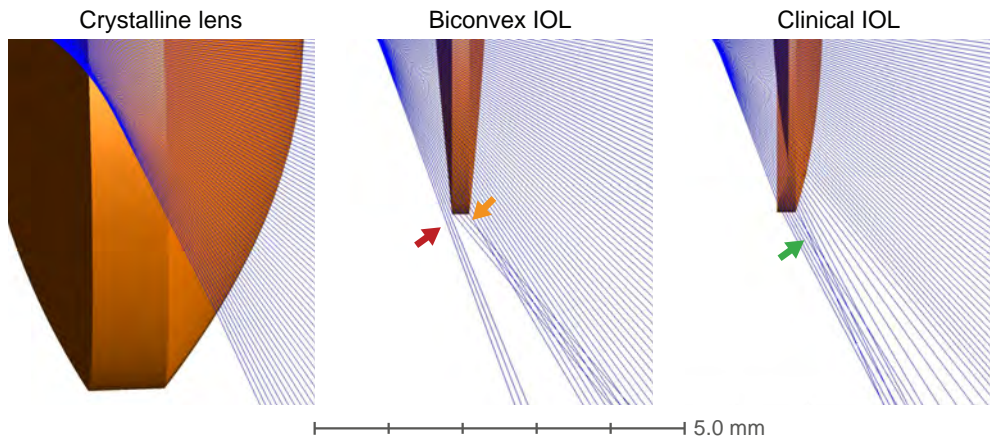


Figure 7.3: Refraction of peripheral rays of light by the crystalline lens and the IOLs. The displayed IOLs are axially positioned with an internal ACD of 5.12 mm (+2 SD). For the crystalline lens, all peripheral rays of light are refracted by the posterior lens surface. For the biconvex IOL, light originating from far peripheral visual field angles is refracted by the IOL edge rather than by the posterior IOL surface (orange arrow). The IOL edge refracts the light to a relatively more central retinal location. Light originating from even higher angles is not refracted by the IOL (red arrow). For the clinical IOL, the convex-concave anterior IOL surface generally results in a more continuous illumination of the peripheral retina, but some light rays are not refracted as expected (green arrow).

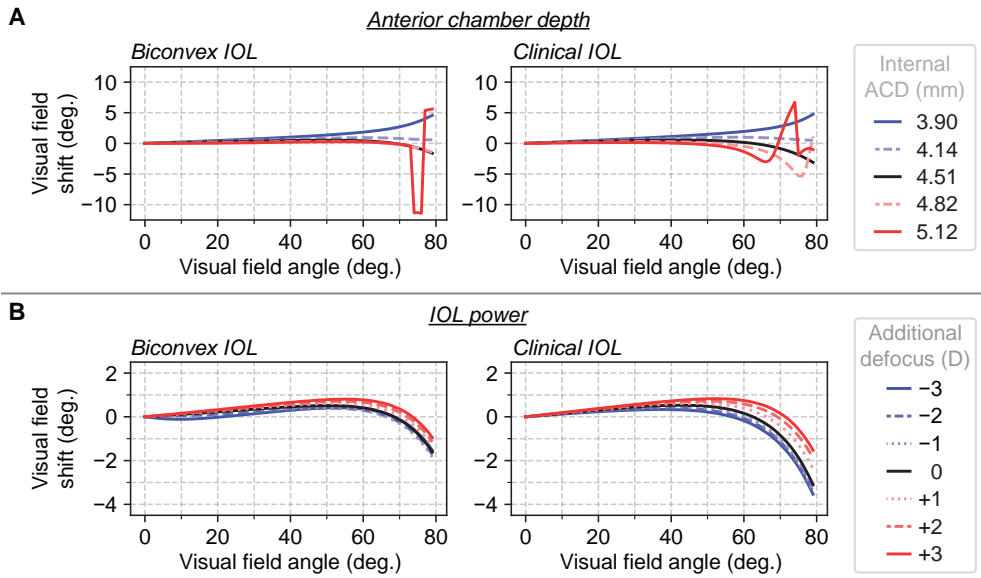


Figure 7.4: Effect of axial IOL position and IOL power on the visual field shift. A) Visual field shifts with the IOL positioned at various internal anterior chamber depths (ACD) for the biconvex IOL (left) and the clinical IOL (right). B) Visual field shifts with varying IOL power for the biconvex IOL (left) and the clinical IOL (right). Data is shown based on the additional defocus induced in the eye model by the new IOL power. A negative visual field shift corresponds to a shift towards central vision.

7.4 Discussion

This study evaluated whether the implantation of an IOL induces a shift in the visual field. The induced shifts were small for central vision up to visual field angles of approximately 30 degrees, with visual field shifts of 1 degree or less regardless of the axial position or IOL power. Stronger effects were apparent for the more peripheral visual field, where IOLs in specific configurations can induce an over 5 degrees shift in the visual field. The exact magnitude of the shift depended mainly on the design and axial position of the IOL (Figure 7.4).

These visual field shifts, especially the shifts toward central vision, can potentially affect how subjects experience peripheral optical phenomena. For example, perimetry measurements showed that the shadow experienced by pseudophakic patients with negative dysphotopsia might be measured between 70 and 75 degrees in the visual field using a kinetic perimeter.²³ The results of perimetry are quantified using the location of the light stimulus in the visual field, which corresponds to the visual field angle used in this paper. The results of this study show that this object space based annotation might not reflect the subject's experience as the light source could illuminate a more central or peripheral part of the retina than anticipated. For example, negative dysphotopsia measured between 70 and 75 degrees²³ can be experienced by the patient between 65 and 70 degrees, making it more noticeable and burdensome. In addition, at even higher visual field angles, a shift towards central vision could result in peripheral visual phenomena shifting onto the functional retina, and thereby becoming noticed by the subject. However, it is important to acknowledge that neuroadaptation might over time (partly) compensate for these visual field shifts.

Since the magnitude and direction visual field shift showed to be dependent on the design and axial position of the IOL, the shift will differ between subjects. These differences might explain why only a subset of patients experience peripheral visual complaints, and why treatments for these complaints, such as a piggyback IOL implantation or IOL-exchange,^{15,24–26} are effective in some, but not all patients. This effectiveness will however likely depend on the interplay between ocular anatomy and IOL design and therefore, the current results cannot directly be applied to an individual patient and a specific IOL design. Similarly, only one model of the crystalline lens was used although both its shape and refractive index varies in the population.^{27,28} However, additional simulations with varying lens shapes showed minimal, less than 0.5 degrees, changes in the results (Supplementary Figure 7.1).

Nonetheless, it is noteworthy that the shift in retinal illumination in the pseudophakic eye will directly affect the image size on the peripheral retina. The change from a slightly positive to a progressively more negative shift will result in a reduction of the image size. Such changes can directly affect clinical imaging of the peripheral retina, which can in turn affect treatments. For example, ultra-wide-field fundusoscopic images are used as an input in ocular radiotherapy planning,^{29,30} and such distortions could therefore result in errors in tumor definition.

As with any simulation study, some limitations should be considered when interpreting the results. Firstly, only one specific eye model and two types of IOLs were evaluated. It is however likely that the observed relation between visual field angle and location of retinal illumination will depend on the subject's biometry and corneal shape (Figure 7.2B).³¹

While there are inter-subject variations in those anatomical properties,³² these variations likely have a relatively minor impact on the observed visual field shifts, as these shifts are determined relative to the phakic state of the same eye. Furthermore, this study evaluated a small subset of the possible variations in IOL designs and properties. Although some design parameters, such as the posterior IOL shape, appeared to have little effect on the observed shifts, increasing the diameter of the optic is expected to have a more significant impact on far peripheral vision.^{8,33} Similarly a more different IOL geometry, such as the recently introduced meniscus shaped optic,³⁴ will likely have larger effects. Frosting the IOL edge, another common IOL property,³⁵ would induce a random scatter of rays that pass through the IOL edge resulting in a loss or relation to a specific retinal location.

Secondly, a rotationally symmetric model of the eye was used in these evaluations while it is known that the eye has a certain amount of asymmetry.¹³ The use of a population average shift of 5 degrees, related to the angle alpha, has been proposed,⁴ but care has to be taken when applying such a generic correction as the relevant ocular asymmetries can differ between groups of subjects.¹³ Furthermore, this correction would be based on the assumption that angle alpha is unaffected by the cataract surgery. While such a correction would change the visual field angle at which a certain visual field shift is experienced, the magnitude of this shift will also be unaffected.

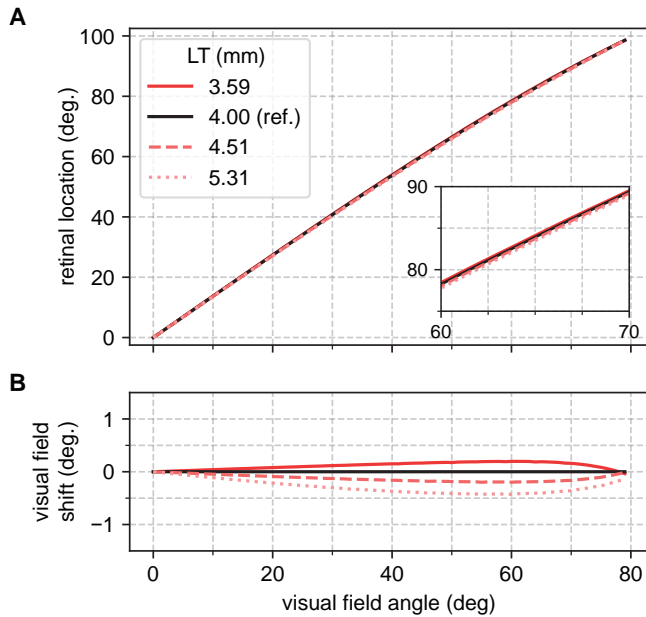
In conclusion, ray tracing showed that IOL implantation tends to induce little changes in the central visual field but could induce a peripheral visual field shift of over 5 degrees shift in the perceived peripheral eccentricities. These shifts should be taken into account when evaluating the peripheral vision of pseudophakic subjects through ray tracing simulations, as they can have a direct impact on the subject's perception.

7.5 References

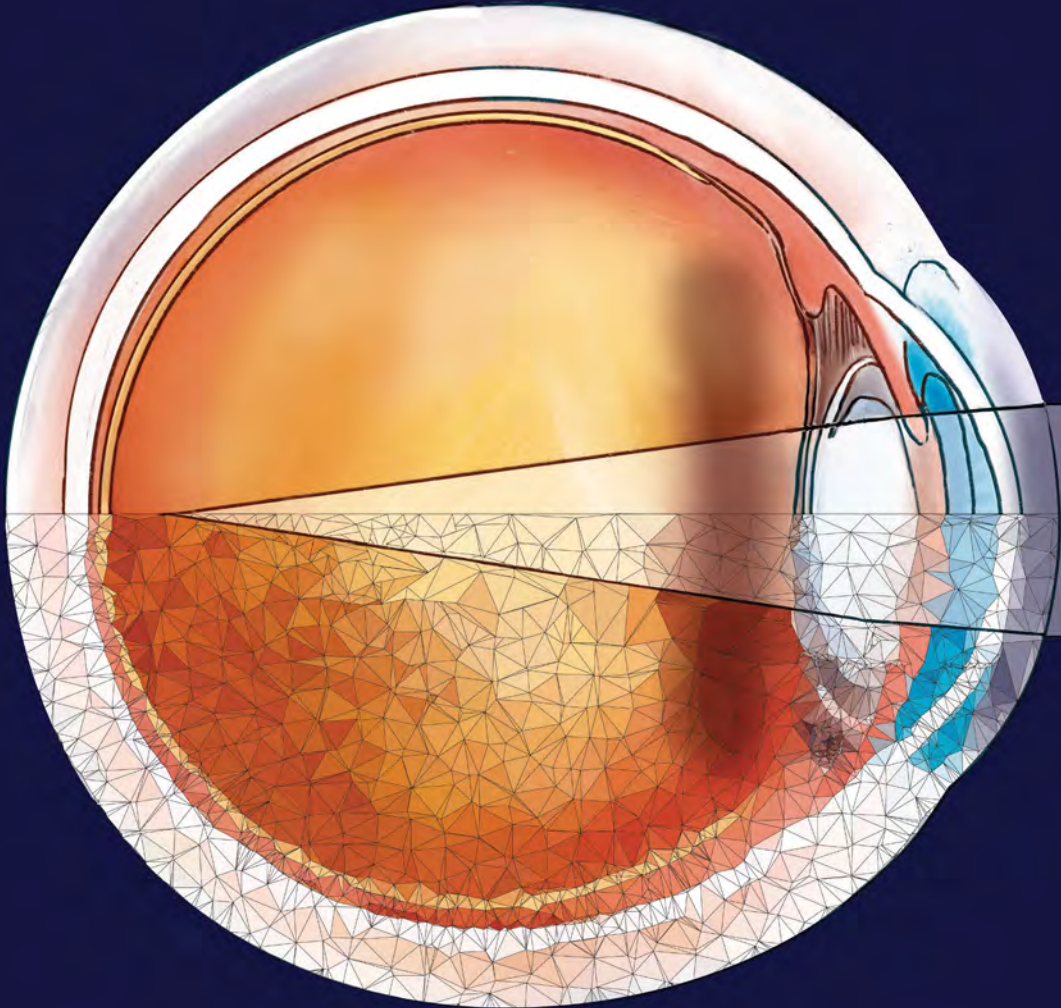
1. Erie JC, Bandhauer MH. Intraocular lens surfaces and their relationship to postoperative glare. *J Cataract Refract Surg.* 2003;29(2):336–41. doi: 10.1016/s0886-3350(02)01442-6.
2. Simpson MJ. Double image in far peripheral vision of pseudophakic eye as source of negative dysphotopsia. *J Opt Soc Am A Opt Image Sci Vis.* 2014;31(12):2642–9. doi: 10.1364/josaa.31.002642.
3. Holladay JT, Simpson MJ. Negative dysphotopsia: Causes and rationale for prevention and treatment. *J Cataract Refract Surg.* 2017;43(2):263–275. doi: 10.1016/j.jcrs.2016.11.049.
4. Simpson MJ. Simulated images of intraocular lens negative dysphotopsia and visual phenomena. *J Opt Soc Am A Opt Image Sci Vis.* 2019;36(4):B44–B51. doi: 10.1364/josaa.36.000b44.
5. Simpson MJ. Intraocular lens far peripheral vision: image detail and negative dysphotopsia. *J Cataract Refract Surg.* 2020;46(3):451–458. doi: 10.1097/j.jcrs.000000000000103.
6. Vught L van, Que I, Luyten GPM, Beenakker JWM. Effect of anatomical differences and intraocular lens design on negative dysphotopsia. *J Cataract Refract Surg.* 2022;48(12):1446–1452. doi: 10.1097/j.jcrs.0000000000001054.
7. Erie JC, Simpson MJ, Bandhauer MH. Effect of a sulcus-fixated piggyback intraocular lens on negative dysphotopsia: Ray-tracing analysis. *Journal of Cataract & Refractive Surgery.* 2019;45(4):443–450. doi: <https://doi.org/10.1016/j.jcrs.2018.10.041>.
8. Erie JC, Simpson MJ, Mahr MA. Effect of a 7.0 mm intraocular lens optic on peripheral retinal illumination with implications for negative dysphotopsia. *J Cataract Refract Surg.* 2022;48(1):95–99. doi: 10.1097/j.jcrs.0000000000000822.
9. Polans J, Jaeken B, McNabb RP, Artal P, Izatt JA. Wide-field optical model of the human eye with asymmetrically tilted and decentered lens that reproduces measured ocular aberrations. *Optica.* 2015;2(2):124–134. doi: 10.1364/optica.2.000124.
10. Canovas C, Artal P. Customized eye models for determining optimized intraocular lenses power. *Biomed Opt Express.* 2011;2(6):1649–62. doi: 10.1364/boe.2.001649.
11. Escudero-Sanz I, Navarro R. Off-axis aberrations of a wide-angle schematic eye model. *J Opt Soc Am A Opt Image Sci Vis.* 1999;16(8):1881–91. doi: 10.1364/josaa.16.001881.
12. Tabernero J, Benito A, Nourrit V, Artal P. Instrument for measuring the misalignments of ocular surfaces. *Optics Express.* 2006;14(22):10945–10956. doi: 10.1364/oe.14.010945.
13. Vught L van, Luyten GPM, Beenakker JWM. Distinct differences in anterior chamber configuration and peripheral aberrations in negative dysphotopsia. *J Cataract Refract Surg.* 2020;46(7):1007–1015. doi: 10.1097/j.jcrs.0000000000000206.
14. Jaeken B, Lundström L, Artal P. Fast scanning peripheral wave-front sensor for the human eye. *Opt Express.* 2011;19(8):7903–13. doi: 10.1364/oe.19.007903.
15. Makhotkina NY, Dugrain V, Purchase D, Berendschot T, Nuijts R. Effect of supplementary implantation of a sulcus-fixated intraocular lens in patients with negative dysphotopsia. *J Cataract Refract Surg.* 2018;44(2):209–218. doi: 10.1016/j.jcrs.2017.11.013.
16. Rozendal LRW, Vught L van, Luyten GPM, Beenakker JWM. The Value of Static Perimetry in the Diagnosis and Follow-up of Negative Dysphotopsia. *Optom Vis Sci.* 2022;99(8):645–651. doi: 10.1097/oxp.0000000000001918.
17. Drasdo N, Fowler CW. Non-linear projection of the retinal image in a wide-angle schematic eye. *Br J Ophthalmol.* 1974;58(8):709–14. doi: 10.1136/bjo.58.8.709.
18. Suheimat M, Zhu HF, Lambert A, Atchison DA. Relationship between retinal distance and object field angles for finite schematic eyes. *Ophthalmic Physiol Opt.* 2016;36(4):404–10. doi: 10.1111/opo.12284.
19. Jaeken B, Mirabet S, Marin JM, Artal P. Comparison of the optical image quality in the periphery of phakic and pseudophakic eyes. *Invest Ophthalmol Vis Sci.* 2013;54(5):3594–9. doi: 10.1167/iops.13-11956.
20. Vught L van, Beenakker JWM. ZOSPv. Computer Program. Version 0.6.1. 2021. doi: 10.5281/zenodo.5590764.
21. Johnson & Johnson Vision. *TECNIS® Monofocal 1-Piece IOL.* Accessed on: March 8, 2022. <https://www.jnjvisionpro.com/products/tecnis%C2%AE-1-piece-iol>.

22. Plat J, Hoa D, Mura F, Busetto T, Schneider C, Payerols A, Villain M, Daien V. Clinical and biometric determinants of actual lens position after cataract surgery. *J Cataract Refract Surg.* 2017;43(2):195–200. doi: 10.1016/j.jcrs.2016.11.043.
23. Makhotkina NY, Berendschot TT, Nuijts RM. Objective evaluation of negative dysphotopsia with Goldmann kinetic perimetry. *J Cataract Refract Surg.* 2016;42(11):1626–1633. doi: 10.1016/j.jcrs.2016.09.016.
24. Davison JA. Positive and negative dysphotopsia in patients with acrylic intraocular lenses. *J Cataract Refract Surg.* 2000;26(9):1346–55. doi: 10.1016/s0886-3350(00)00611-8.
25. Vamosi P, Csakany B, Nemeth J. Intraocular lens exchange in patients with negative dysphotopsia symptoms. *J Cataract Refract Surg.* 2010;36(3):418–24. doi: 10.1016/j.jcrs.2009.10.035.
26. Taubenslag KJ, Groos EB, Parker MG, Ewald MD, Pilkinton RD. Successful treatment of negative dysphotopsia with in-the-bag intraocular lens exchange using a wide ovoid IOL. *J Cataract Refract Surg.* 2016;42(2):336–7. doi: 10.1016/j.jcrs.2016.01.012.
27. Meng J, Wei L, He W, Qi J, Lu Y, Zhu X. Lens thickness and associated ocular biometric factors among cataract patients in Shanghai. *Eye Vis (Lond).* 2021;8(1):22. doi: 10.1186/s40662-021-00245-3.
28. Uhlhorn SR, Borja D, Manns F, Parel JM. Refractive index measurement of the isolated crystalline lens using optical coherence tomography. *Vision Research.* 2008;48(27):2732–2738. doi: <https://doi.org/10.1016/j.visres.2008.09.010>.
29. Fantaguzzi F, Servillo A, Sacconi R, Tombolini B, Bandello F, Querques G. Comparison of peripheral extension, acquisition time, and image chromaticity of Optos, Clarus, and EIDON systems. *Graefes Arch Clin Exp Ophthalmol.* 2022. doi: 10.1007/s00417-022-05923-z.
30. Wulff J, Koska B, Heufelder J, Janson M, Backer CM, Siregar H, Behrends C, Baumer C, Foerster A, Bechrakis NE, Timmermann B. Commissioning and validation of a novel commercial TPS for ocular proton therapy. *Med Phys.* 2023;50(1):365–379. doi: 10.1002/mp.16006.
31. Hastings GD, Banks MS, Roorda A. Radial and Tangential Retinal Magnifications as Functions of Visual Field Angle Across Spherical, Oblate, and Prolate Retinal Profiles. *Transl Vis Sci Technol.* 2022;11(9):10. doi: 10.1167/tvst.11.9.10.
32. Vught L van, Shamonin DP, Luyten GPM, Stoel BC, Beenakker JWM. MRI-based 3D retinal shape determination. *BMJ Open Ophthalmol.* 2021;6(1):e000855. doi: 10.1136/bmjophth-2021-000855.
33. Bonsemeyer MK, Becker E, Liekfeld A. Dysphotopsia and functional quality of vision after implantation of an intraocular lens with a 7.0 mm optic and plate haptic design. *J Cataract Refract Surg.* 2022;48(1):75–82. doi: 10.1097/j.jcrs.0000000000000735.
34. Villegas EA, Marin JM, Ginis H, Robles C, Alcon E, Hervella L, Prieto PM, Tana-Rivero P, Artal P. Peripheral Refraction and Contrast Detection Sensitivity in Pseudophakic Patients Implanted With a New Meniscus Intraocular Lens. *J Refract Surg.* 2022;38(4):229–234. doi: 10.3928/1081597x-20220113-01.
35. Meacock WR, Spalton DJ, Khan S. The effect of texturing the intraocular lens edge on postoperative glare symptoms: a randomized, prospective, double-masked study. *Arch Ophthalmol.* 2002;120(10):1294–8. doi: 10.1001/archophth.120.10.1294.

7.6 Supplementary data



Supplementary Figure 7.1: Illuminated retinal location and visual field angle with different crystalline lens models. Three additional crystalline lens models have been analyzed using ray tracing. These lenses had a center thickness of respectively 3.59, 4.51 and 5.31 mm,²⁸ and were compared to the results of the original crystalline lens with lens thickness of 4.00 mm. The anterior surface of the additional lenses was solved such that the central refraction with a 3.0 mm pupil matched the central refraction of the originally used phakic model. A) Illuminated retinal location as function of visual field angle for all tested crystalline lenses, showing minimal differences. B) Visual field difference with respect to the original crystalline lens, showing minimal differences of <0.5 degrees for every other evaluated crystalline lens model. LT = lens thickness, deg. = degrees, ref. = reference.



8

Effect of anatomical differences and intraocular lens design on negative dysphotopsia

This chapter is published as:

L. van Vught, I. Que, G.P.M. Luyten, J.W.M. Beenakker
**Effect of anatomical differences and intraocular
lens design on negative dysphotopsia**
Journal of Cataract & Refractive Surgery, 2022
DOI: 10.1097/j.jcrs.0000000000001054

Abstract

Purpose: To assess the effect of ocular anatomy and intraocular lens (IOL) design on negative dysphotopsia.

Setting: Department of Ophthalmology, Leiden University Medical Center, Leiden, the Netherlands.

Design: Ray tracing study based on clinical data.

Methods: Ray tracing simulations were performed to assess the effect of anatomical differences and differences in IOL design on the peripheral retinal illumination. To that end, eye models that incorporate clinically measured anatomical differences between eyes of patients with negative dysphotopsia (ND) and eyes of pseudophakic controls were created. The anatomical differences included pupil size, pupil centration and iris tilt. The simulations were performed with different IOL designs, including a simple biconvex IOL design and a more complex clinical IOL design with a convex-concave anterior surface. Both IOL designs were analyzed using a clear edge as well as a frosted edge. As ND is generally considered to be caused by a discontinuity in peripheral retinal illumination, this illumination profile was determined for each eye model and the severity of the discontinuity was compared between eye models.

Results: The peripheral retinal illumination consistently showed a more severe discontinuity in illumination with ND-specific anatomy. This difference was the least pronounced, 8%, with the frosted edge clinical IOL and the most pronounced, 18%, with the clear edge biconvex IOL.

Conclusion: These results show that small differences in the ocular anatomy or IOL design affect the peripheral retinal illumination. Therewith, they can increase the severity of ND by up to 18%.

8.1 Introduction

Negative dysphotopsia (ND) is a relatively common complaint after cataract surgery or refractive lens exchange with intraocular lens (IOL) implantation, often described as a shadow or missing area in the temporal peripheral visual field.¹⁻³ The incidence is reported to be up to 19% when actively evaluated during clinical follow-up, but fortunately in most cases it resolves over time.^{4,5} However, complaints remain present in approximately 3% of the patients with little chance on further improvement.⁵ The severity of the remaining shadow differs between patients, leaving some patients with mild visual field defects while others experience bothersome complaints that disturb their daily life.^{3,6} Clinical studies have identified multiple factors that potentially contribute to ND, including a smaller pupil size,^{3,6-8} a tilted anterior chamber geometry,⁷ a larger overlap of the anterior capsule,^{3,6,8,9} an increased angle kappa,⁷ a non-inferotemporal orientation of the optic-haptic junction of the IOL,¹⁰ and a smaller IOL diameter.¹¹ While ND can occur with different types of in-the-bag implanted IOLs, it has not been reported with anterior chamber IOLs or sulcus-fixated IOLs.⁸ One of the major problems in the clinical evaluation of ND is the lack of methods to objectively quantify this far-peripheral visual complaint. Thus far, only Goldmann perimetry has been able to show the loss of peripheral vision in some, but not all, eyes.¹²

To overcome this lack of objective measurements and to obtain additional insight, multiple ray tracing studies of ND have been performed. Within these studies, the path of light through the eye is calculated. Based on these studies, it is proposed that ND is caused by a gap in the illumination of the nasal retina, which is then experienced as a shadow in the temporal visual field.^{2,13-15} These simulations showed that this gap is the result of a discontinuity between light passing between the iris and IOL (the iris-IOL gap) and light refracted by the IOL. Many factors that potentially affect this gap have been proposed through these simulations, including a larger angle kappa,¹³ a smaller pupil diameter,^{13,16} the axial distance between the IOL and the iris,¹³ the refractive index, the diameter of the IOL and the shape of the IOL.^{13,16,17}

While these ray tracing simulations have provided valuable insights in potential causes of ND, they used generic eye models that do not fully reflect the anatomy of eyes with ND. Recently, we presented clinical data of a cohort of pseudophakic eyes with and without ND, showing that eyes with ND have a smaller and more temporally decentered pupil as well as a larger temporal tilt of the iris (Figure 8.1).⁷ Furthermore, we showed that the anterior chamber distance, the distance between the iris and the IOL, and the peripheral retinal shape were comparable between both groups.^{7,18} Within this study, we aim to assess the optical consequences of the anatomical differences observed in the ND population as well as the effect of different IOL designs on the peripheral illumination, in particular related to the temporal shadow that is perceived by ND patients.

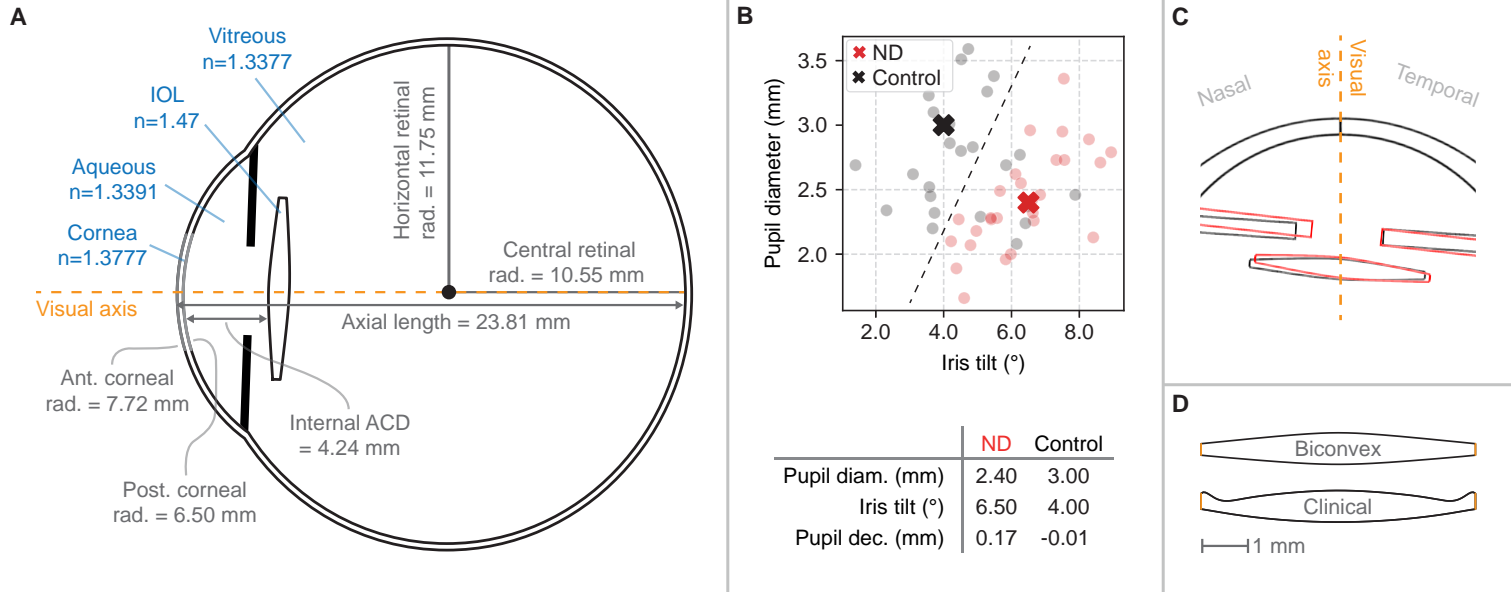


Figure 8.1: Eye model specifications. A) Schematic view of the eye model including principal model specifications. B) Anterior chamber geometry of patients with ND (red) and pseudophakic controls (black). Actual values used for the eye models are given in the table and annotated in the plot using crosses. C) Detailed overview of the anterior chamber anatomy of patients with ND (red) and pseudophakic controls (black). D) Schematic view of the biconvex (upper) and clinical (lower) IOL model. The edge of the IOL (orange) were defined as either a clear edge or an edge with Lambertian scattering.

8.2 Methods

To accurately assess the relation between anatomical properties of the eye and the occurrence of ND, ray tracing simulations were performed using eye models that closely reflect the actual ocular anatomy of eyes with and without ND. Based on the reported clinical differences between eyes with and without ND,^{7,18} two eye models were designed, one with a typical anatomy for patients with ND and one with a typical anatomy for pseudophakic controls (Figure 8.1). The anatomical aspects of these eye models were derived from clinical measurements obtained from 37 patients with ND and 26 pseudophakic controls who participated in the ESCRS vRESPOND study (CCMO-registry number: NL58358.058.16). Prior to participation, all subjects provided written informed consent. The study was performed in conformance with the tenets of the Declaration of Helsinki and was approved by the local Medical Ethics Committee.

Model design

Simulations were performed in OpticStudio (version 20.3.2, Zemax LCC) using a highly modified version of the Escudero-Sanz eye model and a 543 nm light source (Figure 8.1).¹⁹ The entire process of constructing eye models and performing the non-sequential ray tracing simulations was fully automated through the OpticStudio API and Python (version 3.7) using the open source ZOSPy package.²⁰ The resulting ND eye model and control eye model, both with a biconvex IOL, are available in the supplementary information (Supplemental Data available at <https://github.com/MREYE-LUMC/ZOSPy/tree/main/examples>).

To correspond to the clinical measurements and to reflect the subject's perception, the eye models were constructed relative to the visual axis, instead of to the more commonly used, but clinically less relevant, optical axis. The anatomical properties of the eye that have shown to be significantly different between patients with ND and pseudophakic controls, including iris tilt, pupil centration and pupil diameter,⁷ were adjusted in each model (Figure 8.1B). All other anatomical properties were based on either the average of both groups combined or to the values reported by Escudero-Sanz et al. (Figure 8.1A).^{7,18,19}

As the average corneal shape did not differ significantly between patients with ND and pseudophakic controls,⁷ the corneal shape of the Escudero-Sanz eye model eye was used.¹⁹ The anterior corneal surface was modeled as an ellipsoidal surface with a radius of 7.72 mm and a conic constant of -0.26, while for its posterior surface a radius of 6.50 mm without conic component was used.¹⁹ The central thickness of the cornea was 0.55 mm, and its refractive index was modelled as 1.3777.¹⁹ The refractive indices of the anterior chamber and vitreous body were defined as 1.3391 and 1.3377 respectively.¹⁹

As the anterior chamber depth (ACD) and iris-IOL distance were found to be similar in patients with ND and pseudophakic controls,^{7,18} a common distance of 3.12 mm between the posterior corneal surface and the anterior iris surface was used for both groups. Furthermore, the iris thickness was 0.55 mm,²¹ and the pupil edges were sloping inward towards the center.²² To match the clinically measured differences in iris orientation and pupil location and size, the iris was tilted temporally by 6.5 degrees in the ND model and 4.0 degrees in the control model. Furthermore, the pupil diameter was defined as 2.4 mm in the ND model and 3.0 mm in the control model. Finally, the pupil center of the ND model was moved 0.17 mm temporally with respect to the visual axis, while the pupil center of the control model was shifted 0.01 mm nasally.⁷

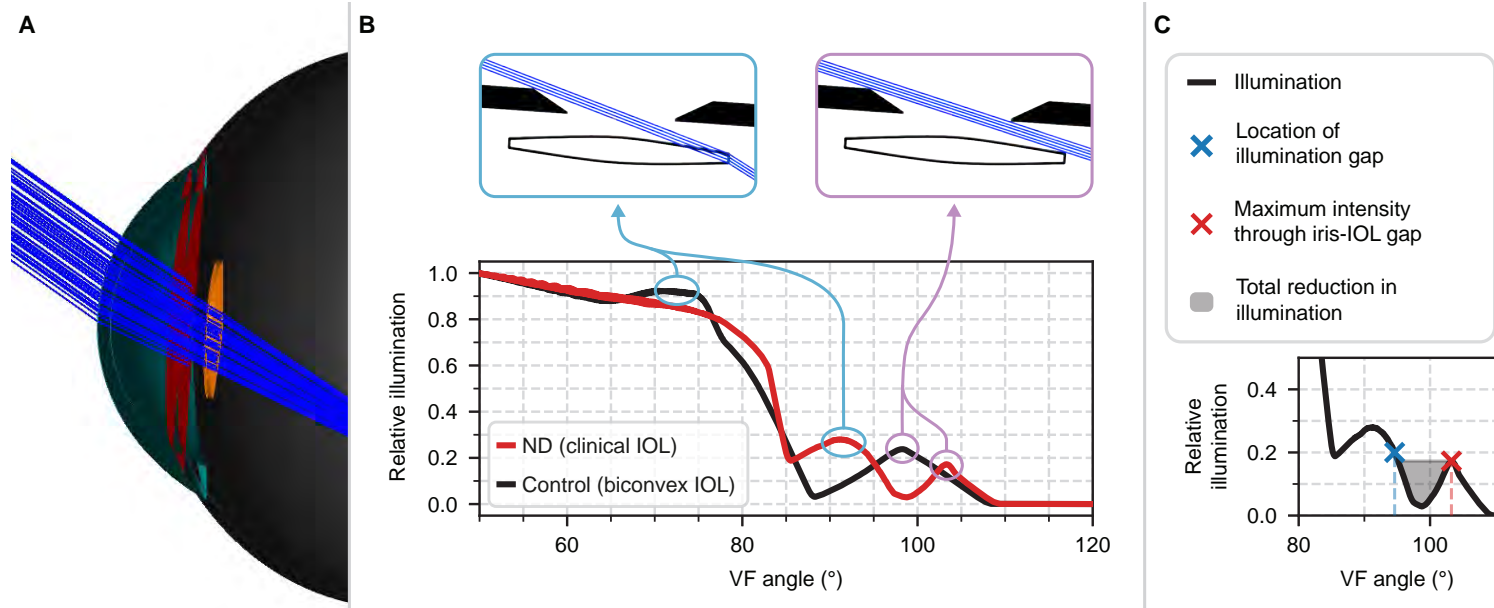


Figure 8.2: Examples of the total retinal illumination profile. A) Example of a 3D eye model illuminated by a peripheral beam of light. B) Breakdown of the total peripheral retinal illumination as function of the visual field (VF) angle for the ND model with a clinical IOL (red) and the control model with biconvex clinical IOL (black). The contributions of rays passing through the IOL edge (light blue circles, left insert) and those passing through the iris-IOL gap (light purple circles, right insert) show distinct differences between IOL designs. Discontinuities in peripheral illumination are visible at approximately 88 and 98 degrees. With the clinical IOL, this gap is partially filled by rays passing through the IOL edge. C) Example of quantification of the discontinuity in peripheral retinal illumination. VF = visual field.

As ND has been reported to occur with a wide variety of posterior chamber IOL designs,^{7,8} each eye model was analyzed with four different IOL designs (Figure 8.1C). The first design consisted of a simple biconvex IOL design, similar to those used in earlier ray tracing studies.^{2,13,16} In reality, however, IOLs often have a more complex design.²³ Therefore, the second design matched the convex-concave anterior surface and convex posterior surface of the ZCB00 IOL (Johnson & Johnson vision),²⁴ as obtained through μ CT scanning (Supplementary Figure 8.1). Clinically, the shape of the edge differs between IOLs,^{25,26} and some IOLs have a frosted edge that is intended to scatter incident rays.^{24,27} Unfortunately, the optical characteristics, including the edge shape and scattering properties, are not available for most IOLs. As the μ CT-images showed the edge of the clinical IOL to be straight, this was used as a reference to model the edges of both IOLs. Additionally, the ray tracing study by Franchini et al. suggests the maximum scattering of a frosted IOL edge to be 17.5%.²⁸ To assess the effect of a frosted edge, the edge of each IOL was thus modeled as both a 0% and a 17.5% Lambertian scattering surface (Figure 8.1C). All IOLs had a refractive index of 1.47 and the distance between the posterior iris surface and the IOL was 0.57 mm for all IOLs.¹⁸ The IOLs were positioned parallel to the (tilted) iris and centered on the pupil center.¹⁸

As the peripheral retinal shape did not significantly differ between patients with ND and controls, a common ellipsoid model was used to describe the retina, with a horizontal and vertical radius of 11.75 mm and a central radius of 10.55 mm (Figure 8.1A).^{18,29} The axial length of both models was 23.81 mm, reflecting the average of the study population.¹⁸

Peripheral retinal illumination

The peripheral retinal illumination was assessed using a 4.0 mm wide circular light source that emitted 10^5 parallel rays of light. This source rotated from visual field angles of -10 degrees nasally to 120 degrees temporally in 0.25 degree steps. The retinal surface consisted of detectors with a resolution of 0.1 degree horizontally by 0.1 mm vertically. The location of each detector was expressed as its angle with respect to the visual axis and retinal center. Similar to the study of Simpson,²² a separate set of simulations was performed to relate the location of each detector to the visual field angle experienced by the subject (Supplementary Figure 8.2). The illumination profiles of all visual field input angles were summed to obtain the total retinal illumination profile (Figure 8.2). As pupil diameters differ between models, all results were normalized to the total illumination perceived at 50 degrees temporally in the visual field.

To determine which image features corresponded to rays passing through the iris-IOL gap or through the IOL edge, separate simulations were performed in which these specific rays were isolated from the other rays (Figure 8.2B).

Quantification

Three aspects of the peripheral retinal illumination were quantified (Figure 8.2C). First, the start of the retinal illumination gap, defined as the visual field angle with a relative retinal illumination below 0.2, was determined. Additionally, the maximum intensity of the rays passing through the iris-IOL gap was determined, together with the corresponding visual field angle. Finally, the severity of the retinal illumination gap, defined as the total reduction in relative illumination compared to the maximum intensity of the rays passing through the iris-IOL gap, was calculated.

8.3 Results

All eye models were successfully simulated and analyzed. An example of a resulting eye model is shown in Figure 8.2A. The central spherical equivalent of refraction of the eye models ranged from -1.2 to +0.5 Diopter. All models showed an approximately equal relation between retinal angle and perceived visual field angle. The same relation was therefore used for all models, approximated by a second order polynomial:

$$\alpha_{VF} = \frac{1.1 * 10^{-3}}{\text{degree}} \alpha_R^2 - 0.60 \alpha_R + 0.17 \text{ degree} \quad (8.1)$$

with α_{VF} being the apparent visual field angle and α_R the retinal angle, both in degrees (Supplementary Figure 8.2).

In all eye models, the simulations showed a similar gradually decreasing illumination towards peripheral vision. At a visual field angle of 50 degrees, the angle used as a normalisation reference for subsequent evaluations, the control model received a 1.5 times higher illumination than the ND model, reflecting the smaller pupil size in the ND population. The reference illumination did not differ between the studied IOLs. A strong decrease in illumination was observed starting at approximately 80 degrees (Figure 8.3), which was partially caused by rays passing through the IOL edge instead of through the posterior IOL surface, and partially by vignetting of the iris. The profile of this decrease and the visual field angle at which it occurred depended strongly on IOL design. An area of low illumination, the retinal illumination gap, was observed. This area was followed by a local increase in illumination that was the result of rays passing through the iris-IOL gap. A complete overview of the contribution of rays passing through specific intraocular structures is provided in Figure 8.4 and summarized in Figure 8.2B.

Differences in peripheral retinal illumination were clearly visible between IOL designs (Figure 8.3) and were predominantly induced by rays passing through the IOL edge (Figure 8.4).

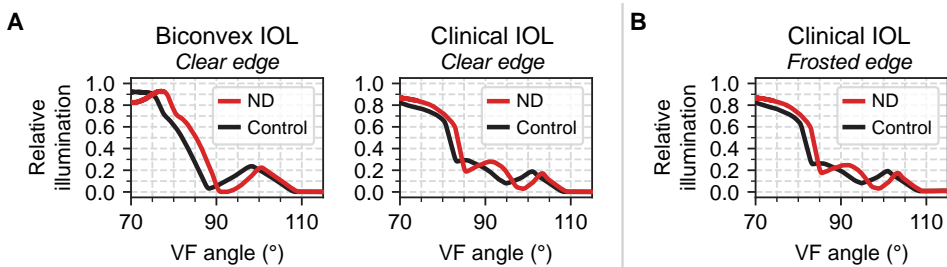


Figure 8.3: Peripheral retinal illumination. Normalized retinal illumination profiles for the ND model (red) and the control model (black). A) Illumination with a clear edge design. Clear differences between the biconvex and clinical IOL are visible, primarily caused an increase in illumination at a visual field angle of approximately 90 degrees with the clinical IOL. This increase is attributed to rays passing through the IOL edge (Figure 8.4) that partially fill the illumination gap. B) The illumination profile of a clinical IOL with a frosted edge design shows slight differences in the maximum intensity around a visual field angles of 90 degrees as the rays through the edge of the IOL are partially dispersed by the frosted edge. Data for the biconvex IOL with a frosted edge showed similar profile compared to the clear edge design and are shown in Figure 8.4. VF = visual field.

For the biconvex IOL with a clear edge, the relative illumination decreased below 0.2 between visual field angles of 85 and 90 degrees (Table 8.1) and rays passing through the edge induced a local increase in illumination at a visual field angle of approximately 75 degrees (Figure 8.3). For the clinical IOL design, however, the relative illumination decreased below 0.2 between 90 and 95 degrees (Table 8.1) and the local increase in illumination caused by rays passing through the edge was observed at approximately 90 degrees. Additionally, part of these rays illuminated the illumination gap, resulting in a lower depth of the shadow (Figure 8.3). With a frosted IOL edge, the rays were dispersed over the peripheral retina for both IOL designs. This dispersion had an insignificant effect on the peripheral illumination profile of the biconvex IOL design and a small effect on the peripheral illumination profile of the clinical IOL design, reducing the visual field angle at which the relative illumination decreased below 0.2 by approximately 1 degree (Figure 8.3, Table 8.1).

The far peripheral illumination, caused by light passing through the iris-IOL gap, differed between IOL designs. Overall, the visual field angle at which light started passing through this gap was about 2 degrees lower in the control models. Additionally, approximately 1.9 times more light rays passed through the iris-IOL gap in simulations with the biconvex IOL model than in simulations with the clinical IOL model. Furthermore, the number of light rays passing through the iris-IOL gap was 2.4 times higher with the control models compared to the ND models.

For all IOL designs, a more severe shadow was observed in the ND model. For the biconvex IOL with a clear edge design, the severity was 18% higher in the ND model compared to the control model. A similar increase in shadow severity was observed with the clinical IOL, where the reduction in illumination was 15% stronger in the ND model. For the biconvex IOL, the simulations with the frosted edge did not differ from those with a clear edge. For the clinical IOL design, however, a frosted edge reduced the shadow severity from 15% to 8% (Figure 8.3B, Table 8.1).

Table 8.1: Quantification of the peripheral illumination gap. The apparent visual angle at which the illumination decreases below 0.2 and the angle of maximum illumination through the iris-IOL gap are given for all models. The shadow severity in ND is expressed as % difference with the corresponding control model. The models with ND consistently showed a more severe shadow compared to their equivalent control models. ND = negative dysphotopsia, Con = control.

	Biconvex IOL <i>Clear edge</i>		Clinical IOL <i>Clear edge</i>		Biconvex IOL <i>Frosted edge</i>		Clinical IOL <i>Frosted edge</i>	
	ND	Con	ND	Con	ND	Con	ND	Con
Location of illumination gap (° visual field angle)	89	86	95	91	89	86	94	90
Location of maximal illumination through iris-IOL gap (° visual field angle)	101	98	103	101	101	98	103	101
Shadow severity (% difference with control)	18	—	15	—	17	—	8	—

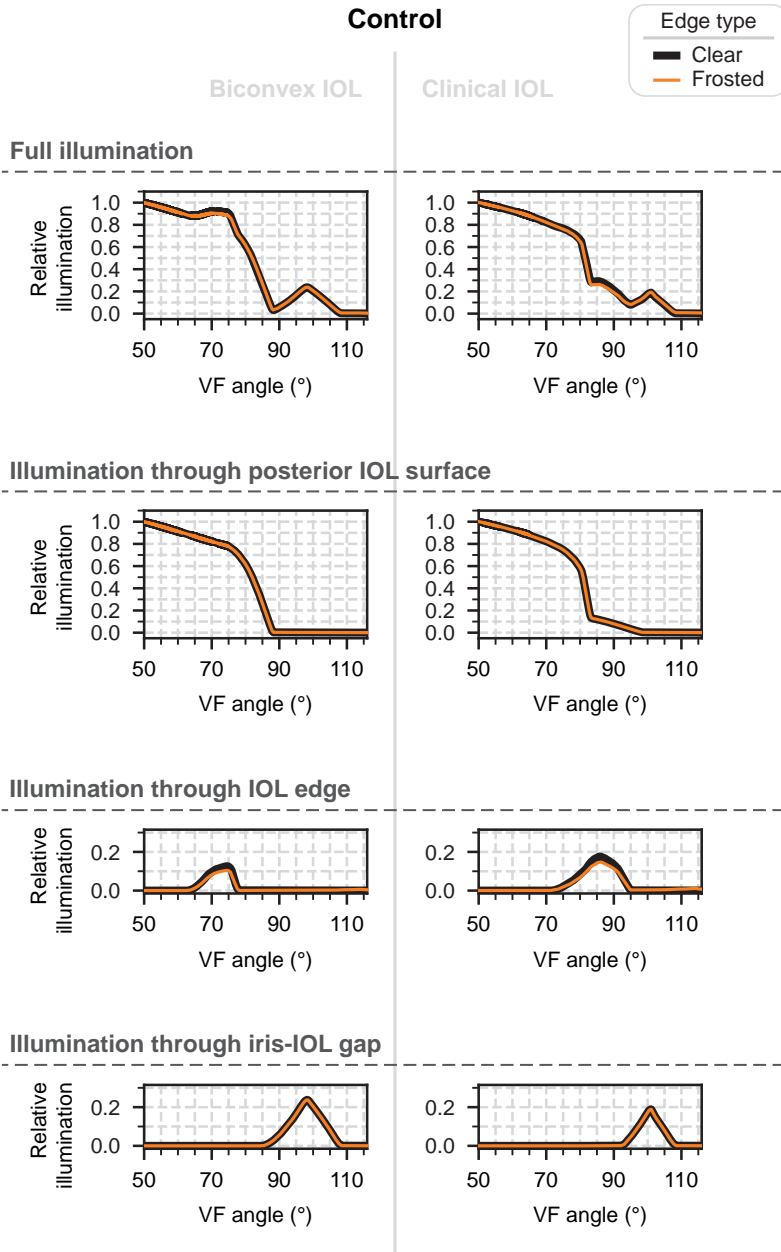


Figure 8.4: The influence of specific sets of rays on the peripheral illumination profile. Data is shown for the control (left page) and ND (right page), as well as for the biconvex IOL (left column) and clinical IOL (right column), both with a clear edge design (black) and a frosted edge design (cyan). The complete illumination, illumination by rays through the posterior IOL surface, illumination by rays through the IOL edge and illumination by rays through the iris-IOL gap is shown. Local increases in illumination can clearly be seen for rays passing through the IOL edge and rays passing through the iris-IOL gap. VF = visual field.

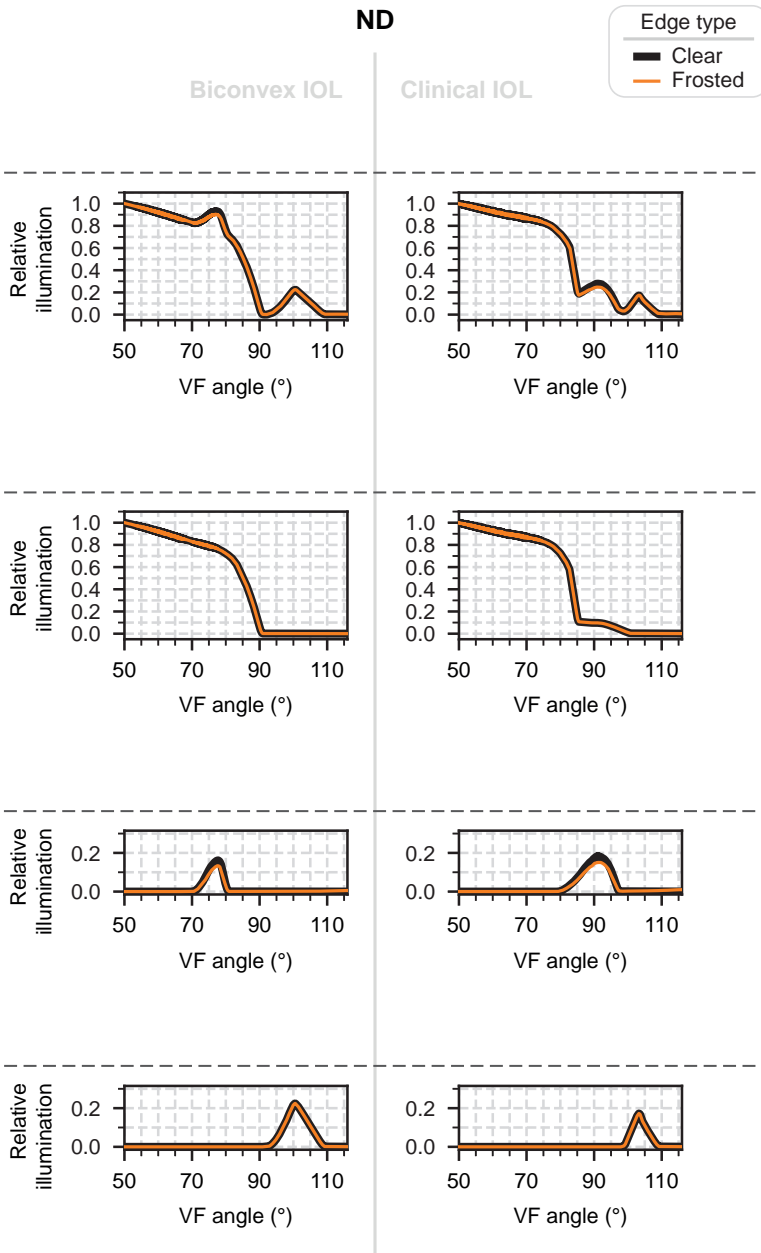


Figure 8.4 (cont.)

8.4 Discussion

Within this study, we demonstrated that ND-related anatomical differences can decrease the peripheral retinal illumination. Additionally, we showed the effects of IOL design on the retinal illumination profile. Combined, they can increase the severity of a shadow-like area on the peripheral retina by an up to 18%. These results strengthen the common assumption^{13,15,16} that ND is related to an illumination gap of the peripheral retina, as proposed by Holladay and Simpson.^{13,15,16} Furthermore, we introduced several new improvements to the conventional ray tracing methods which aim provide a more realistic assessment of the optics in a specific patient population as well as a better relation between the results and clinical measurements.

As the results from any simulation study depend strongly on the used model, clinically measured anatomical differences in pupil diameter and iris tilt were incorporated in the eye models. Although some studies have already assessed the effect of specific anatomical variations of a generic eye model,^{13,16} the clinical value of these studies was generally limited as they did not incorporate the ocular anatomy that is specific for ND patients. Additionally, more realistic IOL designs were included in the evaluations. However, even though the clinical IOL design was based on μ CT-data of the ZCB00 IOL, the exact design of the IOL was not known. As the study showed a direct relation between IOL edge design and peripheral illumination profile, additional information on the edge curvature and type of frosting could further improve the accuracy of the simulations.^{23,28} As the μ CT-images (Supplementary Figure 8.1) do not show any curvature at the IOL edge, a curved edge such as used for the Clareon CNA0T0 IOL,²³ is not expected. A different scattering profile could, however, strongly affect the peripheral retinal illumination, as shown by additional simulations with a 100% Lambertian scattering edge (Supplementary Figure 8.3). Nonetheless, such high scattering coefficients have not been reported for IOLs.²⁸

In this study, the visual axis, instead of the more conventional optical axis, was used as reference axis for the eye model. This allows for a better correlation between simulations, patient's vision and clinical measurements, as the latter two are determined relative to the visual axis.¹² To this end, the relation between retinal location and visual field angle was determined. Although an extrapolated relation was used for visual field angles above 78 degrees, we do not expect this to affect the study results as the scaling proved to be the same for the studied models.

Another difference with most earlier ray tracing studies is the use of non-sequential instead of sequential ray tracing.^{15,16,22} In sequential ray tracing, rays of light are assumed to pass through all defined surfaces sequentially. Although this assumption allows for many powerful analyses, such as the determination of the ocular aberration profile,^{7,19,30,31} these analyses are erroneous when light rays miss an optical element, which is one of the proposed origins of ND. The use of non-sequential ray tracing can explain the differences between the presented retinal illumination profiles and the profiles of earlier sequential studies,¹⁶ which appear to miss the contribution of light rays passing through the edge of the IOL (Supplementary Figure 8.2). However, ray aiming, an OpticStudio feature which assures that the complete pupil is illuminated, is not available for non-sequential ray tracing. This limitation was resolved by using a relatively large input beam diameter of 4.0 mm, which assures the complete illumination of the pupil at high input angles.

This study showed that the incorporation of relevant clinical differences in the eye model have a direct effect on the peripheral vision, as it resulted in an up to 18% increase of the peripheral illumination gap and other differences in the peripheral illumination. In the ND eye model with a frosted edge clinical IOL design, for example, the peripheral illumination profile shows a large area of low illumination, in contrast to the smaller area with a total absence of illumination which was observed with the clear edge biconvex IOL used in earlier studies.^{16,22} These differences might explain why some patients describe ND as completely missing a part of the temporal visual field, while others describe it as a shade.¹²

In the peripheral illumination of the pseudophakic control model, an area of decreased illumination was also observed. Although it is less pronounced than in the corresponding ND models, this finding was unexpected as these subjects did not report any ND-related complaints. It was furthermore unexpected that the decrease in peripheral illumination was the least pronounced with the frosted edge clinical IOL design, as the clinical IOL on which the model was based is reported to cause ND in some patients.^{7,24} However, the identified 8% difference might still be sufficient to experience ND and more research on the relation with the experienced shadow is required, especially since additional simulations with a higher degree of scattering seem to further reduce severity of ND (Supplementary Figure 8.3, Supplementary Table 8.1).

This unexpected observation might also show the necessity to fully personalize the ray tracing models, so they can be directly related to the subjects' visual perception. For central vision, such simulations have been proposed.³² For the far peripheral vision, these simulations are of higher complexity, especially since photoreceptor density and extend of the functional retina likely differ between subjects.^{14,33} However, these assessments might contribute to the understanding of why the illumination gap observed in the control population, although less severe, is not perceived as a burdensome temporal shadow.

This study showed the effect of IOL design on the peripheral illumination profile, in particular on the light passing through the iris-IOL gap. These differences might explain why certain surgical interventions, such as IOL exchange with a wide optic IOL or orienting the haptics horizontally upon IOL implantation,^{10,11,34} can resolve ND by interacting with the iris-IOL gap. However, the analyses presented in this study only evaluated a subset of the possible IOL design choices, which for example also include the refractive index, edge thickness and position with respect to the pupil. Future studies will therefore likely require detailed modeling of the implanted IOL, as these optical effect of all these factors interact with each other and this study shows that even small changes have a direct impact on the peripheral illumination profile.

Similarly, as small variations in the ocular anatomy of an individual patient can influence the peripheral illumination profile,^{7,30,31,35} a one-size-fits-all solution for ND is unlikely and probably requires full personalization of the eye model. An extension of the current analyses, including wide optic IOLs, piggyback IOL implantation or variation in IOL haptics orientation,^{10,11,17,36} might therefore aid to determine which treatment is optimal for a specific ocular anatomy. To that end, the eye models have been made available online (Supplemental data available at <https://github.com/MREYE-LUMC/ZOSPpy/tree/main/examples>) and the ZOSPpy package, used to automate the design and evaluation of the eye models in OpticStudio, has been published open source.²⁰

In conclusion, this research demonstrates that clinically observed differences in the ocular anatomy of ND patients have a strong, up to 18%, effect in the severity of the discontinuation of peripheral retinal illumination. It furthermore demonstrated the impact of the IOL design on this peripheral shadow.

8.5 References

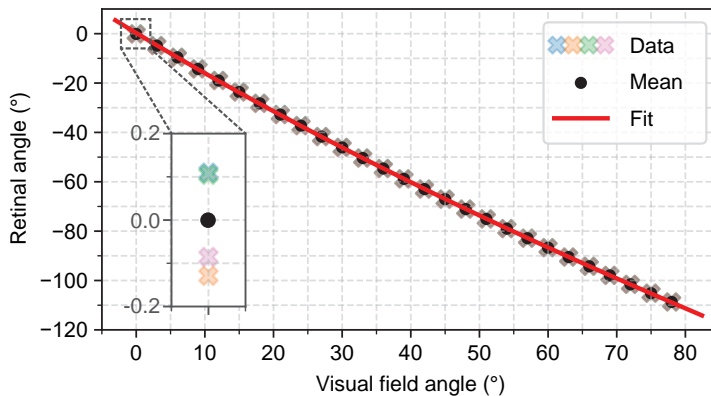
1. Davison JA. Positive and negative dysphotopsia in patients with acrylic intraocular lenses. *J Cataract Refract Surg.* 2000;26(9):1346–55. doi: 10.1016/s0886-3350(00)00611-8.
2. Holladay JT, Zhao H, Reisin CR. Negative dysphotopsia: the enigmatic penumbra. *J Cataract Refract Surg.* 2012;38(7):1251–65. doi: 10.1016/j.jcrs.2012.01.032.
3. Masket S, Fram NR. Pseudophakic Dysphotopsia: Review of Incidence, Cause, and Treatment of Positive and Negative Dysphotopsia. *Ophthalmology.* 2021;128(11):e195–e205. doi: 10.1016/j.ophtha.2020.08.009.
4. Makhotkina NY, Nijkamp MD, Berendschot T, Borne B van den, Nuijts R. Effect of active evaluation on the detection of negative dysphotopsia after sequential cataract surgery: discrepancy between incidences of unsolicited and solicited complaints. *Acta Ophthalmol.* 2018;96(1):81–87. doi: 10.1111/aos.13508.
5. Osher RH. Negative dysphotopsia: long-term study and possible explanation for transient symptoms. *J Cataract Refract Surg.* 2008;34(10):1699–707. doi: 10.1016/j.jcrs.2008.06.026.
6. Henderson BA, Geneva I. Negative dysphotopsia: A perfect storm. *J Cataract Refract Surg.* 2015;41(10):2291–312. doi: 10.1016/j.jcrs.2015.09.002.
7. Vught L van, Luyten GPM, Beenakker JWM. Distinct differences in anterior chamber configuration and peripheral aberrations in negative dysphotopsia. *J Cataract Refract Surg.* 2020;46(7):1007–1015. doi: 10.1097/j.jcrs.0000000000000206.
8. Masket S, Fram NR. Pseudophakic negative dysphotopsia: Surgical management and new theory of etiology. *J Cataract Refract Surg.* 2011;37(7):1199–207. doi: 10.1016/j.jcrs.2011.02.022.
9. Folden DV. Neodymium:YAG laser anterior capsulectomy: surgical option in the management of negative dysphotopsia. *J Cataract Refract Surg.* 2013;39(7):1110–5. doi: 10.1016/j.jcrs.2013.04.015.
10. Henderson BA, Yi DH, Constantine JB, Geneva I. New preventative approach for negative dysphotopsia. *J Cataract Refract Surg.* 2016;42(10):1449–1455. doi: 10.1016/j.jcrs.2016.08.020.
11. Bonsemeyer MK, Becker E, Liekfeld A. Dysphotopsia and functional quality of vision after implantation of an intraocular lens with a 7.0 mm optic and plate haptic design. *J Cataract Refract Surg.* 2022;48(1):75–82. doi: 10.1097/j.jcrs.0000000000000735.
12. Makhotkina NY, Berendschot TT, Nuijts RM. Objective evaluation of negative dysphotopsia with Goldmann kinetic perimetry. *J Cataract Refract Surg.* 2016;42(11):1626–1633. doi: 10.1016/j.jcrs.2016.09.016.
13. Holladay JT, Simpson MJ. Negative dysphotopsia: Causes and rationale for prevention and treatment. *J Cataract Refract Surg.* 2017;43(2):263–275. doi: 10.1016/j.jcrs.2016.11.049.
14. Simpson MJ. Mini-review: Far peripheral vision. *Vision Res.* 2017;140:96–105. doi: 10.1016/j.visres.2017.08.001.
15. Simpson MJ. Double image in far peripheral vision of pseudophakic eye as source of negative dysphotopsia. *J Opt Soc Am A Opt Image Sci Vis.* 2014;31(12):2642–9. doi: 10.1364/josaa.31.002642.
16. Simpson MJ. Simulated images of intraocular lens negative dysphotopsia and visual phenomena. *J Opt Soc Am A Opt Image Sci Vis.* 2019;36(4):B44–B51. doi: 10.1364/josaa.36.000b44.
17. Erie JC, Simpson MJ, Mahr MA. Effect of a 7.0 mm intraocular lens optic on peripheral retinal illumination with implications for negative dysphotopsia. *J Cataract Refract Surg.* 2022;48(1):95–99. doi: 10.1097/j.jcrs.0000000000000822.
18. Vught L van, Dekker CE, Stoel BC, Luyten GPM, Beenakker JWM. Evaluation of intraocular lens position and retinal shape in negative dysphotopsia using high-resolution magnetic resonance imaging. *J Cataract Refract Surg.* 2021;47(8):1032–1038. doi: 10.1097/j.jcrs.0000000000000576.
19. Escudero-Sanz I, Navarro R. Off-axis aberrations of a wide-angle schematic eye model. *J Opt Soc Am A Opt Image Sci Vis.* 1999;16(8):1881–91. doi: 10.1364/josaa.16.001881.
20. Vught L van, Beenakker JWM. ZOSPy. Computer Program. Version 0.5.1. 2021. doi: 10.5281/zenodo.5590764.
21. Invernizzi A, Cigada M, Savoldi L, Cavuto S, Fontana L, Cimino L. In vivo analysis of the iris thickness by spectral domain optical coherence tomography. *Br J Ophthalmol.* 2014;98(9):1245–9. doi: 10.1136/bjophthalmol-2013-304481.
22. Simpson MJ. Intraocular lens far peripheral vision: image detail and negative dysphotopsia. *J Cataract Refract Surg.* 2020;46(3):451–458. doi: 10.1097/j.jcrs.0000000000000103.

23. Das KK, Werner L, Collins S, Hong X. In vitro and schematic model eye assessment of glare or positive dysphotopsia-type photic phenomena: Comparison of a new material IOL to other monofocal IOLs. *J Cataract Refract Surg.* 2019;45(2):219–227. doi: 10.1016/j.jcrs.2018.09.017.
24. Johnson & Johnson Vision. *TECNIS® Monofocal 1-Piece IOL.* Accessed on: March 8, 2022. <https://www.jnjvisionpro.com/products/tecnis%C2%AE-1-piece-iol>.
25. Nanavaty MA, Spalton DJ, Boyce J, Brain A, Marshall J. Edge profile of commercially available square-edged intraocular lenses. *J Cataract Refract Surg.* 2008;34(4):677–86. doi: 10.1016/j.jcrs.2007.12.024.
26. Nanavaty MA, Zukaite I, Salvage J. Edge profile of commercially available square-edged intraocular lenses: Part 2. *J Cataract Refract Surg.* 2019;45(6):847–853. doi: 10.1016/j.jcrs.2018.12.004.
27. Bausch & Lomb Incorporated. *enVista IOL.* Accessed on: March 8, 2022. <https://www.bausch.com/ecp/our-products/cataract-surgery/lens-systems/envista-iol>.
28. Franchini A, Gallarati BZ, Vaccari E. Analysis of stray-light effects related to intraocular lens edge design. *J Cataract Refract Surg.* 2004;30(7):1531–6. doi: 10.1016/j.jcrs.2003.10.020.
29. Vught L van, Shamonin DP, Luyten GPM, Stoel BC, Beenakker JWM. MRI-based 3D retinal shape determination. *BMJ Open Ophthalmol.* 2021;6(1):e000855. doi: 10.1136/bmjophth-2021-000855.
30. Canovas C, Abenza S, Alcon E, Villegas EA, Marin JM, Artal P. Effect of corneal aberrations on intraocular lens power calculations. *J Cataract Refract Surg.* 2012;38(8):1325–32. doi: 10.1016/j.jcrs.2012.03.033.
31. Canovas C, Artal P. Customized eye models for determining optimized intraocular lenses power. *Biomed Opt Express.* 2011;2(6):1649–62. doi: 10.1364/boe.2.001649.
32. Tabernero J, Piers P, Benito A, Redondo M, Artal P. Predicting the optical performance of eyes implanted with IOLs to correct spherical aberration. *Invest Ophthalmol Vis Sci.* 2006;47(10):4651–8. doi: 10.1167/iovs.06-0444.
33. Song H, Chui TY, Zhong Z, Elsner AE, Burns SA. Variation of cone photoreceptor packing density with retinal eccentricity and age. *Invest Ophthalmol Vis Sci.* 2011;52(10):7376–84. doi: 10.1167/iovs.11-7199.
34. Rozendal L, Vught L van, Beenakker J, Luyten G. “Clinical outcomes of bag-to-bag intraocular lens exchange with a wide optic lens for the treatment of dysphotopsia (Conference abstract)”. In: vol. 99. *Aacta Ophthalmologica.* Pp. 43–43.
35. Atchison DA, Pritchard N, Schmid KL, Scott DH, Jones CE, Pope JM. Shape of the retinal surface in emmetropia and myopia. *Invest Ophthalmol Vis Sci.* 2005;46(8):2698–707. doi: 10.1167/iovs.04-1506.
36. Makhotkina NY, Berendschot TT, Beckers HJ, Nuijts RM. Treatment of negative dysphotopsia with supplementary implantation of a sulcus-fixated intraocular lens. *Graefes Arch Clin Exp Ophthalmol.* 2015;253(6):973–7. doi: 10.1007/s00417-015-3029-8.

8.6 Supplementary data



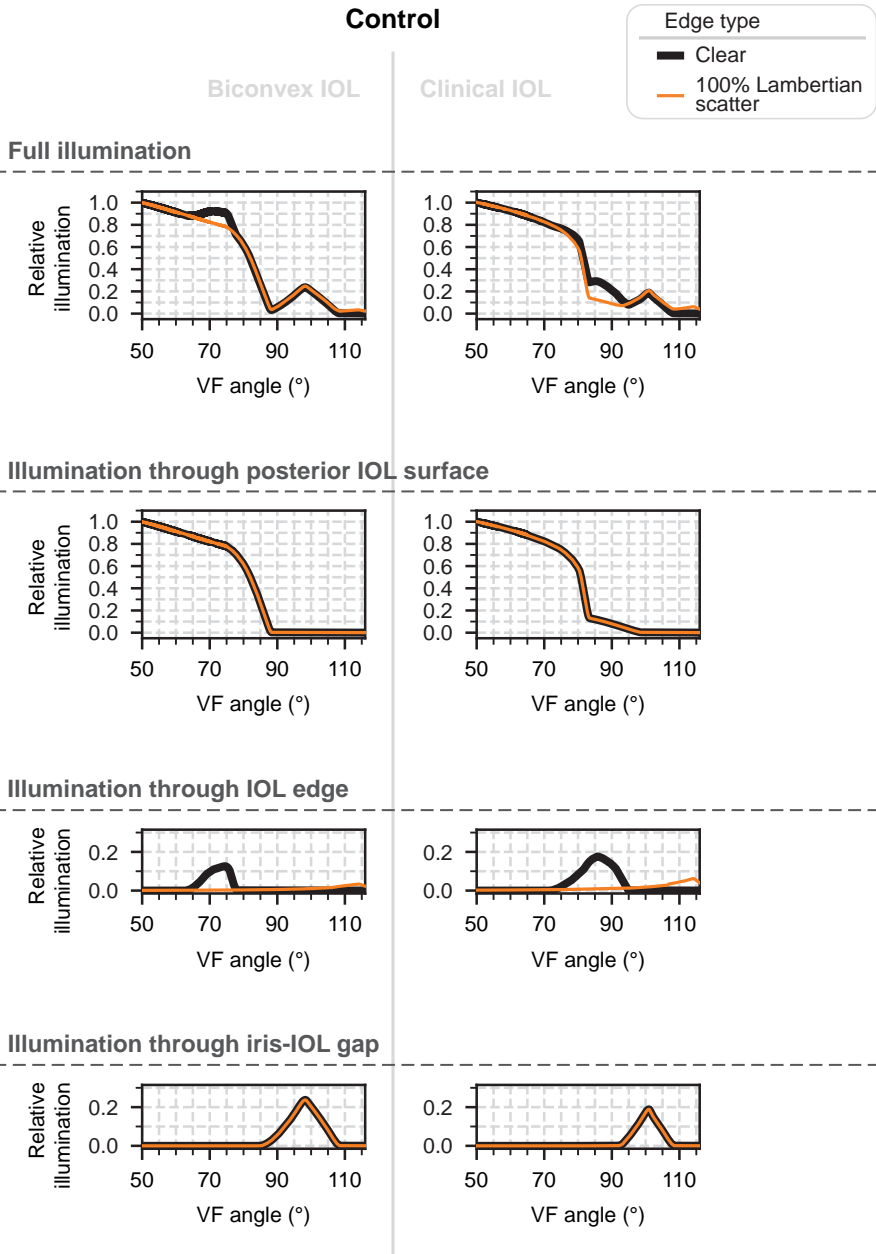
Supplementary Figure 8.1: μ CT scan of the ZCB00. The images were acquired on a SkyScan 1076 μ CT scanner (Bruker Corporation) using a round scanning trajectory with a step size of 0.3 degrees, an exposure of 1250 ms and an isotropic resolution of 9 μ m. The 3D images were automatically segmented using an in-house developed analysis pipeline in MeVisLab (version 3.0.2, MeVis Medical Solutions AG), and the result is shown in red.



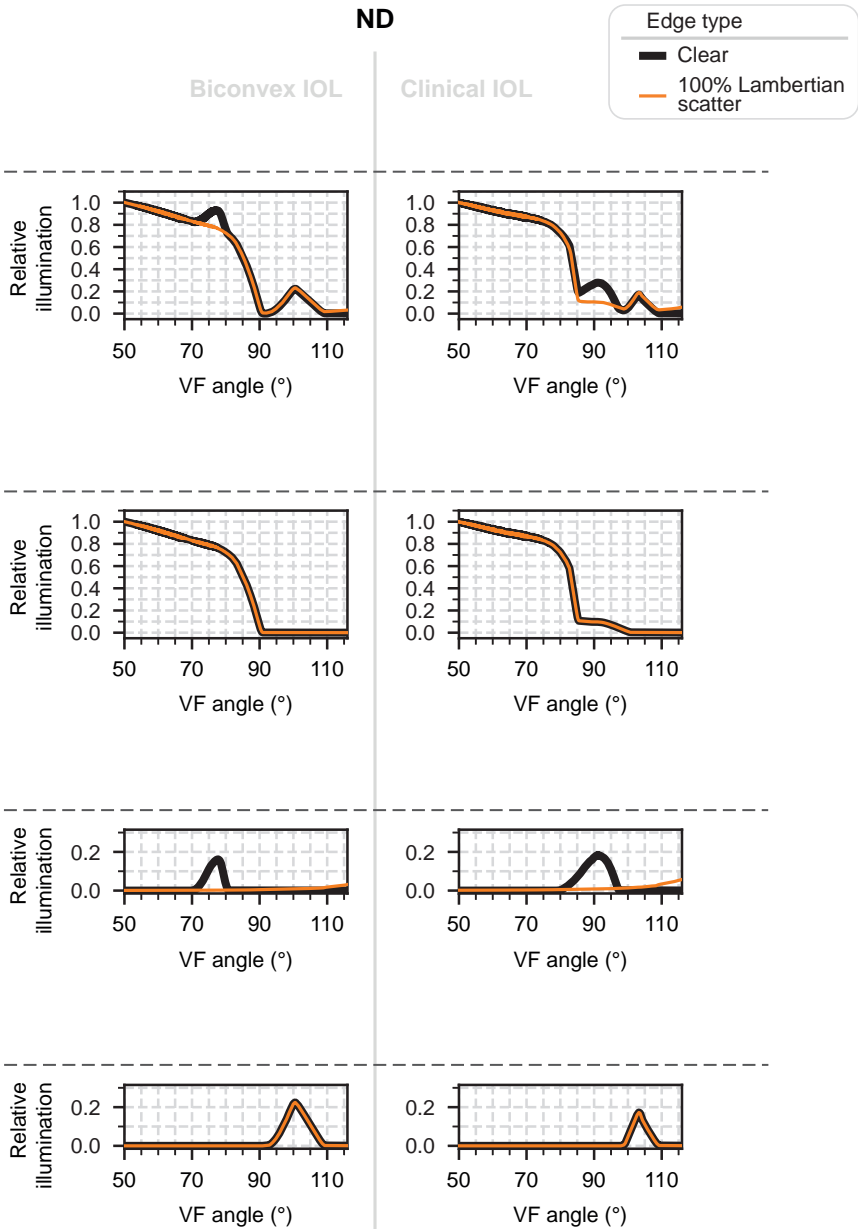
Supplementary Figure 8.2: Relation between visual field angle and retinal location. As the difference between models was less than 0.4 degrees (insert), the average location was used to determine the relation. This resulted in the following, second order polynomial, relationship:

$$\alpha_{VF} = \frac{1.1 * 10^{-3}}{\text{degree}} \alpha_R^2 - 0.60 \alpha_R + 0.17 \text{ degree}$$

with α_R being the retinal angle and α_{VF} the apparent visual field angle. The relationship was extrapolated beyond the measured data for far peripheral retinal angles. VF = visual field.



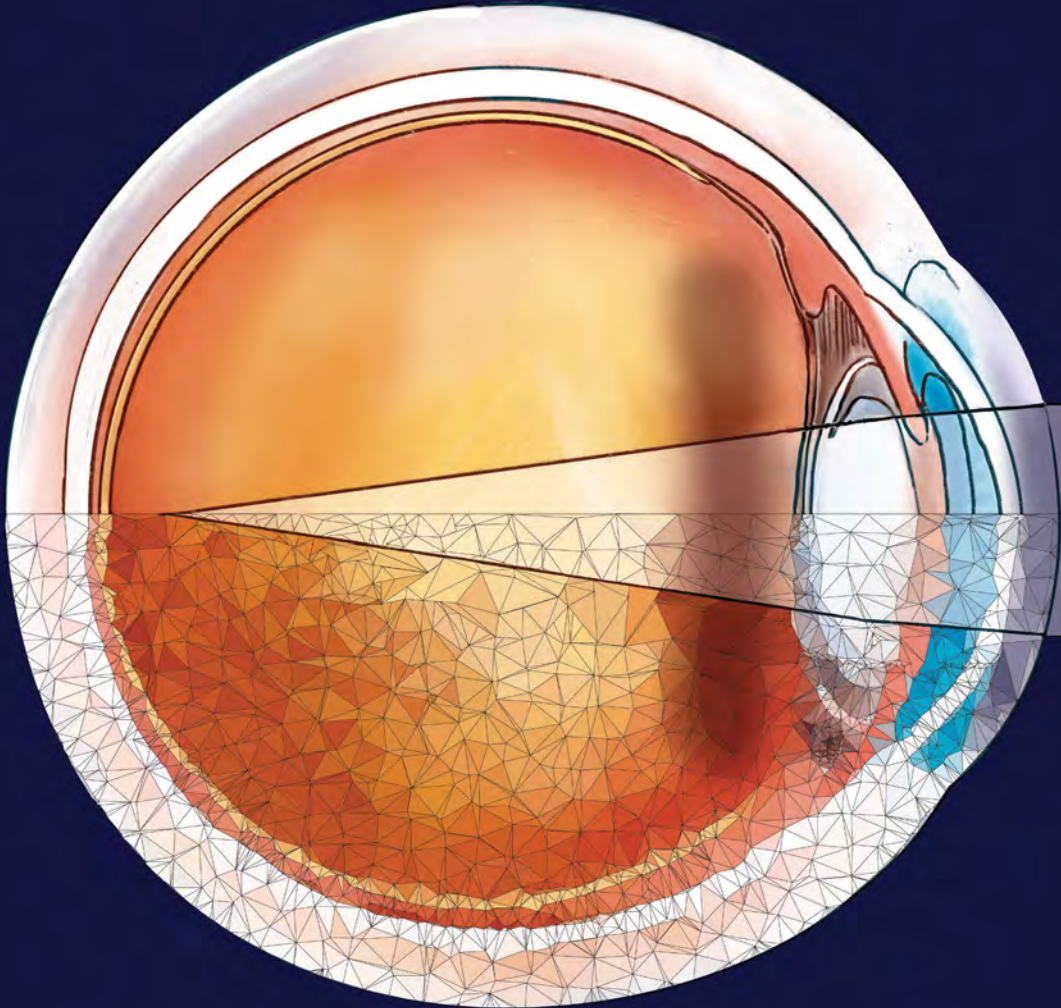
Supplementary Figure 8.3: The influence of specific sets of rays on the peripheral illumination profile with a 100% Lambertian scattering edge. Data is shown for the control (left) and ND (right), as well as for the biconvex IOL (left column) and clinical IOL (right column), both with a clear edge design (black) and a 100% Lambertian scattering edge design (cyan). The complete illumination, illumination by rays through the posterior IOL surface, illumination by rays through the IOL edge and illumination by rays through the iris-IOL gap is shown. Local increases in illumination can clearly be seen for rays passing through the IOL edge and rays passing through the iris-IOL gap. VF = visual field.



Supplementary Figure 8.3 (cont.)

Supplementary Table 8.1: Quantification of the peripheral illumination gap. The apparent visual angle at which the illumination decreases below 0.2 and the angle of maximum illumination through the iris-IOL gap are given for all models. The shadow severity in ND is expressed as % difference with the corresponding control model. The models with ND consistently showed a more severe shadow compared to their equivalent control models. ND = negative dysphotopsia, Con = control.

	Biconvex IOL <i>100% Lambertian scattering edge</i>		Clinical IOL <i>100% Lambertian scattering edge</i>	
	ND	Con	ND	Con
Location of illumination gap <i>(° visual field angle)</i>	89	86	85	83
Location of maximal illumination through iris-IOL gap <i>(° visual field angle)</i>	101	98	103	101
Shadow severity <i>(% difference with control)</i>	17	—	3	—



9

Summary and general discussion

9.1 Summary

Negative dysphotopsia (ND) is a bothersome shadow that can occur in the temporal visual field of the pseudophakic eye.¹⁻³ ND is typically present directly after the implantation of the intraocular lens (IOL).⁴ It disappears over time in most patients, but becomes a chronic problem in some.⁴ When the research for this thesis was initiated, the origin of ND was still unknown but multiple hypotheses on this topic existed.^{3,5-7} All hypotheses assumed that there is a locally reduced or absent illumination of the peripheral retina that resulted in the experience of a shadow in the peripheral visual field. However, each hypothesis assumed a different causal mechanism behind the locally reduced illumination. In addition, it was also unclear why ND disappeared in most patients, which some attributed to opacification of the capsular bag or to neuroadaptation.² Due to the lack of devices that were able to measure the far peripheral vision and therewith quantify ND, these hypotheses could not be confirmed using objective clinical data. Therefore, it was vital to go beyond the sole use of clinical measurements to gain more insight into the origins of ND.

To that end, we initiated the vRESPOND study (CCMO registry number: NL58358.058.16) in cooperation with the European Society of Cataract and Refractive Surgeons (ESCRS), which formed the basis for this thesis. In the vRESPOND study, the eyes of patients with ND and pseudophakic controls were extensively measured using both ophthalmic measurements and ocular MRI scans. The ophthalmic measurements included visual acuity, objective refraction, biometry, anterior segment tomography, peripheral aberrometry, and peripheral visual field measurements. All measurements except the visual field measurements are part of this thesis. The visual field measurements are published elsewhere.⁸ Ultimately, the vRESPOND study aimed at using all performed measurements to create atomically accurate models of the eye and subsequently analyzing the peripheral vision of these models using ray tracing simulations to gain more insight into the origin of ND. To that end, several underlying questions had to be answered:

- I. Are there anatomical differences between the eyes of pseudophakic patients with and without ND that affect peripheral vision?
- II. How to incorporate the anatomy of patients with and without ND into the eye models that are used for peripheral vision simulations?
- III. How do the results of peripheral vision simulations relate to the peripheral vision experienced by the patient?

Question I is addressed in **Chapters 2 and 3**. In these chapters, anatomical measurements of 37 pseudophakic patients with ND and 26 pseudophakic controls were used to assess whether there are anatomical differences between those groups that could affect peripheral vision. The utilized anatomical measurements included anterior segment tomography, ocular biometry, peripheral aberrometry, and high-resolution magnetic resonance imaging (MRI) of the eye. **Chapter 2** contains analyses of the anterior segment of the eye, where significant differences between the patients with ND and the pseudophakic controls were found. Patients with ND had a significantly smaller pupil, a significantly stronger temporal decentration of the pupil center, and a significantly stronger tilt of the iris towards the temporal side of the eye. These anatomical differences were further supported by a significant difference in peripheral aberrations, which could in turn be reproduced using ray tracing simulations that reflected these anatomical differences. **Chapter 3** contains analyses of

the IOL position and retinal shape using high-resolution MRI, which showed no significant differences between patients with ND and pseudophakic controls.

Question II is addressed in **Chapters 4, 5, and 6**. The initial challenge that had to be overcome to perform peripheral vision simulations using eye models that reflect specific anatomy was the combination of a large number of variables required to define an eye model and the computational time required for the subsequent ray tracing simulations. This combination makes peripheral vision simulations for a larger number of eye models both error-prone and time-consuming. Automating the entire process from constructing the eye model to performing the simulations would solve these issues to a large extent. OpticStudio, the software in which the ray tracing simulations are performed, provides an application programming interface (API) that allows users to automate the entire process. This API however requires considerable proficiency in programming, which researchers in the medical field often do not have. Therefore, **Chapter 4** focusses on ZOSPy, an open-source software package that was developed to simplify controlling ray tracing simulations through Python.⁹

The subsequent challenge for question II was determining the optimal methods to model the cornea and retina for peripheral vision simulations, which was addressed in **Chapters 5 and 6**. **Chapter 5** tests 7 different methods to model the cornea based on topography measurements. The results showed that surfaces that are normally used to model the central cornea, such as spheres and ellipsoids, have limited accuracy when modeling the peripheral corneal shape. The surfaces that could describe the peripheral cornea with sufficient accuracy were a surface based on raw topography data, a 6th order Zernike surface, and an 8th order Zernike surface. However, the surface based on raw topography cannot be extrapolated beyond the measured cornea. Moreover, the 8th order Zernike surface was unstable upon that same extrapolation. As the peripheral cornea is not always fully measured by corneal topographers, a certain degree of extrapolation beyond the measured area is essential, rendering the 6th order Zernike surface the best tradeoff between accuracy and stability upon extrapolation. In **Chapter 6**, MRI is used to image the retina, after which the optimal way to obtain the retinal shape from 3D MRI data is determined. The results showed that the peripheral retinal shape is best determined by fitting an ellipsoid over a sufficiently large part, ≥ 220 degrees, of the retinal surface.

Question III is addressed in **Chapter 7**. ND is thought to be the result of a locally reduced illumination of the peripheral retina,^{3,5-7,10} and ray tracing can be used to calculate this retinal illumination in eye models that resemble the anatomy of the eye. However, the clinical relevance of these simulations depends however on how the illuminated retina translates back into the visual field. This translation will likely differ between phakic and pseudophakic eyes, especially since the IOL of a pseudophakic eye refracts light rays differently than the approximately four times thicker crystalline lens of the phakic eye.¹¹ In this chapter, the relation between the actual location of an object in the visual field and the corresponding location where that object illuminates the retina was determined for one phakic eye model and 24 variations of 2 pseudophakic eye models. Subsequently, the retinal illumination of the phakic model was used as a reference to convert the retinal illumination of the pseudophakic models back to the location in the visual field where the object was perceived. The results showed that IOLs can induce a shift of over 5 degrees in the perceived peripheral visual field towards central vision. Such shifts should be considered when performing ray

tracing studies of the peripheral vision in pseudophakic subjects, as they can have a direct impact on the subject's perception.

The results of **Chapters 2-7** are combined in **Chapter 8** to address the main goal of this thesis, gaining more insight into the origin of ND. In this chapter, two eye models were created, one eye model that incorporates the anatomy of patients with ND and one eye model that incorporates the anatomy of pseudophakic controls. Each model was combined with four different IOL designs. Non-sequential ray tracing simulations were used to determine the retinal illumination for each combination of eye model and IOL design. The results showed a gap in the illumination of the peripheral retina in both the ND and the control model. This gap was consistently more severe in the ND model. Moreover, the gap was more severe with specific IOL designs. The maximal difference in the severity of the illumination gap in the ND and the control model was 18%, with a more severe illumination gap in the ND model. These results show that small differences in the ocular anatomy or IOL design affect the peripheral retinal illumination and can increase the severity of ND by up to 18%.

9.2 General discussion

Negative dysphotopsia (ND) was first described in 2000.¹ While the incidence of ND is up to 19% directly after cataract surgery,^{4,12} and up to 3% of patients still report ND one year after the surgery,⁴ little effort was initially made to understand this visual complaint. However, the interest in ND is rising over time. In 2016, when the research for this thesis started, most insights were based on case reports or theoretical analyses and were yet to be confirmed using larger sets of clinical data.^{1,3,5-7,13-15} This lack of clinical data was mainly caused by a lack of objective clinical measurements that could quantify peripheral vision and therewith quantify ND. Thus, other methods to gain additional insight into ND based on clinical data were required. Within this thesis, we sought that insight by creating eye models that reflect the anatomy of either patients with ND or of pseudophakic controls without ND, and subsequently determining if these models had a reduced illumination of the retina that could be perceived as ND using ray tracing simulations (Chapter 8). To achieve this, we not only had to thoroughly analyze the anatomy of pseudophakic eyes with and without ND, (Chapters 2 and 3) but also develop methods to perform a large number of peripheral vision simulations using eye models that incorporate that anatomy (Chapters 4-6) as well as methods to relate these simulations to the patients' experience (Chapter 7). The knowledge that was obtained within that process is not only relevant for research towards ND but also holds relevance for other research fields. Therefore, this general discussion is divided into two parts, *Negative dysphotopsia* and *Relevance outside the field of negative dysphotopsia*.

Negative dysphotopsia

Under
embargo

Under
embargo

Under
embargo

Under
embargo

Under
embargo

Under
embargo

Under
embargo

Relevance outside the field of negative dysphotopsia

Other applications of this work

The insights into accurately modeling the eye for peripheral vision simulations (Chapters 5 and 6) as well as the possibility to programmatically control these simulations through ZOSP_y (Chapter 4) hold relevance for multiple other research topics besides ND. Using these methods, it has already been shown that the extent of an intraocular tumor can be overestimated during tantalum-clip surgery (Figure 9.1A).¹⁶

Furthermore, they could be used to improve the accuracy of ophthalmic imaging devices, for instance by correcting central and peripheral fundus imaging for any scaling or distortion caused by the optics of the eye (Figure 9.1B).¹⁷ In addition, they can be used to gain more insight into the effect of peripheral refraction on myopia development in children.¹⁸ Finally, they can also be applied to improve the outcome of cataract surgery in special cases, for example by simulating the outcome of various IOL types for patients with a keratoconus to determine the optimal IOL for implantation.

Modeling the peripheral anatomy of the eye

This thesis relied heavily on analyzing eye models using ray tracing simulations to quantify the peripheral vision of the eye. The accuracy of these simulations, and thus their clinical relevance, depends on how well the eye model matches the actual peripheral ocular anatomy. The results of this thesis provide multiple insights into modeling that peripheral anatomy correctly. Overall, the structures that have to be modeled accurately include the cornea, the iris, and the retina. In addition, the IOL, which is not an anatomical but rather an artificial structure, should also be modeled accurately.

The cornea, the most dominant refractive component of the eye,¹⁹ is often modeled using either a spherical or an ellipsoidal surface.^{10,20,21} These surfaces can provide a reasonable description of the central cornea. However, the description of the peripheral cornea can be inaccurate, which can result in large errors in peripheral vision simulations (Chapter 5). Some studies have chosen to improve the accuracy of the cornea model by using raw topography data,^{22,23} which theoretically provides the most accurate model of the corneal surface. However, as the topographers do not provide full corneal coverage and the raw data cannot be extrapolated, this method limits the extent to which the peripheral vision can be analyzed. Chapter 5 showed that higher order Zernike surfaces are able to approximate the full corneal geometry with decent accuracy and can also be extrapolated beyond the area covered by the topographer. Therefore, these Zernike surfaces should be used to model the cornea for peripheral vision simulations.

The iris is often modeled as an annulus with no thickness that is oriented perpendicular to the optical or visual axis.^{10,20,21,24} This is valid for simulations of central vision as light is passing through the pupil in a convergent manner. However, Chapter 8 showed that the physical space between the iris and the IOL is of importance for peripheral visual complaints. Furthermore, Chapter 2 showed that the iris can have a slight tilt with respect to the visual axis, and ?? shows the relevance of this tilt for the illumination of the peripheral retina. Therefore, both the iris thickness and the tilt of the iris should be accounted for when simulating far peripheral vision, especially when assessing complaints such as ND.

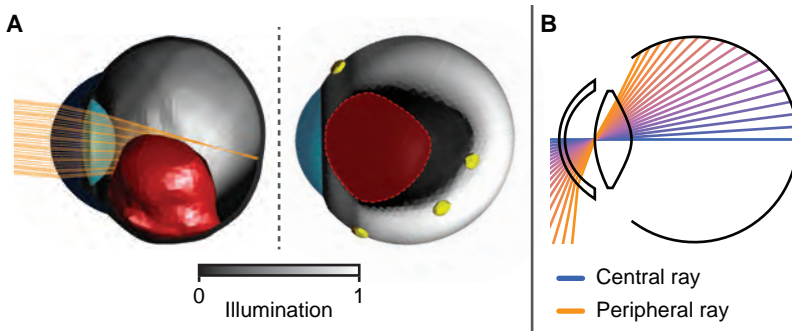


Figure 9.1: Other applications of this work. A) Ray tracing analysis of eye with an intraocular tumour. Left: analysis showing that the tumour (red) casts a shadow). Right: simulation result showing that the tantalum clip (yellow) is placed near the boundary of the shadow rather than near the boundary of the tumour (red). B) Ray tracing analysis used to evaluate scaling and distortion induced by the optics of the eye for central and peripheral rays of light.

Theoretically, modeling the IOL should not be a problem as the IOL is artificial and its design should thus be known. However, these designs are not publicly available nor are they easily provided by the manufacturers. As a result, ray tracing studies often have to revert to in-house developed IOL designs rather than the actual IOL designs. Given the often complex peripheral shape of clinically used IOLs, this affects the accuracy of peripheral vision simulations.

Finally, the retina is often modeled using a spherical surface,^{10,20,25} while it generally has an ellipsoidal shape (chapter 6). This difference is of little importance for central vision simulations as these simulations are affected to a far greater extent by the axial position of the retina than by its peripheral shape. For example, changing the axial position of the retina by 1 mm would induce a change of about 3 Diopter in central refraction.²⁶ However, if a similar relation is assumed for peripheral vision and that assumption is combined with the large variation in peripheral retinal shapes (Chapters 3 and 6, ??), it is clear that the peripheral retinal shape is important for peripheral vision simulations. One of the challenges is however the lack of techniques to measure the retinal shape in a clinical setting. Thus far, research has proposed to either use off-axis laser interferometry,²⁷⁻³⁰ or MRI.³¹⁻³³ While off-axis laser interferometry could be performed with a slight adjustment of current clinical devices, it is only able to measure the central 35 degrees of the retina.²⁶ MRI, on the other hand, can be used to determine the far peripheral retinal shape (Chapters 3 and 6), but is generally not available for this purpose in a clinical setting. Some measurement devices that are still under development, such as a small low-field MRI scanner,³⁴ have the potential to be used for this purpose and might change the future of ocular modeling.

Programmatically controlling ray tracing simulations

This thesis required the analysis of many eye models using ray tracing simulations. As creating an eye model requires the specification of many variables and one has to wait for the ray tracing simulation to finish before the next eye model can be created, this process would have been both error-prone and time-consuming if done manually. Therefore, the entire process was automated using the Application Programming Interface (API) of OpticStudio.

However, interacting with this API is complex and requires considerable proficiency in programming. This will likely limit the number of researchers that use this API. Therefore, we have created ZOSPy,⁹ an open-source software package that greatly reduces the complexity of interacting with the API, as described in Chapter 4. ZOSPy allows researchers to automate optical modeling and ray tracing simulations without investing considerable time in learning how to do so. Thus far, ZOSPy has already been used and improved by multiple contributors.

Standard for peripheral vision simulations

A large part of this thesis is dedicated to improving the clinical relevance of ray tracing simulation results by modeling the eye as accurately as possible, as this improves the agreement between the ray tracing results and the actual functioning of the human eye. However, this agreement does not only depend on the accuracy of the eye model but also on the settings that were used for these simulations. These settings do not only include the choice between sequential and non-sequential ray tracing, but also settings such as the definition of the input field, the definition of the aperture, and the use of ray aiming. Since there is no gold standard, each research project has to determine appropriate settings by itself. Furthermore, the chosen settings are often not fully reported, which hinders the comparison of the results of different studies. Within this thesis, we have strived to report the settings as clearly as possible, but acknowledge that other researchers might have made other choices. Therefore, we advocate the creation of a standard for vision simulations, as we believe that this would greatly improve the scientific value of ray tracing simulations.

Open Science

ZOSPy, the software package described in Chapter 4, furthermore has the potential to contribute to Open Science. Scientific publications based on ray tracing simulations do not always provide limited insight in their exact methodology. As ZOSPy allows users to write clear and concise code to perform simulations, this code can easily be shared between scientist or attached to a scientific publication, providing complete insight in the exact methodology. The example folder in the ZOSPy repository already shows the potential of this feature. This would not only be a step forward for studies within field of ophthalmology, but also for studies in other fields.

9.3 Concluding remarks

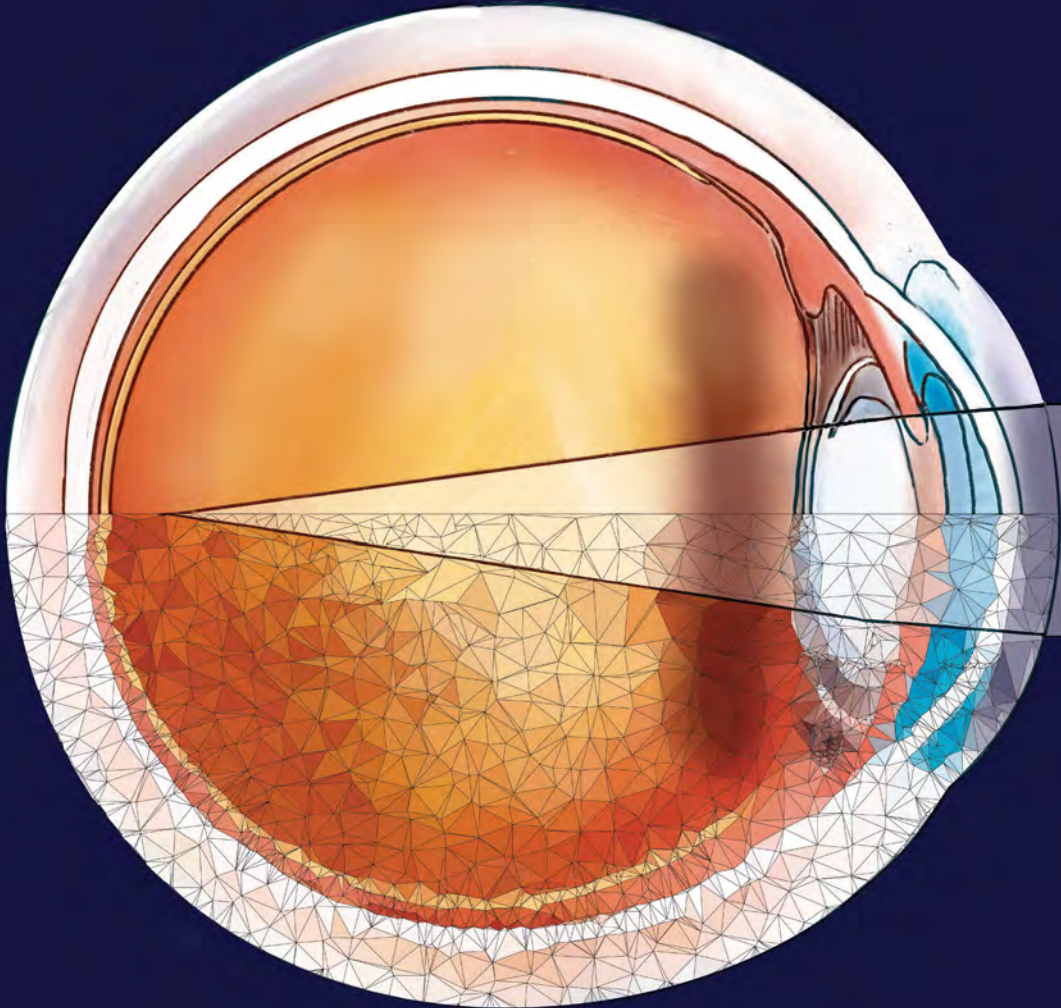
The exact nature of negative dysphotopsia (ND) was unclear for a long time. This thesis has provided valuable new insight into the origin of ND. Not only did it use ray tracing simulations based on clinical data to confirm the hypothesis that ND is caused by a gap in the illumination of the peripheral retina,¹⁰ but it also introduced nuance into that hypothesis by showing that that same gap is, to a lesser extent, also present on the retina of pseudophakic patients without ND.

These insights could not have been obtained without the scientific reports published by others, as this thesis built upon that knowledge. However, various methods had to be developed to obtain the results of this thesis. These methods mainly regarded peripheral vision simulations using personalized eye models. By thoroughly describing our methods in scientific manuscripts and making part of the developed software available open source,⁹ we encourage other researchers to in turn build upon our developed methods and move towards personalized vision simulations. These personalized vision simulations will not only provide more insight into the origin of ND, but also facilitate the improvement of treatments for ND and even the development of preventative measures.

9.4 References

1. Davison JA. Positive and negative dysphotopsia in patients with acrylic intraocular lenses. *J Cataract Refract Surg.* 2000;26(9):1346–55. doi: 10.1016/s0886-3350(00)00611-8.
2. Henderson BA, Geneva I. Negative dysphotopsia: A perfect storm. *J Cataract Refract Surg.* 2015;41(10):2291–312. doi: 10.1016/j.jcrs.2015.09.002.
3. Holladay JT, Zhao H, Reisin CR. Negative dysphotopsia: the enigmatic penumbra. *J Cataract Refract Surg.* 2012;38(7):1251–65. doi: 10.1016/j.jcrs.2012.01.032.
4. Osher RH. Negative dysphotopsia: long-term study and possible explanation for transient symptoms. *J Cataract Refract Surg.* 2008;34(10):1699–707. doi: 10.1016/j.jcrs.2008.06.026.
5. Simpson MJ. Double image in far peripheral vision of pseudophakic eye as source of negative dysphotopsia. *J Opt Soc Am A Opt Image Sci Vis.* 2014;31(12):2642–9. doi: 10.1364/josaa.31.002642.
6. Masket S, Fram NR. Pseudophakic negative dysphotopsia: Surgical management and new theory of etiology. *J Cataract Refract Surg.* 2011;37(7):1199–207. doi: 10.1016/j.jcrs.2011.02.022.
7. Hong X, Liu Y, Karakelle M, Masket S, Fram NR. Ray-tracing optical modeling of negative dysphotopsia. *J Biomed Opt.* 2011;16(12):125001. doi: 10.1117/1.3656745.
8. Rozendal LRW, Vught L van, Luyten GPM, Beenakker JWM. The Value of Static Perimetry in the Diagnosis and Follow-up of Negative Dysphotopsia. *Optom Vis Sci.* 2022;99(8):645–651. doi: 10.1097/OPX.0000000000001918.
9. Vught L van, Haasjes C, Beenakker JWM. *ZOSP*y. Computer Program. 2023. doi: 10.5281/zenodo.7759530.
10. Holladay JT, Simpson MJ. Negative dysphotopsia: Causes and rationale for prevention and treatment. *J Cataract Refract Surg.* 2017;43(2):263–275. doi: 10.1016/j.jcrs.2016.11.049.
11. Jaeken B, Lundstrom L, Artal P. Fast scanning peripheral wave-front sensor for the human eye. *Opt Express.* 2011;19(8):7903–13. doi: 10.1364/oe.19.007903.
12. Makhotkina NY, Nijkamp MD, Berendschot TTJM, Borne B van den, Nuijts RMMA. Effect of active evaluation on the detection of negative dysphotopsia after sequential cataract surgery: discrepancy between incidences of unsolicited and solicited complaints. *Acta Ophthalmologica.* 2018;96(1):81–87. doi: 10.1111/aos.13508.
13. Cooke DL. Negative dysphotopsia after temporal corneal incisions. *J Cataract Refract Surg.* 2010;36(4):671–2. doi: 10.1016/j.jcrs.2010.01.004.
14. Cooke DL, Kasko S, Platt LO. Resolution of negative dysphotopsia after laser anterior capsulotomy. *J Cataract Refract Surg.* 2013;39(7):1107–9. doi: 10.1016/j.jcrs.2013.05.002.
15. Makhotkina NY, Berendschot TT, Beckers HJ, Nuijts RM. Treatment of negative dysphotopsia with supplementary implantation of a sulcus-fixated intraocular lens. *Graefes Arch Clin Exp Ophthalmol.* 2015;253(6):973–7. doi: 10.1007/s00417-015-3029-8.
16. Jaarsma-Coes MG, Ferreira TA, Marinkovic M, Vu THK, Vught L van, Haren GR van, Rodrigues MF, Klaver YLB, Verbist BM, Luyten GPM, Rasch CRN, Beenakker JWM. Comparison of Magnetic Resonance Imaging-Based and Conventional Measurements for Proton Beam Therapy of Uveal Melanoma. *Ophthalmol Retina.* 2023;7(2):178–188. doi: 10.1016/j.oret.2022.06.019.
17. Haasjes C, Pors LJ, Beenakker JWM. “Mapping of fundus photography to 3D imaging for ocular radiotherapy”. In: *European Association for Vision and Eye Research (EVER)*.
18. Charman WN, Radhakrishnan H. Peripheral refraction and the development of refractive error: a review. *Ophthalmic Physiol Opt.* 2010;30(4):321–38. doi: 10.1111/j.1475-1313.2010.00746.x.
19. Atchison DA, Smith G. Refracting components: cornea and lens. In: DA Atchison, G Smith, eds. *Optics of the Human Eye*. Butterworth-Heinemann; 2000:11–20. doi: 10.1016/b978-0-7506-3775-6.50006-7.
20. Escudero-Sanz I, Navarro R. Off-axis aberrations of a wide-angle schematic eye model. *J Opt Soc Am A Opt Image Sci Vis.* 1999;16(8):1881–91. doi: 10.1364/josaa.16.001881.
21. Polans J, Jaeken B, McNabb RP, Artal P, Izatt JA. Wide-field optical model of the human eye with asymmetrically tilted and decentered lens that reproduces measured ocular aberrations. *Optica.* 2015;2(2):124–134. doi: 10.1364/optica.2.000124.
22. Canovas C, Abenza S, Alcon E, Villegas EA, Marin JM, Artal P. Effect of corneal aberrations on intraocular lens power calculations. *J Cataract Refract Surg.* 2012;38(8):1325–32. doi: 10.1016/j.jcrs.2012.03.033.

23. Canovas C, Artal P. Customized eye models for determining optimized intraocular lenses power. *Biomed Opt Express*. 2011;2(6):1649–62. doi: 10.1364/boe.2.001649.
24. Simpson MJ. Simulated images of intraocular lens negative dysphotopsia and visual phenomena. *J Opt Soc Am A Opt Image Sci Vis*. 2019;36(4):B44–B51. doi: 10.1364/josaa.36.000b44.
25. Liou HL, Brennan NA. Anatomically accurate, finite model eye for optical modeling. *J Opt Soc Am A Opt Image Sci Vis*. 1997;14(8):1684–95. doi: 10.1364/josaa.14.001684.
26. Atchison DA, Jones CE, Schmid KL, Pritchard N, Pope JM, Strugnell WE, Riley RA. Eye shape in emmetropia and myopia. *Invest Ophthalmol Vis Sci*. 2004;45(10):3380–6. doi: 10.1167/iovs.04-0292.
27. Atchison DA, Charman WN. Can partial coherence interferometry be used to determine retinal shape? *Optom Vis Sci*. 2011;88(5):E601–7. doi: 10.1097/oxp.0b013e318212ae56.
28. Verkicharla PK, Mathur A, Mallen EA, Pope JM, Atchison DA. Eye shape and retinal shape, and their relation to peripheral refraction. *Ophthalmic Physiol Opt*. 2012;32(3):184–99. doi: 10.1111/j.1475-1313.2012.00906.x.
29. Verkicharla PK, Suheimat M, Pope JM, Sepehrband F, Mathur A, Schmid KL, Atchison DA. Validation of a partial coherence interferometry method for estimating retinal shape. *Biomed Opt Express*. 2015;6(9):3235–47. doi: 10.1364/boe.6.003235.
30. Verkicharla PK, Suheimat M, Schmid KL, Atchison DA. Peripheral Refraction, Peripheral Eye Length, and Retinal Shape in Myopia. *Optom Vis Sci*. 2016;93(9):1072–8. doi: 10.1097/oxp.0000000000000905.
31. Beenakker JWM, Shamonin DP, Webb AG, Luyten GP, Stoel BC. Automated retinal topographic maps measured with magnetic resonance imaging. *Invest Ophthalmol Vis Sci*. 2015;56(2):1033–9. doi: 10.1167/iovs.14-15161.
32. Ferreira TA, Grech Fonk L, Jaarsma-Coes MG, Haren GGR van, Marinkovic M, Beenakker JWM. MRI of Uveal Melanoma. *Cancers (Basel)*. 2019;11(3). doi: 10.3390/cancers11030377.
33. Pope JM, Verkicharla PK, Sepehrband F, Suheimat M, Schmid KL, Atchison DA. Three-dimensional MRI study of the relationship between eye dimensions, retinal shape and myopia. *Biomed Opt Express*. 2017;8(5):2386–2395. doi: 10.1364/boe.8.002386.
34. O'Reilly T, Teeuwisse WM, Gans D de, Koolstra K, Webb AG. In vivo 3D brain and extremity MRI at 50 mT using a permanent magnet Halbach array. *Magn Reson Med*. 2021;85(1):495–505. doi: 10.1002/mrm.28396.





Addendum

Nederlandse samenvatting

Cataract is een vertroebeling van de kristallijne lens van het oog. Dit kan behandeld worden door de eigen kristallijne lens te verwijderen en een kunstmatige intraoculaire lens (IOL) te implanteren op dezelfde plek. Hierna wordt het oog pseudofaak genoemd. Na de implantatie van de IOL ontwikkelen sommige mensen negatieve dysfotopsie (ND), een hinderlijke schaduw in het temporale gezichtsveld van het pseudofake oog. Patiënten waarbij ND ontstaat zijn zich over het algemeen direct na de implantatie van de IOL op bewust van de schaduw. Bij de meeste patiënten verdwijnt ND na verloop van tijd, maar soms wordt het een chronisch probleem. Toen het onderzoek voor deze thesis werd gestart, was het niet bekend wat de oorzaak van ND was, maar bestonden hierover wel meerdere hypothesen. In al deze hypothesen werd uitgegaan van een lokaal verminderde of afwezige belichting van het perifere netvlies van het oog, wat door de patiënt als een schaduw in het perifere gezichtsveld wordt ervaren. Elke hypothese veronderstelde echter een ander causaal mechanisme voor de lokale verminderde belichting van het netvlies. Daarnaast was het ook onduidelijk waarom ND bij de meeste patiënten weer verdween, wat door sommigen werd toegeschreven aan opacificatie van de kapselzak of aan neuroadaptatie. Het ontbreken van apparatuur om het perifere zicht, en daarmee ND, te meten, vormde een aanzienlijke belemmering voor het bevestigen of weerleggen van deze hypothesen op basis van objectieve klinische gegevens. Om een beter inzicht te krijgen in het mechanisme achter het ontstaan van ND was het daarom noodzakelijk om meer dan conventionele klinische metingen te gebruiken.

Daartoe zijn wij in samenwerking met de European Society of Cataract and Refractive Surgeons (ESCRS) de vRESPOND studie gestart (CCMO-registratienummer: NL58358.058.16). Deze studie vormde de basis voor dit proefschrift. In de vRESPOND studie werden de ogen van patiënten met ND en van een pseudofake controlegroep zonder ND uitgebreid in kaart gebracht met zowel oogheelkundige metingen als MRI-scans van het oog. De uitgevoerde oogheelkundige metingen omvatten visusmetingen, objectieve refractiemetingen, biometrie, tomografie van het voorsegment, perifere aberrometrie en perifere gezichtsveldmetingen. Het uiteindelijke doel van de studie was om op basis van de uitgevoerde metingen anatomisch nauwkeurige virtuele oogmodellen te creëren en het perifere zicht van deze modellen te analyseren met behulp van ray tracing simulaties, om zo meer inzicht te krijgen in het ontstaansmechanisme van ND. Daartoe moesten verschillende onderliggende vraagstukken worden beantwoord:

- I. Zijn er anatomische verschillen tussen de ogen van pseudofake patiënten met en zonder ND die het perifere zicht beïnvloeden?
- II. Hoe kan de anatomie van patiënten met en zonder ND verwerkt worden in oogmodellen die worden gebruikt voor simulaties van het perifere zicht?
- III. Hoe verhouden de resultaten van simulaties van het perifere zicht zich tot het perifere zicht dat ervaren wordt door de patiënt?

Vraagstuk I wordt behandeld in **Hoofdstuk 2** en **Hoofdstuk 3**. In deze hoofdstukken worden anatomische metingen van de ogen van 37 patiënten met ND en 26 pseudofake controles gebruikt om te beoordelen of er tussen deze groepen anatomische verschillen zijn die het perifere zicht kunnen beïnvloeden. De metingen die hiervoor worden gebruikt zijn: tomografie van het voorsegment, oculaire biometrie, perifere aberrometrie en hoge resolutie

Magnetic Resonance Imaging (MRI) van het oog. **Hoofdstuk 2** bevat analyses van de anatomie van het voorsegment van het oog. Deze analyses tonen significante verschillen tussen de anatomie van de patiënten met ND en van de pseudofake controles. Patiënten met ND hebben een significant kleinere pupil, een significant sterkere temporale decentratie van het pupilcentrum, en een significant sterkere kanteling van de iris naar de temporale zijde van het oog. Daarnaast tonen de analyses ook een verschil in de perifere aberraties van het oog. Dit verschil kon worden gereproduceerd met behulp van ray tracing simulaties met oogmodellen waarin de gevonden anatomische verschillen waren verwerkt. De simulaties laten zien dat de anatomische verschillen en de verschillen in perifere aberraties in lijn zijn met elkaar. **Hoofdstuk 3** bevat analyses van de positie van de IOL en de vorm van het netvlies op basis van hoge-resolutie MRI. Deze analyses laten geen significante verschillen zien tussen de patiënten met ND en de pseudofake controles.

Vraagstuk II wordt behandeld in de **Hoofdstukken 4, 5 en 6**. De eerste uitdaging voor het meenemen van anatomische variatie in oogmodellen die gebruikt worden voor zichts simulaties is de combinatie van het grote aantal variabelen die gedefinieerd moeten worden om een oogmodel te maken en de benodigde rekentijd voor de daaropvolgende ray tracing simulaties met dat oogmodel. Deze combinatie maakt het uitvoeren van perifere zichts simulaties met een groot aantal oogmodellen zowel foutgevoelig als tijdrovend. In principe zouden deze problemen grotendeels opgelost kunnen worden door het gehele proces te automatiseren. OpticStudio, de software waarin de ray tracing simulaties worden uitgevoerd, biedt de mogelijkheid tot dergelijke automatiseren via een Application Programming Interface (API). Deze API vereist echter een aanzienlijke vaardigheid in programmeren, wat het gebruik lastig maakt voor veel onderzoekers in het medische veld. Daarom wordt **Hoofdstuk 4** ZOSPy beschreven, een open-source softwarepakket dat is ontwikkeld om het automatiseren van ray tracing simulaties via Python te vereenvoudigen.

Op zichzelf is dat softwarepakket niet voldoende om Vraagstuk II op te lossen, dit vereist namelijk ook het bepalen van de optimale methode om het hoornvlies en het netvlies te modelleren voor perifere zichts simulaties. Dat wordt gedaan in **Hoofdstuk 5** en **Hoofdstuk 6**. In **Hoofdstuk 5** worden zeven verschillende methoden getest om het hoornvlies te modelleren op basis van topografische metingen. De resultaten van dit hoofdstuk laten zien dat de soorten oppervlakken die normaal worden gebruikt voor het modelleren van het centrale hoornvlies, zoals een bol of een ellipsoïde, een beperkte nauwkeurigheid hebben als ze worden gebruikt voor het modelleren van het perifere hoornvlies. De oppervlakken die de vorm van het perifere hoornvlies wel met adequate nauwkeurigheid konden beschrijven waren een 6^e orde Zernike-oppervlak, een 8^e orde Zernike-oppervlak, en een oppervlak direct gebaseerd op de ruwe data van de topografiemeting. Aangezien het perifere hoornvlies niet altijd volledig gemeten wordt door corneatopografen, is de mogelijkheid om te extrapoleren buiten het gemeten gebied essentieel voor het modelleren van dit deel van het hoornvlies. Het oppervlak gebaseerd op de ruwe data ondersteunt dergelijke extrapolatie niet, en het 8^e orde Zernike-oppervlak vertoont instabiliteit bij diezelfde extrapolatie. Uiteindelijk toont het 6^e orde Zernike-oppervlak de beste balans tussen nauwkeurigheid in de beschrijving van de perifere cornea en stabiliteit bij extrapolatie buiten het gemeten gebied, waarmee dit het optimale oppervlak is om het perifere hoornvlies te modelleren voor perifere zichts simulaties. In **Hoofdstuk 6** wordt MRI gebruikt om het netvlies in beeld te brengen, waarna wordt bepaald wat de optimale manier is om de perifere netvliesvorm te bepalen op basis van de driedimensionale MRI-data. De resultaten tonen aan dat de perifere vorm van het

netvlies het best kan worden bepaald door een ellipsoïde te fitten over minimaal 220 graden van het netvliesoppervlak.

Vraagstuk III wordt behandeld in **Hoofdstuk 7**. De hypothesen rondom het mechanisme achter ND gaan uit van een lokaal verminderde belichting van het netvlies, en ray tracing simulaties met modellen van het oog kunnen worden gebruikt om de belichting van het perifere netvlies te berekenen. De klinische relevantie van deze simulaties hangt echter af van hoe het verlichte netvlies zich verhoudt tot het gezichtsveld dat wordt waargenomen. Deze verhouding zal waarschijnlijk verschillen tussen ogen met een kristallijne lens en pseudofake ogen met een IOL, zeker omdat de refractie van perifere lichtstralen zal verschillen tussen de IOL en de vier keer dikkere kristallijne lens. In dit hoofdstuk wordt voor een oogmodel met een kristallijne lens en 24 variaties van 2 pseudofake oogmodellen bepaald wat de relatie is tussen de fysieke locatie van een object rondom het oog en de locatie op het netvlies die wordt belicht door lichtstralen vanuit dat object. Vervolgens wordt de netvliesbelichting van het oogmodel met de kristallijne lens gebruikt als referentie om de netvliesbelichting van de pseudofake oogmodellen om te zetten in het gezichtsveld dat wordt waargenomen. Deze berekeningen laten zien dat het vervangen van de kristallijne lens voor een IOL het waargenomen perifere gezichtsveld meer dan 5 graden richting het centraal kan verschuiven, wat kan beïnvloeden hoe het gezichtsveld en eventuele gezichtsveldklachten worden ervaren. Ray tracing studies van het perifere zicht moeten daarom rekening houden met dergelijke verschuivingen.

De resultaten van de eerder hoofdstukken worden gecombineerd in **Hoofdstuk 8** om zo het uiteindelijke doel van dit proefschrift te kunnen realiseren, namelijk het verkrijgen van meer inzicht in het ontstaansmechanisme van ND. In dit hoofdstuk worden twee oogmodellen gemaakt, een met de anatomische eigenschappen van patiënten met ND en een met de anatomische eigenschappen van pseudofake controles. Elk oogmodel wordt daarna gecombineerd met vier verschillende IOL-ontwerpen. Vervolgens worden niet-sequentiële ray tracing simulaties gebruikt om de belichting van het netvlies te berekenen voor elke combinatie van oogmodel en IOL-ontwerp. Deze simulaties laten een lokaal verminderde belichting van het perifere netvlies zien in zowel het oogmodel voor patiënten met ND als het oogmodel voor pseudofake controles. De mate van lokaal verminderde belichting is afhankelijk van het IOL-ontwerp en is consequent heviger in het oogmodel voor patiënten met ND, met een maximaal verschil van 18% tussen de oogmodellen. Dit laat zien dat kleine anatomische verschillen en verschillen in IOL-ontwerp van invloed zijn op de belichting van de perifere retina, wat de ernst van ND met 18% kan verergeren.

Uiteindelijk worden in **Hoofdstuk 9** de verdere implicaties van deze thesis besproken. De resultaten van deze thesis bevestigen niet alleen de hypothese dat ND wordt veroorzaakt door een lokaal verminderde belichting van de perifere retina, maar geven daarbij ook de kanttekening dat deze lokaal verminderde belichting in mindere mate ook optreedt in pseudofake ogen zonder ND. De logische vervolgstap binnen het onderzoeksveld is het uitvoeren van gepersonaliseerde zichts simulaties. Om dat te stimuleren wordt de methodologie achter de uitgevoerde simulaties uitgebreid beschreven in deze thesis en is een deel van de ontwikkelde software open-source beschikbaar. Zo kunnen via gepersonaliseerde zichts simulaties voor individuele patiënten met en zonder ND niet alleen additioneel inzicht in ND verkregen worden, en kunnen er ook behandeling of preventieve maatregelen worden ontwikkeld.

List of publications

van Vught L, Haasjes C, Beenakker JWM. ZOSPy: optical ray tracing in Python through OpticStudio. *Journal of Open Source Software*. 2024;9(96):5756. doi: 10.21105/joss.05756.

Makhotkina NY, Nijkamp MD, Berendschot TTJM, van den Borne B, Aelen-van Kruchten M, **van Vught L**, Beenakker JWM, Krijgh E, Aslam T, Pesudovs K, Nuijts R. Measuring quality of vision including negative dysphotopsia. *Acta Ophthalmol*. 2024;102(4):e510–e519. doi: 10.1111/aos.15762.

van Vught L, Luyten GPM, Beenakker JWM. Peripheral visual field shifts after intraocular lens implantation. *J Cataract Refract Surg*. 2023;49(12):1270–1274. doi: 10.1097/j.jcrs.0000000000001299.

Jaarsma-Coes MG, Ferreira TA, Marinkovic M, Vu THK, **van Vught L**, van Haren GR, Rodrigues MF, Klaver YLB, Verbist BM, Luyten GPM, Rasch CRN, Beenakker JWM. Comparison of Magnetic Resonance Imaging-Based and Conventional Measurements for Proton Beam Therapy of Uveal Melanoma. *Ophthalmol Retina*. 2023;7(2):178–188. doi: 10.1016/j.oret.2022.06.019.

van Vught L, Que I, Luyten GPM, Beenakker JWM. Effect of anatomical differences and intraocular lens design on negative dysphotopsia. *J Cataract Refract Surg*. 2022;48(12):1446–1452. doi: 10.1097/j.jcrs.0000000000001054.

Islamaj E, **van Vught L**, Jordaan-Kuip CP, Vermeer KA, Ferreira TA, de Waard PWT, Lemij HG, Beenakker JWM. Magnetic resonance imaging reveals possible cause of diplopia after Baerveldt glaucoma implantation. *PLoS One*. 2022;17(10):e0276527. doi: 10.1371/journal.pone.0276527.

Rozendal LRW, **van Vught L**, Luyten GPM, Beenakker JWM. The Value of Static Perimetry in the Diagnosis and Follow-up of Negative Dysphotopsia. *Optom Vis Sci*. 2022;99(8):645–651. doi: 10.1097/oxp.0000000000001918.

Keene KR, **van Vught L**, van de Velde NM, Ciggaar IA, Notting IC, Genders SW, Verschuuren JJGM, Tannemaat MR, Kan HE, Beenakker JWM. The feasibility of quantitative MRI of extra-ocular muscles in myasthenia gravis and Graves' orbitopathy. *NMR Biomed*. 2021;34(1):e4407. doi: 10.1002/nbm.4407.

van Vught L, Shamonin DP, Luyten GPM, Stoel BC, Beenakker JWM. MRI-based 3D retinal shape determination. *BMJ Open Ophthalmol*. 2021;6(1):e000855. doi: 10.1136/bmjophth-2021-000855.

van Vught L, Dekker CE, Stoel BC, Luyten GPM, Beenakker JWM. Evaluation of intraocular lens position and retinal shape in negative dysphotopsia using high-resolution magnetic resonance imaging. *J Cataract Refract Surg*. 2021;47(8):1032–1038. doi: 10.1097/j.jcrs.0000000000000576.

van Vught L, Luyten GPM, Beenakker JWM. Distinct differences in anterior chamber configuration and peripheral aberrations in negative dysphotopsia. *J Cataract Refract Surg*. 2020;46(7):1007–1015. doi: 10.1097/j.jcrs.0000000000000206.

Curriculum Vitae

Luc van Vught was born on the 26th of September in Berkel en Rodenrijs, the Netherlands. He began his bachelor's in medicine at Leiden University in 2012. In the final year of his bachelor's degree, he completed a small literature research project at the Department of Ophthalmology at Leiden University Medical Center. This experience sparked his interest in ophthalmology. Consequently, he started the research component of his master's in medicine at the same department in 2015. His research addressed dysphotopsia and was conducted under the supervision of dr. J.W.M. Beenakker and prof. dr. G.P.M. Luyten. The resulting master's thesis, titled *Patient-specific Eye Models for Resolving Pseudophakic Dysphotopsia*, was nominated for the Leiden University Thesis Awards.

Upon completing the research component of his master's degree, he was granted the opportunity to continue in the same line of research as a PhD candidate. He decided to fully embrace this opportunity, temporarily putting the clinical component of his master's degree on hold. From 2016 to the end of 2020, he worked full-time on his PhD, aimed at uncovering the origin of negative dysphotopsia. This thesis is the result of that work. In January 2021, Luc resumed the clinical portion of his master's degree to become a medical doctor while continuing his PhD research part-time. In 2023, he completed his master's degree with honors, after which he began his residency in ophthalmology at the Leiden University Medical Center.

Acknowledgements

This thesis would not have been possible without the support of many people. I want to take this opportunity to express my gratitude towards them.

First and foremost, I have to extend a huge thanks to all patients and volunteers for participating in our research. I am very grateful that so many people are willing to support science.

Then, I also owe great gratitude to my supervisors dr. Beenakker and prof. dr. Luyten. Dear dr. Beenakker, dear Jan-Willem, thank you for all the insightful scientific and personal discussions, for your mentorship throughout the years, and for granting me the freedom to obtain new skills and apply them to my research. I am forever grateful that you accepted me as your PhD student, it has opened up a new world for me. Dear prof. dr. Luyten, dear Gré, you have not only taught me a lot about the eye but also about myself. I admire how you always managed to make the department feel like a big family, and I felt like a valued member of that family from day one.

To all members of the MReye research group: thank you so much! It was amazing to see this group grow over time. Myriam, Kevin, Lisa, Michael, Corné, and Lorna, thank you for all the valuable discussions regarding different aspects of my research. It is inspiring to see people with different backgrounds work together so well on imaging of the eye.

I am equally thankful to all members of the C.J. Gorter Center. While the group is too large to thank each of you individually, know that I appreciate all of you. A special thanks to Joep, Mathijs, Paul, Jedrek, and Jeroen for providing me with such a welcoming and knowledgeable office when I started my research. Furthermore, I have to thank Melissa, Marc, Thijs, Sanneke, Kirsten, Thomas, Marjolein, Celine, Lydiane, Leon, Léonie, and everyone else for all your help and support over the years! Andrew and Thijs, I am glad to have been part of your amazing group and grateful for all the runs that helped me clear my mind. Wouter, thank you for the countless engaging discussions we had about MR safety. Last but not least, Tom and Ece. We jokingly named ourselves the Gorter Inhabitants once as we all were working very long hours, and I cannot think of better people to do that with!

My gratitude also extends to all members of the Department of Ophthalmology of the Leiden University Medical Center! As said before, the department feels like a big family, and I am glad to have been a part of that. A special thanks to the members of the FotoFunctie, especially Christine and Noor, for your help with acquiring all measurements, to Vera and Ferda for your help with trial coordination, and to Annelies and all other members of the staff secretariat for help with all the other logistical matter. Elon, thank you for always having an open door and being willing to share your thoughts. Niels, Thomas, Cindy, Thanh, Danial, and the other PhD students, I truly appreciated our insightful discussions and conference trips. Ingrid, Zoraida, Gwyneth, and all other (current and former) residents and ophthalmologists, thank you for all the clinical lessons and insights.

Furthermore, I could not have done this without the invaluable support of everyone outside of work. Daan, Alexandre, Bas, Jorrit, Joris, and Joren, you have been a constant factor in my life ever since 2012. Thank you for giving me a place to laugh and vent. Joost (Wensveen), although we do not see each other often, our conversations are always invigorating and inspiring. Siddiq, Scott, and Joost (Kempers), thank you for the unconditional support and

for helping me recharge. Jerome, I could not wish a better neighbor than you. Our conversations, in which we briefly solve all the problems in the world, really help me with taking my mind off work.

Dear Mom and Dad, thank you for your endless support and faith in me. I am so grateful for everything you have done for me and for all the opportunities you have given me. Tom, Lieke, Mara, and Maeve, thank you for always cheering me on. I couldn't ask for a better family.

To Winston and Lily - although you will never be able to read this - know that I am so glad to have you. Our daily walks help me to find balance. Winston, I want to give a special thanks for pulling me through the lockdown of 2020.

And finally, to my dear Anushiya. The last few years have been a rollercoaster, and I cannot think of anyone better to have had by my side. You have changed my life for the better. I am looking forward to our future adventures. Thank you for everything.

Negative dysphotopsia is a bothersome shadow in the peripheral visual field that can occur after cataract surgery. This thesis aims at uncovering its origin. To do so, the ocular anatomy of pseudophakic patients with and without negative dysphotopsia is extensively measured. These anatomical measurements are incorporated in geometric eye models, which are then analyzed using ray tracing simulations. The results of these simulations provide valuable insights into the origin of negative dysphotopsia.
